

Designing Functional 2D and 3D Structures: From Ultrathin Coatings to Laser Lithography

Zur Erlangung des akademischen Grades eines

DOKTORS DER NATURWISSENSCHAFTEN

(Dr. rer. nat.)

von der KIT-Fakultät für Chemie und Biowissenschaften

des Karlsruher Instituts für Technologie (KIT)

genehmigte

DISSERTATION

von

M. Sc. Markus Michael Zieger

aus

Pforzheim, Deutschland

1. Referent: Prof. Dr. Christopher Barner-Kowollik

2. Referent: Prof. Dr. Hans-Achim Wagenknecht

Tag der mündlichen Prüfung: 18.07.2018

Die vorliegende Arbeit wurde vom Februar 2015 bis Juni 2018 unter der Anleitung von Prof. Dr. Christopher Barner-Kowollik und Prof. Dr. Martin Wegener am Karlsruher Institut für Technologie (Universitätsbereich) angefertigt.

In tiefer Dankbarkeit meiner Familie gewidmet.

Hiermit erkläre ich wahrheitsgemäß, dass die vorliegende Doktorarbeit im Rahmen der Betreuung durch Prof. Dr. Christopher Barner-Kowollik von mir verfasst wurde und keine anderen als die angegebenen Quellen und Hilfsmittel verwendet wurden. Wörtlich oder inhaltlich übernommene Passagen sind mit dem entsprechenden Zitat kenntlich gemacht. Darüber hinaus wurde die Satzung des Karlsruher Instituts für Technologie (KIT) zur Sicherung guter wissenschaftlicher Praxis beachtet, insbesondere die Abgabe und Archivierung der Primärdaten gemäß Abs. A (6). Ebenfalls bestätige ich, dass die elektronische Version der Arbeit mit der schriftlich abgegebenen übereinstimmt. Des Weiteren erkläre ich, dass ich mich derzeit in keinem weiteren laufenden Promotionsverfahren befinde und keine vorausgegangenen Promotionsversuche unternommen habe.

Karlsruhe, den 24.01.2019

Markus Michael Zieger

Er gibt dem Müden Kraft
und Stärke genug dem Unvermögenden.

Jesaja 40:29

Abstract

The design of novel and functional two-dimensional (2D) and three-dimensional (3D) structures constitutes an important field of current research to develop highly specialized systems for substrate-independent coatings, surface modification strategies, adhesives, 3D printing on the micro- and macroscale, metamaterials, drug delivery, and tissue engineering.

Within the present thesis, a newly designed system allowing for the preparation of functional monomolecular layers was prepared. Based on this innovation, the coating and diverse post-modifications on various substrates are presented. The immobilization is facilitated by catechol anchors of a multifunctional precisely defined cyclic catechol material (CyCat), which was synthesized from *ortho*-dimethoxybenzene, utilizing a phenolic resin-like synthesis strategy. The deprotection of the hydroxyl groups yielded the desired catechol units. To assess the chemical structure of the CyCat, matrix-assisted laser desorption ionization time-of-flight mass spectrometry (MALDI-TOF), high resolution electrospray ionization mass spectrometry (ESI MS), diffusion ordered spectroscopy (DOSY), and proton nuclear magnetic resonance (^1H NMR) were conducted. The analysis confirmed the prevalence of macrocycles with up to 32 catechol units. Due to the tendency of the CyCat to form colloidal aggregates in alkaline solution, dynamic light scattering (DLS) measurements were performed as a function of time. The aggregates were further verified via Kelvin probe force microscopy (KPFM) of highly oriented pyrolytic graphite (HOPG) substrates drop casted with CyCat from solution. Assessing the adsorption behavior of the CyCat in real time, surface plasmon resonance (SPR) of coated gold (Au) substrates was conducted. The thin coatings (1.6-2.1 nm) on Au, silicon dioxide (SiO_2), and titanium oxide (TiO_2) substrates were further investigated via spectroscopic ellipsometry (SE) and X-ray photoelectron spectroscopy (XPS). The detected aggregates in solution were not incorporated into the films, which was verified by atomic force microscopy (AFM). In addition, the homogeneous monomolecular films perfectly replicated the surface structure of the underlying substrates. To demonstrate the high functional nature of the monomolecular CyCat coatings, post-modification reactions with amine-bearing small molecules and polymers was performed. Employing a multifunctional amine facilitated the preparation of multilayers utilizing a facile procedure of alternating immersion in solutions of the CyCat and the amine linker. The thicker coatings (up to 12 nm) were further post-modified

with small molecules and polymers via “grafting-to” and “grafting-from” approaches utilizing prior immobilized atom transfer radical polymerization (ATRP) initiators.

The selective removal of printed material plays an important role in various fields of application such as the fabrication of complex geometries, the spatial resolved deposition of, e.g., metal layers, and cleavage of cell scaffolds after cell cultivation. The design of a multifunctional phenacyl sulfide linker (PSL) pioneered the preparation of a cleavable photoresist for the fabrication of 3D microstructures via direct laser writing (DLW). Photoactivation generates reactive thioaldehyde species that can readily react with a thiol functionalized linker in a radical-free step-growth polymerization, yielding networks exclusively resting on disulfide crosslinks. The bond formation was verified in solution with monofunctional thiols via ESI MS. To induce cleavage of the printed networks, the reversible nature of the disulfide crosslinks allowed for the thiol-disulfide exchange reaction, employing the chemical trigger dithiothreitol (DTT). The mild cleavage conditions did not affect adjacent acrylate-based structures. To emphasize this aspect, the incorporation of disulfide-based structural elements into scaffolds written with an acrylate photoresist was demonstrated. Immersion of the object in DTT solution facilitated the selective cleavage of the disulfide crosslinked element, obtaining the unaffected original acrylate-based scaffold. To assess the lateral resolution of the PSL photoresist, well-defined line gratings were successfully fabricated for distances of 300 nm.

Taking into account that the community for 3D printing involves many non-chemical fields, the development of a cleavable photoresist solely containing commercially available components is of high interest. Therefore, photoinduced radical thiol-ene polymerization was utilized and a variety of accessible containing alkene linkers with functionalities that are prone to be cleaved upon a chemical trigger were examined. Due to the facile exchange of linker moieties, the photoresist offers fast adaptation of its property profile. The fabrication of macroscopic objects that is often prevented by high synthetic efforts, was readily performed on a commercially available stereolithography (SLA) 3D printer. To cleave the micro- and macroscopic structures, immersion in an ethanolamine solution demonstrated the facile and residue-free removal of the networks. The cleavage was followed via time-lapse optical microscopy and analyzed by ^1H NMR and Fourier-transform infrared spectroscopy (FT-IR). The mechanical properties of the SLA printed material were assessed via nanoindentation. To

demonstrate the accessibility of freely suspended geometries via DLW, a rope bridge model was successfully printed on the microscale by the assistance of a supportive cleavable element based on the thiol-ene photoresist composed of commercially available multifunctional components.

Zusammenfassung

Die Gestaltung von neuartigen und funktionalen zweidimensionalen (2D) und dreidimensionalen (3D) Strukturen repräsentiert ein wichtiges gegenwärtiges Forschungsgebiet für die Entwicklung von hochspezialisierten Systemen für substratunabhängige Beschichtungen, die Modifizierung von Oberflächen, Klebstoffe, 3D Druck Anwendungen im mikroskopischen und makroskopischen Bereich, Metamaterialien, gezielten Wirkstofftransport und biotechnologische Gewebearbeitung.

Die vorliegende Doktorarbeit beschäftigt sich mit einer neu konzipierten organischen Verbindung, die für die Herstellung von monomolekularen Schichten verwendet wurde. Die innovative Idee ermöglichte die Beschichtung und vielfältige Modifizierungsmöglichkeiten auf verschiedenen Trägermaterialien. Die Immobilisierung beruht auf der Verankerung von Catechol Gruppen eines multifunktionalen und präzise definierten zyklischen Catechol Materials (CyCat). Zur Herstellung wurde *o*-Dimethoxybenzol in einer Phenolharz-analogen Synthese umgesetzt. Um die gewünschte Catechol Gruppe zu erhalten, wurde die Entschützung der Hydroxylgruppen durchgeführt. Die chemische Struktur des CyCat wurde mit Hilfe von Matrix-unterstützter Laser-Desorption/Ionisation Flugzeitmassenspektrometrie (MALDI-TOF), hochauflösender Elektrospray-Ionisations-Massenspektrometrie (ESI MS), Kernspinresonanzspektroskopie (NMR) und diffusionsaufgelöster NMR-Spektroskopie (DOSY) untersucht. Anhand der Messungen konnten Makrozyklen mit bis zu 32 Catechol Einheiten nachgewiesen werden. Das CyCat bildete kolloidale Aggregate in basischer Lösung aus und ihre zeitabhängige Veränderung wurde mittels dynamischer Lichtstreuung (DLS) analysiert. Die Aggregate wurden darüber hinaus anhand Kelvinsondenkraftmikroskopie (KPFM) untersucht, indem gelöstes CyCat auf eine hochorientierte pyrolytische Graphitoberfläche (HOPG) aufgebracht wurde. Um das Absorptionsverhalten des CyCat in Echtzeit zu analysieren, wurden Oberflächenplasmonenresonanz (SPR) Messungen mit beschichteten Gold (Au) Oberflächen durchgeführt. Die dünnen Beschichtungen (1.6-2.1 nm) wurden des Weiteren mit Hilfe von spektroskopischer Ellipsometrie (SE) und Röntgenphotoelektronenspektroskopie (XPS) analysiert. Rasterkraftmikroskopie (AFM) Messungen zeigten, dass die zuvor in Lösung nachgewiesenen Aggregate nicht in die Beschichtungen eingeschlossen werden. Zusätzlich wurde nachgewiesen, dass die Oberflächenstruktur des Trägermaterials

perfekt nachgebildet wurde. Um den funktionalen Charakter der CyCat beschichteten Oberflächen zu zeigen, wurden Amin funktionalisierte Verbindungen, ein kleines organisches Molekül und ein Polymer, zur Reaktion gebracht. Der Einsatz eines multifunktionalen Amin Derivats ermöglichte die Bildung von mehrlagigen Beschichtungen durch abwechselndes Eintauchen der Proben in Lösungen mit CyCat und dem Amin-basierten Linker. Dickere Beschichtungen (bis zu 12 nm) wurden erhalten und erneut mit kleinen organischen Verbindungen und Polymeren funktionalisiert. Hierzu wurden „grafting-to“ und „grafting-from“ Methoden verwendet. Letztere bediente sich Funktionalitäten, die zuvor durch die Anbindung von einem Initiator bereitgestellt wurden, der zur radikalischen Polymerisation unter Atomtransfer (ATRP) geeignet ist.

In vielen Anwendungsbereichen spielt die gezielte Entfernung von zuvor ausgehärtetem Material eine entscheidende Rolle. Hierzu gehören die Herstellung von komplexen Bauteilen, die orts aufgelöste Abscheidung von beispielsweise Metallfilmen und das Ablösen von Zellen nach der Kultivierung in Gerüststrukturen. Die Gestaltung eines multifunktionalen Phenacyl Sulfid Linkers (PSL) ermöglichte die Herstellung eines spaltbaren Photolacks, der für die Mikrostrukturierung mittels direktem Laserschreiben (DLW) eingesetzt wurde. Die Photoaktivierung führt zu der Bildung von reaktiven Thioaldehyden, die in einer radikalfreien Stufenwachstumsreaktion mit Thiol funktionalisierten Verknüpfungs-Molekülen umgesetzt werden können. Die Quervernetzungen in den erhaltenen Netzwerken bestehen ausschließlich aus Disulfidbrücken. Die Verbindungsknüpfung wurde in Lösung mit Hilfe eines monofunktionalen Thiol Derivats durch ESI MS nachgewiesen. Die reversible Natur der Bindung wurde in einer Thiol-Disulfid-Austauschreaktion mit dem chemischen Auslöser Dithiothreitol (DTT) genutzt, um die Disulfid basierten Netzwerke zu spalten. Die milden Bedingungen, die hierfür notwendig sind, beeinträchtigten die Qualität von benachbarten Objekten auf Acrylatbasis nicht. Um diesen Aspekt hervorzuheben, wurden Disulfid basierte Netzwerke mit Acrylat basierte Gerüststrukturen verbunden. Um die Disulfide gezielt zu spalten, musste die Probe lediglich in eine DTT Lösung eingetaucht werden und die Acrylat-basierten Objekte wurden einwandfrei zurückerhalten. Um die laterale Auflösung des Photolacks zu bestimmen, wurden wohldefinierte Linienarrays mit einem Linienabstand von 300 nm gedruckt.

Um der Allgemeinheit der 3D-Druck Nutzer gerecht zu werden, die viele Chemie-fremde Anwendungsbereiche einschließt, wurde die Entwicklung eines weiteren spaltbaren

Photolacks in Angriff genommen. Alle verwendeten Komponenten sollten hierbei kommerziell erhältlich sein. Um die hohe Auswahl an multifunktionalen Alkenverbindungen mit chemisch spaltbaren Funktionalitäten nutzen zu können, wurde die photoinduzierte radikalische Thiol-En Polymerisation angewendet. Das Eigenschaftenprofil der Photolacke konnte durch das einfache Austauschen der Komponenten schnell verändert werden. Darüber hinaus wurde ein kommerziell erhältlicher Stereolithographie (SLA) 3D Drucker verwendet, der die Herstellung von makroskopischen Objekten ermöglichte. Dies wäre im Falle von synthetisch herzustellenden Komponenten mit einem gewaltigen Zeitaufwand einhergegangen. Die Spaltung der 3D gedruckten mikroskopischen und makroskopischen Strukturen wurde durch das Eintauschen der Proben in eine Ethanolamin-haltige Lösung bewerkstelligt, die eine rückstandslose Entfernung des Materials ermöglichte. Durch die Verwendung von Zeitrafferaufnahmen konnten die Prozesse beim Auflösen in Echtzeit verfolgt werden. Zusätzlich wurden die Veränderungen bei der Spaltung mit ^1H NMR und Fourier-Transformations-Infrarotspektroskopie (FT-IR) Messungen untersucht. Nanoindentation ermöglichte die Bestimmung der mechanischen Eigenschaften der SLA gedruckten Objekte. Darüber hinaus wurde der einfache Zugang zu freischwebenden Geometrien anhand eines DLW Modelles gezeigt: Eine mikroskopisch kleine Hängebrücke konnte durch den Einsatz von Stützstrukturen auf Basis des auflösbaren Thiol-En Photolacks erfolgreich gedruckt werden.

Publications Arising from this Thesis

Ultrathin Monomolecular Films and Robust Assemblies Based on Cyclic Catechols

Zieger, M. M.; Pop-Georgievski, O.; de los Santos Pereira, A.; Verveniotis, E.; Preuss, C. M.; Zorn, M.; Reck, B.; Goldmann, A. S.; Rodriguez-Emmenegger, C.; Barner-Kowollik, C. *Langmuir* **2017**, *33*, 670-679.

Cleaving Direct Laser Written Microstructures on Demand

Zieger, M. M.; Mueller, P.; Quick, A. S.; Wegener, M.; Barner-Kowollik, C. *Angew. Chem. Int. Ed.* **2017**, *56*, 5625-5629.

A Subtractive Photoresist Platform for Micro- and Macroscopic 3D Printed Structures

M. M. Zieger, P. Müller, E. Blasco, C. Petit, V. Hahn, L. Michalek, H. Mutlu, M. Wegener, C. Barner-Kowollik, *Adv. Funct. Mater.* **2018**, 1801405.

Additional Publications

A Bioinspired Light Induced Avenue for the Design of Patterned Functional Interfaces

Preuss, C. M.; Tischer, T.; Rodriguez-Emmenegger, C.; Zieger, M. M.; Bruns, M.; Goldmann, A. S.; Barner-Kowollik, C. *J. Mater. Chem. B* **2014**, *2*, 36-40.

Fusing Catechol-Driven Surface Anchoring with Rapid Hetero Diels–Alder Ligation

Preuss, C. M.; Zieger, M.; Rodriguez-Emmenegger, C.; Zydziak, N.; Trouillet, V.; Goldmann, A. S.; Barner-Kowollik, C. *ACS Macro Lett.* **2014**, *3*, 1169–1173.

Photo-Induced Tetrazole-Based Functionalization of Off-Stoichiometric Clickable Microparticles

Wang, C.; Zieger, M. M.; Schenzel, A. M.; Wegener, M.; Willenbacher, J.; Barner-Kowollik, C.; Bowman, C. *Adv. Funct. Mater.* **2017**, *27*, 1605317.

Molecular Switch for Sub-Diffraction Laser Lithography by Photoenol Intermediate-State Cis-Trans Isomerization

Mueller, P.; Zieger, M. M.; Richter, B.; Quick, A. S.; Fischer, J.; Mueller, J. B.; Zhou, L.; Nienhaus, U.; Bastmeyer, M.; Barner-Kowollik, C.; Wegener, M. *ACS Nano* **2017**, *1*, 6396-6403.

Dual Gated Chain-Shattering Based on Light Responsive Benzophenones and Thermally Responsive Diels-Alder Linkages

Steinkoenig, J.; Zieger, M. M.; Mutlu, H.; Barner-Kowollik, C. *Macromolecules* **2017**, *50*, 5385-5391.

Contents

Abstract.....	vii
Zusammenfassung.....	x
1 Introduction.....	1
2 Theory and Background.....	5
2.1 Surface Functionalization.....	6
2.1.1 Bioinspired Dopamine Coatings.....	8
2.1.2 Post-modification of PDA Coatings.....	11
2.1.3 Surface Modification via Catechol Chemistry.....	14
2.1.4 Provision of Catechol Containing Systems.....	16
2.1.5 Cyclotrimeratrylene and Cyclotricatechylene.....	18
2.1.6 Reactivity of Catechol Units.....	20
2.2 Three-dimensional (3D) Printing.....	21
2.2.1 Photochemistry.....	22
2.2.2 Microscopic Printing via Direct Laser Writing (DLW).....	25
2.2.2.1 Fundamentals of DLW.....	26
2.2.2.2 Experimental and Commercially Available Setups for DLW.....	27
2.2.2.3 Fabrication Process of DLW Structures.....	29
2.2.2.4 Common and Experimental Photoresists for DLW.....	30
2.2.2.5 Fields of application for DLW.....	33
2.2.3 Macroscopic 3D Printing via Stereolithography (SLA).....	35
2.2.4 Network Formation.....	37
2.2.4.1 Conjugation via Photogenerated Thioaldehydes.....	38
2.2.4.2 Reversible Bond Formation via Disulfide Bridges.....	40
2.2.4.3 Thiol-Ene Chemistry.....	42

2.2.4.4	RadicalMediated Thiol-yne Polymerization	46
2.2.4.5	Cleavage of Polymers and Networks.....	49
3	Results and Discussion	53
3.1	Ultrathin Coatings via Catechol Chemistry.....	55
3.1.1	Synthesis and Analysis of the Protected CyCat.....	56
3.1.2	Synthesis and Analysis of the CyCat.....	57
3.1.3	Investigation of CyCat Aggregates	58
3.1.4	Provision of Monomolecular Layers via Catechol Chemistry	60
3.2	Post-modification of CyCat Layers.....	65
3.2.1	Assessing Remaining Functionalities of CyCat Coated Surfaces	67
3.2.2	Formation of Multilayers on Monomolecular CyCat Coatings	68
3.2.3	Post-modification of Multilayers	70
3.3	Provision of Novel and Cleavable Photoresists	74
3.3.1	Photoresists for Direct Laser Writing (DLW)	74
3.3.2	Removal of Structures based on Reversible Bonds	75
3.3.3	Disulfide Formation of Photo-caged Thioaldehydes.....	75
3.3.4	Deformation after Development	76
3.3.5	Adjusting Writing Parameters.....	78
3.3.6	Design of the Phenacyl Sulfide Photoresist	79
3.3.7	Reactivity of the Phenacyl Sulfide Linker	81
3.3.8	Fabrication of Cleavable 3D Microstructures via DLW	82
3.3.9	Lateral Resolution	86
3.3.10	A Readily Accessible Cleavable Photoresist Platform	90
3.3.11	Stabilized Thiol-Ene Photoresist.....	97
3.3.12	Water Permeable Cleavable Network	99
3.3.13	Macroscopic 3D Printing Employing Stereolithography (SLA)	100

3.4	Cleaving 3D Printed Micro- and Macroscopic Structures on Demand.....	103
3.4.1	Reversible Networks via Disulfide Chemistry	104
3.4.2	Cleavage of Radical Thiol-Ene Polymerized Networks	107
3.4.3	Selective and Orthogonal Removal of Objects Printed via SLA	111
3.4.4	Accessing New 3D Geometries via Cleavable Elements on the Microscale ...	114
4	Concluding Remarks and Outlook	117
5	Experimental Section.....	122
5.1	Materials.....	122
5.2	Characterization Methods and Instrumentation	123
5.3	Synthesis.....	128
5.3.1	Synthesis and Analysis of the Protected CyCat	128
5.3.2	Synthesis and Analysis of the CyCat	136
5.3.3	Synthesis and Analysis of the Phenacyl Sulfide Linker (PSL)	140
5.4	Sample Preparation.....	145
6	Appendix.....	150
	Bibliography.....	171
	List of Figures.....	178
	List of Tables.....	195
	Abbreviations.....	197
	Acknowledgements.....	199

1

Introduction

The constantly growing demand for novel functional two-dimensional (2D) and three-dimensional (3D) structuring technologies stems from the technical progress in many fields of application such as biomedical devices,^[1] advanced implants,^[2-4] complex micro- and nanostructures,^[5, 6] and macroscopic 3D printing.^[7] To satisfy the emerging requirements, the transfer and the improvement of well-investigated chemistries is essential. In addition, complex applications often involve the development of innovative systems, offering advanced property profiles. Allowing for the fast transfer between diverse fields, each providing specific knowledge, the design of procedures that rest on commercially available components, is of high interest.

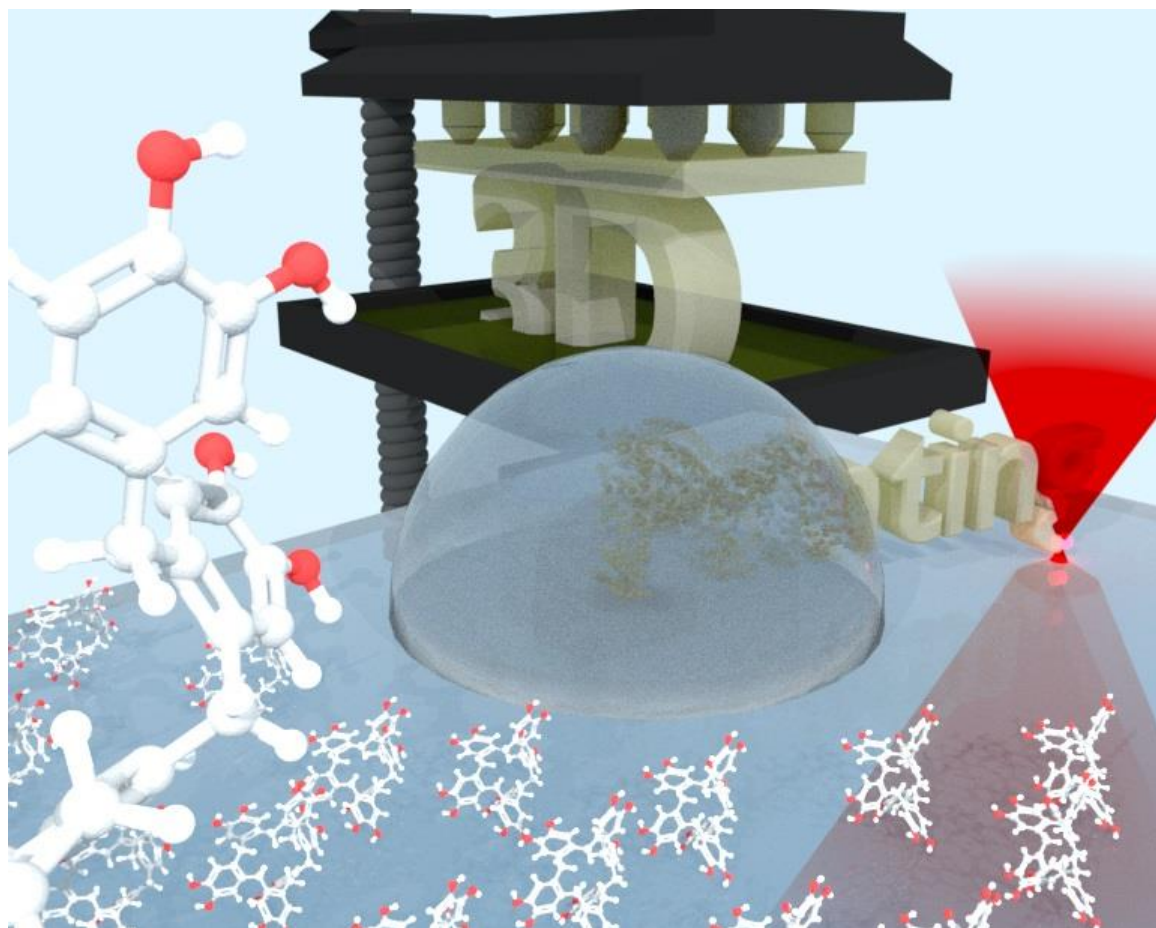
Nature has developed an impressive amount of mechanisms that maintain their adhesive properties even under harsh conditions such as the marine sea. Investigating the mussel byssus,^[8] the self-polymerization of dopamine was discovered and allowed for the virtually substrate-independent formation of films utilizing slightly alkaline conditions.^[9] The highly functional poly(dopamine) (PDA) coatings enabled a variety of novel technologies in various fields of application due to the simplicity of the dip-coating procedure. However, the underlying chemistry for the network formation still remains elusive, even after major endeavors to reveal the polymerization mechanism. In addition, the coatings exhibit a rough surface finish due to the prevalence of aggregates that are formed in solution and immobilized on the substrate.^[10, 11] Catechol units constitute a key role for the adhesion of PDA films and were further investigated. Systems that owe their adhesive properties exclusively to the catechol anchors were examined towards their coating properties.^[12] The well-defined

immobilization of catechol functionalized species on a variety of substrates^[13] enabled the formation of thin films, still offering a highly functional coating employing multifunctional catechol derivatives. Residual catechol groups that are not interacting with the surface allow for diverse post-modification reactions. Therefore, the focus of the current thesis with regard to functional 2D structuring is set on the provision of a novel, highly defined coating system for the preparation of monomolecular films. The adhesion is envisaged to rest entirely on catechol anchors. To demonstrate the functional nature of the coated surfaces, a variety of post-modifications is feasible.^[14]

Furthermore, the fabrication of micro- and nanostructures has introduced diverse approaches to generate unique material properties to the point of the provision of metamaterials.^[15] Commercially available setups enable the fast transfer from fundamental research to other fields of application. Direct laser writing (DLW) offers ready-to-use devices and has emerged as a powerful tool for the laser-based fabrication of almost arbitrary geometries on the microscale.^[5, 16] While the exploration and optimization of already existing photoresists constitutes a major effort, the development of novel photoresists, introducing new functional groups, crosslinks, and polymerization mechanisms, can break new ground for future technologies.^[17] The cleavage of 3D printed structures is often limited to multistep procedures^[18] or the need for harsh conditions such as high temperatures^[19] and plasma etching.^[20] However, the controlled and selective cleavage is a necessity in various fields of application (refer to section 2.2.4.5). Within the current thesis, a novel photoresist that offers a radical-free polymerization mechanism in a step-growth fashion, is demonstrated. The synthesized tetrafunctional phenacyl sulfide linker (PSL) is capable of the precise formation of disulfide crosslinks with multifunctional thiol moieties. Utilizing the reversible nature of the bond, DLW structures were readily cleaved upon a chemical trigger. In addition, the incorporation of structural elements based on disulfide bridges into a scaffold written with a standard acrylic photoresist was performed.^[21]

Taking into account that the majority of DLW users, just like in other fields of 3D printing, are not trained in the synthesis of novel chemical components, the focus was set on the development of a photoresist, resting on only commercially available chemicals. In addition, the prior described ability of the PSL networks, to be cleaved upon a chemical trigger, was a prerequisite for the new system. Utilization of various commercially available multifunctional

carbon-carbon double bond and thiol containing species allowed for the facile preparation of radical-mediated thiol-ene (refer to section 2.2.4.3) photoresists. Evaluation of different mixtures and their tendencies to be cleaved via chemical triggers, a divinyl adipate containing photoresist was obtained that can be cleaved via amidation. The investigated system further facilitated the transfer to macroscopic 3D printing employing a commercially available stereolithography (SLA) printer. Therefore, the versatility of the photoresist is demonstrated expanding the fields of application.^[22]



2

Theory and Background

In the following chapter, an overview of the various topics that are covered in the present thesis is provided, offering key insights into the theoretical background. The literature is reviewed to allow for the understanding of the motivation of the conducted research and to introduce the employed chemical methods and fundamental mechanisms.

After a short introduction to the functionalization of surfaces (refer to section 2.1), mussel-inspired coatings and their underlying chemistry is presented (refer to section 2.1.1 - 2.1.6). Next, the fundamentals of three-dimensional (3D) printing via laser lithography are introduced (refer to section 2.2.1). The working principle, available setups, photoresists and fields of application are discussed for the 3D printing on the micro- (refer to section 2.2.2) and macroscale (refer to section 2.2.3). In addition, an overview of relevant and related chemistries of the utilized polymerization techniques (refer to 2.2.4.1 - 2.2.4.4) and cleaving mechanisms (refer to section 2.2.4.5) is provided.

2.1 Surface Functionalization

Many advances in modern technologies ranging from biomedical applications,^[2-4] to sensing devices,^[23] and highly efficient photocatalysts^[24] rely on a perfectly optimized surface finish. In the past decades, several technologies have proven their suitability for substrate modifications. A well-investigated system is presented by the self-assembled monolayers (SAMs) that are formed by thiols on noble metals such as gold (Au), silver (Ag), and copper (Cu).^[25, 26] The immobilization of alkanethiols on iron (Fe) substrates after removal of the oxide layer was discussed as well.^[27] Among organosilicon monolayers, the formation of SAMs have been investigated for alkyltrichlorosilanes on silicon-silicon dioxide (Si/SiO₂) substrates^[28] enabling, for instance, the protection towards the adsorption of asphaltenes for an optimized chain length of attached species.^[29] Utilization of phosphonic acid derivatives facilitated the covalent immobilization onto metal oxide substrates such as SiO₂^[30] and aluminium oxide (Al₂O₃)^[31] via an acid-base condensation and coordination mechanism.^[31] The fabrication of multicomponent films on solid structures by adsorption of moieties from solution in an layer-by-layer (LbL) fashion constitutes an additional option for the coating of surfaces.^[32] Polyelectrolyte-coated gold nanorods (GNRs) were obtained by a LbL approach employing cetyltrimethylammonium bromide (CTAB).^[33] The usage of plasma immersion ion implantation and deposition (PIII/PIID) has proven to be suitable for the modification of biomaterials for clinical needs to achieve specific cellular responses at the molecular level for titanium (Ti) and Ti alloys, magnesium alloys (Mg), aluminium (Al) and polymeric structures.^[34] In addition, the post-modification with a crosslinked film deposited onto the substrate, often represents a facile solution to tune the properties of a bulk material. An important field of research is the functionalization of oxide surfaces,^[35] of which the coating with silane moieties is a widely employed technique. An additional straightforward fabrication of surface coatings is based on the self-polymerization of dopamine.^[9] The modification of materials with a low surface energy such as teflon, graphene, and Au substrates utilizing an add-layer are facilitated and led to a pronounced change in hydrophilicity (**Figure 1**).^[36] However, the formation of a crosslinked material that is fundamental for the coating process in the case of silanes and dopamine, often requires complex fine-tuning or is not suited to provide defined and small layer thicknesses.^[35] With regard to the increasing importance of nanomaterials such as colloidal inorganic nanoparticles,^[37] the provision of thin films is of high interest.

Furthermore, the underlying chemistry of systems formed via crosslinking is often very complex and poorly understood in the case of dopamine coatings (refer to section 2.1.1), resulting in a wide variety of chemical structures in the final material. To obtain higher molecular control over the modification, the utilization of monolayers is typically favored, enabling monomolecular immobilization of the employed material. In addition, the surface

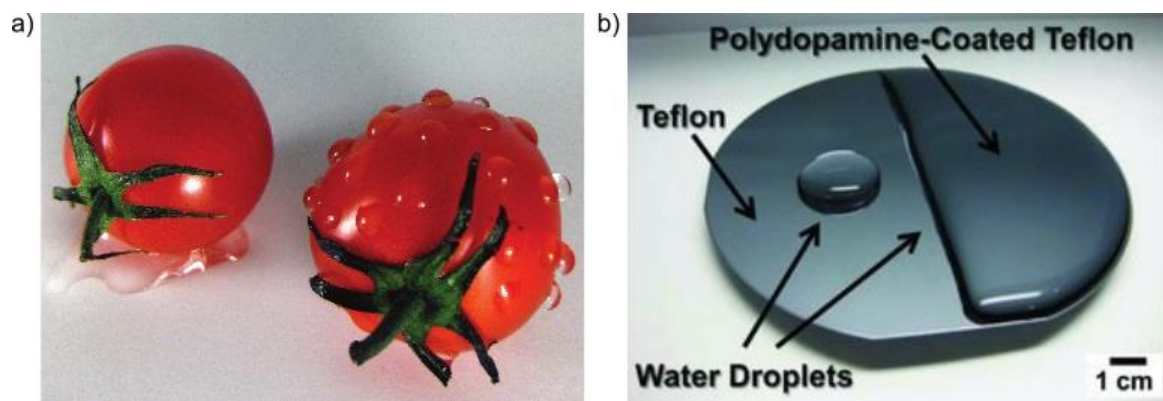


Figure 1: Coating of materials employing the self-polymerization of dopamine. a) The hydrophilicity of a tomato (left) is compared to a polydopamine (PDA) coated one revealing significant changes. b) A teflon substrate that possesses a low surface energy is coated with PDA (right side of the wafer) altering the wettability of the surface. Adapted with permission from Ref.[36]. Copyright 2011 John Wiley and Sons.

3topography is maintained employing the correct chemistry, which can be a prerequisite for biomedical applications, for instance, the control over bacteria attachment onto micro- and nanoparticles and subsequent biofilm formation.^[38] A promising system that proved to be suitable for the coating of a wide variety of substrates is based on the catechol unit that is a significant factor for the adhesive properties of dopamine coatings (refer to section 2.1.3).^[39] The unique ability to attach to a wide variety of substrates forming mainly monomolecular layers is a suitable chemistry for the provision of thin coatings, adding functionality to otherwise inert substrates such as gold.^[39]

2.1.1 Bioinspired Dopamine Coatings

Investigating the mussel byssus to discover new coating components that are resistant to harsh aqueous conditions such as the marine sea, catechol and amine units were identified to play an important role for the fundamental adhesion mechanism used by mussels to adhere to various substrates such as noble metals, metal oxides, semiconductors and synthetic polymer substrates.^[8, 40] Further examination revealed the self-polymerization of dopamine to be a suitable system, enabling the coating of a wide variety of inorganic and organic materials.^[9] The multifunctional surface-adherent polydopamine (PDA) films are obtained by dip-coating of the objects in an aqueous solution and have been applied to a wide range of biomaterials.^[41] To achieve a good understanding of the underlying processes during the film formation of PDA, the resulting structure was investigated in detail. Melanin, a natural pigment group that also comprises eumelanin, is often used as a comparative system to PDA, observing similar species during the formation of the material. Still, different mechanisms describe the self-polymerization with varying intermediates and final structure arrangements. However, most of the published investigations agree that the dopamine is capable to oxidize undergoing cyclization reactions in slightly alkaline conditions in a tris(hydroxymethyl) aminomethane (TRIS) buffer solution (**Figure 2**).^[42] The emerging oxidized species crosslink and form dimers. Further crosslinking reactions lead to the formation of aggregates which are involved in the coating of surfaces, besides the surface initiated polymerization of PDA from

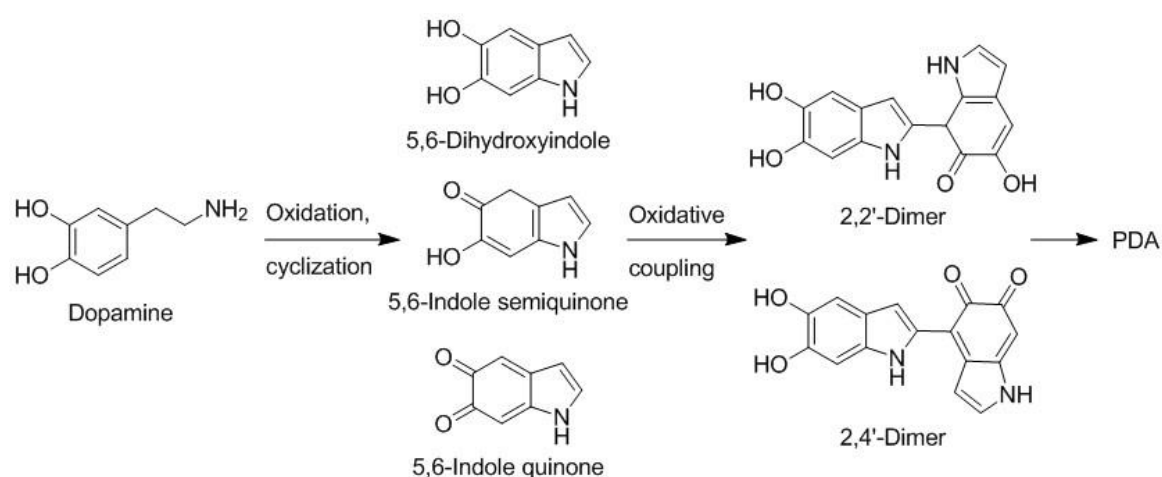


Figure 2: Schematic depiction of the possible processes during the self-polymerization of dopamine in a slightly alkaline TRIS buffer solution. Adapted with permission from Ref.[42]. Copyright 2012 American Chemical Society.

immobilized small units.^[10, 11] In addition to covalent crosslinking reactions in slightly alkaline conditions, the stability of the films is increased by hydrogen bonds^[43] and stacking of layers^[44] of the emerging moieties. Investigating the complex and elusive nature of the resulting structure of PDA, a model that allows changes in the oxidative states of units during the network formation via interactions with the backbone or species in spatial proximity of

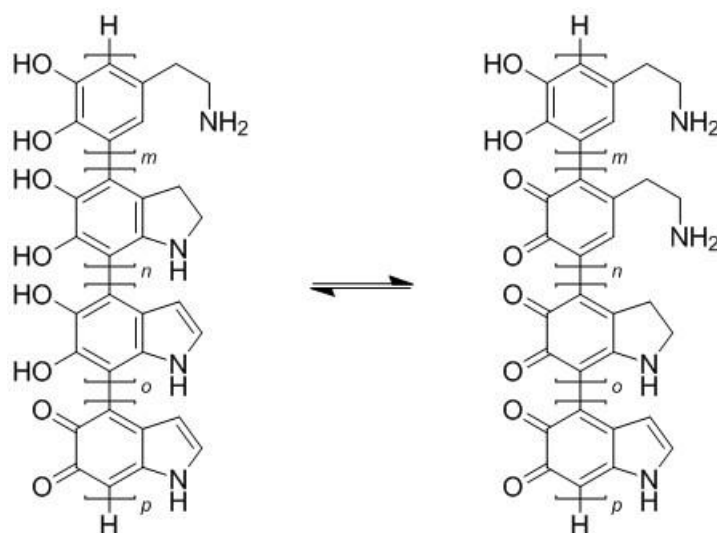


Figure 3: Proposal for the structure of PDA. Different oxidative states are responsible for the formation of mainly linear polymers that form strong, partially covalent, and non-covalent interactions. Adapted with permission from Ref.[45]. Copyright 2013 American Chemical Society.

crosslinked material was suggested (**Figure 3**).^[45] The 4-7'-bridging is believed to be favored in this investigation and, therefore, the resulting structure of PDA is assumed to mainly consist of linear chains with various conjugation lengths. Additional crosslinking points allow the formation of small moieties such as tetramers based on 2,7'-bridging.^[45, 46] These species are believed to mainly form networks via non-covalent interactions.

The variety of different species is further believed to result in the darkening of the coating solution and the broadband absorption of formed PDA films. To verify this assumption, the investigation of 5,6-dihydroxyindole dimers and their oxidized species was conducted, revealing the wide variety of absorption already obtained for small molecules.^[47] Enhancing the study by water-soluble species enabled the analysis of the absorption in aqueous conditions upon oxidation, observing similar results compared to eumelanin-type pigments.^[48] The investigation supports the notion that additionally to the intrinsic basis by the conjugation length, the external interactions between oxidized and reduced moieties

have to be considered. Comparing the PDA material to the underlying chemistry of eumelanin, similar absorbance profiles are observed.^[49] It is assumed that the reason for the broadband absorption in both systems lies in the extreme chemical and structural disorder^[50] of the resulting structures. To demonstrate that the characteristic monotonic absorbance profile of eumelanin and synthetic imitations are readily explainable with overlapping Gaussian functions for the absorption of similar but chemically distinct moieties, a simulation considering 11 species was conducted (**Figure 4**).^[49] In nature, the broadband absorption

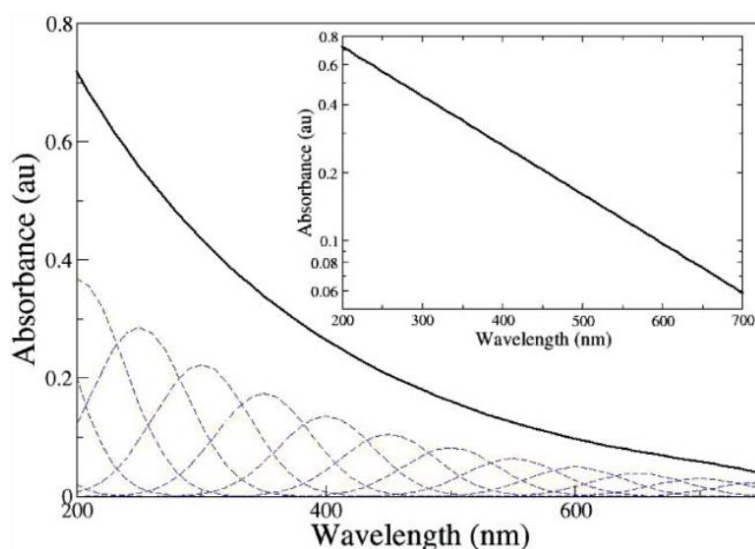


Figure 4: Simulation of the broadband monotonic absorbance profile of eumelanin utilizing a linear combination of 11 Gaussians of similar but chemically distinct species. Reproduced with permission from Ref.[49]. Copyright 2005 Royal Society of Chemistry.

enables photo-protection and immune-response and the extreme chemical and structural disorder^[44] is assumed to be a necessary low-cost natural resource.^[49] However, additional reasons for the broadband absorption have been discussed ranging from scattering effects^[51] to properties of an amorphous semiconductor^[52] to the disorder model,^[44] to name but a few.

The utilization of PDA coatings without further modification can already provide the desired surface properties. To achieve a nanocomposite offering intracellular sensing and therapeutic functions, the simple coating of Fe_3O_4 nanoparticles with PDA was suitable to allow the detection of mRNA and photothermal therapy.^[53] However, most applications require the post-modification of PDA add-layers, which will be discussed in the following pages.

2.1.2 Post-modification of PDA Coatings

The successful coating of a substrate utilizing the immobilization of single molecules or macromolecules such as PDA, often constitutes only the first step towards the desired surface properties. Assessing the added functionalities in a post-modification, the tailoring of the coatings employing a wide variety of chemistries and, therefore, the transfer of well-investigated systems, is readily available. The modification of the PDA ad-layer mainly exploits the reactivity of remaining catechol and amine groups.^[9] An important feature of catechols is the complexation of metal ions.^[54] Utilizing a tetrafunctional dihydroxyphenylalanine (DOPA) linker, the pH-dependent formation of strong, yet reversible crosslinks after gelation with Fe^{3+} ions is demonstrated, providing oxidation-resistant supramolecular hydrogels.^[55] The underlying chemistry is also suited for the electroless deposition of silver and copper metal films onto PDA coated objects via dip-coating into silver nitrate and copper(II) chloride solutions, respectively.^[9] The immobilization of a photoactive species, a tetrazole, further enabled the precise photopatterning of an atom transfer radical polymerization (ATRP) initiator (**Figure 5**).^[56] Subsequently, the surface-initiated ATRP (SI-ATRP) utilizing oligoethylene glycol methyl ether methacrylate (MeOEGMA) resulted in the formation of polymer brushes with an excellent resistance to biofouling. Further investigations address the

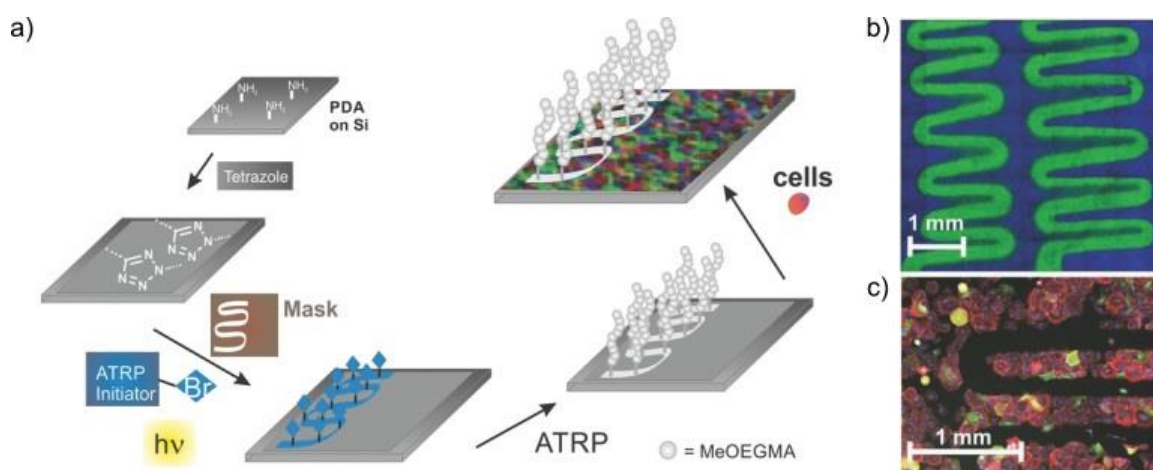


Figure 5: Spatially resolved attachment of non-fouling brushes onto PDA coatings. a) Surface photopatterning via post-modification of PDA films utilizing photoactive tetrazole moieties enabled the precise immobilization of an ATRP initiator. b) To assess the functionalization, time-of-flight secondary ion mass spectrometry (ToF-SIMS) was conducted revealing patterns with a high spatial resolution. c) The growth of poly(MeOEGMA) in a SI-ATRP fashion provided a non-fouling pattern that prevented the adhesion of cells on the protected areas. Adapted with permission from Ref.[56]. Copyright 2013 John Wiley and Sons.

need for novel antibacterial strategies for the modification of clinical devices. The release of silver particles embedded into a PDA coating was combined with attached polyethylene glycol brushes to prevent the formation of biofilms.^[57] In addition, a versatile nanoplatform for multifunctional drug delivery and light-mediated therapy based on PDA capped gold nanorods (GNR) was demonstrated (**Figure 6**).^[58] To prevent the aggregation of GNRs during the self-polymerization of dopamine, cetyltrimethylammonium bromide (CTAB) and subsequently polyethylene glycol (PEG) were immobilized. The thickness of the PDA layers was adjusted via the concentration of dopamine in the coating solution and two kinds of drugs, methylene blue and doxorubicin, were successfully adsorbed onto the nanocomposites via electrostatic and π - π stacking interactions. Furthermore, PDA coated nanoparticles were utilized to attach

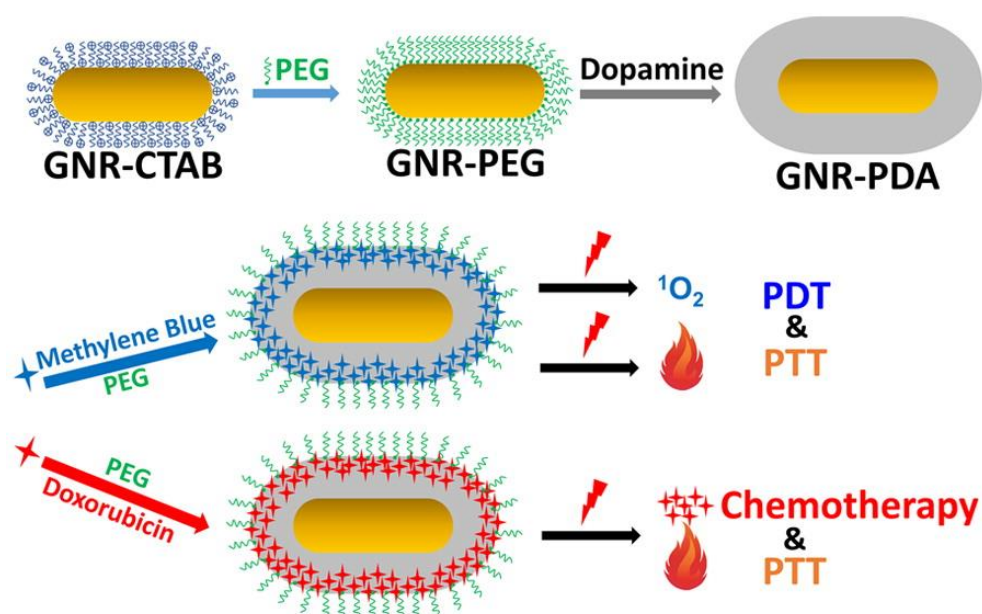


Figure 6: Multifunctional nanoplatform based on gold nanorods (GNR) for photodynamic and photothermal therapy (PDT/PTT). The GNRs are coated with cetyltrimethylammonium bromide (CTAB) and PEG to prevent agglomeration. After coating with PDA, methylene blue and doxorubicin are successfully adsorbed onto the coatings to serve as a drug delivery system. Reproduced with permission from Ref.[58]. Copyright 2016 American Chemical Society.

thiol- and amine-terminated cell-interactive ligands.^[59] Furthermore, the utilization of the PDA film formation onto nanoparticles allowed the fabrication of metal-organic framework (MOF) precursors loaded with or without a metal containing moiety.^[60] The applicability of PDA to biomaterial surfaces was demonstrated by an improved dentin remineralization in calcium and phosphate solutions rendering the approach a viable strategy for dental tissue surfaces.^[61] To extend the variety of applicable photoreactive species, α -methyl

benzaldehyde derivatives of DOPA were synthesized, enabling photoactive coatings that facilitate spatially resolved attachment of species containing an electron-deficient dienophile.^[62] This approach extends the accessible functionalities on PDA coatings and facilitates photoinduced reactions. The ability to bind molecules and particles to the PDA further provided the possibility to detoxify contaminated water in a facile fashion with PDA coated glass beads.^[63] Toxic heavy metals and certain organic compounds were readily immobilized and regeneration of the material was achieved by treatment with dilute acetic acid. The patterning of DNA onto noble metals, metal oxides, semiconductors and synthetic polymer substrates was demonstrated utilizing a synthetic catecholamine polymer, mimicking the mussel-adhesive protein.^[64] It was assumed that the attachment is based on multiple covalent and non-covalent interactions between catechol and amine groups. Furthermore, dopamine-based films also facilitated the covalent binding of terminally modified DNA.^[65] Utilizing a diamine additive during the formation of PDA, amine-rich coatings were obtained, exhibiting good biocompatibility. The post-modification employing biomolecules with carboxylic groups such as heparin is envisaged for biomedical devices.^[66] To address the increasing importance of adding conductive properties to surfaces, a post-modification employing a poly(3-hexylthiophene) was conducted utilizing remaining amine groups on PDA add-layers.^[67] The design allows for the fast transfer to applications in the field of electronic devices due to the ability of PDA add-layers to adhere to virtually any surface.

2.1.3 Surface Modification via Catechol Chemistry

The wide variety of reactions that the catechol or 1,2-dihydroxybenzene group facilitates, including the capability to undergo oxidation to form *o*-quinones, constitutes an important key feature in many biological systems such as the hardening of the cuticle of insects^[68, 69] or the beak of squids.^[70, 71] In addition, the catechol or 1,2-dihydroxybenzene group plays an important role in the formation of PDA and has proven to be a versatile building block for the design of synthetic coatings.^[12] The immobilization of catechol functionalized moieties is feasible for a wide range of surfaces such as TiO₂, Si, Au, hydroxyl or amine functionalized surfaces.^[72, 73] A proposed mechanism for the covalent and non-covalent interactions during the anchoring of catechol units to metal oxide substrates in aqueous conditions is depicted in **Figure 7**. The synthetic homologue of a mussel foot protein facilitated the immobilization on a TiO₂ substrate with a strong adsorption of coacervates that are formed in solution.^[13] Comparing mussel-inspired adhesives with commercial glues, the provision of a copolymer containing high molar ratios of phosphate and catechol moieties facilitated a bond strength

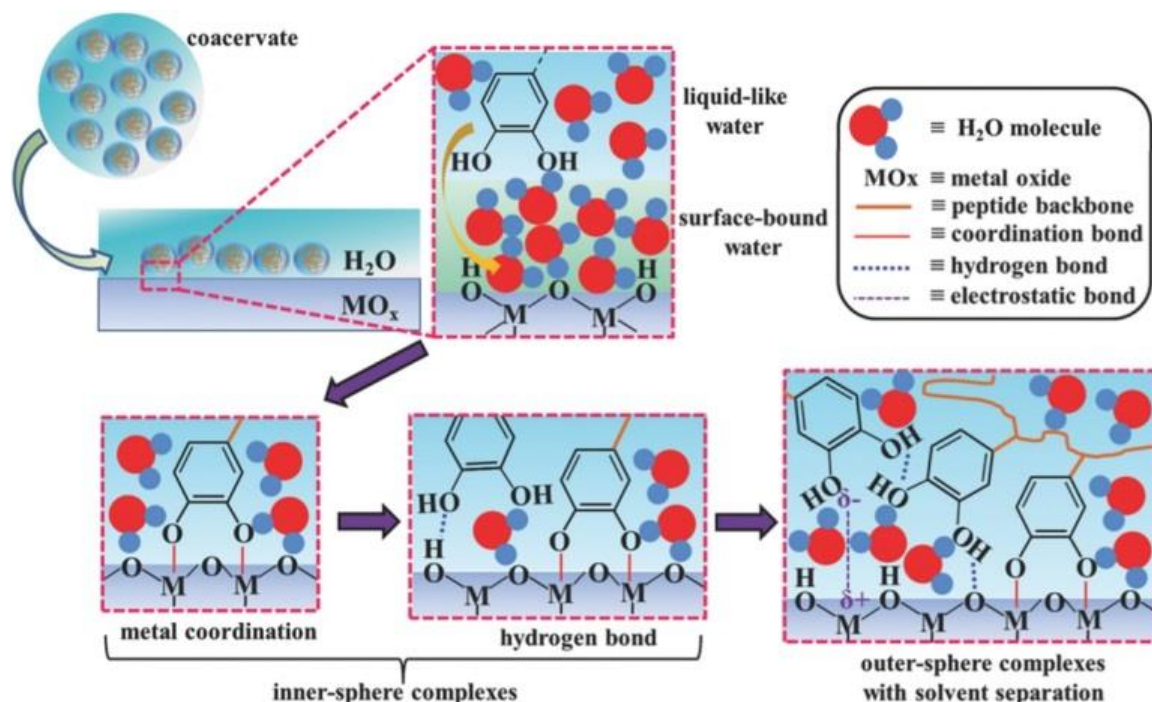


Figure 7: Proposed mechanism for the adhesion of catechol groups under aqueous conditions. The synthetic homologue of a mussel foot protein forms coacervates in solution that are capable to bind to the TiO₂ substrate. It is assumed that inner- and outer-sphere complexes are responsible for the adhesion mechanism. Reproduced with permission from Ref.[13]. Copyright 2016 John Wiley and Sons.

of nearly 40% compared to a commercial cyanoacrylate.^[74] Due to the formed coacervates, the system enables simultaneous adhesion and the encapsulation of bioactives such as antibiotics, pain relievers, and growth factors. Further advances in the challenging field of water-resistant adhesives were provided by the design of interfaces with switchable adhesive properties based on the formation of a copolymer containing catechol and adamantane moieties.^[73] Addition of a cyclodextrin functionalized poly(N-isopropylacrylamide), which offers thermoresponsive properties, led to the desired surface properties of a temperature controlled wettability of the coated Si substrate. Furthermore, the immobilization of catechols onto chitosan films facilitated a distinct redox activity with a limited ability to donate or accept electrons, which could be regenerated by a brief electrochemical treatment.^[75] It is assumed that catechol-modified chitosan films possess a similar behavior compared to biological systems that utilize catechol-quinone redox chemistry for electron transfer. The synthesis of catechol moieties via Diels–Alder chemistry enabled the provision of a thermally driven switching system after the immobilization onto Au, Si, and poly(ethylene), respectively.^[76] To detach the polymer chains, simple heating in toluene triggered the retro Diels–Alder reaction and the reattachment of cyclopentadiene functionalized polymers was readily available at ambient temperatures. In addition, the precise modification of Fe₃O₄ nanoparticles was achieved via the irreversible binding affinity of catechol anchors.^[77] The stability of the particles was significantly increased compared to similar systems, especially with regard to medically relevant properties such as the resistance towards elevated temperatures and ionic strength which is a prerequisite for later applications such as magnetic resonance contrast agents.

2.1.4 Provision of Catechol Containing Systems

The utilization of mussel-inspired chemistry represents an important concept for the development of advanced adhesives.^[8] To facilitate novel systems for coating applications on a large variety of organic and inorganic substrates, catechol derivatives have been investigated and proved their suitability in many fields.^[12] However, the first step is the provision of a potential synthesis pathway to obtain the material in an efficient way. The formation of a dopamine methacrylamide^[78] was conducted in a simple fashion (**Figure 8**) and

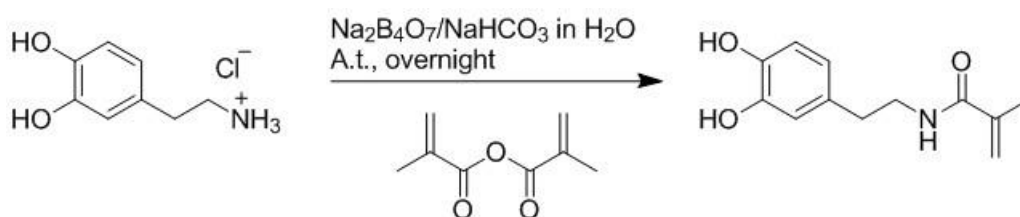


Figure 8: Synthesis route for the provision of a dopamine methacrylamide monomer. The one-step reaction employs dopamine hydrochloride and methacrylic acid anhydride as educts. Adapted with the permission from Ref.[78]. Copyright 2009 American Chemical Society.

allowed for the preparation of various catechol containing polymers. The utilization of comonomers enabled the development of gecko-foot-hair-inspired microfibers with increased adhesion under wet conditions,^[78] photosensitive nanorods,^[79] and pressure-sensitive adhesives.^[80] To enhance the functionality of a polymer via the covalent attachment of catechol moieties, a poly(acrylic acid) backbone was functionalized via amidation with amine-bearing species.^[81] The approach facilitates the step-wise addition of various functionalities. The ratio of the attached moieties is adjusted by the concentration during the post-modification (**Figure 9**). Moreover, Fe_3O_4 nanoparticles were successfully coated with catechol functionalized PEG chains, revealing long-term colloidal stability and high biocompatibility. Remaining reactive functional groups provided a modifiable surface via azide-alkyne cycloaddition.^[81] The enzymatically-driven activation of a peptide-polymer conjugate with tyrosine functionalities was achieved in-situ via the oxidation of the phenol groups utilizing tyrosinase.^[82] Emerging catechol derivatives altered the weak and reversible adhesion strength of the material towards steel substrates into a robust coating system. In addition, the chemoenzymatic synthesis of a copolymers was performed mimicking a foot protein of the blue mussel (*Mytilus edulis*).^[83] The obtained polypeptide contained lysine and tyrosine units, and latter ones where oxidized via tyrosinase and the adhesive properties of

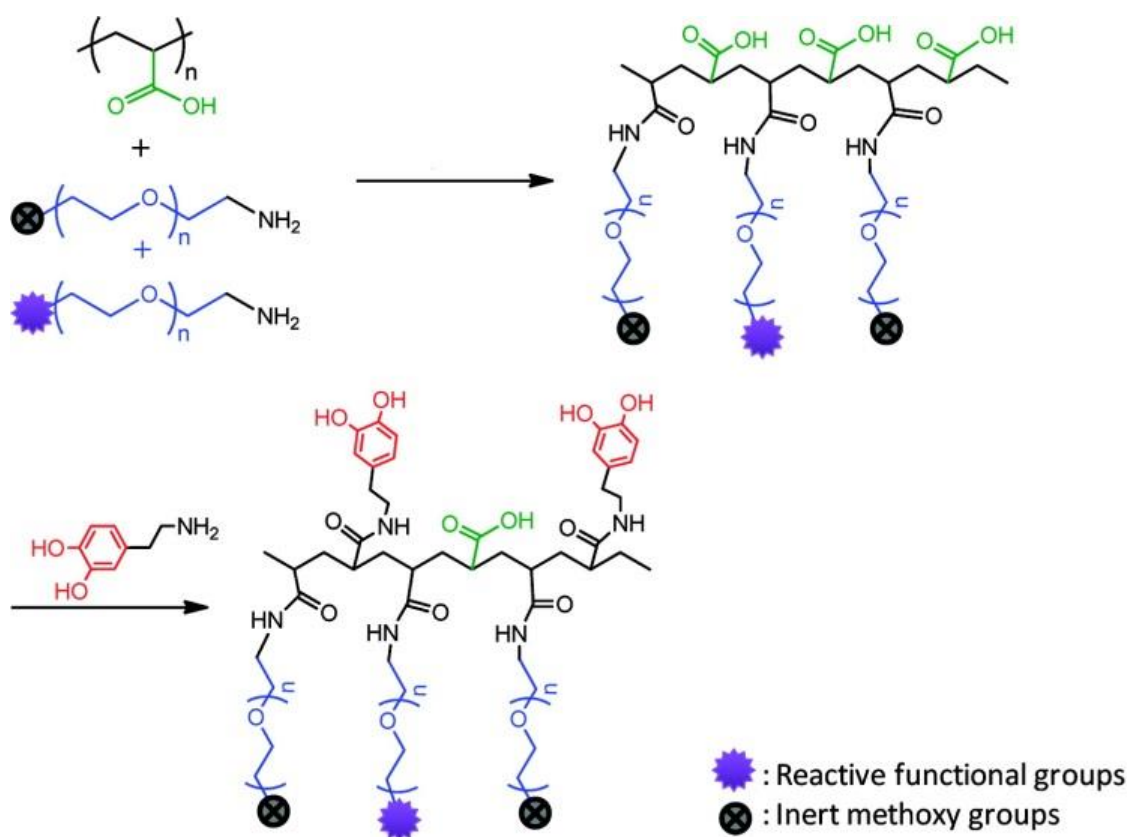


Figure 9: Synthesis of highly functional catechol-containing copolymers via the amidation of poly(acrylic acid). The utilization of reactive endgroups attached to the amine-bearing PEG chains enabled the subsequent modification of the surfaces after immobilization with catechol anchors. Adapted with permission from Ref.[81]. Copyright 2012 American Chemical Society.

the material was investigated with regard to various pH levels causing different protonation and deprotonation states. The investigation revealed an improved adhesion for deprotonated catechol species and the enhanced crosslinking tendency of deprotonated primary amine groups.^[83] To gain further control over the surface chemistry, catechol end-functionalized PEG polymers were synthesized via amidation offering well-defined blockcopolymers.^[84] The terminal catechol units served as reducing agents for metal ions (Au, Ag) and simultaneously enabled the immobilization of the PEG chains onto the emerging particles resulting in core-shell nanoparticles. Plasmon resonance behavior characteristic of noble metal analogues was observed for the final nanoparticles. It is also observed that the emerging *o*-quinone moieties induce crosslinking on the surface with catechol moieties.^[84] Furthermore, the utilization of protected catechol groups during polymerization with subsequent deprotection was performed. To achieve polymers with an improved polydispersity, reversible addition-fragmentation chain transfer (RAFT) polymerization was employed using a commercially available trithiocarbonate as RAFT agent and 3,4-dimethoxystyrene as monomer.^[85]

Subsequently, boron tribromide (BBr_3) was utilized to cleave off the methoxy groups obtaining catechol units that possessed an increased tendency to attach to a zinc substrate.

2.1.5 Cyclotrimeratrylene and Cyclotricatechylene

Cyclotrimeratrylene (CTV) constitutes a well-investigated molecule that is mainly utilized in the field of inorganic chemistry for the preparation of cryptophanes,^[86] for host-guest interactions,^[87] and self-assembled systems,^[88] among others. To synthesize the trimer, veratrole alcohol is exposed to harsh acidic conditions such as sulfuric acid in acetic acid, leading to a condensation reaction with a high tendency to form small cyclic species (**Figure 10**).^[89] An alternative synthesis route uses a phenolic resin-like polymerization of

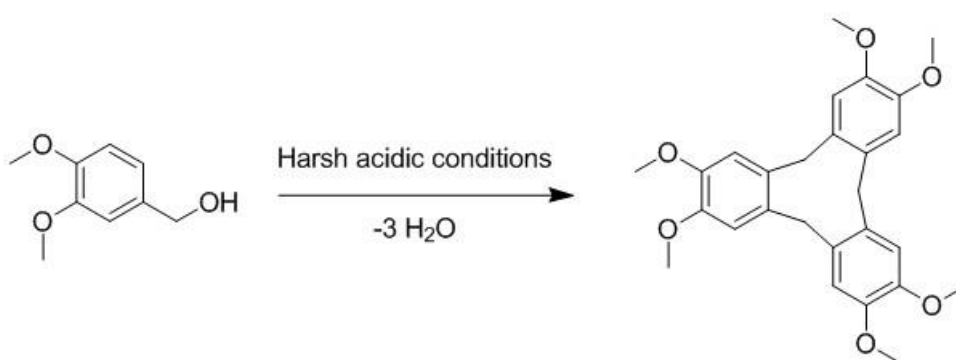


Figure 10: Preparation of cyclotrimeratrylene utilizing the condensation reaction of veratrole alcohol under harsh acidic conditions such as sulfuric acid in acetic acid. The synthesis route exhibits a high tendency towards the formation of small cycles.

o-dimethoxybenzene and formaldehyde in 70% sulfuric acid.^[90] The synthesis of species with a higher degree of polymerization was further investigated under microwave heating and infrared irradiation, obtaining species with up to six repeating units.^[91] Thiol functionalized moieties of CTV are capable to form SAMs on gold substrates facilitating the non-covalent immobilization of the fullerene C_{60} onto the surface.^[92] Further investigations of the interactions with fullerenes revealed the suitability for the formation of self-assembled capsules.^[88] In addition, the precise optimization of the spacer length connecting two CTVs allowed for the purification of higher-order fullerenes to selectively isolate C_{76} , C_{78} and C_{80} .^[87] Introducing acid and amine functionalities, the provision of water soluble CTV derivatives was demonstrated enabling the formation of anisotropic supramolecular hydrogels.^[93] The proposed structure after self-assembly comprises columns of stacked molecules with

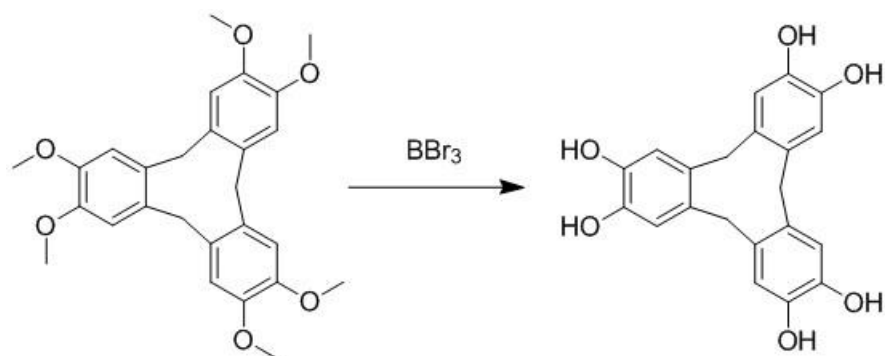


Figure 11: Synthesis of cyclotricatechylene (CTC) via the deprotection of cyclotrimeratrylene (CTV). Utilization of BBr₃ enables the demethylation obtaining catechol units.

pronounced intermolecular non-covalent interactions. Furthermore, the material revealed a pH-dependent reversible gel-to-sol and sol-to-gel transition.^[93] To form the hydroxyl derivative of CTV, deprotection employing BBr₃ allowed the formation of a catechol trimer with short methyl spacers also known as cyclotricatechylene (CTC) (**Figure 11**).^[94] The conversion of CTV to CTC was further conducted via an electrochemical pathway of immobilized CTV on a carbon electrode.^[95] Further investigations of the redox activity of the system facilitated the selective detection of cysteine using an electrocatalytic oxidation reaction. In addition, CTC chemistry represents a promising approach for the provision of microporous polymeric materials offering cavities that can serve as hosts for organic molecules.^[96] The fabrication of a porous crystalline material was demonstrated via the formation of boron esters with multifunctional boronic acid derivatives.^[97] The high surface area of these type of materials is a prerequisite for applications in the field of gas storage, for instance.^[97] In addition, CTC was used as a ligand for Cu generating large (Cu₆CTC₄)¹²⁻ cages.^[98] The anionic tetrahedral complexes were interconnected through sodium cations and water molecules inducing the formation of a highly symmetric diamond-like assembly. Furthermore, CTC is well-suited for host-guest systems extending the possibilities arising from CTV chemistry.^[89]

2.1.6 Reactivity of Catechol Units

With regard to multifunctional coating systems based on catechol anchors, the post-modification of remaining units or the oxidized *o*-quinone species that are not interacting with the substrate offers a facile approach to further alter the properties of the surface (**Figure 12**).^[12] The attachment of thiol and amine functionalized moieties follows the same reaction pathways as already discussed for PDA (refer to section 2.1.2).^[59] An additional modification route is presented by the Michael type addition of imidazole derivatives.^[99] Furthermore, the covalent binding among catechol units and *o*-quinone moieties to form crosslinked networks on surfaces is proposed.^[82]

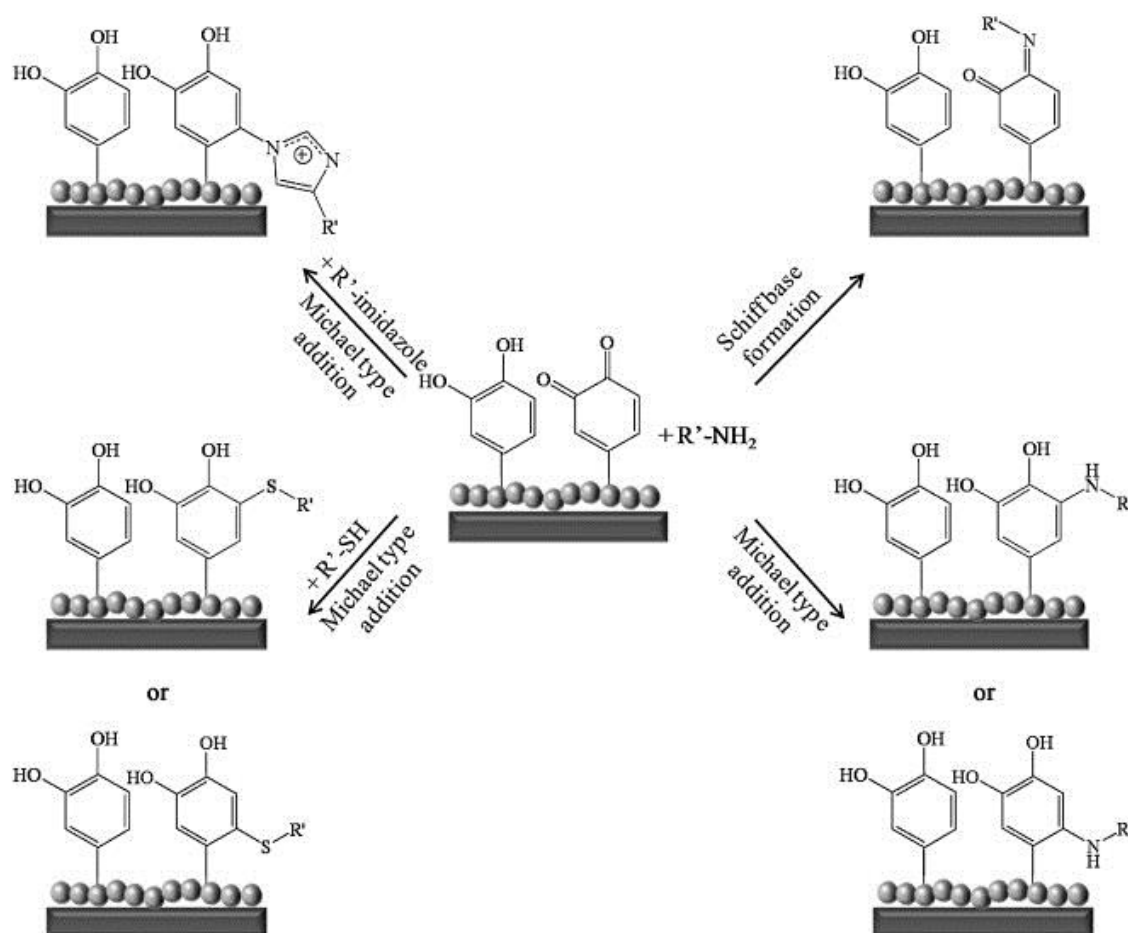


Figure 12: Post-modification of multifunctional catechol coatings. Remaining catechol units and oxidized *o*-quinone groups allow for the covalent attachment of imidazole, amine and thiol functionalized moieties in a Michael-type addition. Utilizing amine-bearing species, the formation of Schiff base derivatives is proposed. Reproduced with permission from Ref.[12]. Copyright 2012 Elsevier Ltd.

2.2 Three-dimensional (3D) Printing

Three-dimensional (3D) printing, also referred to as additive manufacturing, rapidly evolved in the last decades and is envisaged to constitute a disruptive technology for industrial manufacturing in the near future.^[7] Recent investigations focus on a multitude of applications ranging from advanced systems on the microscale,^[15] to the printing of macroscopic objects for our daily routine, and novel approaches to incorporate electronic devices into biological systems.^[100] The variety of 3D printers that are used in diverse fields of application require working across discipline boundaries to, for instance, obtain printable material for custom-built setups. Novel photoresists for processing via laser lithographical devices focus on the provision of features with thus far little or no accessibility such as the fabrication of compound structures with multiple chemistries, objects offering a readily available post-modification, selectively degradable photoresists, and sub-diffraction printing.^[17] The introduction of new chemistries furthermore concentrates on the development of stimuli-responsive materials.^[101] To facilitate the accessibility of the designed photoresists, simple and customizable platform technologies avoiding complex synthetic procedures are required to enable the facile transfer from fundamental research to application-oriented investigations in other fields.

3D printing of microstructures presents a challenging field and is mainly subject of current research.^[102] However, the utilization of commercially available direct laser writing (DLW) setups, allowing for the fabrication of objects with feature sizes on the nanoscale, constitutes an exception (refer to section 2.2.2).^[103] The commonly employed photoresists for DLW are based on acrylate chemistry and the curing is facilitated via the formation of radicals induced by the light exposure of photoinitiators. To extend the range and functional scope of printed structures, suitable chemistries were investigated including the radical-mediated thiol-ene and thiol-yne polymerization (refer to section 2.2.4.3, and 2.2.4.4). High selectivity and fast reaction kinetics constitute a prerequisite for the successful development of novel photoresists. The photoactivation of phenacyl sulfide moieties leads to the formation of reactive thioaldehyde species and presents a suitable system for the provision of new features in microstructures (refer to section 2.2.4.1). Utilizing laser lithography for the fabrication of macroscopic structures, 3D printing via stereolithography (SLA) constitutes a well-investigated technique with broad application and a wide variety of commercially available setups (refer to section 2.2.3).

2.2.1 Photochemistry

Photoinduced reactions are present in many aspects of life including how we perceive the world with our eyes,^[104] to photosynthesis in nature,^[105] providing the basis of our existence. Investigation and implementation of these concepts led to significant developments including laser-based technologies, optics, and photoresists. Regardless of the impressive progress in the last decades, many underlying principles have to be understood in depth to achieve one of the driving aims: efficient light energy harvesters^[50] for applications such as solar fuel-generating devices or solar cells.^[106] Furthermore, the implementation of photoinduced reactions in the field of organic chemistry can open new pathways to simplify synthesis routes, to create environmentally friendly processes and to obtain whole new product families that are not achievable via ground-state reactions.^[107]

To describe the quantitative loss of intensity through the interaction of photons with an absorbing species, the absorbance, the Beer-Lambert law is applied for the usage of monochromatic light (**Figure 13**). Measurements are conducted at low concentrations to prevent electrostatic proximity effects between molecules in the sample. Additional physical processes such as reflection or scattering are not considered by Beer-Lambert's law. Assuming perfect homogeneity of the sample, a linear correlation between the absorbance and the

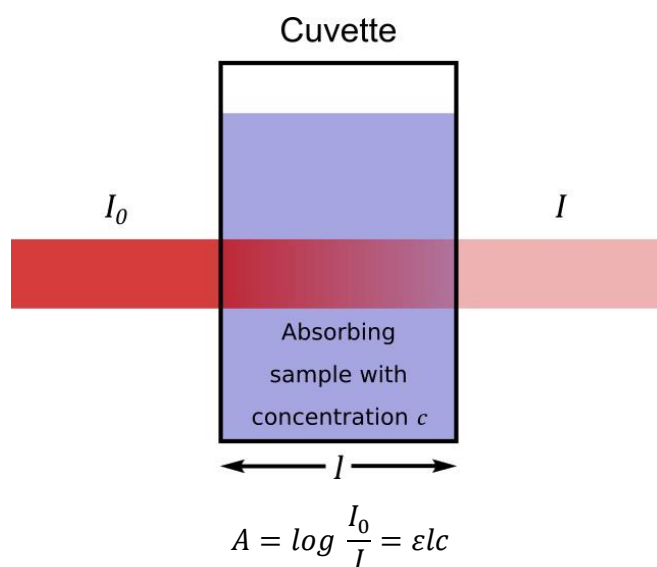


Figure 13: Depiction of Beer-Lambert's law in photochemistry to determine the absorbance A of an absorbing species with initial light intensity I_0 and after the adsorption I . The molar extinction coefficient ϵ can be calculated with the employed concentration c and the length l of the absorption path.

concentration is expected. The obtained molar extinction coefficient ε is wavelength-dependent and describes the absorbance strength of the measured species.

Irradiation of molecules with light results in different behaviors ranging from light emitting, heating, cleavage of covalent bonds to formation of new bonds. In 1933, the different energetic states that are involved for various interactions with one photon were described by Polish physicist Alexander Jablonski.^[108] Initially, the model was based on three energy levels but was extended to the nowadays common illustration including vibrational transitions

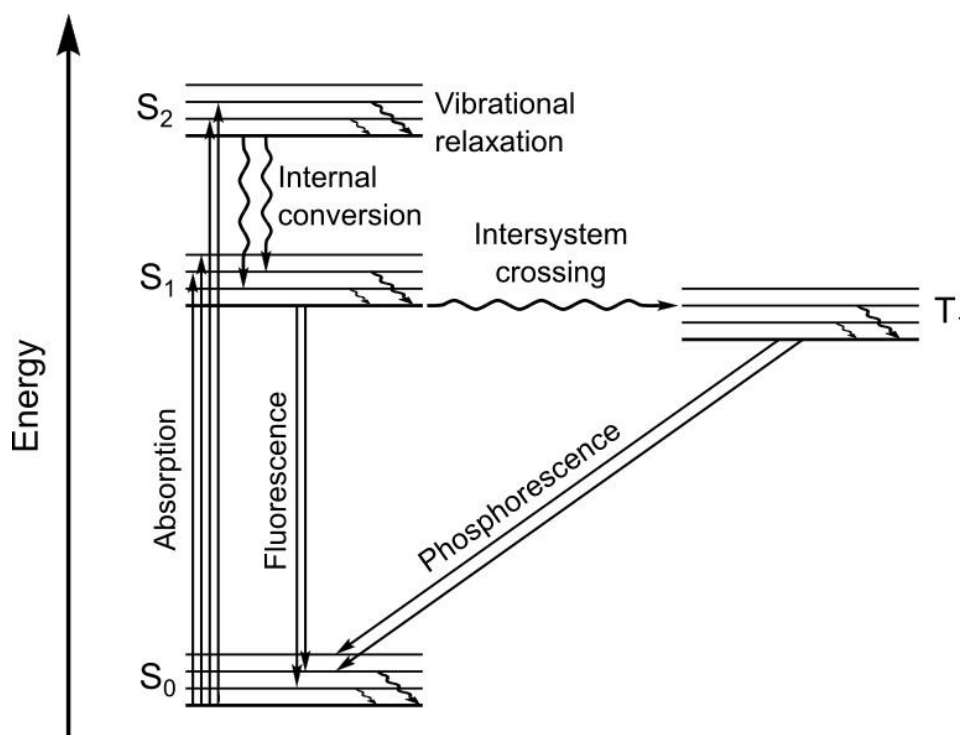


Figure 14: Schematic illustration of the Jablonski diagram. Different energetic states such as the ground state S_0 , the first S_1 and second excited singlet state S_2 and the triplet state T_1 with different vibrational states and various transitions are depicted.

(Figure 14).^[109] After the absorption of a photon in the ground state S_0 , an excited singlet state can be obtained. Subsequently, different pathways allowing to reach lower energy levels are possible. Vibrational relaxation is a non-radiative transition to lower vibrational states of the considered electronic state. In the case of internal conversion, first, the transition from a higher electronic state to an excited state of a lower electronic state proceeds in a radiation-free fashion. Next, vibrational relaxation into lower vibrational states occurs. The spin-forbidden intersystem crossing from an excited singlet state to the lowest triplet state (T_1) constitutes an important step for the formation of radicals in common photoinitiator systems. In the case of fluorescence, the transition from the lowest excited single state (S_1) to the

ground singlet state (S_0) is accompanied by the emission of a photon and commonly takes place on the timescale of nanoseconds. The corresponding spin-forbidden transition from a triplet state (T_1) to the ground singlet state (S_0) also constitutes a luminescent transition but since the multiplicity is changed, it occurs significantly slower (usually seconds to hours). In addition to one photon absorption, multiphoton absorption can be illustrated in the Jablonski diagram in a facile fashion (refer to section 2.2.2.1).

2.2.2 Microscopic Printing via Direct Laser Writing (DLW)

The fabrication of complex micro- and nanostructures constitutes a highly challenging research field. Well-established methods for the 2D structuring of layers are nanoimprint technologies^[110] and electron-beam lithography (EBL).^[111] High lateral resolutions are obtained for EBL, facilitating the patterning of sub-10 nm polymer trenches on substrates.^[112] In addition, the usage of experimental microchemical pens^[113] and atomic force microscopy (AFM) “Dip-Pen” nanolithography^[114] have enabled the 2D deposition of material. However, the transition to true free-form 3D printing technologies has been highly limited. Efforts to further develop the already existing methods led to gray-scale EBL that is based on the dose-modulation of electron beams (**Figure 15**).^[6] Subsequently, the correct annealing

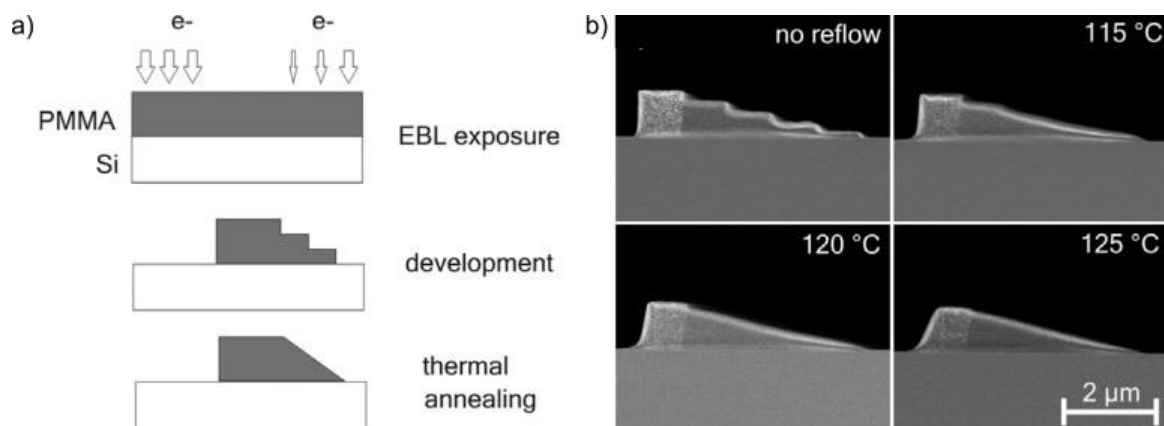


Figure 15: Fabrication of 3D structures via gray-scale electron-beam lithography (EBL). a) Process chain for the provision of 3D shapes via dose-modulated EBL and subsequent annealing. b) Determining the correct annealing temperature is crucial to facilitate a smooth surface. Adapted with permission from Ref.[6]. Copyright 2010 Elsevier.

temperature has to be determined to enable smooth 3D objects. Recently, the focused electron beam induced deposition of material was presented and computer-aided design programs allowed for the fabrication of 3D lattice structures.^[102] Still, features such as undercuts, bridges, and overhangs in complex objects remain highly challenging. Utilizing multiphoton absorption, direct laser writing (DLW) presents a powerful and versatile tool facilitating the fabrication of true free-form 3D structures. The accessibility of commercially available setups further enhances the impact of the technology.^[115] In the following pages, the fabrication of 3D microstructures via DLW is presented.

2.2.2.1 Fundamentals of DLW

The fabrication of microstructures via DLW is based on the multiphoton absorption of molecules in a photoresist. Most systems are activated via a two-photon absorption (2PA) process. Simultaneous absorption of two photons in a single quantum event allows for the employment of photons that possess only half the energy in comparison to the photoactivation in a one-photon absorption (1PA) fashion (**Figure 16**).^[16] Photoinduced

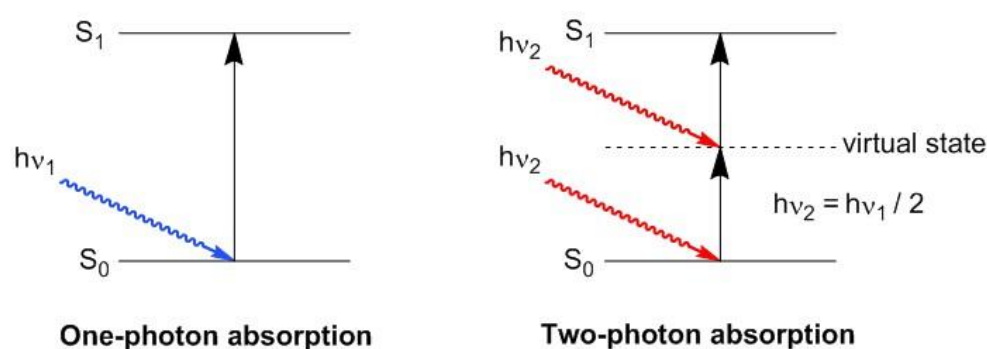


Figure 16: The electronic excitation of a system in a one-photon absorption (1PA, left) and in a two-photon absorption (2PA, right) process is illustrated. a) The absorption of a single photon results in the direct transition into the electronically excited state. b) In a 2PA process, simultaneous absorption of two photons, each with half the energy compared to 1PA, leads to the transition into the electronically excited state.

reactions that require UV light in 1PA are readily accessible with near-infrared (IR) light. The prevalence of 2PA events is proportional to the square of the light intensity. Due to the high intensity that is required, focused near-IR femtosecond pulsed laser beams are utilized. Originating from the nonlinear nature of 2PA, the absorption is limited to the focal point, the so-called voxel, of the optical path (**Figure 17a**).^[16] This statement only holds true for the employment of components that do not absorb near-IR light in a 1PA fashion. The highly defined focal point of 2PA was first utilized for laser scanning fluorescence microscopy in 1990, to provide intrinsic 3D resolution of living cells.^[116] However, the usage of 2PA for the photoactivation of caged effector molecules to enable 3D spatially resolved photochemistry was already suggested at that time. By comparing the optical paths stemming from a UV lamp and from a mode-locked Ti:sapphire laser ($\lambda = 800$ nm) in a solution with absorbing molecules demonstrates the pronounced differences of 1PA and 2PA (**Figure 17b**).^[5] Excluding the penetration depth of the UV light, the absorption rate in the 1PA experiment is constant in all

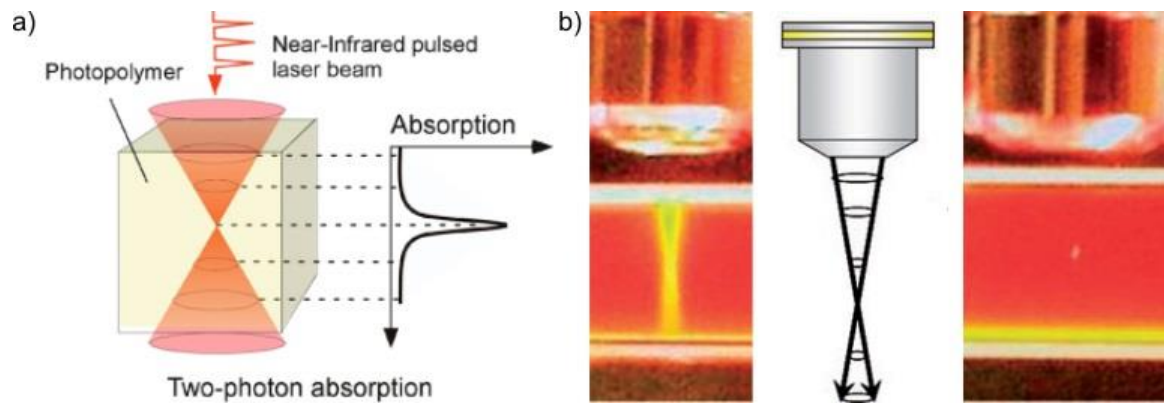


Figure 17: Optical paths of focused UV and near-IR light in a solution with UV absorbing moieties. a) Schematic depiction of the optical path of a near-IR pulsed laser beam in a photoresist and the corresponding local absorption. b) Optical paths of the focused light of a UV lamp (left) and of a mode-locked Ti:sapphire laser ($\lambda = 800$ nm) (right). Adapted with permission from Ref.[5] and Ref.[16]. Copyright 2007 and 2008 John Wiley and Sons.

transverse planes of the focused beam, while in the case of 2PA absorption only occurs in the focal point.

Thus, 2PA facilitates the precise photoactivation of molecules and the fabrication of 2D patterns on surfaces is feasible by the movement of the stage or the voxel in xy-direction. Enabling further the control over the z-coordinate, free-form 3D printing of microstructures is readily available and is presented in the following pages.

2.2.2.2 Experimental and Commercially Available Setups for DLW

Originating from the requirements for 2PA, certain devices are fundamental for commercially available as well as custom-built DLW setups (**Figure 18**). First, a computer is essential operating multiple components including a laser source, a device to tune the intensity of the laser beam, e.g., an acousto-optic modulator (AOM), a component to either move the stage or the voxel, and a camera to allow for the online observation of the processes. In addition, an objective lens to focus the laser beam and a photoactive medium, commonly named photoresist, that is capable to undergo 2PA processes are necessities.^[5, 16, 103] The defined movement in lateral and axial resolution can be achieved via piezoelectronic 3D scanning stages that offer true free-form microfabrication. However, the writing speeds using this scanning mode are often limited to 100 or 200 $\mu\text{m s}^{-1}$. In order to accelerate the process, the lateral movement can be induced by galvanometric mirrors. Here, the printing process is similar to additive manufacturing, scanning each xy-layer after defined steps in z-direction.

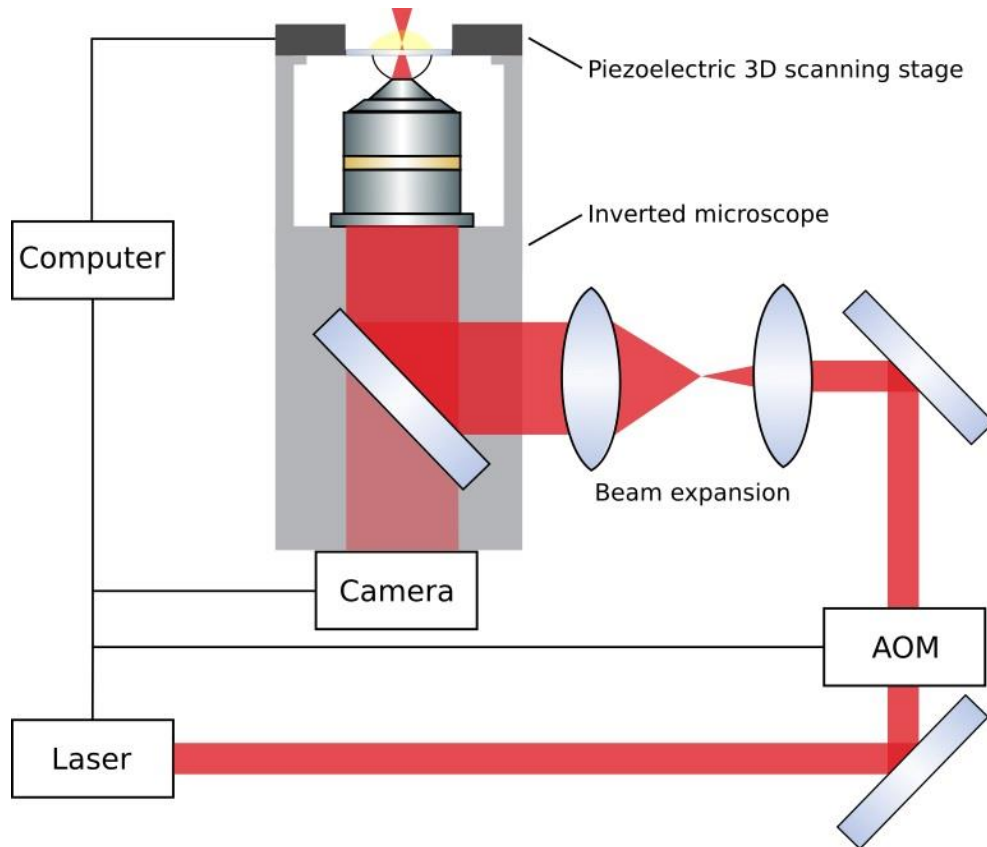


Figure 18: Schematic depiction of the fundamental devices on which commercially available and custom-built DLW setups rely. As an alternative to the piezoelectric 3D scanning stage, lateral movement can be induced via galvanometric mirrors. The tuning of the laser power can also be achieved via shutters instead of the acousto-optic modulator (AOM).

Due to an often small writing window of piezo stages, operating a mechanical stage can facilitate the fabrication of structures with heights in the millimeter range.^[117]

Offering the facile application of DLW, the commercially available setup “Photonic Professional” (Nanoscribe GmbH, Germany) operates at a center wavelength of 780 nm enabling the processing of a wide variety of UV-curable photoresists.^[103] A widely employed laser source is the femtosecond pulsed Ti:sapphire laser that facilitates DLW in a custom-built setup with a center wavelength of 800 nm, a pulse width of 100 fs and a repetition rate of 80 MHz.^[118] Additional DLW setups expand the variety of accessible systems offering a center wavelengths of 700 nm and control over the repetition rate.^[119, 120]

2.2.2.3 Fabrication Process of DLW Structures

The fabrication of microstructures via DLW is based on a 2PA process (refer to section 2.2.2.1) utilizing a femtosecond pulsed near-IR laser beam that is tightly focused into a photoresist (**Figure 19**). To enable a defined writing process, the optical path passes through immersion oil employing an oil-immersion objective. The refractive indices of the immersion oil and the glass substrate are matched, however, the employed photoresist can exhibit a deviating value. Therefore, high structures require a correction along the z-direction to allow for the

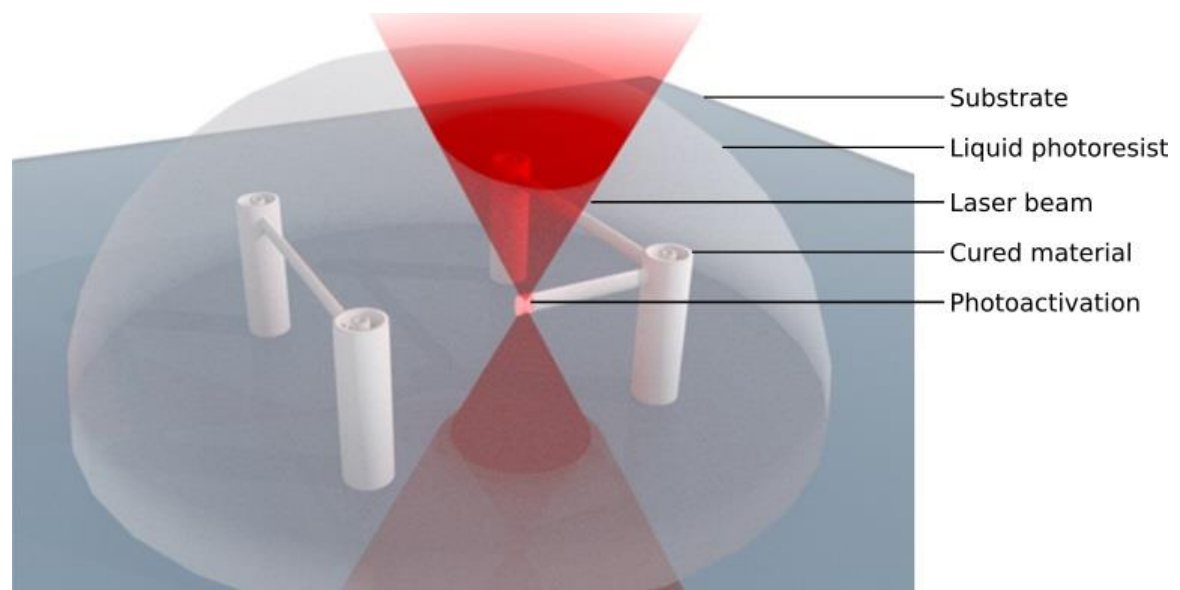


Figure 19: Schematic depiction of the fabrication of microstructure utilizing a negative-tone photoresist in DLW. Photoactivation in the voxel is enabled via 2PA processes and the polymerization of the photoresist is facilitated yielding a cured crosslinked material.

accurate fabrication of the corresponding 3D model. By tracing the optical path, photoactivation and curing of liquid negative-tone photoresists occurs only in the focal point, the voxel. The precise movement of the voxel is enabled via piezoelectric stages or via galvanometric mirrors (also refer to section 2.2.2.2) facilitating the fabrication of complex microstructures. After rinsing with an appropriate solvent that dissolves the still liquid photoresist, the final object is obtained. This step is also referred to as the development of the structure. To ensure the adhesion of the printed material, the employed substrate is often coated with a functional silane that allows for the covalent attachment of the object to the surface. Furthermore, the addition of a different photoresist after development enables the fabrication of compound or multimaterial structures containing diverse chemistries, in the case that sufficient adhesion between the two materials exists.

2.2.2.4 Common and Experimental Photoresists for DLW

The majority of employed photoresists for multiphoton absorption processes are based on radical polymerization of multifunctional acrylate moieties.^[5] Acrylic photoresists further offer rapid polymerization rates enabling fast writing speeds, a highly crosslinked material after curing exhibiting a low tendency to swell or shrink, and a fast removal of the liquid parts due to their good solubility in common solvents such as ethanol.^[5] In addition, a variety of photoinitiators are well-investigated allowing for the fast provision of new photoresist mixtures with adjusted properties. Due to their broad use in industry, a variety of suitable components is readily available. A selection of commonly employed acrylic components and photoinitiators is depicted in **Figure 20**.^[5] Acrylic resins belong to the class of negative-tone photoresists due to the induced crosslinking reaction via light.

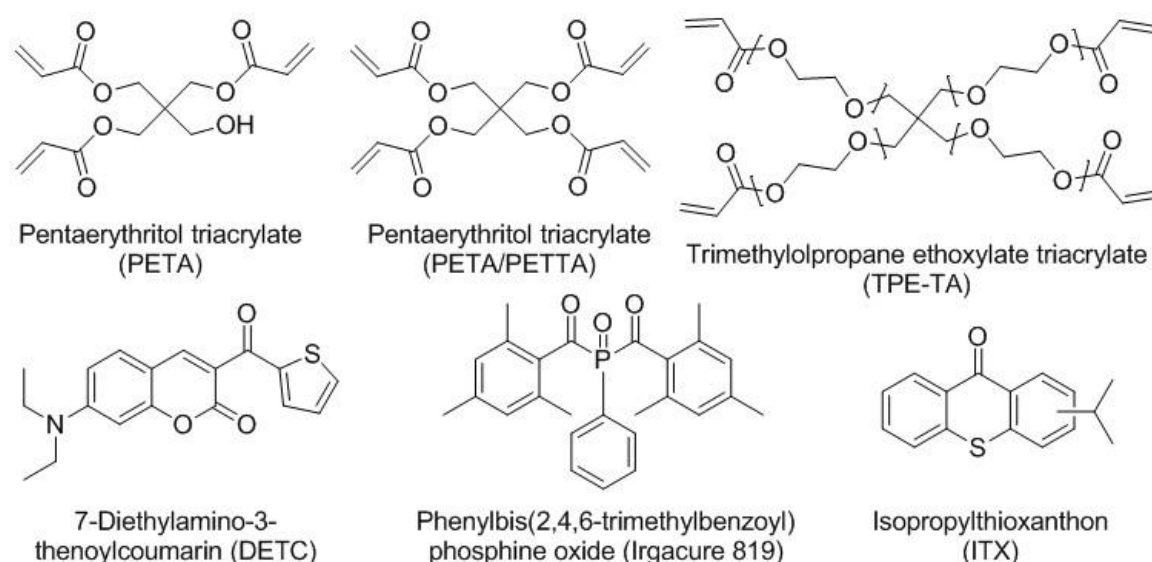


Figure 20: Commonly employed multifunctional acrylate moieties (top row) and photoinitiators (bottom row) for DLW photoresists. PETA (top left) and DETC (bottom left) constitute the main components in the commercially available IP-L 780 that was utilized for reference structures in the present thesis.

Other commonly used photoresists are epoxy-based mixtures, e.g. SU-8, which is based on cationic polymerization.^[121] In comparison to acrylate photoresist, the fabrication of SU-8 involves additional preparation steps (**Figure 21**). After spin-coating of a film containing the multifunctional epoxy moiety and a photoacid generator, a prebake is required. Photoactivation leads to the formation of acidic species that initiate the cationic ring-opening polymerization of the epoxy groups. Due to the high number of functionalities, i.e. eight epoxy

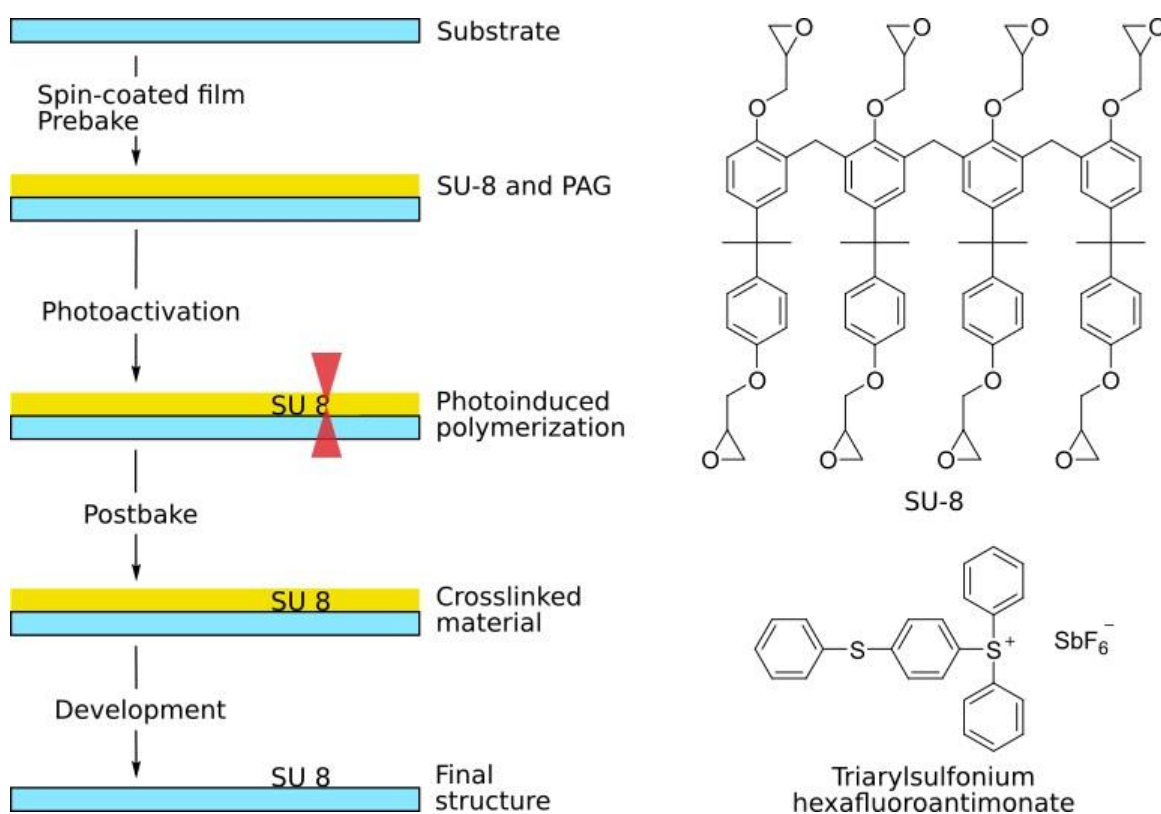


Figure 21: Schematic depiction of the fabrication procedure for epoxy resins (left) and the chemical structure of the main components (right): the multifunctional epoxy moiety and the photoacid generator (PAG).

group per monomer, a highly crosslinked material is obtained. Subsequently, the film is postbaked and the final structures are obtained via development in organic solvents. The amount of additional procedural steps compared to acrylic photoresists first seem to be a significant disadvantage. However, the fine-tuning of each step can improve the quality of the final product, enabling highly specialized material properties.^[118]

In addition to the commonly employed acrylic and epoxy photoresists, an increasing library of applicable chemistries for DLW has been provided in the last few years.^[122] The development of thiol-ene and thiol-yne photoresists allowed for radical-mediated polymerizations in a step-growth fashion enabling the fabrication of networks with highly defined crosslinks, which can be subsequently functionalized (refer to section 2.2.4.3 and 2.2.4.4).^[123, 124]

Utilization of photoinduced Diels–Alder reactions enabled novel systems for DLW. A similar procedure compared to SU-8 photoresists was employed to cure a multifunctional furan monomer and a maleimide linker.^[125] Subsequently, multifunctional thiol species embedded into the network allowed for the photoinduced crosslinking of the material and disabled the ability of reacted units to undergo a retro Diels–Alder (rDA) reaction. Heating of the sample

facilitated the rDA reaction of non-irradiated areas and left behind the thiol-ene based structures.^[125] Further investigations of Diels–Alder chemistry utilized the photoinduced formation of a dienophile, an *o*-quinodimethane, that readily allowed for the crosslinking with maleimide species utilizing the usage of multifunctional linkers.^[126] The spatially resolved deactivation of the dienophile via an isomerization-induced reverse reaction, employing a continuous light source and a phase mask, facilitated sub-diffraction-resolution of 2D patterns.

Recently, novel material classes have been introduced to DLW. The usage of multilayered graphene sheets that were photopatterned via DLW, enabled the fabrication of flexible micro-supercapacitors with an excellent electric conductance.^[127] In addition, the fabrication of glass objects and patterns was facilitated, employing a reaction mixture of a UV curable photoresist mixed with silica nanopowder (**Figure 22**).^[128] After irradiation and crosslinking, the debinding and sintering utilizing temperatures of 1300 °C was demonstrated and complex structures on the microscale based on glass were obtained via DLW.

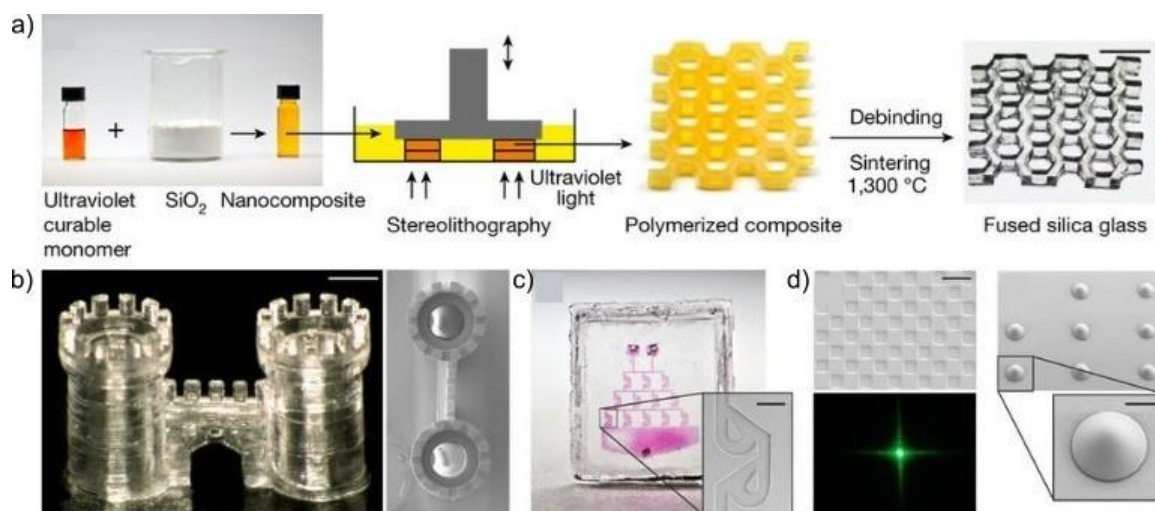


Figure 22: Fabrication of glass structures via laser lithography. a) The mixture of a UV curable monomer and amorphous silica nanopowder is 3D printed via laser lithography. Through thermal debinding and sintering, fused silica glass is obtained (scale bar, 7 mm). b) Microscopic structures were fabricated via microstereolithography (a) (scale bar, 270 μm) and microlithography utilizing a microfluidic chip (b) (inset scale bar, 200 μm). c) Depiction of the optical projection pattern (bottom) employing a micro-optical diffractive structure (scale bar, 100 μm). d) Microlens array fabricated via grayscale lithography (inset scale bar, 100 μm). Adapted with permission from Ref.[128]. Copyright 2017 Springer Nature.

2.2.2.5 Fields of application for DLW

Allowing for the facile fabrication of 3D microstructures, DLW constitutes a versatile tool for a wide variety of applications ranging from waveguide-based systems,^[129] to tissue engineering,^[130] to micromachines^[131], to metamaterials,^[15, 132] to sub-diffractive printing,^[133] and microfluidic systems.^[134] Here, only a small selection is introduced.

To mimic biological tissue, a high control over the adhesion of various cells to each other as well as interactions with employed scaffolds has to be achieved. A multimaterial scaffold was utilized containing passivating structural elements, a network prone to post-modification via biotinylation, and an additional material with a high tendency to immobilize fibronectin on the surface (**Figure 23a-b**).^[130] The selective and cell type-specific adhesion was demonstrated, offering an advanced platform for the study of, e.g., cellular responses to multiple extracellular influences. To allow for the precise motion of microstructures based on

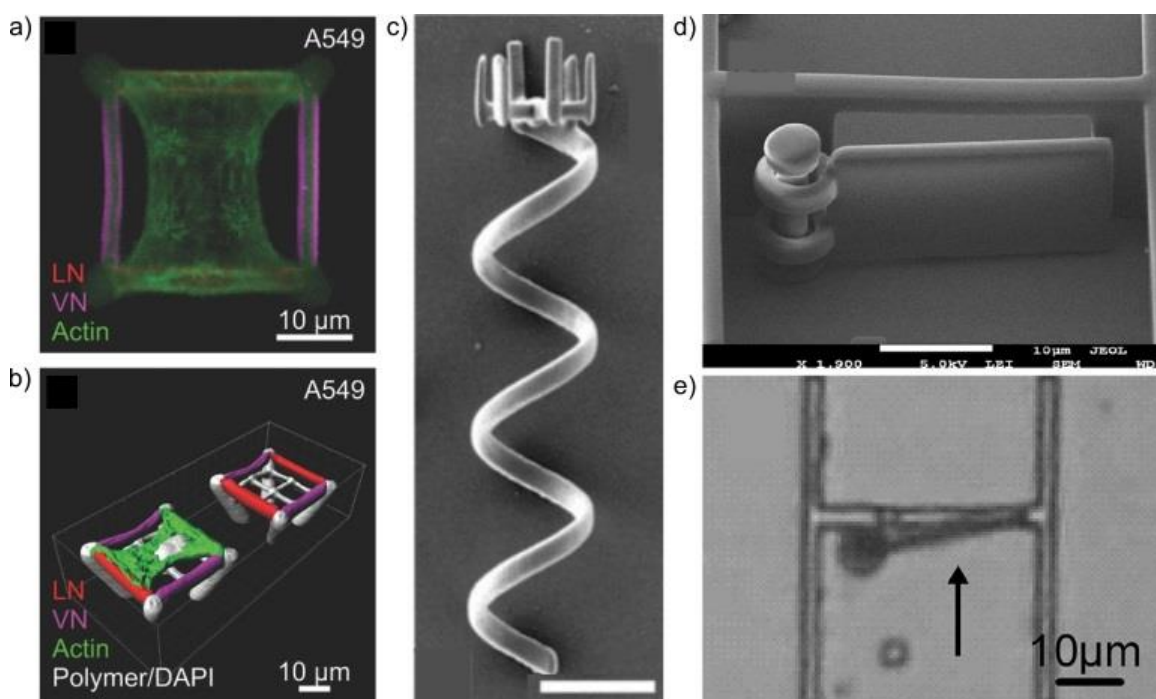


Figure 23: Small selection of applications that were enabled via DLW. a-b) Scaffolds written with multiple materials that allowed for the selective adhesion of proteins were introduced. High control over the cell attachment behavior of, here, epithelial (A549) cell lines was demonstrated. c) Helical micromachines with a microholder to transport cargo were fabricated via DLW. Motion of the microswimmers in solution is induced via rotation (scale bar, 10 μm). d) A microfluidic system was expanded by a DLW printed microvalve that facilitates the switching switches between an open and a closed state. Adapted with permission from Ref.[130], [131], and [134]. Copyright 2016 and 2012 John Wiley and Sons, 2009 Royal Society of Chemistry.

rotation, magnetic helical micromachines were printed via DLW (**Figure 23c**).^[131] The swimming in solution is based on a steerable corkscrew motion revealing high speed in deionized water. To attach a cargo, a microholder was utilized and successful transport of the cargo was facilitated in three dimensions. The use of the microswimmers as drug delivery device appears to be highly promising.^[131] In the field of microfluidic systems, DLW enabled new approaches by the fabrication of a microvalve (**Figure 23d**).^[134] Employing the corresponding flow direction, the microscopic gate either freely opens or motion is hindered due to the gate frame.

2.2.3 Macroscopic 3D Printing via Stereolithography (SLA)

Stereolithography (SLA) belongs to the group of laser lithographical techniques and it allows for the facile fabrication of prototypes, small series products, complex objects, and further offers a fast customization.^[135] Two slightly different types of SLA 3D printers are available (**Figure 24**).^[136] In a bottom-up setup, each spot of a layer is scanned successively employing a laser. The top-down type SLA printer utilizes a digital mirror device, enabling the simultaneous curing of each spot of a layer.^[135, 136] A major advantage of 3D printing via SLA

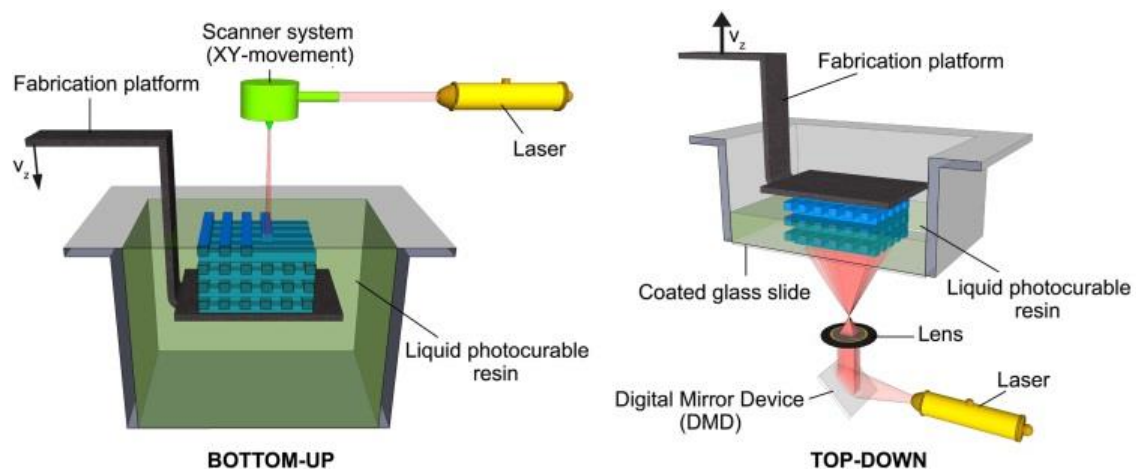


Figure 24: Schematic depiction of the two types of stereolithography (SLA) 3D printers. In a bottom up setup (left), each spot of a layer is scanned successively employing a laser. The top-down SLA 3D printer utilizes digital mirror devices (DMD), allowing for the simultaneous irradiation of each spot of a layer. After curing of each layer, the fabrication platform is lowered (bottom-up setup) or elevated (top-down SLA 3D printer). Adapted with permission from Ref.[136]. Copyright 2012 Elsevier.

is the excellent control over the porosity and permeability of the resulting objects. In addition, the size, shape, and even the interconnectivity of pores in printed materials are tunable, making SLA a promising 3D printing method for the fabrication of tissue scaffolds.^[137] However, the biocompatibility of most commonly employed materials has to be optimized.^[138] SLA further offers a high resolution of the printed objects and a custom-built setup was reported, facilitating a lateral resolution of 5 μm and an axial of 10 μm .^[135]

Standard photoresists for SLA are mainly based on the polymerization of acrylates and epoxides. Acrylic resins exhibit fast reaction kinetics, but reveal the tendency to shrink after the crosslinking. Epoxy-based photoresists possess a higher dimensional stability, but possess slower curing rates.^[139]

Extending the variety of photoresists for SLA 3D printing is crucial to obtain advanced property profiles of printed material. A thiol-ene based photoresist was developed and enabled the fabrication of structures with a resolution of $50\ \mu\text{m}$.^[140] The material exhibited high elastic moduli and self-healing properties and is highly promising for applications in the field of soft robotics. Utilizing a methacrylic macromonomer, the fabrication of 3D printed shape memory objects was demonstrated.^[141] The responsive structures could be used in sensors and wearable electronics. To allow for the application of 3D printed material in advanced devices operating at high temperature and harsh conditions, the fabrication of ceramic components via SLA was demonstrated (**Figure 25**).^[142] The usage of methacrylate functionalized polysiloxanes facilitated the processing via a top-down SLA 3D printer. To obtain the final ceramic structure, pyrolysis of the printed objects at $1000\ ^\circ\text{C}$ was conducted. The material exhibited an optimal surface quality and the fabrication of cellular geometries with feature sizes of approximately $200\ \mu\text{m}$ opens up a wide range of application fields.^[142]

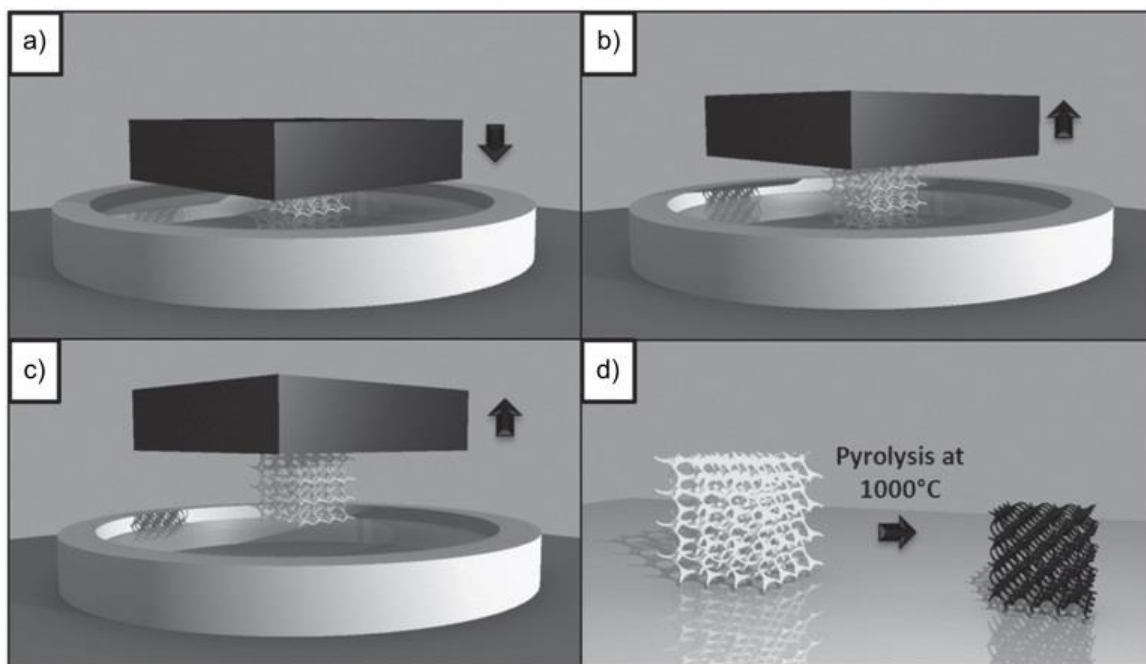


Figure 25: Schematic depiction of the fabrication of preceramic photopolymers via SLA. a) The stage is lowered into the photoresist leaving a gap between the transparent bottom and the stage that defines the thickness of each layer of the object. b) Upwards motion releases the structure, before the stage is lowered again for the layer-by-layer fabrication. c) After the printing process is completed, the 3D component is removed from the moving stage. d) To obtain the SiOC ceramic microcomponent (right), pyrolysis at $1000\ ^\circ\text{C}$ is conducted. Adapted with permission from Ref.[142]. Copyright 2015 John Wiley and Sons.

2.2.4 Network Formation

The most common polymerization technique utilized for photoinduced 3D printing applications, is the free radical polymerization employing (meth)acrylates. However, all chemical reactions that form a bond between two molecules can theoretically be utilized for network formation via the usage of multifunctional moieties. Each reaction step leads to a new crosslink in the material and, accordingly, the mechanism is referred to as step-growth polymerization. The usage of difunctional monomers results in the formation of polymer chains that can form physically bonded networks. To facilitate covalently crosslinked materials, the sum of reactive functionalities for two reaction partners has to be bigger than five with each linker moiety carrying at least two. Applying step-growth polymerization to photochemically triggered 3D printing, the chosen conjugation method has to be selective to assure the formation of a highly defined network. In addition, fast reaction kinetics are required to achieve good writing speeds and, therefore, achieve appropriate time frames for 3D printing. Especially in the case of commercially available setups that do not allow for the adjustment of parameters such as the curing time, a rapid timescale for network formation is essential. In recent years, the transfer of organic synthesis strategies to polymer science enabled the fabrication of novel networks to develop unique materials with various properties.^[17, 143] The photoenol conjugation is a prime example introducing a step-growth based photoresist to DLW.^[126] Extending the range of printable photoresist further facilitated the simple post-modification of structures.^[144] In addition, novel functionalities are accompanied by unique properties such as those enabling sub-diffraction laser lithography by deactivation of reactive species with a second laser beam.^[133] To provide a better understanding for applicable chemistries, suitable conjugation methods are discussed in the following pages.

2.2.4.1 Conjugation via Photogenerated Thioaldehydes

Thioaldehyde chemistry offers a valuable strategy for the incorporation of sulfur heteroatoms to obtain heterocycles or natural products. Despite the highly reactive nature of the group, a wide variety of synthetic routes for both, stable and transient, thioaldehydes is provided in literature.^[145, 146] To increase the stability of components at ambient temperatures, the spontaneous oligomerization has to be prevented by the introduction of electronic or steric stabilization employing thioamides, thioesters, or bulky substituents.^[145] The cycloaddition of thioaldehydes in a Diels–Alder reaction with dienes constitutes a well-investigated conjugation procedure.^[146] Combining the advantages of stable components and highly reactive functional groups, the photofragmentation of phenacyl sulfides was introduced.^[147] The in-situ generation of thioaldehydes facilitated the conjugation with various diene moieties in a Diels–Alder reaction. Transferring this model to polymer chemistry, an efficient conjugation tool for the spatially resolved patterning of polymers onto phenacyl sulfide functionalized substrates was established (**Figure 26**).^[146] The photoinduced generation of

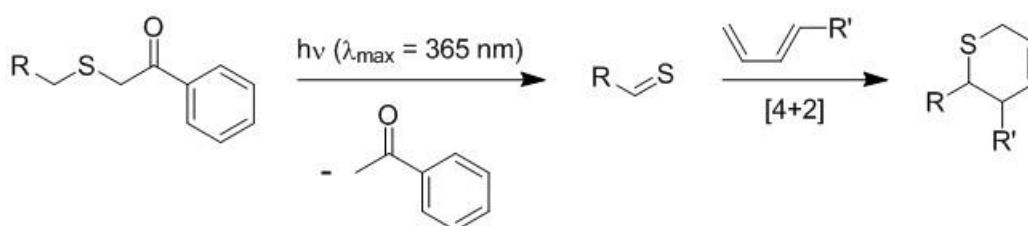


Figure 26: In-situ generation of thioaldehydes via the photofragmentation of phenacyl sulfide moieties. The [4+2] cycloaddition employing dienes yields the Diels–Alder adduct. In the presented study, the R group contained a silane for the immobilization onto a surface and the R' comprised a PEG chain.

thioaldehydes at ambient temperatures on the surface allowed for the immobilization of cyclopentadiene functionalized PEG. In addition, a carboxylic acid-bearing phenacyl sulfide moiety was immobilized onto a cellulose substrate via esterification.^[148] Spatially resolved post-modification of the surface was readily achieved employing a diene functionalized peptide sequence or cyclopentadiene end-capped poly(trifluoro ethyl methacrylate). To further extend the chemical variety of applicable reaction partners, the photogenerated thioaldehydes were examined towards their suitability to react with additional functional groups. The investigation evaluated various nucleophiles, affording a successful conjugation utilizing primary amines, hydroxylamine derivatives, and thiols (**Figure 27**).^[149] Employing

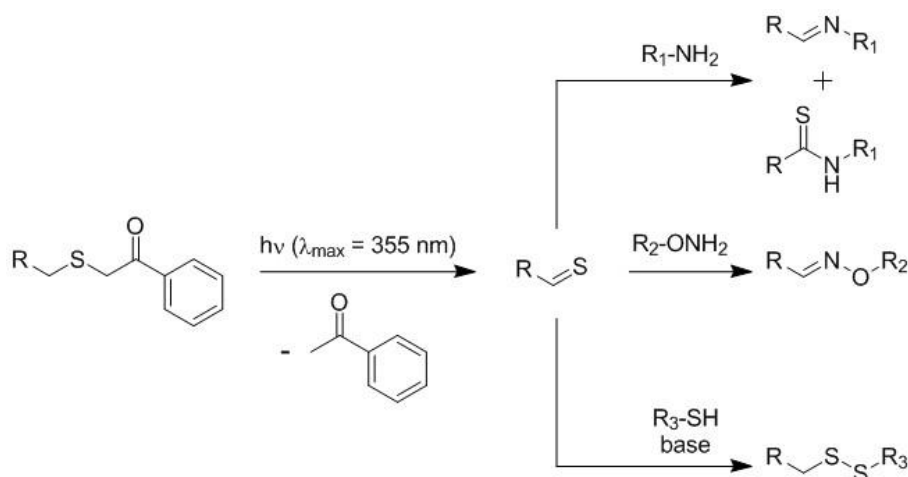


Figure 27: The reactivity of photogenerated thioaldehydes was examined towards nucleophiles. After the photoactivation of a phenacyl sulfide moiety, primary amines, hydroxylamine derivatives and thiolates were reacted with the emerging thioaldehydes. Adapted with permission from Ref.[149]. Copyright 2013 Royal Society of Chemistry.

primary amines, the corresponding imines were obtained, which revealed the tendency to form thioamide species via subsequent oxidation by sulfur species. Hydroxylamine derivatives resulted in the formation of oximes that exhibited a higher stability towards oxidation. In addition, thiolates were reacted with the thioaldehydes, obtaining disulfide bridges.^[149] The extension of applicable chemistries led to the defined step-wise folding of single-chain nanoparticles (Figure 28).^[150] Block copolymers with phenacyl sulfide and α -methyl benzaldehyde units were irradiated in the presence of difunctional thiol linkers, obtaining disulfide crosslinks with the formed thioaldehyde groups. Subsequently, the photoactivated α -methyl benzaldehyde species were crosslinked with diacrylates.^[150]

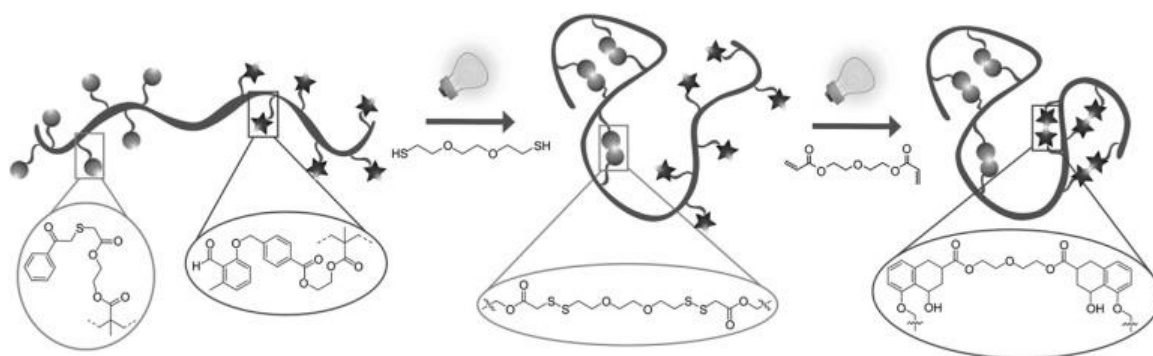


Figure 28: Step-wise folding of single-chain nanoparticles utilizing the reactivity of photoactivated phenacyl sulfides with thiol groups to form disulfide bridges. Subsequently, irradiation of an α -methyl benzaldehyde in the presence of an acrylate linker led to crosslinking via Diels–Alder reactions. Adapted with permission from Ref.[150]. Copyright 2017 John Wiley and Sons.

2.2.4.2 Reversible Bond Formation via Disulfide Bridges

The disulfide bridge is a model example for reversible bonds that represents a covalent conjugation, however, still can be readily cleaved and restored upon various triggers such as reductants and oxidants (**Figure 29**).^[151] To establish complex effects in biological systems

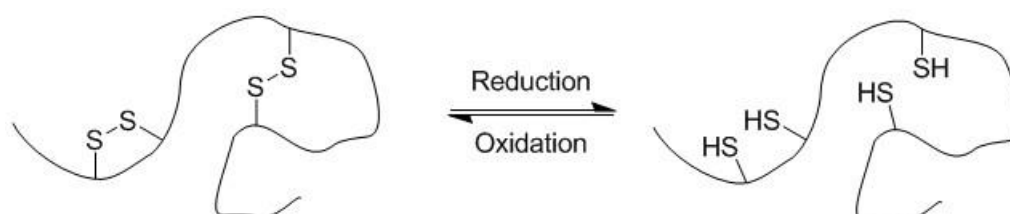


Figure 29: Dynamic disulfide bridges are capable to be cleaved and restored upon reduction and oxidation.

such as proteins, nature often utilizes disulfides for the formation of the final structure. Mimicking of the properties relies on an in-depth understanding of the fundamental reasons for the use of these weak bonds.^[152] Peptides are often linked via disulfides, for instance in disulfide-bridged peptide bicycles.^[153] In these comparatively small biological systems, the disulfide bond was observed to be less prone to reduction and did not constitute the main factor for the peptide stability. A common synthetic method to form the bond between two sulfur atoms relies on the oxidation of thiols that can already occur in the presence of atmospheric oxygen.^[154] In addition, the utilization of suitable leaving groups facilitates a nucleophilic S_N2 reaction with thiol functionalized components. This synthesis strategy is favored for the formation of unsymmetrical disulfides, but commonly suffers from long reaction times and is prone to thiol-disulfide exchange reactions.^[154] The stability of disulfide

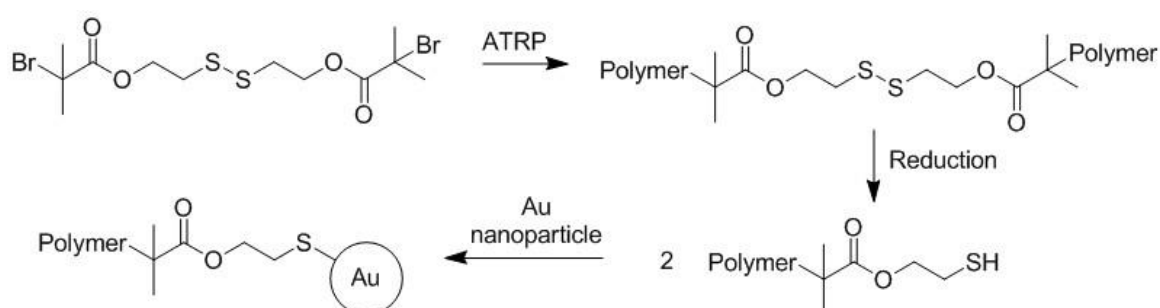


Figure 30: Synthetic scheme for the provision of disulfide containing block copolymers via ATRP that were readily reduced to the thiol derivatives and immobilized onto Au nanoparticles. Adapted with the permission from Ref.[155]. Published by The Royal Society of Chemistry.

bridges facilitated their usage as core functionality of an ATRP initiator (**Figure 30**).^[155] To enable the immobilization of the synthesized polymers onto a gold nanoparticle, reductive conditions were employed obtaining thiol functionalized components with half the molecular weight compared to the original species. For a wide variety of applications, the provision of crosslinked material is of high interest. Therefore, the oxidation of multifunctional thiol moieties was conducted via a photoinduced procedure (**Figure 31**).^[156] Due to the usage of

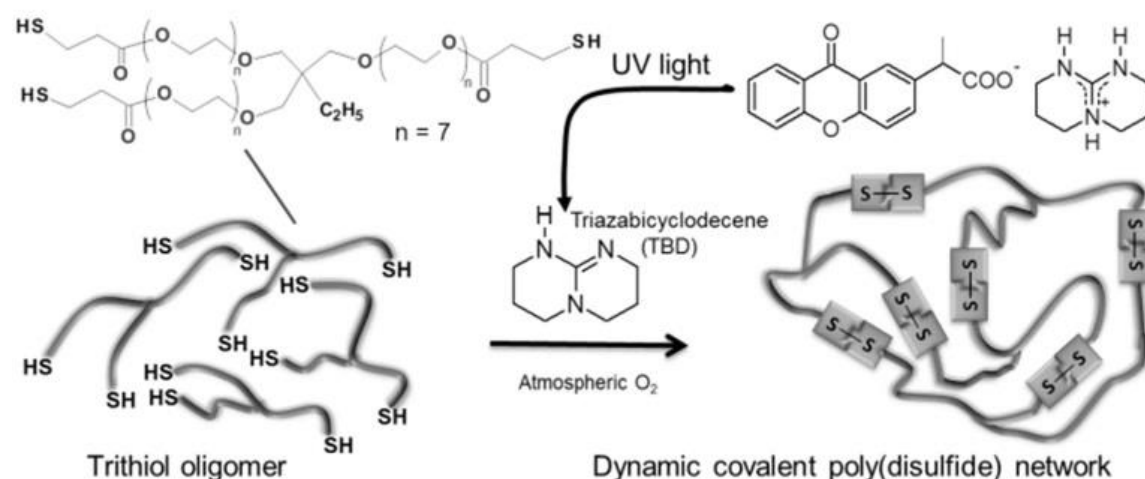


Figure 31: Photoinduced oxidation of a trithiol oligomer to obtain dynamic covalently bond poly(disulfide) networks. Adapted with permission from Ref.[156]. Copyright 2015 John Wiley and Sons.

light, photopatterning was readily achieved and the crosslinks of the resulting networks were exclusively based on disulfide bridges. The obtained network belongs to the group of poly(disulfide)s containing disulfide repeats in their main chain.^[151] Recently, the incorporation of disulfide bridges into organosilica frameworks received increasing attention. In the case of drug delivery, the possibility for responsive biodegradation via the intracellular reductive microenvironment in cells is of high interest, while the high structural stability of the silica framework is maintained.^[157] Therefore, a wide variety of disulfide containing organosilicas were synthesized and investigated towards their suitability for physiological stable but still biodegradable release systems. Taking advantage of the disulfide interchange reaction, the autonomous healing in a covalently crosslinked rubber was explored.^[158] After polymerization via anionic ring-opening copolymerization employing an epoxy resin, a cut in the material disappeared after heating to 60 °C for 1 h. In addition, the utilization of the thiol-disulfide exchange reaction, presenting a side reaction in thiolysis,^[154] can allow for the provision of novel synthetic pathways for disulfide containing networks. Introducing a UV-

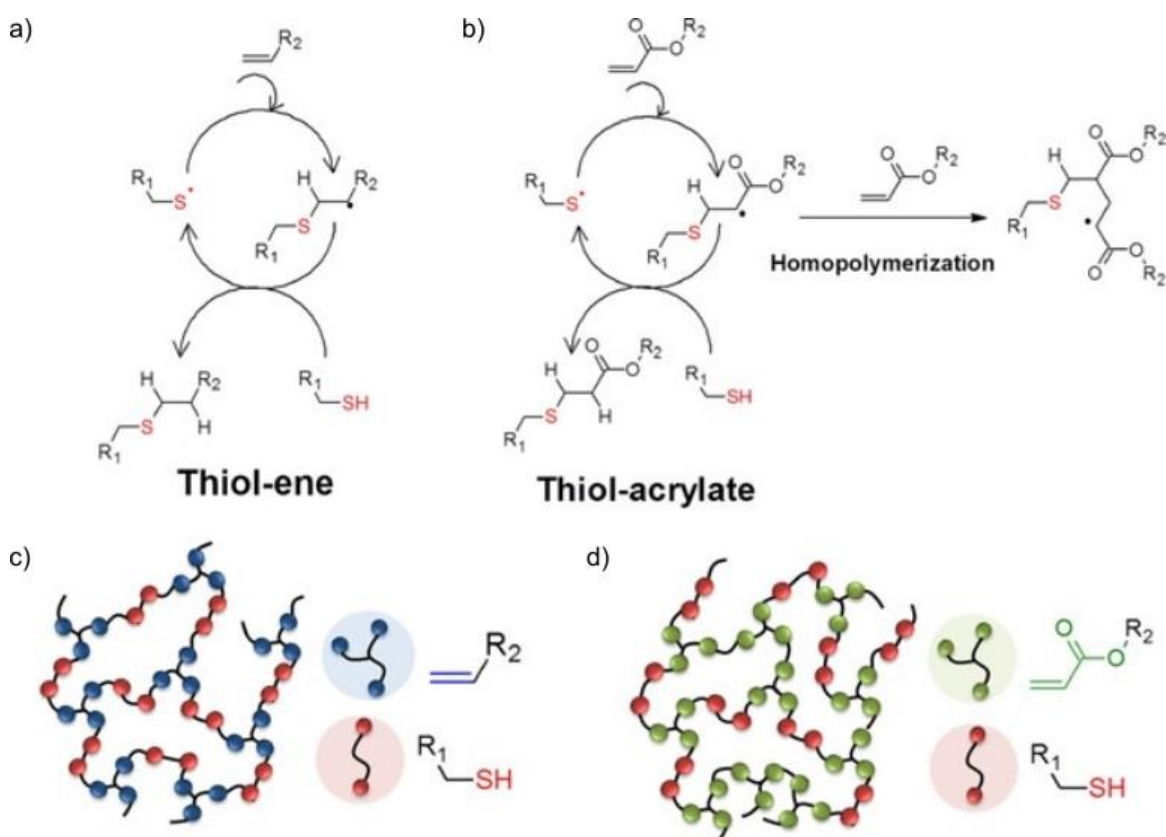


Figure 33: Schematic representation of the underlying chemistry during radical thiol-ene (a) and radical thiol-acrylate (b) polymerization and depiction of the resulting networks utilizing a difunctional thiol and trifunctional ene monomer. Adapted with permission from Ref.[161]. Copyright 2016 John Wiley and Sons.

increasing focus on the radical thiol-ene reaction was observed.^[143] In comparison to free-radical polymerization of, e.g., acrylates that is based on the chain growth forming homopolymers for the usage of one monomer, radical thiol-ene polymerizations proceed in a step-growth fashion (**Figure 33a**).^[161] Employing an acrylate linker as ene moiety, the reaction kinetics were mainly determined by the simultaneous chain growth of the acrylate monomer (**Figure 33b**). To enhance the penetration depth of UV light, the photoinduced polymerization of thiol-ene and thiol-acrylate photoresists without the use of photoinitiators was investigated.^[162] Curing was feasible with light centered around 365 nm, however, faster reaction kinetics were observed for the usage of 254 nm. The provision of thin layers, validating the resistance towards ambient oxygen, and thick layers, utilizing the increased penetration depth of light, was successfully demonstrated.^[162] In recent years, the development of reactions that can be initiated by visible light have attracted increasing attention.^[163] Therefore, the formation of the key thiyl radical that is essential for the radical thiol-ene reaction was examined.^[164] Employing a transition metal-based polypyridyl

photocatalyst, the thiyl radical was obtained with a blue LED ($\lambda = 450$ nm). Due to the mild conditions, visible light mediated thiol-ene reactions are suited for bioconjugation of thiol functionalized biomolecules.^[164] To identify the influence of the ene moiety, various carbon-carbon double bond derivatives were investigated in a small-molecule study with methanethiol (**Figure 34**).^[160] The computational and kinetic analysis revealed the importance

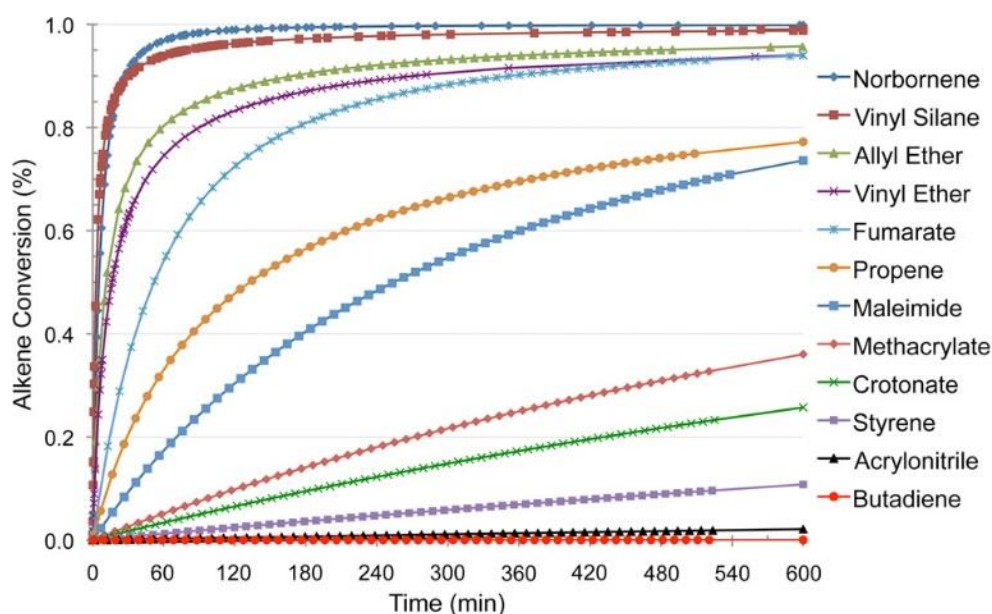


Figure 34: Kinetic modeling of a photoinitiated radical thiol-ene reaction utilizing various alkenes in a small-molecule study with methanethiol. Adapted with permission from Ref.[160]. Copyright 2012 American Chemical Society.

of the radical intermediate and determined the order of the employed components with regard to their reactivity in thiol-ene reactions. Norbornene, vinyl silane, allyl ether and vinyl ether derivatives indicated the highest suitability for fast reaction kinetics.^[165] In addition, the high yields and selectivity of the thiol-ene reaction allowed for the facile preparation of dendrimers.^[166] A dihydroxyl functionalized thiol was reacted with a trifunctional alkene species and subsequently esterified with a double bond derivative. Repetition of the last two steps enabled the synthesis of precise dendrimers allowing for the end-capping with various thiol functionalized components after the esterification step.^[166] In the challenging field of fracture fixation, thiol-ene networks facilitated a high adhesion strength on wet bone substrates that surpasses commercially available acrylate systems.^[167] The adhesive revealed a high biocompatibility and no adverse effects on bone healing. Further investigations of the modification of polymers via Michael addition thiol-ene reactions incorporated *o*-nitrobenzyl

protected thiol moieties into the backbone of an ATRP polymer.^[168] Irradiation with UV light ($\lambda_{\text{max}} = 320 \text{ nm}$) yielded free thiol groups that were readily functionalized with maleimide derivatives in a Michael addition reaction. The provision of norbornene functionalized poly(carbonate)s via ring-opening polymerization allowed for an undemanding method to access multifunctionalized materials.^[169] To adjust the ratios of attached moieties, varying the functional reactants and their relative proportions was sufficient in a non-demanding one-pot reaction. In addition, the photoinduced emulsion polymerization of thiol-acrylate photoresist provided highly porous polymer scaffolds with pore diameters ranging from 30 to 60 μm .^[170] The post-modification of the material was demonstrated via both radical and Michael addition of the remaining thiol functionalities on the surface. Better results were obtained for the usage of the Michael addition procedure, presumably due to the opacity of the networks and

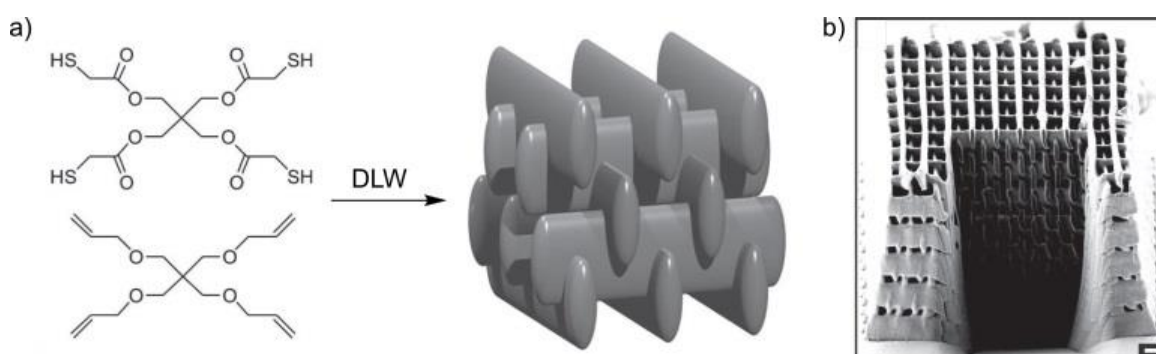


Figure 35: Fabrication of microscopic structures via DLW. a) Utilization of a multifunctional thiol, allyl ether and a photoinitiator allowed for the provision of complex structures. b) SEM image of a woodpile-type object revealing the interior quality of the print after focused ion beam milling (scale bar, 1 μm). Adapted with permission from Ref.[171]. Copyright 2013 John Wiley and Sons.

a strongly limited penetration depth of light.^[170] Utilizing radical thiol-ene polymerization for 3D printing devices, the scope of possibilities and applications is greatly enhanced. Microscopic structures were fabricated via DLW employing commercially available components and a multifunctional allyl ether that was synthesized in a one-step procedure (**Figure 35**).^[171] To demonstrate the versatility of the system, woodpile-type structures with a rod spacing of 2 μm were printed and residual thiol groups on the cured material enabled the facile post-modification with maleimide derivatives. Furthermore, a spiroacetal-based photoresist allowed for the fabrication of macroscopic 3D printed structures.^[172] Assessment of the mechanical properties was conducted for different annealing conditions, revealing high values for the yield strength and toughness after tempering the samples at 40 $^{\circ}\text{C}$ for 120 h.

The presented investigations and applications demonstrate that radical thiol-ene chemistry is a versatile tool that enables the provision of a variety of diverse systems. However, the possibility of side reactions such as the prior described homopolymerization, termination reactions between radical species and the requirement for high ratios to facilitate the conjugation of a polymer with small molecules should be taken into account.^[173] Verifying these limitations, the coupling of polymers, the synthesis of star-type polymers and the end-capping of a polymer with small molecules was conducted via both, the thermally and UV initiated radical thiol-ene reaction.

2.2.4.4 Radical Mediated Thiol-yne Polymerization

Radical mediated thiol-yne conjugation combines the addition of a thiol to an alkyne derivative and the subsequent thiol-ene reaction of an additional thiol with the formed vinyl sulfide moiety (**Figure 36**). Examining the kinetics of the photopolymerization of 1,9-dodecadiyne and pentaerythritol tetra(3-mercaptopropionate), the thiol-yne reaction

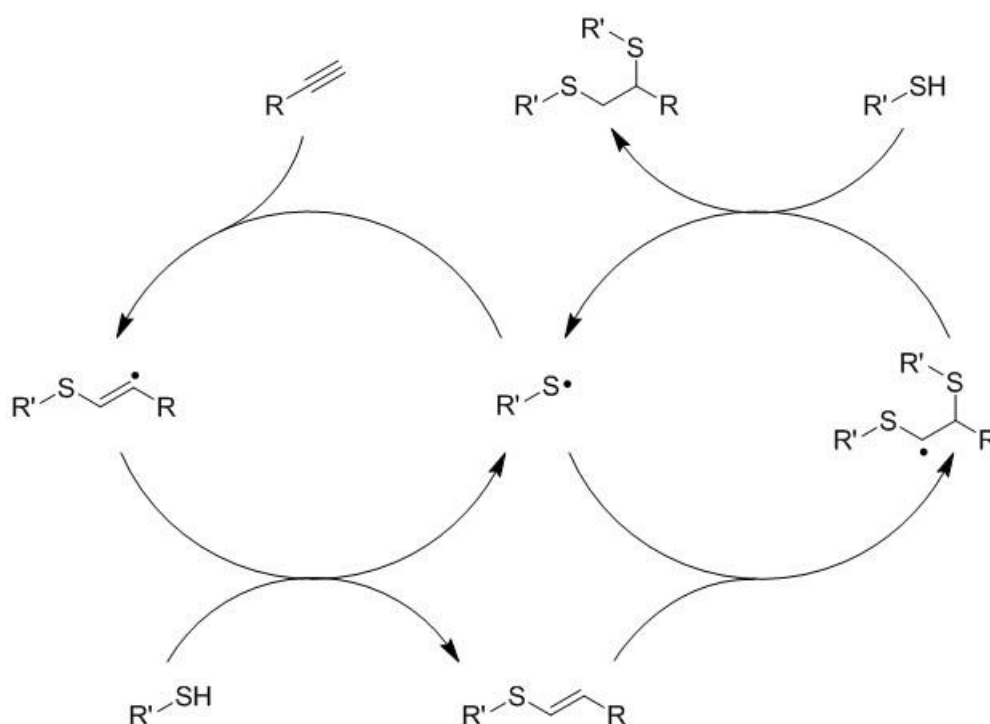


Figure 36: Schematic reaction scheme of the radical thiol-yne reaction. After the addition of a thiyl radical to an alkyne derivative forming a vinyl sulfide (left cycle), a subsequent thiol-ene reaction via the addition of a second thiyl radical to the carbon-carbon double is feasible (right cycle).

was found to be three times slower compared to the subsequent thiol-ene reaction.^[174] Overall, the combined reactions proceeded rapidly obtaining nearly 100% conversion. Transferring the thiol-yne reaction to polymer chemistry, the reaction is well suited for the preparation of multifunctional and (hyper)branched materials.^[175] However, due to the involved thiol-ene reaction, similar drawbacks as discussed in 2.2.4.3 are expected. The polymerization proceeds in a step-growth fashion^[176] excluding the possibility of side reactions such as the homopolymerization. Utilization of a trifunctional alkyne core and a carbon-carbon triple bond functionalized thiol moiety enabled the preparation of hyperbranched architectures.^[177] The obtained polymers exhibited a high degree of branching, well-controlled molecular weights, and low dispersities. In addition, the formation of multi-armed block copolymers was demonstrated using a tetrafunctional alkyne, containing a disulfide bridge.^[178] The obtained polymers self-assembled into micelles and hydrogels in aqueous solution, offering subsequent modification via the reduction of the disulfide bond. Fast reaction kinetics and high degrees of crosslinking are also very beneficial

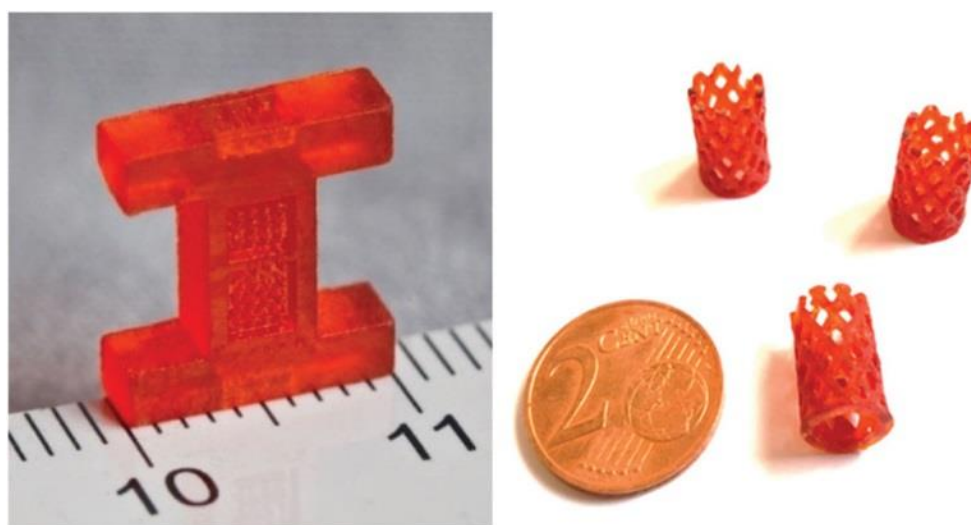


Figure 37: 3D printed test patterns utilizing a photoinduced radical thiol-yne polymerization employing multifunctional alkyne and thiol derivatives. Reproduced with permission from Ref.[179]. Copyright 2016 Royal Society of Chemistry.

for 3D printing applications. Mixtures of multifunctional alkyne species with incorporated carbonate functionalities and various thiol linkers exhibited curing rates similar to comparable acrylate derivatives, offering significantly higher conversions.^[179] The photoresist was processed via digital light processing (DLP) 3D printing (**Figure 37**) and the resulting material revealed considerably lower cytotoxicity compared to (meth)acrylates and an impact strength in the range of poly(lactic acid). In addition, radical thiol-yne mediated polymerization was

employed in the context of DLW.^[117] Utilization of tetrafunctional linker moieties enabled the fabrication of microstructures that were readily post-modified via thiol-ene Michael addition and copper-catalyzed azide-alkyne click reactions. The photoresist mixture was carefully designed to further match the refractive index with regard to the objective lens, facilitating the fabrication of an 1 mm high object in dip-in configuration.^[117]

2.2.4.5 Cleavage of Polymers and Networks

The cleavage of functional groups that are incorporated into a polymer backbone,^[180] functionalized nanoparticles^[181] and nanotubes,^[182] vesicles,^[183] micelles,^[184, 185] adhesives,^[186] and hydrogels^[187] play an important role in various fields of application such as drug delivery systems,^[188] tissue engineering,^[186] 3D printing of demanding geometries,^[189] defined structuring of metal^[190] and metal oxides,^[19] and the provision of biodegradable plastics for our daily life.^[191]

To remove scaffolds for the precise shaping of deposited metal or metal oxides, multi-step procedures are required using a sacrificial material that can be lifted off with solvents (**Figure 38**).^[18] The removal can also be facilitated via harsh conditions such as plasma etching^[20] and high temperatures to burn out polymeric networks.^[19] To reduce the required steps for easily removable structures, a water-soluble photoresist based on dimethylacrylamide was developed. The resin enabled the 3D printing via SLA allowing for a feature resolution of 200 μm .^[192] The subsequent cleavage of the material was performed in 1 M NaOH at 50 °C and resulted in a residue-free removal of the object after 2 h. To fabricate highly demanding geometries in 3D printing, the utilization of support structures is often

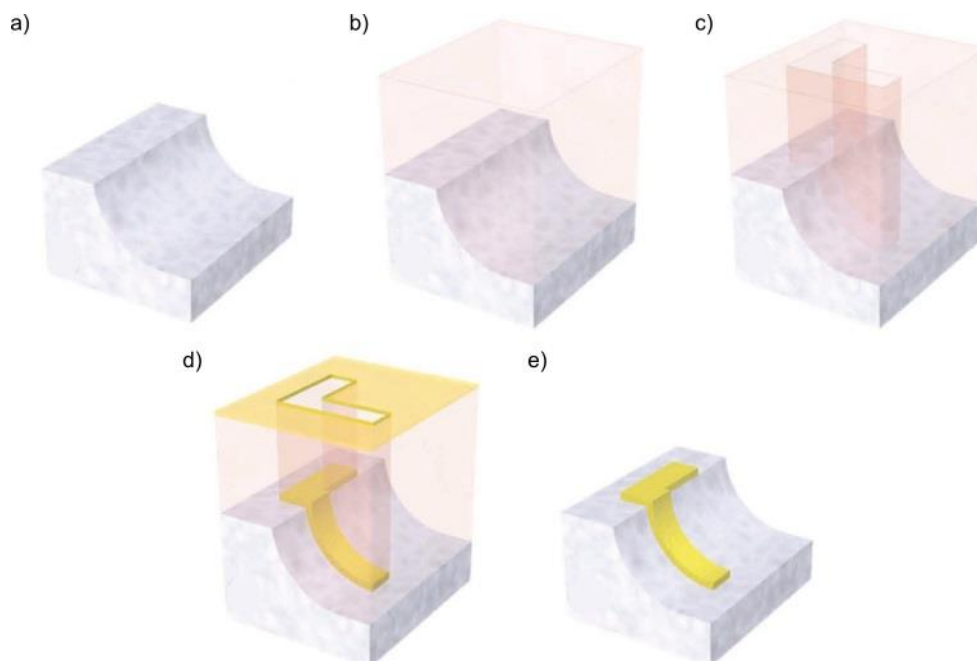


Figure 38: Schematic fabrication sketch for the precise deposition of gold. A pre-structured template (a) was spin-coated employing an electron beam resist (b). Multiple steps were involved to structure the material (c) before the deposition of gold (d) and subsequent lift-off (e). Adapted with permission from Ref.[18]. Copyright 2012 John Wiley and Sons.

inevitable.^[189] Within certain limitations, the precise adjustment of the local shape can prevent the need for supportive elements for the fabrication of overhangs in objects.^[193] The design of polymers and crosslinked materials with selectively cleavable functionalities offers a high control and circumvents the need for rough cleaving conditions. For example, the development of micelles based on boronate ester crosslinks allowed for the controlled release of enclosed drugs in acidic conditions prevalent in, e.g., tumor cells (**Figure 39**). In addition, the selective cleavage of crosslinks in materials facilitated the self-shaping of hydrogels.^[194] The photoinduced cleavage of *o*-nitrobenzyl induced a spontaneous asymmetric swelling of the investigated network without the loss of its physical integrity and robustness.

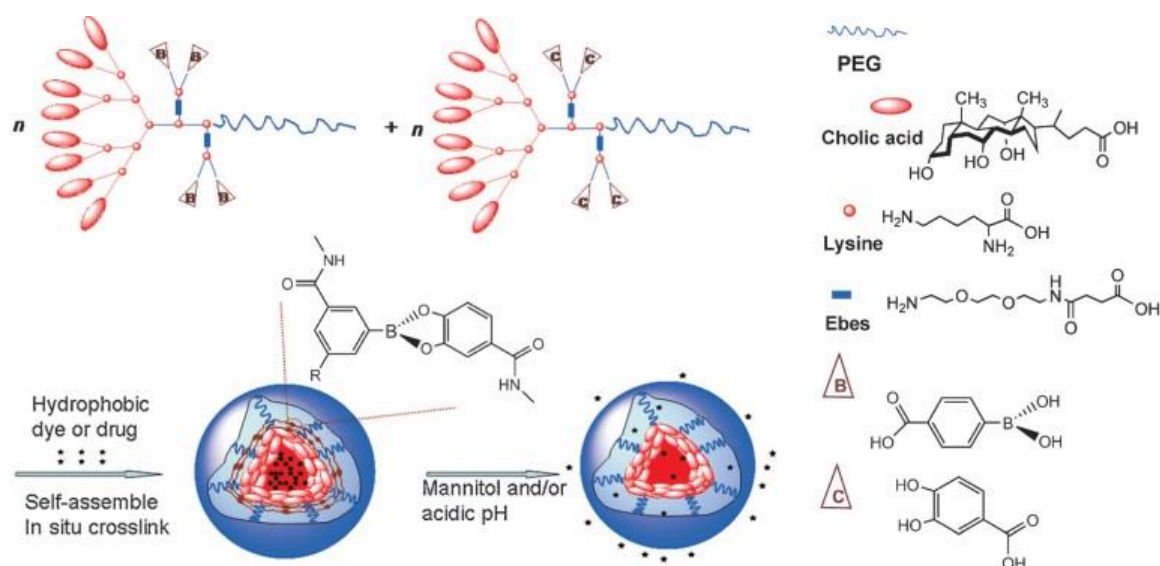


Figure 39: Schematic depiction of the utilized dendrimers for the formation of micelles that are crosslinked via boronate esters. The crosslinks are cleaved in the acidic conditions of the targeted cell, e.g., tumor cells, releasing enclosed molecules. Adapted with permission from Ref.[194]. Copyright 2012 John Wiley and Sons.

Furthermore, the incorporation of the prior described disulfide bridge (refer to section 2.2.4.2) constitutes a suitable approach for the provision of polymers and materials with predetermined breaking points. A disulfide-based network was readily cleaved upon the chemical trigger dithiothreitol (DTT).^[156] The reaction mixture after cleavage further facilitated the recycling of the thiol derivative regaining 40% of the starting material. Disulfide-based polymer micelles were also introduced as drug delivery systems that release the entrapped molecules due to the thiol-disulfide exchange reaction with intracellular glutathione species.^[195] However, the cleavage of a disulfide bridges can also allow for the

functionalization of the formed thiols. The functionalization of disulfide containing proteins was demonstrated employing sulfone leaving groups (**Figure 40**).^[196] After the addition of the first thiol in a Michael addition fashion, sulfinic acid elimination generates a carbon-carbon double bond and the second thiol addition reaction proceeds. In addition, crosslinks arrived from Diels–Alder reactions can provide a suitable platform for thermally^[197] or chemically triggered cleavage^[187] via retro Diels–Alder reactions.

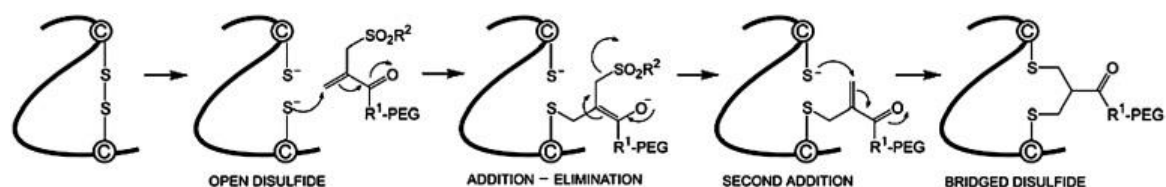


Figure 40: Schematic reaction procedure for the incorporation of PEG chains into peptide structures. Adapted with the permission from Ref.[196]. Copyright 2007 Elsevier.

Combining two degradable systems, photoinduced and thermal degradation of a polymer backbone was demonstrated.^[198] A benzophenone moiety containing two diene groups was polymerized with a difunctional dienophile in a step-growth polymerization. The benzophenone unit was cleaved after the photoinduced formation of a hydroxyl group that readily reacts with the ester functionality in *ortho*-position resulting in lactone species.^[198] Employing elevated temperatures (125 °C), the polymer was cleaved due to the retro Diels–Alder reaction and starting material can be recycled.

3

Results and Discussion

In the current chapter, newly designed 2D and 3D structuring technologies are presented. First, a bioinspired catechol containing material (CyCat) allowed for the defect-free monomolecular film formation of metallic and metal oxide substrates (refer to section 3.1). The highly functional nature of the coating was demonstrated via post-modification reactions and the preparation of multilayered films (refer to section 3.2). Parts were adapted or reproduced with permission from Ref.[14]. Copyright 2017 American Chemical Society.

In the field of 3D printing technologies, two innovative systems are presented, enabling the fabrication and the selective cleavage of micro- and macroscopic structures. The first photoresist is based on a multifunctional phenacyl sulfide linker (PSL). Upon photoactivation via direct laser writing (DLW) in the presence of a tetrathiol, networks exclusively crosslinked by disulfide bridges are formed (refer to section 3.3.6). Next, the reversible nature of the disulfide-based photoresist allowed for a thiol-disulfide exchange reaction that cleaved the printed structures employing a chemical trigger (refer to section 3.4.1). Parts were adapted or reproduced with permission from Ref.[21]. Copyright 2017 John Wiley and Sons.

To ensure broad applicability, a second photoresist resting on commercially available components was developed. The radical-mediated step-growth polymerization of thiols and carbon-carbon double bonds was investigated. A variety of photoresists is presented (refer to section 3.3.10), utilizing the facile exchange of the multifunctional linker moieties. Micro- and

macroscopic structure were fabricated via laser lithography employing DLW and stereolithography (SLA). Subsequently, selective cleavage of the printed objects is demonstrated (refer to section 3.4.2). In addition, a freely-suspended microscopic rope bridge was printed, utilizing the thiol-ene photoresist for the fabrication of support structures (refer to section 3.4.4). Parts were adapted or reproduced with permission from Ref.[22]. Copyright 2018 John Wiley and Sons.

3.1 Ultrathin Coatings via Catechol Chemistry

Many applications in modern technology are reliant on the extraordinary advances in the development of micro- and nanostructured materials and devices in the last decades. Critically, the full control over solid/soft interfaces is necessary to ensure the envisaged functionality. The successful implementation of an implant, for instance, relies on a perfectly adapted surface to be accepted by the organism.^[2-4] In addition, the topography of the bulk material plays a crucial role and should not be altered by a coating, requiring monomolecular coatings to add functionality.^[199] Nature provides a variety of strategies for the formation of adhesive systems that are stable even under very harsh conditions. The ability to adhere to virtually all surfaces in a marine environment renders the mussel byssus a model example. To enable the usage of similar systems, the underlying chemistry was examined and indicated that the molecule dopamine is capable to provide a similar material. Its ability to self-polymerize under mildly alkaline conditions forming cross-linked polymers facilitates the coating of a wide range of surfaces with a poly(dopamine) (PDA) ad-layer, leading to a crucial extension of coating technologies. However, the polymerization is still poorly understood and varying concepts are presented in literature (refer to section 2.1.1). In addition, the system is

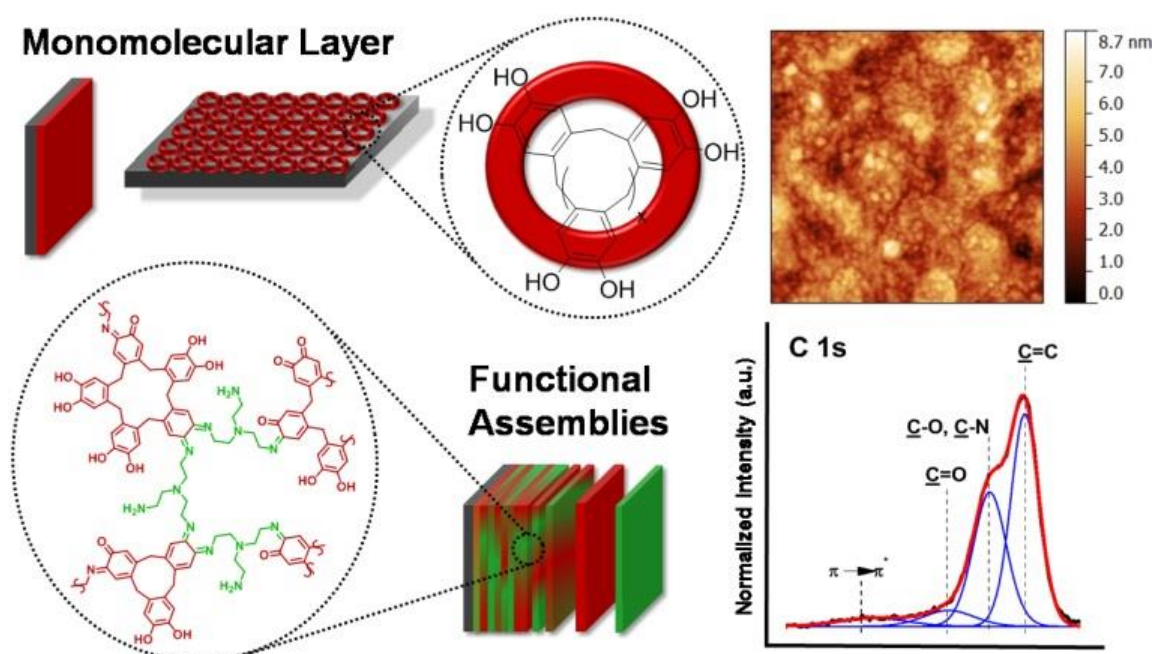


Figure 41: Schematic depiction of the provision of an adhesive system based on catechol units that facilitates the adhesion to surfaces on a monomolecular basis. Subsequently, the post-modification via a multifunctional amine enables the step-wise fabrication of a multi-layer coating. Reproduced with permission from Ref.[14]. Copyright 2017 American Chemical Society.

not resulting in a monomolecular layer, which is essential for thin coatings. Playing a key role for the interaction with metallic and metal oxide surfaces, the catechol functionality has proven to facilitate the immobilization of molecules with a defined mechanism (refer to section 2.1.3). In the following pages, the provision of a system, that enables the straightforward functionalization of gold (Au), silicon dioxide (SiO₂) and titanium dioxide (TiO₂) without altering the morphology of the substrates is presented. Furthermore, post-modification of the monomolecular samples is conducted (**Figure 41**), demonstrating the variety of procedures that are feasible with the cyclic catechol oligomers ranging from immobilization of small molecules and polymers via “grafting-to” of phenacyl sulfides to the “grafting-from” via Atom Transfer Radical Polymerization (ATRP). In addition, the formation of functional multi-layers is performed employing an alternating reaction procedure.

3.1.1 Synthesis and Analysis of the Protected CyCat

Immobilization of molecules via a catechol functionality was already widely demonstrated with monofunctional moieties. However, to achieve a coating that additionally enables a post-modification pathway, multifunctional derivatives were envisaged. A simple two-step procedure was explored and provided a cyclic catechol material (CyCat) connected via a methyl group. The first reaction step was already investigated in earlier studies (refer to the Experimental Section, 5.3.1) leading to protected moieties. ¹H NMR analysis (refer to the Experimental Section, **Figure 79**) exhibited upfield shifts for the aromatic protons indicating the coexistence of variable ring sizes. Further investigations utilizing DOSY measurements (refer to the Experimental Section, **Figure 82**) focused on a better understanding for the molecular structure. Selected resonances were investigated to enable an assignment of smaller and bigger species. The singlet at 6.8 ppm, the doublet at 4.8 ppm and the singlet at 3.8 ppm possess similar values while the upfield shifted multiplets reveal a clear continuously decreasing trend with respect to their diffusion coefficients. It is assumed that the doublet at 4.8 ppm stems from small cyclic species with a restricted number of conformational degrees of freedom due to a small amount of repeating units. Decreasing values for the diffusion coefficient indicate moieties with an increasing number of repeating units. To further clarify the structural occurrence of the CyCat, in-depth analysis via ESI MS (refer to the Experimental Section, **Figure 80** and **Table 4**) and MALDI-TOF (refer to the Experimental Section, **Figure 81**,

Table 5 and **Table 6**) was conducted and evidenced the formation of predominately cyclic species. Moieties with m/z values of above 1000 Th exhibit an increasing tendency for a linear structure assuming that the ionization of molecules with a similar amount of repeating units does not differ strongly. The ESI MS measurements reveal the presence of species with up to 14 protected catechol functionalities. However, the MALDI-TOF analysis evidence the occurrence of moieties with up to 32 units (m/z 4828.65 Th). Thus, the protected CyCat provides a well-understood system with a high density of functionalities.

3.1.2 Synthesis and Analysis of the CyCat

To enable the envisaged surface immobilization of the synthesized material, the *ortho*-dimethoxybenzene derivatives were deprotected employing BBr_3 to obtain the catechol units with the characteristic *ortho*-dihydroxybenzene functionalities (**Figure 42**). The ^1H NMR

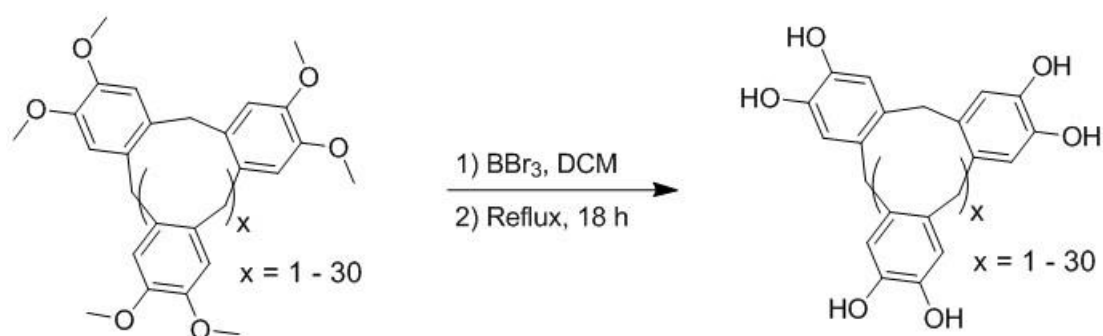


Figure 42: Deprotection of the methoxy groups via BBr_3 to achieve the CyCat with a high amount of catechol units of up to 32 in one macrocycle.

measurement (refer to the Experimental Section, **Figure 83**) indicates only a small amount of remaining methoxy groups by the resonance at 4.5 ppm. The broad peak at 8.5 ppm from the emerging catechol units verifies the successful deprotection. However, the material incorporated molecules of the employed solvents ethyl acetate and water. Heating to $150\text{ }^\circ\text{C}$ for 2 h was sufficient to dry the material revealing a pronounced stability against higher temperature of the CyCat. In addition, ESI MS measurements were performed. Positive ion mode did not result in a sufficient ionization. Due to the ability of the hydroxyl groups to form ions, the analysis was conducted in negative ion mode (refer to the Experimental Section, **Figure 84**). The clear identification of mainly cyclic molecules with up to eight catechol functionalities was possible, however, higher m/z values were not detectable. In addition,

linear species for the smallest ring sizes of three to five units were observed that could not be verified in the protected CyCat. To further facilitate ionization in the region of m/z 1000-2000 Th, a collision-induced dissociation (CID) value of 15 eV was used revealing deprotected species with up to 14 catechol units in their backbone. Due to the employed conditions, moieties stemming from partial fragmentation are also detected. It is assumed that the conditions employed during deprotection are selectively impacting the methoxy groups and, therefore, the earlier validated molecules with higher amounts of units are still existent. Thus, the provision of a defined system providing macrocycles with up to 32 catechol functionalities was successfully conducted. The in-depth analysis of the straightforward coating and the subsequent utilization of remaining catechol units that do not interact with the surface in a post-modification, were the focus of the further investigations.

3.1.3 Investigation of CyCat Aggregates

During the self-polymerization of dopamine in alkaline conditions, a well-known and essential step is the formation of *o*-quinones due to an oxidation of the catechol groups. The subsequent processes until a PDA layer is obtained have not been fully elucidated, but the existence of colloidal aggregates is clearly part of it.^[10] These particles limit the accessibility of small species with low steric demands. However, to mimic the topography of substrates, the immobilized units have to form thin, in the ideal scenario, monomolecular films. Therefore, the CyCat (1 mg mL^{-1}) was investigated regarding the processes under coating conditions in a 0.1 M NaHCO_3 solution via DLS to monitor the change in particle sizes (refer to the Experimental Section, **Figure 85**). The measurement clearly shows the existence of oligomers with a size of a few nanometers of hydrodynamic diameter (D_h) for the first four hours, however, already after 30 to 60 min, an additional distribution with $D_h = 150\text{-}300 \text{ nm}$ is detected. Aiming for thin coatings that mimic the topography, the coating has to be completed before the aggregation process consumed the macrocycles in solution. After 6.5 h, no small particles are observed anymore. The emerging aggregates with a few hundred nanometers of D_h exhibit no significant further growth with regard to their sizes after four hours. To further examine the formed particles, X-ray photoelectron spectroscopy (XPS) and Kelvin probe force microscopy (KPFM) measurements were performed (**Figure 43**). A drop utilizing the same conditions as in the DLS measurement was placed on an ultraflat highly

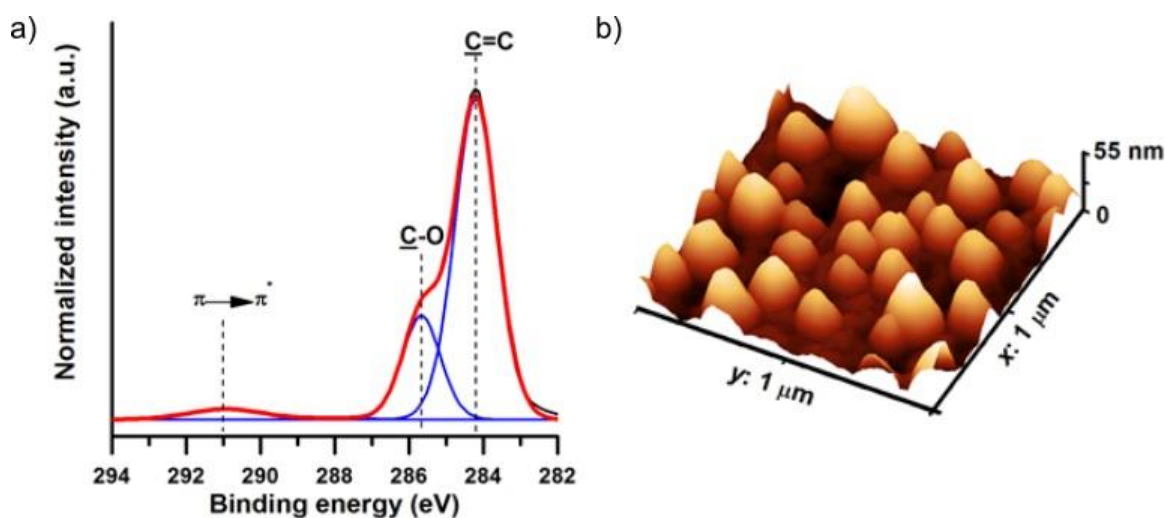


Figure 43: XPS and KPFM measurements of the CyCat aggregates. A drop (4 μl) of aqueous 0.1 M NaHCO_3 with 1.0 mg mL^{-1} dissolved CyCat was deposited onto a HOPG sample and the solvent was allowed to evaporate. Adapted with permission from Ref.[14]. Copyright 2017 American Chemical Society.

oriented pyrolytic graphite (HOPG) sample and the solvent was allowed to evaporate. The XPS spectrum (**Figure 43a**) verifies the existence of the CyCat moieties with peaks at 284.2 and 285.7 eV that can be assigned to the C=C bonds of aromatic moieties and to the C-O catechol units, respectively. In addition, the minor signal at 291.0 eV stems from the $\pi \rightarrow \pi^*$ shake up structure. The direct observation of the size and morphology of the sample was achieved by KPFM and the prior identified particles are clearly visible in the height image (**Figure 43b**). Notably, KPFM enables the investigation of the aggregates in the dried state, whereas DLS assesses the D_h in solution. The mean grain size parameters of the particles that were distributed across the surface was determined via the height image, obtaining a mean height of $h_{\text{grain}} = 68.7 \pm 1.5$ nm and a radius of $R_{\text{eq}} = 75.5 \pm 5.6$ nm. Furthermore, the root mean square roughness of $R_{\text{RMS}} = 11.4 \pm 1.1$ was obtained. The occurrence of comparable aggregates of similar size and morphology was also observed in natural eumelanins (*Sepia officinalis*). In addition, synthetic melanins utilizing dopamine reveal similar particles in solution during the polymerization and in the resulting surface-adsorbed layers.^[11, 200] However, analysis of PDA, revealed the occurrence of aggregates incorporated into the films as a potential source of instability.^[10] Crucially, the potential maps (refer to the Appendix, **Figure 91**) verified the adsorption of CyCat molecules in between the immobilized particles, which is a necessity to obtain thin films. In comparison to the maximum surface potential of the aggregate particles exhibiting a value of 100-120 mV higher than the HOPG substrate, the inter-particle regions validate the presence of a homogenous layer obtaining a surface

potential that is 10-15 mV higher than the HOPG carrier. However, the suitability of the CyCat to form monomolecular ad-layers on different materials strongly depends on the diffusion and adsorption behavior of the macrocycles and of the emerging aggregates during the coating of surfaces. Therefore, the processes during the immersion of Au, SiO₂ and TiO₂ substrates in an alkaline solution of the catechol-based material are investigated in the next section.

3.1.4 Provision of Monomolecular Layers via Catechol Chemistry

Achieving thin films is essential for applications that require the perfect mimicking of the topography of the sample to add functionality to highly specified systems.^[199] Therefore, it is a necessity that the observed aggregates (refer to section 3.1.3) are not interfering with the formation of a monomolecular add-layer of CyCat. To examine the processes during the coating of Au, SiO₂ and TiO₂, the substrates were cleaned (refer to the Experimental Section, 5.4) and immersed in an aqueous 0.1 M NaHCO₃ solution with dissolved CyCat (1 mg mL⁻¹) for

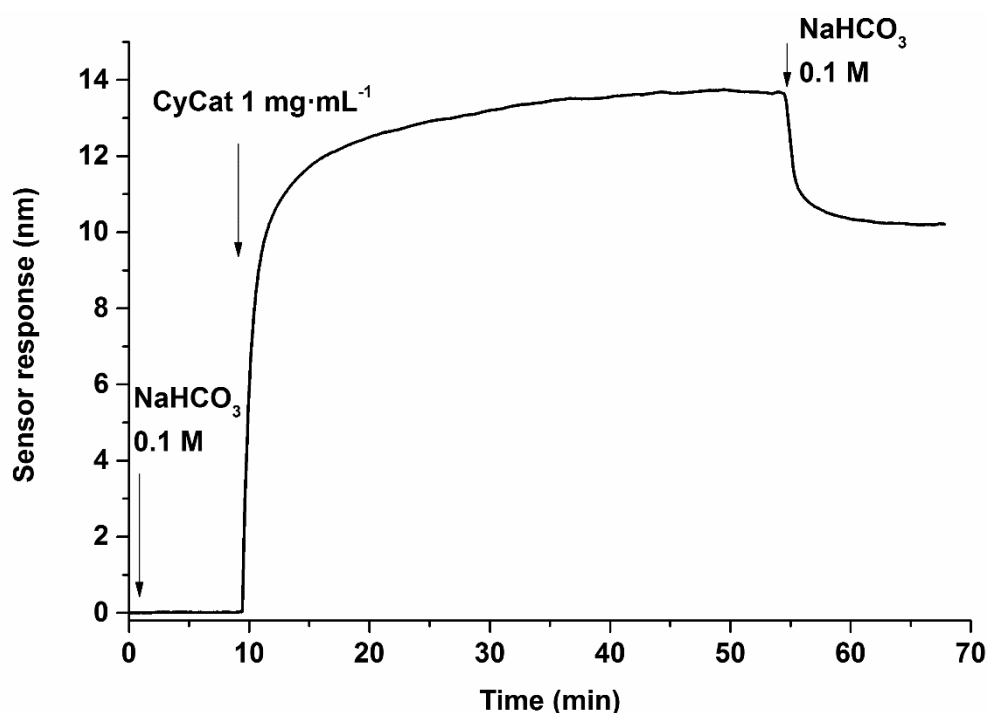


Figure 44: Sensogram of the SPR measurement during the immersion of a Au substrate in the CyCat (1 mg mL⁻¹) coating mixture. As solvent, an aqueous 0.1 M NaHCO₃ solution was employed and injected for 10 min to obtain a stable baseline. After 55 min, the reaction mixture was replaced again by the solvent. Reproduced with permission from Ref.[14]. Copyright 2017 American Chemical Society.

45 min. Subsequently, the surfaces were rinsed with an aqueous 0.1 M NaHCO₃ solution and deionized water. Surface plasmon resonance (SPR) measurements enabled the investigation of the coating in real time. However, the analysis requires a metal interface for the generation of plasmons and, therefore, the SiO₂ and TiO₂ substrates were not suited. The SPR sensogram of the Au sample depicts the adsorption kinetics during the immersion in the CyCat solution (**Figure 44**). After a stable baseline was obtained for the employed solvent (aqueous 0.1 M NaHCO₃), the coating mixture was inserted after approximately ten minutes. A rapid adsorption of the CyCat within the first minutes was observed with only small additional adsorption after 15 min of immersion. After an injection time of 45 min, the reaction mixture was exchanged by the pure solvent (aqueous 0.1 M NaHCO₃). A slight decrease in the resonant wavelength after replacement was exhibited due to different refractive indices of the solutions with and without CyCat. The shift of the resonant wavelength in comparison to the original baseline indicates the successful immobilization of molecules on the surface. The only small changes in the sensogram after a few minutes indicate that the emerging aggregates in solution (refer to section 3.1.3) do not interfere with the immobilization of the CyCat. However, further analysis is a necessity to confirm the formation of a monomolecular layer on the surface.

To assess the thickness of the immobilized material, spectroscopic ellipsometry (SE) was conducted for the three substrates. The same conditions with regard to the SPR measurements were employed (refer to the Experimental Section, 5.4). The characterization strongly indicated the formation of monomolecular layers due to the obtained thicknesses of 1.6 ± 0.5 nm, 1.8 ± 0.4 nm and 2.1 ± 0.4 nm for Au, SiO₂ and TiO₂ samples, respectively. To further determine the chemical nature of the immobilized molecules, XPS measurements of the surfaces were performed (**Figure 45a-c**). After the immersion in the coating mixture for 45 min, the surfaces revealed signals stemming from the chemical structure of the CyCat. In addition to the prior observed signals of the C=C and C-O contributions, a signal at 287.8 eV originating from the C=O functionality of quinone moieties was detected. Due to the longer reaction time in comparison to the analysis of the aggregates, the catechol units can undergo a partial autoxidation under the utilized basic conditions during the layer formation. The lack of O-C(=O)-O carbonate contributions at 289.3 eV in the high resolution XPS C 1s spectra for the different surfaces indicates that the bicarbonate ions are not incorporated into the structure of the formed layers.

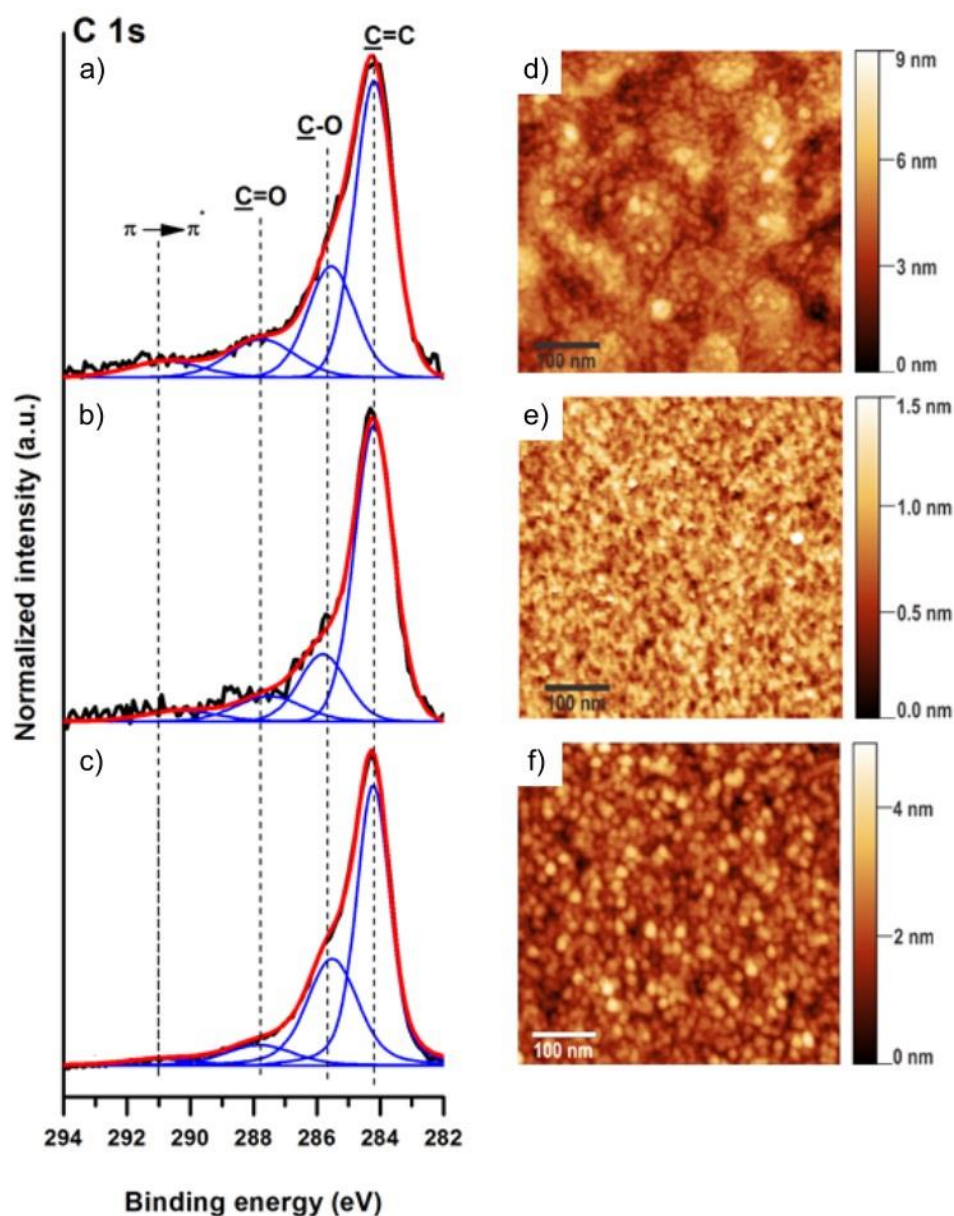


Figure 45: High resolution C 1s XPS spectra and AFM surface height topographic maps ($500 \times 500 \text{ nm}^2$) of Au (a, d), SiO₂ (b, e) and TiO₂ (c, f) after immersion in the CyCat coating mixture. Adapted with permission from Ref.[14]. Copyright 2017 American Chemical Society.

To verify the absence of large particles and aggregates after the coating, the samples were further investigated via atomic force microscopy (AFM) (**Figure 45d-f** and refer to the Appendix, **Figure 92**, **Figure 94**, and **Figure 96**). The comparison of the values for the particle surface density, h_{grain} , R_{eq} and R_{RMS} (**Table 1** and refer to the Appendix, **Figure 93**, **Figure 95**, and **Figure 98**) reveal no significant changes before and after coating. In addition, only small phase shifts are observed in the AFM phase data. Therefore, the obtained insights strongly indicate the formation of confluent defect-free layers perfectly replicating the topography of

the underlying substrates. Critically, no deposition of larger aggregates is observed, probably due to the enhanced diffusion coefficients of the macrocycles as a result of their much smaller sizes (refer to the Stokes-Einstein equation) leading to a rapid adsorption of the CyCat molecules.

	Grain density [μm^{-2}]	h_{grain} [nm]	R_{eq} [nm]	R_{RMS} [nm]
Pure Au	1192	4.6 ± 0.1	6.2 ± 0.5	1.4 ± 0.3
CyCat on Au	1256	3.7 ± 0.1	4.7 ± 0.3	1.1 ± 0.1
Pure SiO ₂	952	0.9 ± 0.1	5.7 ± 0.9	0.2 ± 0.2
CyCat on SiO ₂	1060	0.9 ± 0.1	6.2 ± 2.1	0.3 ± 0.1
Pure TiO ₂	1604	2.0 ± 0.1	6.3 ± 1.1	0.6 ± 0.1
CyCat on TiO ₂	1812	2.0 ± 0.2	8.6 ± 0.4	0.6 ± 0.2

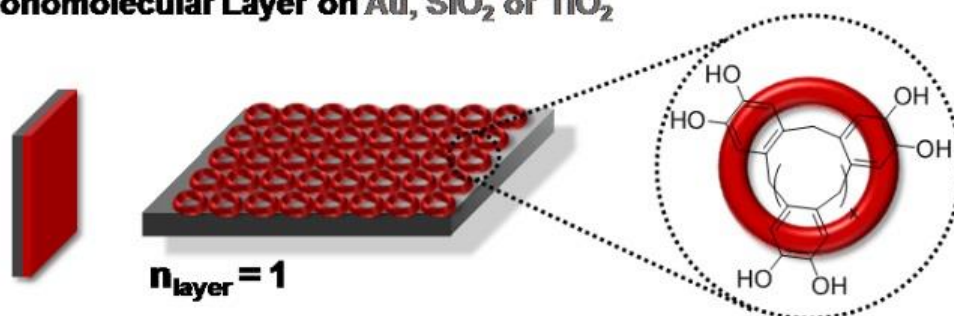
Table 1: AFM analysis of the layer formation of CyCat on Au, SiO₂ and TiO₂ substrates in comparison to the uncoated samples.

Therefore, a straightforward two-step synthesis without the need of complex purification and the simple coating of various metallic and metal oxide substrates by immersion into the CyCat solution represents an innovative approach to modify and add functionality to otherwise inert surfaces. In addition, the monomolecular coatings perfectly preserves the topography of the underlying Au, SiO₂ and TiO₂ substrates without the interference of aggregates that are formed in solution. The provision of the highly defined CyCat add-layer further facilitates straightforward post-modification due to the well-understood surface chemistry (see 3.2).

3.2 Post-modification of CyCat Layers

The ultrathin monomolecular layers employing CyCat enable the straightforward coating of otherwise inert surface such as Au, SiO₂, and TiO₂ (refer to section 3.1.4). However, the added functionality has to prove its suitability for subsequent reactions. To demonstrate the straightforward accessibility and versatility of the monomolecular CyCat coating, different post-modifications were carried out. Utilizing the remaining catechol and *o*-quinone functionalities that are not interacting with the underlying surface, amine reactants were attached covalently extending the incorporation of additional functionalities in a facile fashion. Highly functional multilayer films were provided by the alternating reaction of multifunctional moieties (**Figure 46**) exhibiting the possibility of defined increases in

Monomolecular Layer on Au, SiO₂ or TiO₂



Functional Assemblies on Au, SiO₂ or TiO₂

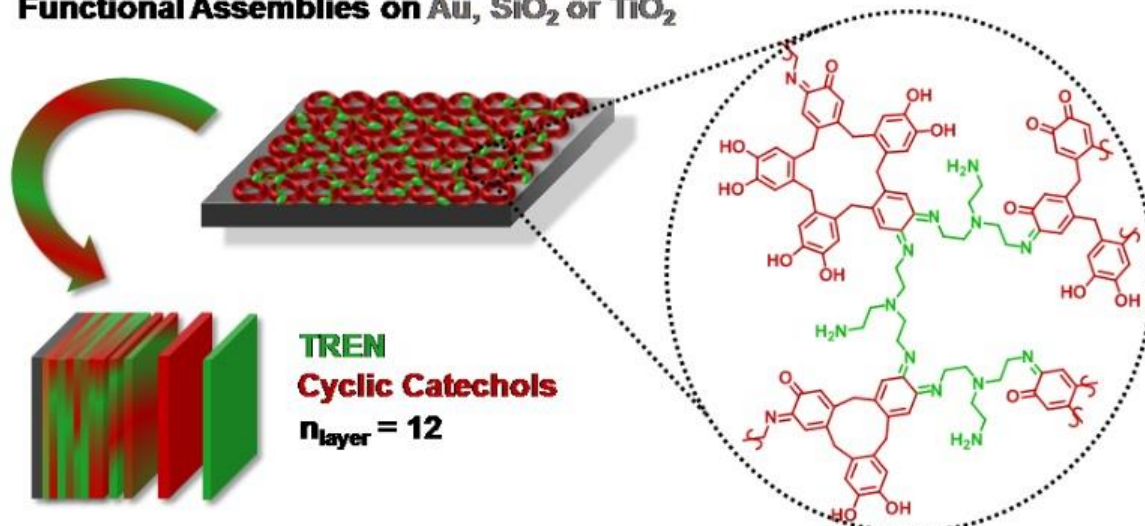


Figure 46: Schematic depiction of the formation of monomolecular CyCat layers on various substrates (Au, SiO₂ and TiO₂) (top) and illustration of the preparation of multilayers via post-modification in an alternating reaction procedure with multifunctional moieties (bottom). Reproduced with permission from Ref.[14]. Copyright 2017 American Chemical Society.

thickness. In addition, the attachment of molecules and polymers to the multilayers was demonstrated ranging from the immobilization of small molecules to polymers and the grafting-from of polymer brushes.

Furthermore, the post-modification of the fabricated 3D printed objects is discussed. The extended library of suitable chemistries for DLW utilizing the PSL and the straightforward usage of a commercially accessible photoresist based on thiol-ene chemistry greatly enhances the possible post-modifications in a facile fashion.

3.2.1 Assessing Remaining Functionalities of CyCat Coated Surfaces

To serve as a priming coating on various materials without the prior mentioned disadvantages of common melanin-based anchor layers, the presence and accessibility of reactive groups has to be verified by conducting post-modification reactions. The catechol and *o*-quinone groups of the CyCat layer are utilized to covalently bind amine functionalized moieties. As a small organic molecule, 4-bromophenethylamine was employed. In addition, a difunctional amine bearing poly(ethylene glycol) (PEG), NH₂-PEG-NH₂, 1500 Da, was used to demonstrate the stability of the monomolecular layers towards the immobilization of polymers. The analysis via SE exhibit increases in thickness of 0.6 ± 0.1 nm after the reaction employing the bromine moiety and 1.5 ± 0.2 nm for the PEG derivative. Furthermore, the samples were examined by XPS (**Figure 47** and refer to the Appendix, **Figure 114**) indicating the covalent attachment via Michael addition and Schiff base reactions in the C 1s and N 1s spectra for the

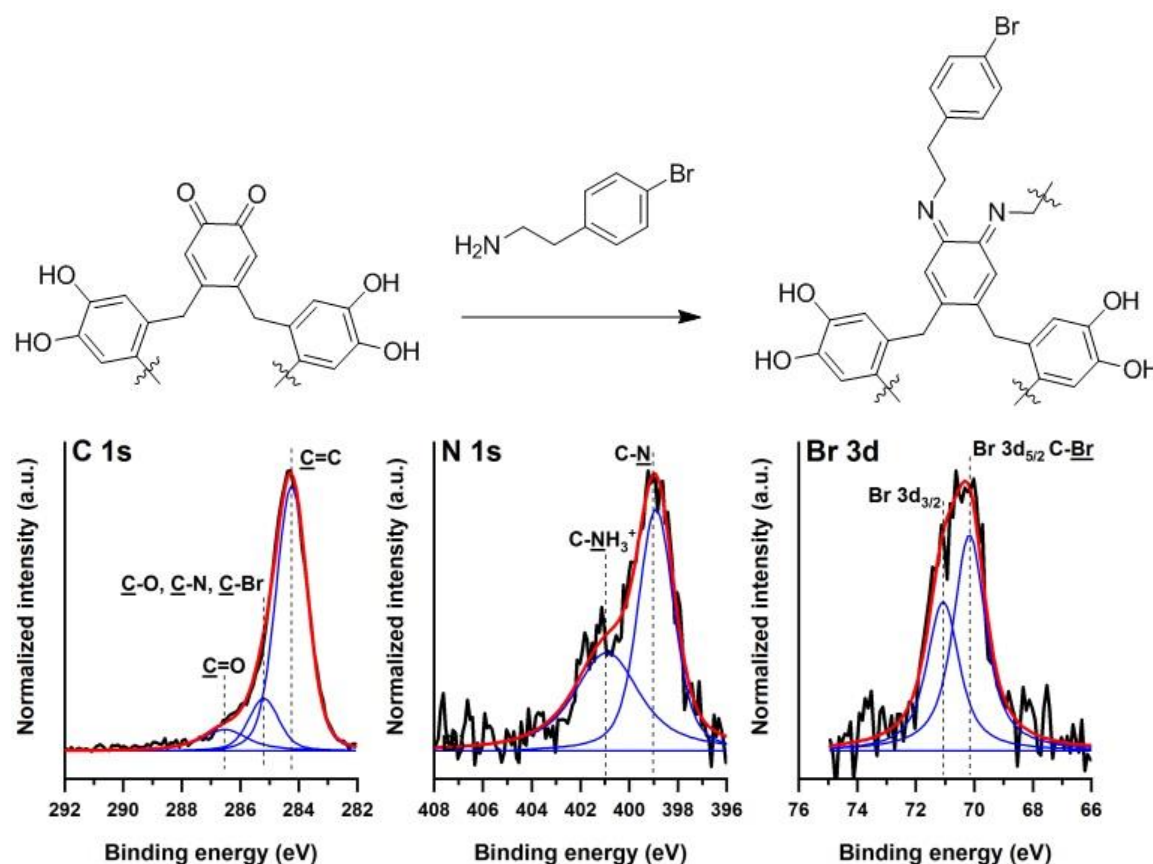


Figure 47: The reaction of quinone moieties remaining after the monomolecular layer formation of CyCat with a primary amine is depicted (top) and the corresponding high resolution C 1s, N 1s and Br 3d XPS data after the attachment (bottom). Adapted with permission from Ref.[14]. Copyright 2017 American Chemical Society.

employed molecules. Therefore, the successful and straightforward post-modification of monomolecular films of CyCat was demonstrated utilizing amine functionalized moieties. To further extend the control over the surface properties, multifunctional linkers were used alternately to provide the formation of highly functional multilayers.

3.2.2 Formation of Multilayers on Monomolecular CyCat Coatings

To further improve the versatility of the CyCat coatings, the preparation of highly functional multilayer films on Au, SiO₂ and TiO₂ substrates was conducted. This approach demonstrates the defined control over the thickness of the coating and enhances the versatility for post-modification providing primary amine groups. The multifunctional amine, tris(2-aminoethyl)-amine (TREN), enabled the covalent attachment via Michael addition and Schiff base formation, immobilizing still unreacted amine groups for additional functionalization. The attachment of moieties that are reactive towards primary amines is readily accessible (refer to section 3.2.3). To achieve the multilayer formation, the surfaces were simply immersed alternately in a solution of TREN and CyCat after the substrates are coated with the monomolecular layer of the catechol macrocycles. After six cycles resulting in 12 layers, the samples were analyzed via SE verifying the successful reactions with thicknesses of 10.9 ± 1.0 nm, 12.9 ± 0.6 nm and 12.1 ± 0.3 nm for Au, SiO₂ and TiO₂, respectively. The stability of the formed coating was assessed via immersion of the SiO₂ substrate in water for 24 h (**Table 2**) exhibiting only a minor decrease in thickness (8%) and, therefore, confirming a

Incubation time	Dry thickness by SE
[h]	[nm]
0	10.6 ± 0.6
24	9.7 ± 0.4

Table 2: SE analysis of the CyCat-TREN multilayer film (6 cycles) on a SiO₂ substrate after the immersion in water for 24 h.

distinct stability of the system. In addition, XPS measurements were performed to increase the understanding of the surface chemistry (**Figure 48**). The increase of the signal at 286 eV originates from the presence of C-N bonds validating the formation of Schiff bases during the attachment of TREN to CyCat layers. In comparison to the multilayers, the monomolecular

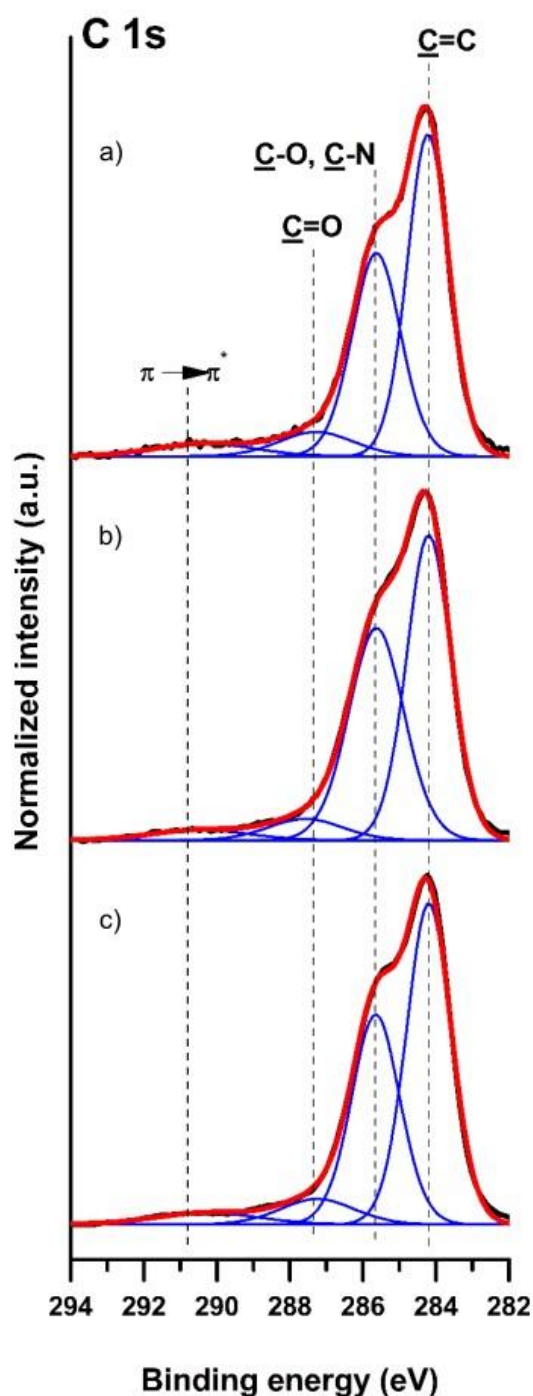


Figure 48: High resolution C 1s XPS spectra verifying the formation of CyCat-TREN multilayers on Au (a), SiO₂ (b) and TiO₂ (c) substrates. Adapted with permission from Ref.[14]. Copyright 2017 American Chemical Society.

coatings only revealed signals assigned to the C-O of the catechol units (refer to **Figure 43**). In addition, the signals at 399.0 and 401.0 eV of the high-resolution N 1s spectra can be assigned to the N-C bond and to N⁺ moieties (refer to the Appendix, **Figure 115**). Therefore, the fabrication of multilayers employing a multifunctional amine demonstrates the simplicity and

versatility of the monomolecular CyCat coating. The application for otherwise inert surfaces possess great potential providing a film formation with adjustable thicknesses in a facile fashion and the accessibility of a high density of functionalities for post-modifications. In comparison to PDA ad-layers achieved by the self-polymerization of dopamine in a one-pot approach, the multilayer fabrication of CyCat is more time-consuming due to the alternating dipping in two solutions. However, the thickness and functionality of each layer can be assessed by the amount of cycles and the employed multifunction catechol and amine linkers.

3.2.3 Post-modification of Multilayers

To further enhance the accessible modifications of otherwise inert surfaces, post-modification of the multilayer assemblies was performed utilizing the remaining amine groups (TREN as final layer). Multilayers with various functionalities that are based on CyCat and multifunctional amine species can be functionalized with a monofunctional moiety as additional layer. A variety of functional moieties was examined, resulting in covalently bound trifluoroacetyl, tetrazole, and 2-bromo-2-methylpropanoyl groups. To verify the successful attachment, SE analysis was conducted, exhibiting an increase in thickness of 0.9 ± 0.2 nm, 1.1 ± 0.1 nm, and 0.9 ± 0.3 nm for the functionalization of the multilayers with trifluoroacetyl, tetrazole, and 2-bromo-2-methylpropanoyl species, respectively. In addition, the high-resolution XPS measurements confirm the post-modification via the presence of new ester and amide contributions. The signals stemming from the newly attached groups are also detected in the high-resolution F 1s, N 1s and Br 3D spectra (refer to the Appendix, **Figure 116**, **Figure 117**, and **Figure 118**). Furthermore, the attachment of the tetrazole groups has been utilized for photopatterning via the nitrile imine-mediated tetrazole-ene cycloaddition (NITEC),^[56] while the 2-bromo-2-propionyl groups have facilitated the growth of polymers in a “grafting-from” approach via surface-initiated atom transfer radical polymerization (SI-ATRP).^[201] The post-modification of surfaces with polymer chains is of high value for the engineering of interface properties. Therefore, the immobilization of a phenacyl sulfide-terminated PEG moiety was conducted in a “grafting-to” manner.^[149] The photoinduced activation results in the formation of reactive thioaldehydes that can readily react with remaining amine groups of the CyCat-TREN multilayer coating. The sample was investigated via SE verifying the attachment by an increase in thickness of 1.3 ± 0.4 nm.

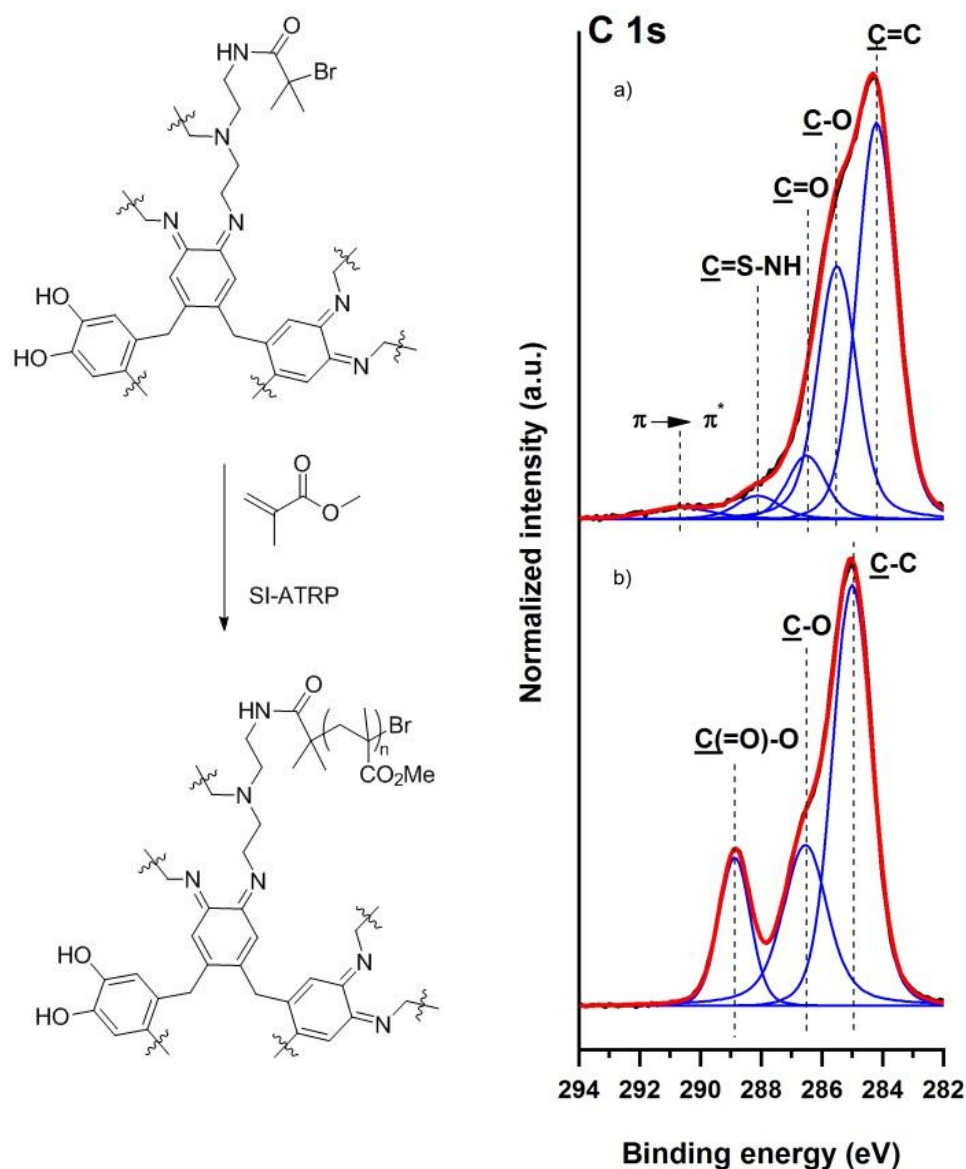


Figure 49: A schematic depiction of the SI ATRP employing methyl methacrylate utilizing the post-modified CyCat-TREN surfaces after the attachment of 2-bromo-2-methylpropionyl bromide (left). The corresponding high resolution C 1s of the surfaces after the immobilization of 2-bromo-2-methylpropanoyl groups (a) and after the SI ATRP (b) are presented. Adapted with permission from Ref.[14]. Copyright 2017 American Chemical Society.

Assessing the bromide of the attached 2-bromo-2-propionyl groups, SI-ATRP was conducted employing methyl methacrylate, obtaining an increase in thickness of 11.5 ± 0.5 nm in the SE analysis stemming from the poly(methyl methacrylate) brushes. The immobilization of polymer chains on the CyCat-TREN multilayers were further investigated via XPS measurements (**Figure 49** and refer to the Appendix **Figure 119**). A distinct increase of the signal at close to 286.0 eV that can be assigned to the C-O contributions and the signal at 288.1 eV originating from the formed thioamide C(=S)-NH contribution verifies the

attachment of the phenacyl sulfide-PEO. In addition, the high-resolution S 2p spectrum reveals signals stemming from the phenacyl sulfide reaction. After the SI-ATRP with methyl methacrylate, the signals originally detected for the catechol layer in the C 1s region got strongly dampened, while new signals emerge at 285.0, 286.5, and 288.9 eV that can be assigned to the aliphatic C-C and C-H distributions, the carbon atoms of \underline{C} -O-(C=O) and immobilized ester C(=O)-O distributions, respectively. Notably, the robustness of the CyCat-TREN multilayer assemblies was demonstrated by the successful post-modification via polymers due to the implied mechanical stress, rendering the coating suitable for a wide variety of surfaces and applications.

The preparation of a wide variety of differently post-modified CyCat monomolecular layers, the provision of CyCat-TREN coatings and the post-modification of the multilayers emphasize the simplicity and versatility of the procedure, demonstrating a high potential for applications regarding substrate-independent functionalization of otherwise inert surfaces.

3.3 Provision of Novel and Cleavable Photoresists

The technical progress in many fields of application such as complex micro- and nanostructure fabrication^[5, 6] and macroscopic 3D printing^[7] constantly demands for novel 3D structuring technologies (refer to section 3.3.6). In the case that well-investigated photoresists are reaching limitations, the development of novel innovative systems offering advanced property profiles is essential.^[17] The utilization of a multifunctional phenacyl sulfide linker (PSL) facilitates the 3D printing of structures exclusively crosslinked by disulfide bridges (refer to section 3.3.8). To allow for the fast transfer from fundamental research to a variety of fields of application, especially those without a chemical background, a photoresist resting only on commercially available components is introduced (refer to section 3.3.11). The underlying chemistry that leads to the crosslinking, is based on the radical-mediated step-growth thiol-ene polymerization (refer to section 2.2.4.3).

3.3.1 Photoresists for Direct Laser Writing (DLW)

Commercially available negative tone photoresists for DLW predominantly rest on the well-known free radical polymerizations (FRP) of (meth)acrylates. Their advantages are highly efficient crosslinking, commercial availability, and the chemical and dimensional stability of the resulting structures. Clear disadvantages are the low functionality of the resulting networks, light-independent polymerization after the activation of one photoactive species, and the inaccessibility of the formed C-C bond for subsequent modification. Extension of the established chemistry for DLW has already proven to establish advanced fabrication procedures and straightforward functionalization pathways.^[17, 202] However, certain properties such as the direct assessment of the formed chemical crosslinks in a post-modification manner was not feasible. Earlier studies have shown that the photoclick chemistry of photo-caged dienes utilizing multi-functional moieties is suitable for DLW.^[126] In comparison to the commercially available photoresists, the polymerization process is based on a step-growth mechanism. Thus, the activation and chemical reaction of one photoactive species results in the formation of one bond in the network, leading to high control of each crosslink in the resulting structures. Consequently, the employed chemistry has to be highly efficient with fast reaction kinetics to be applicable for DLW. In addition, the fabricated

networks have to be sufficiently stable to withstand the development with often organic solvents to dissolve non-irradiated, still liquid parts when using negative-tone photoresists.

3.3.2 Removal of Structures based on Reversible Bonds

Removal of structures or structural elements is often necessary to achieve complex geometries or defined structuring of globally deposited material, for instance. Thus, photoresists that combine facile fabrication, high chemical and dimensional stability and effective removal of the printed structures are of high interest. Introducing reversible bonds is possible with two approaches: Implementing the functionality into the core of the multifunctional linker or introducing a reversible bond via the crosslinking reaction itself. The fabrication of structures with well-defined, reversible crosslinks, however, does not render the product cleavable. To address the bonds that are incorporated into the network, the permeability of the final object has to be sufficient to allow for a chemical trigger in a solvent to permeate and react. Diffusion through the network can be highly dependent on the employed solvent, on the covalently bonded functionalities in the networks and the crosslink density.

3.3.3 Disulfide Formation of Photo-caged Thioaldehydes

The thiol-disulfide exchange reaction represents a model example for reversible chemistry exhibiting high versatility and is furthermore employed in diverse fields of application ranging from biology to self-healing materials. Different approaches have been exploited to generate the reversible sulfur-sulfur bond, with the thiol oxidative coupling as the most common example. However, oxidative conditions increase the prevalence of side reactions leading to

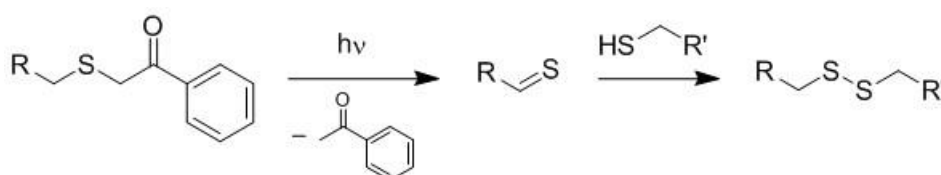


Figure 50: Schematic depiction of the disulfide formation with phenacyl sulfide moieties. After irradiation with light, a benzophenone is released and the reactive thioaldehyde is formed. Subsequently, the reaction with a thiol derivative is proceeding, obtaining the disulfide bridge.

higher oxidized moieties such as sulfinothiates, disulfoxides and thiosulfonates. Critically, the photocaged thioaldehyde bearing group phenacyl sulfide is capable of forming disulfide functionalities under light irradiation with thiol bearing moiety. In addition, a benzophenone molecule is formed (**Figure 50**). The subsequent reaction with small molecules is known for fast reaction kinetics due to the low stability of the thioaldehyde, presenting ideal prerequisites for DLW.

3.3.4 Deformation after Development

The utilization of a chemistry with step-growth nature for DLW requires, besides the beforehand mentioned high effectivity for the network formation and high selectivity for the subsequent application, a certain amount of functionalities in the linker moieties. In FRP of (meth)acrylates, a monofunctional mixed with a difunctional derivative is sufficient, even so the mostly used cores are tri- or tetrafunctional. To achieve the crosslinks, necessary for the formation of a stable thermoset network, the sum of functionalities assuming two linkers employing a step-growth polymerization has to be greater than five with each linker containing at least two functionalities. However, the development in solvents to remove still liquid photoresist often faces the problem of a deformation of the printed structures. After irradiation of a certain volume, still liquid parts such as solvent from the photoresist mixture, small molecules that are released during the curing process, or unreacted parts can be dissolved and removed from the network. Depending on the mobility of fragments in the thermoset, the newly gained free volume is filled and supramolecular interactions can result in additional shrinkage of the printed object. In certain cases, the employed solvent for the development swells the cured network strongly resulting in a deformation that leads to highly undefined and often smooth surfaces. To decrease these effects, the employed solvents and the timescales of immersion can be adjusted. Furthermore, the higher the amount of crosslinks in the final network, which usually correlates with the concentration of functionality in the starting photoresist, the better the dimensional stability of the resulting products. To prepare a homogeneous mixture of all photoresist components, the usage of a solvent is often inevitable. Therefore, it is highly desirable to achieve a high concentration of functionality by highly functional linker moieties to effectively decrease the deformation of printed structures.

An alternative approach is the minimization of required solvent by matching the solubility of the employed components.

3.3.5 Adjusting Writing Parameters

Even with a perfect design of new photoresists and promising curing tests with one-photon absorption (1PA) utilizing a light emitting diode with a comparable wavelength, the application with a 3D printer operating on the basis of two-photon absorption (2PA) irradiation can often require additional adaptation. A poorly understood phenomenon is the occurrence of a spherical change of the photoresist around the irradiated voxel with a radius of sometimes many μm , colloquially referred to as “microexplosions”. Most photoresists exhibit such a behaviour for laser power values that are substantially higher than the threshold value and for very low writing speeds. The resulting structures are strongly deformed, parts can be completely missing or dislocated and the entire area of the spherical change can cure to a certain degree. A problem often limiting the application of custom made photoresists is the overlap of the threshold value with the occurrence of microexplosions. Trying to avoid these circumstances, the first step is to change the writing speed and employed laser power to eventually find parameters that result in sufficient writing conditions. Furthermore, applying lower doses of intensity per laser pulse by the usage of a beam splitter can avoid microexplosions.

3.3.6 Design of the Phenacyl Sulfide Photoresist

For the previously mentioned reasons, it is of high interest to design a photoresist based on phenacyl sulfide chemistry that offers accessibility of the formed crosslinks to selectively remove the printed structures or incorporated structural elements (**Figure 51**). Irradiation is

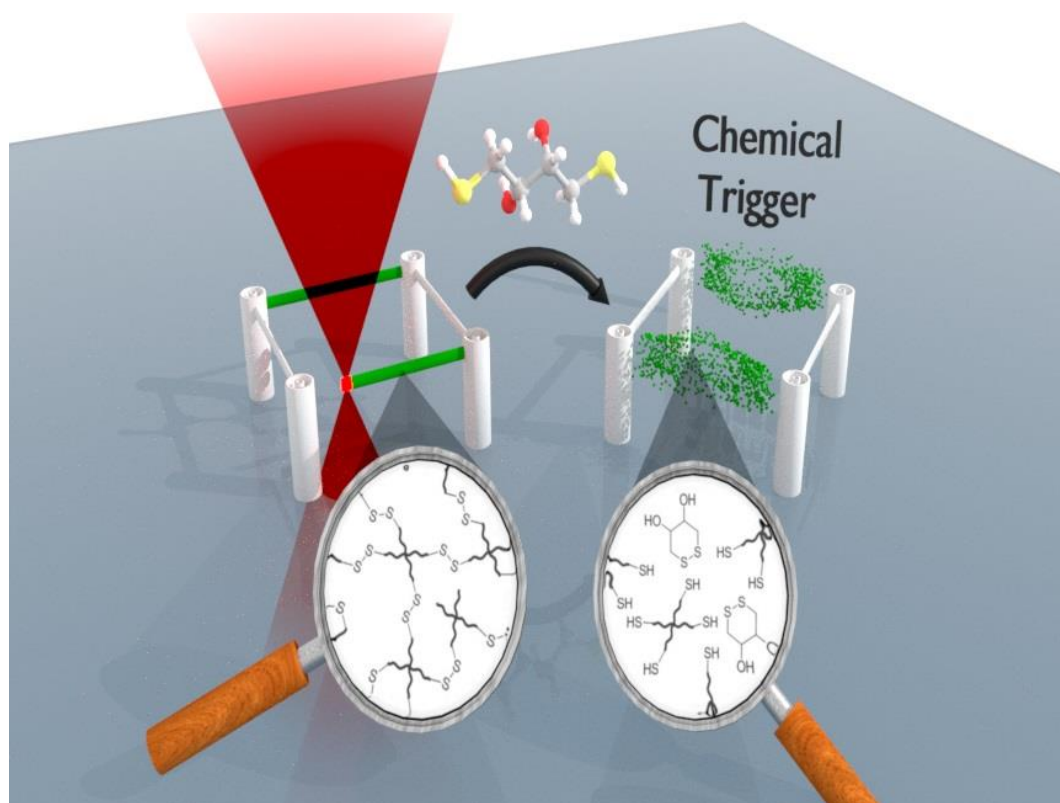


Figure 51: Schematic depiction of the utilization of reversible bonds, namely disulfide bonds, to chemically trigger the cleavage of 3D printed parts. The thiol-disulfide exchange reaction with dithiothreitol (DTT) is responsible for the removal of the structural element that is incorporated in a scaffold based on standard photoresist. Adapted with permission from Ref.[21]. Copyright 2017 John Wiley and Sons.

envisaged to result in solidification and therefore the approach belongs to the group of negative-tone photoresists. The formed disulfide crosslinks via the phenacyl sulfide conjugation with a thiol moiety can be cleaved via a thiol-disulfide exchange reaction. To ensure the diffusion of the chemical trigger, the small dithiol dithiothreitol (DTT) that forms a thermodynamically stable six-membered ring after the reaction is utilized. Aiming for a good dimensional stability, a tetrafunctional phenacyl sulfide linker (PSL) was the focus of the synthetic efforts. As tetrathiol component, specifically the widely used pentaerythritol based tetrathiol pentaerythritol tetrakis(mercaptoacetate) was employed. Non-characteristically, the thiol compound possesses a low odor. Bearing the solubility of all photoresist components

in mind, the utilization of a derivative of the thiol linker for the phenacyl sulfide moiety is desirable. Fortunately, it was feasible to optimize the reaction pathway so that the tetrathiol itself can serve as the starting material in a one-step procedure. In addition, only cost efficient chemicals were employed (**Figure 52**). The obtained product was received as a highly viscous component. It was analyzed via NMR (**Figure 86**, **Figure 87**), ESI MS (**Figure 88**) and UV-Vis

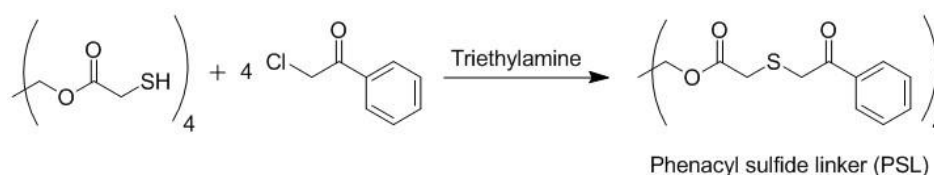


Figure 52: Synthesis of the tetrafunctional phenacyl sulfide moiety. The optimized one-step procedure to synthesize the phenacyl sulfide linker requires only cost-efficient chemicals and utilizes pentaerythritol tetrakis(mercaptoacetate) as starting material, which also serves as thiol linker in the photoresist.

spectroscopy (**Figure 89**). Possessing the same core molecule, it was readily mixable with the tetrathiol. Unfortunately, DLW was not possible due to the before mentioned overlap of the threshold value and the occurrence of a spherical change of the photoresist around the irradiated voxel. The utilization of a beam splitter to lower the intensity per pulse could avoid this problem, but it requires the modification of the custom build DLW setup and decreases the applicability of the photoresist. Therefore, the occurrence of the explosions was assumed to relate to the high concentration of functionality and the high viscosity of the photoresist. Lowering the amount of photoactive species in the voxel was readily achieved by the addition of a solvent. Furthermore, the mixture became less viscous. As solvent, tetrahydrothiophen-1,1-dioxide, also known as sulfolane, was employed and readily mixable with the PSL and the tetrathiol. Bearing a significantly low vapor pressure, a constant mixture over many hours of writing without the need to cover the photoresist drop was ensured. Fortunately, this change enabled the separation of the threshold value from undesirable events in DLW such as microexplosions or lower writing speeds, facilitating the fabrication of microstructures.

3.3.7 Reactivity of the Phenacyl Sulfide Linker

At low concentrations, the phenacyl sulfide conjugation with thiols is improved by the addition of a tertiary amine. However, in the case of the highly concentrated photoresist, the shelf life was drastically reduced and a self-initiated polymerization occurred. Therefore, no tertiary amine was added to the reaction mixture without affecting the processing via DLW. In addition, the proximity of emerging thioaldehydes could influence the reactivity towards thiol functionalities. To ensure the formation of disulfide bonds, the PSL was tested in a small molecule study with a monofunctional thiol moiety. The analysis of the reaction mixture via mass spectrometry (refer to the Experimental Section, **Figure 90** and **Table 8**) after irradiation for 1 h in a custom-built photoreactor equipped with a compact low-pressure fluorescent lamp (36 W, Philips CLEO Compact PL-L: $\lambda_{\max} = 355$ nm) validated the formation of a tetrafunctional linker via disulfide bridge formation. In addition, thiol containing moieties were detected that are likely to emerge after the cleavage of disulfide bridges. To obtain a stable network, the cleavage of the formed bonds after network formation should not occur dominantly. However, the low stability of the disulfide bridges in the ESI MS analysis makes a thiol-disulfide exchange reaction via the addition of a chemical trigger appear very promising. To eliminate the possibility that unexpected reactions dominate the network formation, control photoresists were prepared excluding components in a step-wise manner and were exposed to DLW conditions. None of the obtained mixtures cured (**Table 3**) and, therefore, the reaction between thioaldehydes and thiols was fortified.

Photoresist	PSL	Tetrathiol	Sulfolane (solvent)	DLW feasibility
1	+	+	+	+
2	+	-	+	-
3	-	+	+	-
4	-	-	+	-

Table 3: Control photoresists to eliminate the possibility of side reactions that compete with the disulfide formation between thioaldehydes and thiols during DLW.

3.3.8 Fabrication of Cleavable 3D Microstructures via DLW

To assess the printing properties of the PSL photoresist, a variety of test structures was fabricated. The diversity of shapes for 3D printing is limitless, however, most geometries are based on lines arranged in 2D, rods in 3D, layers, or bulk material. Therefore, a line array, a woodpile-type structure, a layer and a block were chosen representing ideal test microobjects. To further compare the phenacyl sulfide-based networks with those of a

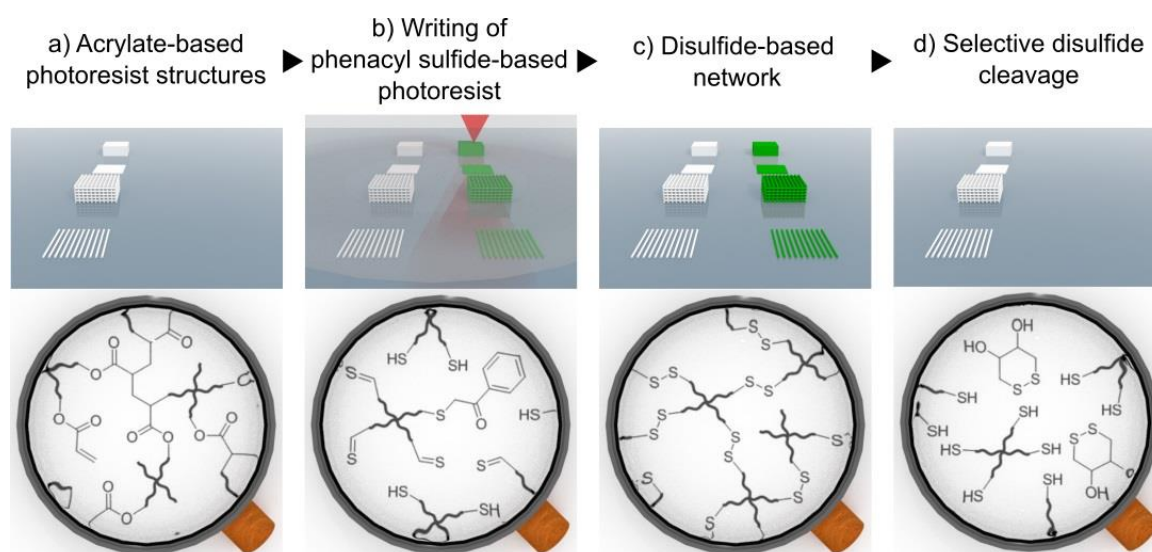


Figure 53: Overview of the procedure to prepare samples with phenacyl sulfide-based structures next to identical objects written with an acrylate-based standard photoresist (IP-L 780, Nanoscribe GmbH, Germany) and the underlying chemistry. a) Identical control structures are fabricated with a commercially available DLW setup (Photonic Professional GT, Nanoscribe GmbH, Germany). b) The PSL photoresist is printed with a custom-built DLW setup allowing the adaptation of the center wavelength to $\lambda = 700$ nm. c) The formed thioaldehydes react with thiol linkers and form a disulfide-based network. d) Utilization of the reversible crosslinks, cleavage is introduced via a thiol-disulfide exchange reaction with dithiothreitol (DTT). Adapted with permission from Ref.[21]. Copyright 2017 John Wiley and Sons.

standard photoresist, identical control structures were fabricated employing IP-L 780 (Nanoscribe GmbH, Germany). Subsequently, the cleavage of the disulfide-based objects employing the chemical trigger dithiothreitol (DTT) was performed via a thiol-disulfide exchange reaction (**Figure 53**). To achieve stable covalent bonds that attach the printed objects to the surface, suitable functionalities have to be immobilized on the glass substrate. In the case of acrylate-based photoresists, a methacrylate bearing silane is utilized after plasma activation of the sample. Unfortunately, the formed thioaldehyde is not reactive towards this functionalization and solidified parts in DLW were lifted and suspended. Thus, an

additional silane containing a thiol functionality was employed. Both silanes were simply added during the silanization of the glass slides and provided stable, covalently bonded structures in DLW for the standard and PSL photoresist. Acrylate-based structures can be fabricated with the commercially available DLW setup Photonic Professional GT (Nanoscribe, Germany), which operates at a center wavelength of $\lambda = 780$ nm. The photoactivation of the phenacyl sulfide to obtain the reactive thioaldehyde requires irradiation with $\lambda = 350$ nm in 1PA. To achieve the required energy in 2PA, a custom-built DLW setup equipped with a tunable Ti:sapphire laser is utilized to tune the wavelength to $\lambda = 700$ nm.^[119] The earlier described beam splitter was not used and excluded from the optical path of the laser beam. The obtained DLW structures were analyzed by scanning electron microscopy (SEM) and revealed defined structures under magnification (**Figure 54**). Compared to the objects written with the standard photoresist, the disulfide-based networks possessed a stronger shrinkage implying a distinct swelling behavior. To access the incorporated crosslinks in a post-treatment with DTT utilizing the reversible nature of the system, the employed solvent has to

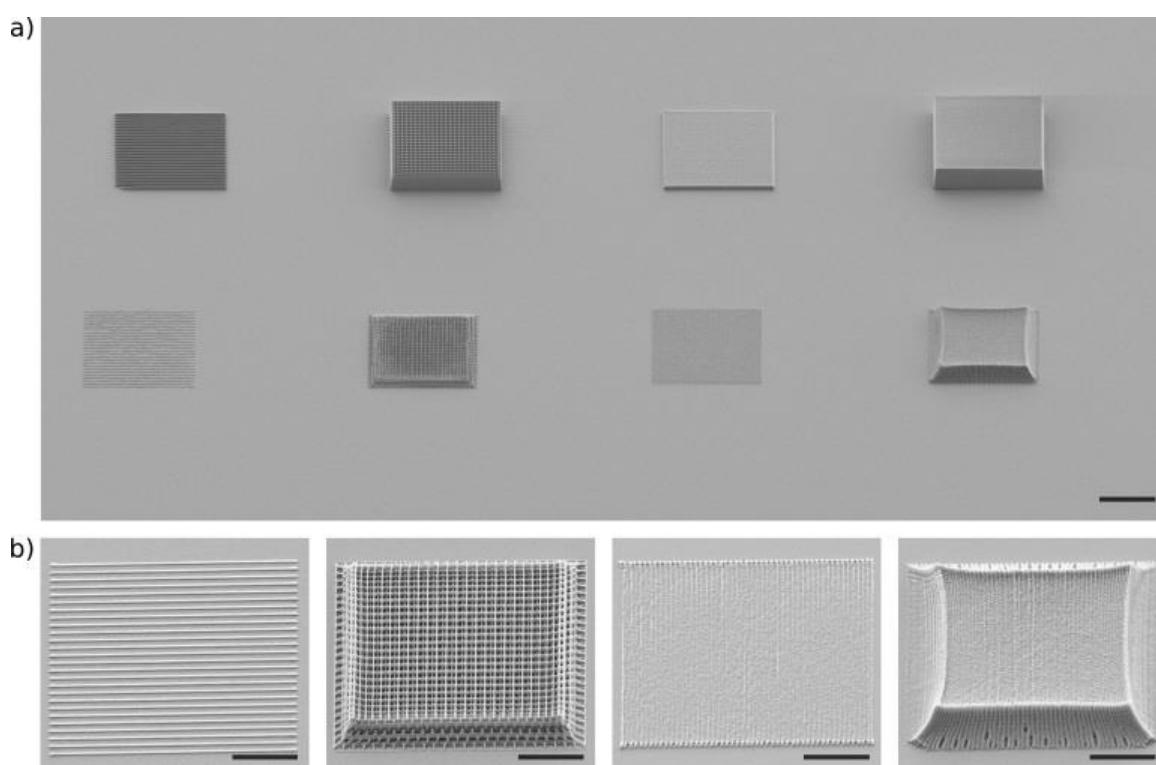


Figure 54: Test objects to assess the printing properties of the PSL system. a) SEM images of control structures written with IP-L 780 (top row) and phenacyl sulfide-based objects (bottom row, scale bar, 10 μm). b) Magnification of the line array, woodpile-type object, layer and block with disulfide bridges as crosslinks (scale bars, 5 μm). Adapted with permission from Ref.[21]. Copyright 2017 John Wiley and Sons.

penetrate the fabricated structures to ensure the diffusion of the chemical trigger through the network. However, the shrinkage after development limits the accessibility of structures with a low filling factor. To illustrate the effect of deformation, woodpile-type objects with an increasing distance between rods in lateral orientation and the variation of the employed laser power were fabricated (**Figure 55**). Varying the power from 6 to 9 mW exhibited a less pronounced deformation compared to the different rod spacings. The forces after development with acetone, 2-propanol and water were significant for a spacing of 2 μm and deformed the cuboidal model (**Figure 55b**). In comparison, a highly symmetric structure was obtained for 0.8 μm that revealed a small step-wise change from the bottom to the upper

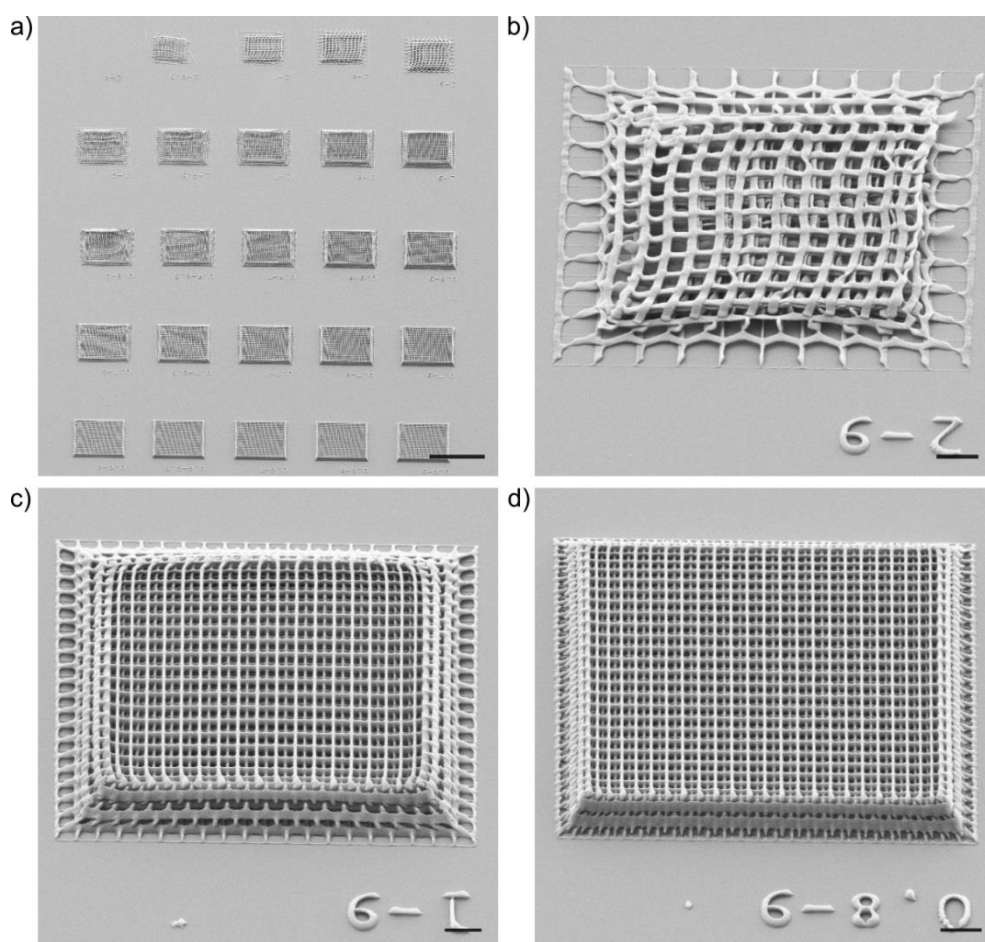


Figure 55: Array of woodpile-type structures (a) to assess the effect of shrinkage with increasing spacing (bottom to top) and laser power (left to right, scale bar, 20 μm). The SEM images reveal a strong deformation for a lower filling factor in the woodpile with a distance between written rods of 2 μm (b) in comparison to the spacing of 1 μm (c). Increasing the amount of cured volume further, the object with the lowest distance between printed rods (d) shows the best performance after development (scale bars, 2 μm , b-d).

layer due to shrinkage (**Figure 55d**). However, an additional influence of DLW affects the observed trend, namely, the so called proximity effect. The possibility to write a line or rod with the smallest diameter achievable does not translate into the same lateral resolution. It is assumed, that the still liquid parts of the photoresist, surrounding cured material, have been exposed to a certain amount of irradiation. A volume that is irradiated a second or multiple times by this reduced amount of intensity can reach the threshold value by the summed up energy and eventually solidifies. In addition, written structures with partially uncured, embedded functional groups can undergo a post-polymerization resulting in additional crosslinks.

3.3.9 Lateral Resolution

To determine the actual lateral resolution, line arrays were fabricated with varied spacing and laser power (**Figure 56**). To obtain assessable patterns, the interface has to be located precisely in the z-axis prior to the fabrication process, otherwise, the laser voxel is located inside the glass slide or the structures are insufficiently bonded to the surface and can tilt or

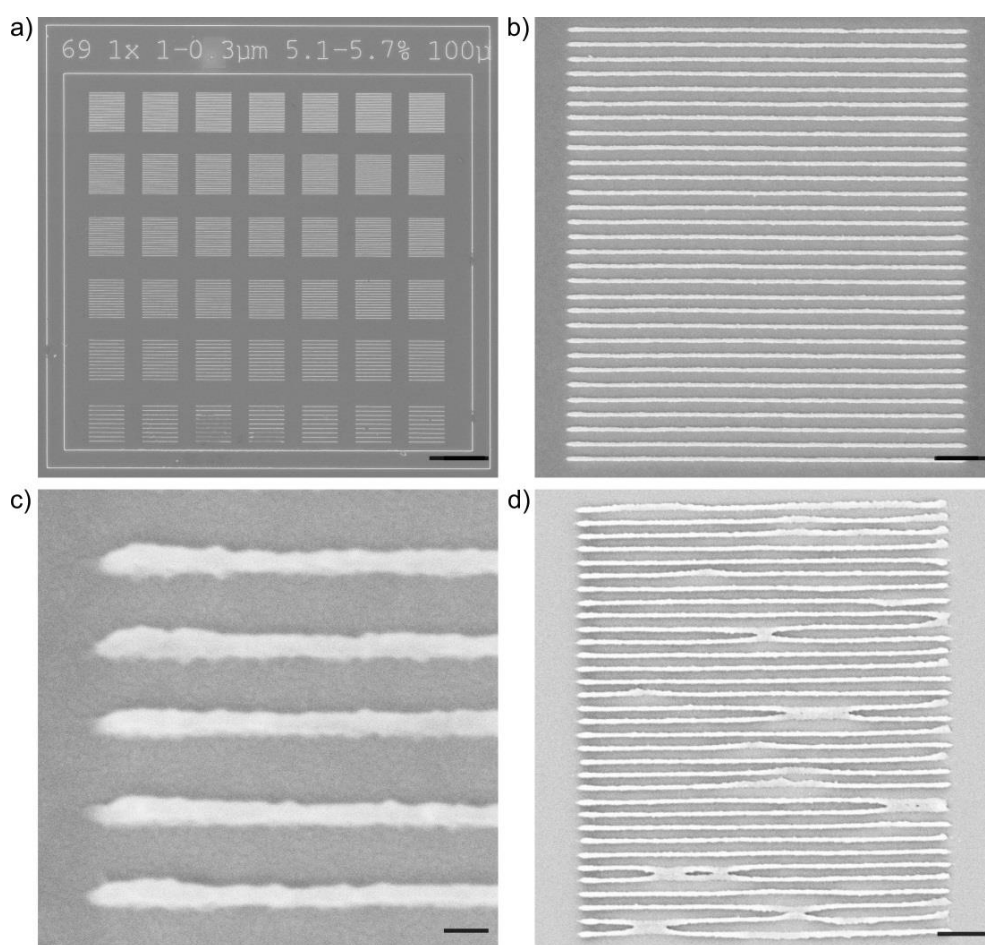


Figure 56: Line arrays printed with varying laser power and line spacing (a). b)-c) Magnification of written lines for optimized conditions. d) Deformed line array for overlapping voxels in DLW. Adapted with permission from Ref.[21]. Copyright 2017 John Wiley and Sons.

even fall over. In the case of cured material that shrinks after development, the achieved best lateral resolution still appears to be below its optimum due to the empty spaces between written lines (**Figure 56b-c**). However, reducing the line distance further reveals the overlap of the structures during fabrication. After development, the connected lines shrink and deform the fabricated array (**Figure 56d**). In addition, the before noted proximity effects are

beneficial for the connection of adjacent lines during the writing process. In comparison to standard (meth)acrylate-based photoresists, however, it is less pronounced, but can be challenging for the fabrication of bulk material that is based on interconnected geometries. This problem was clearly visible during the fabrication of compound boxing-like structures. The horizontal connections of the IP-L 780 based scaffold were fabricated with the phenacyl sulfide photoresist. However, SEM analysis revealed the insufficient crosslinking between adjacent structural elements of the spiral and were replaced with rods (**Figure 57**). Generally favored for less proximity effects, in this case, the utilization of step-growth polymerization leads to insufficient crosslinking between the loops of the spiral and the resulting structure was not stable and dropped to the surface (**Figure 57a**). To wrap the spirals around a prior printed rod revealed the strong shrinkage of the disulfide-based network leading to a structural element slightly thicker than the rod and critically thinner than the connections

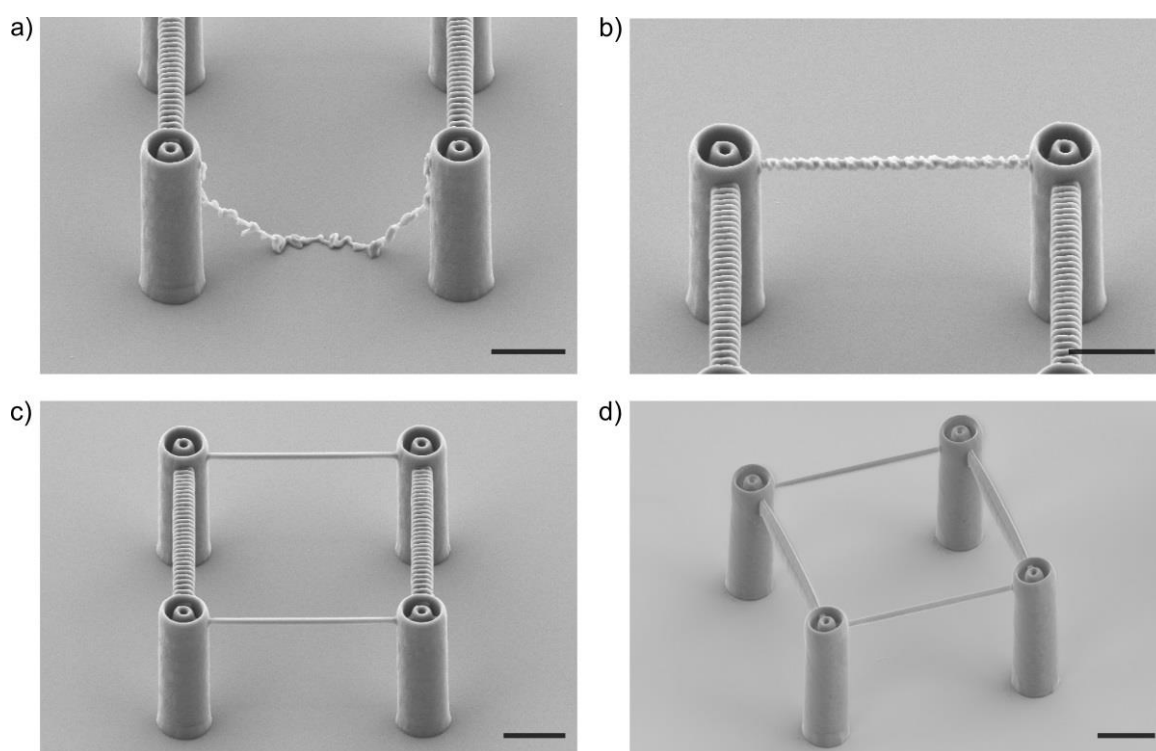


Figure 57: Fabrication of a boxing-like compound structure utilizing the disulfide-based network. a) The incorporation of connections of the phenacyl sulfide-based photoresist into a scaffold written with IP-L 780 revealed insufficient crosslinking of adjacent cured material. b) Spiral connection wrapped around a prior printed rod. c) Disulfide-based connection with multiple rods. d) Adjusted standard photoresist scaffold using the same geometry for the vertical connections. Final rods were printed with a writing speed of $100 \mu\text{ms}^{-1}$, a spacing of 200 nm in lateral orientation, and 500 nm in z-direction (scale bars, 5 μm). Adapted with permission from Ref.[21]. Copyright 2017 John Wiley and Sons.

with IP-L 780 (**Figure 57b**). Therefore, multiple adjacent rods were printed and successfully integrated into the scaffold (**Figure 57c**). To obtain a better comparison, the standard photoresist connections were also fabricated with the same geometry (**Figure 57d**). It was assumed that the main influence stems from the step-growth fashion of the polymerization. Utilizing radical polymerizations for DLW, the photoactivation of a photoinitiator molecule in the outer areas of the voxel results in a growing chain, whereas for the phenacyl sulfide photoresist, only a dimer is formed. The fabrication of compound structures faces additional challenges, namely the adhesion or bonding between two networks with different functional groups and the destruction of structures resulting from the interaction of the laser voxel with already cured material. Covalent bonds should not be formed between the photoactive species phenacyl sulfide or the activated thioaldehyde and the residual acrylate functionalities of the standard photoresist, however, a thiol-ene reaction of residual thiol groups incorporated into the disulfide network is conceivable. In addition, polymer chains in a thermoset that is printed in close proximity to already cured material can form entanglements and adhesion is additionally supported by van der Waals interactions. To avoid the destruction of already cured material for the fabrication of compound structures, precise tuning of the laser power, writing speed and parameters such as the starting and ending point of the voxel have to be optimized (refer to the Appendix, **Figure 97**). A promising application for removable photoresists is the modification of expensive or unique samples that are extended by, for instance, wire bonds. Adjusting or changing the printed objects would not be possible utilizing standard acrylate photoresists that require harsh conditions for the removal.^[203] Therefore, the fabrication of a wire bond was envisaged employing the disulfide-based network. Achieving smooth surfaces of the printed objects is often required for optical applications. However, shrinkage after development and the deformation of prior written lines by adjacent printing led to deformed structures (**Figure 58a-c**). Utilizing a spiral with a high filling factor to fabricate the wire bond gave the best results, however, the underlying geometry of the object was still clearly visible (**Figure 58d**).

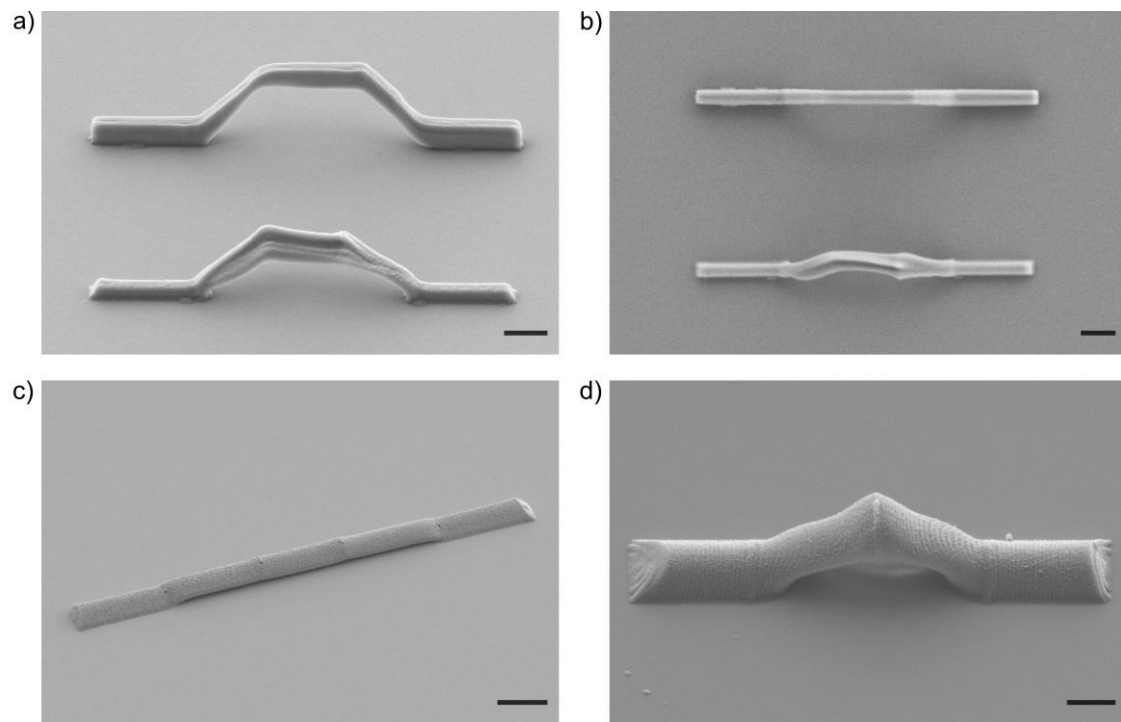


Figure 58: Attempts to fabricate wire bonds for optical applications. Structures obtained by the printing of adjacent rods revealed a deformation (a, side view, b, top view). Prior written lines were influences and were out of shape after development. The underlying geometry was changed to spirals with a low filling factor (c) and a high filling factor (d).

3.3.10 A Readily Accessible Cleavable Photoresist Platform

Taking into account that the research fields of DLW and 3D printing on the macroscale is full of non-chemists such as physicists or material scientists, readily accessible photoresist platforms are critically required. In addition, the transfer to other 3D printers operating on the macroscale would be feasible (**Figure 59**). Recent insights into the area of functional

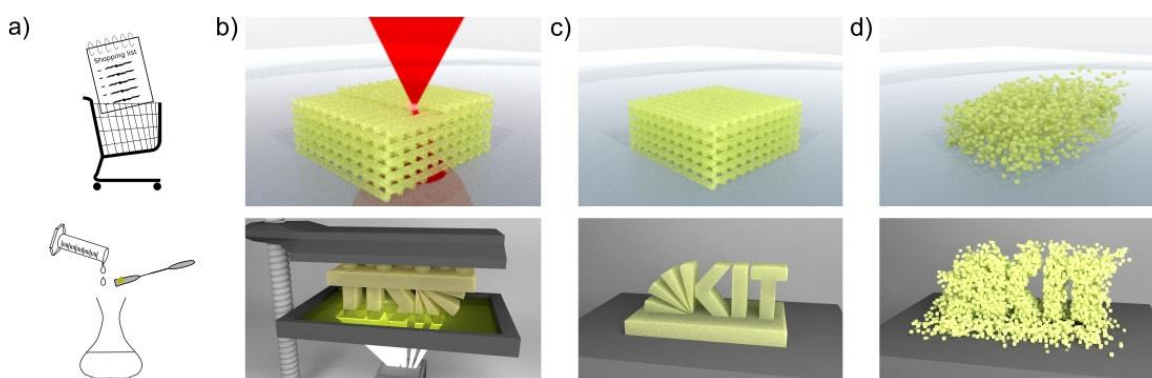


Figure 59: Fundamental idea of a platform photoresist technology with commercially available components (a), applicable for different 3D printing devices such as DLW and SLA (b). The resulting structures are envisaged to be dimensionally stable (c), yet still provide the selective removal of the networks (d). Adapted with permission from Ref.[22]. Copyright 2018 John Wiley and Sons.

photoresist development reveal promising ligation alternatives to the common use of (meth)acrylates, namely thiol-ene and thiol-yne based polymerizations. The reaction can be triggered with radicals or proceed in a Michael addition pathway (refer to section 2.2.4.3). However, the requirement for synthesized linkers remained. Thus, commercially available linker molecules were examined for their suitability to be implemented in a cleavable

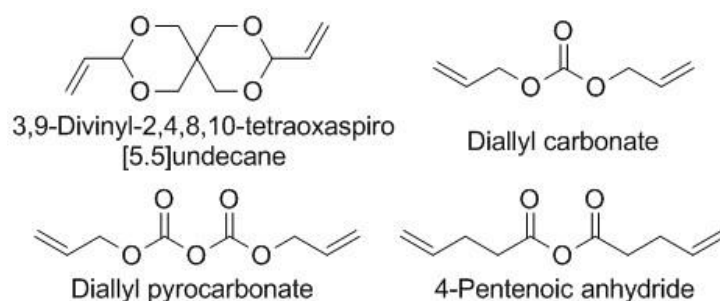


Figure 60: Commercially available divinyl, diallyl and double bond bearing derivatives of acetals (3,9-divinyl-2,4,8,10-tetraoxaspiro[5.5]undecane), carbonates (diallyl carbonate), pyrocarbonates (diallyl pyrocarbonate) and anhydrides (4-pentenoic anhydride) were employed for the provision of a cleavable platform photoresist.

photoresist for DLW. In addition, the moieties should possess the ability to undergo a subsequent chemical reaction resulting in the cleavage of the printed networks. The utilized divinyl, diallyl and double bond bearing derivatives are depicted in **Figure 60**. As thiol linker the tetrathiol pentaerythritol tetrakis(mercaptopropionate), similar to the thiol linker serving as a readily accessible moiety for the PSL photoresist, was employed. Broadly used and available in a wide variety, the acetale group appeared promising for our purpose to provide a readily accessible photoresist offering the cleavage of fabricated structures in a facile fashion. The divinyl derivative was employed in a radical polymerization with bis(2,4,6-trimethylbenzoyl)-phenylphosphineoxide (Irgacure 819, BASF, Germany). Modifying the photoresist composition of earlier reports (refer to **Figure 65**),^[123] the curing of the photoresist was achieved with a UV hand lamp (Bluephase Style, Ivoclar Vivadent GmbH, Germany). Fast solidification after a short period of time (30 s) was obtained, indicating the

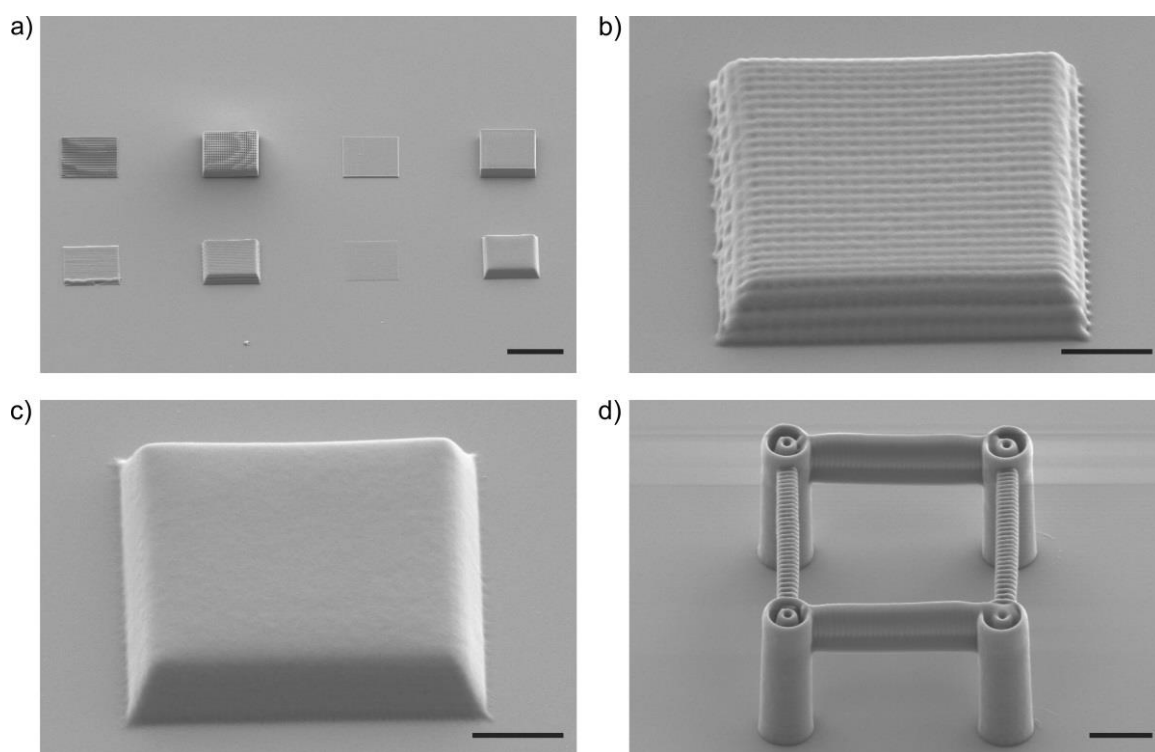


Figure 61: SEM images of DLW structures printed with a thiol-ene based photoresist. As divinyl species, an acetale containing moiety was employed. a) To assess the printing properties, a selection of structures, namely a line array, a woodpile-type structure, a layer and a block were fabricated with the thiol-ene photoresist (bottom row) and, in addition, with a standard photoresist as reference (IP-L 780, top row). Furthermore, a magnification of the woodpile-type structure (b) and the block (c) are depicted. In the boxring-type scaffold (d) only the horizontal connections were written with the thiol-ene based photoresist. The rest of the scaffold is based on IP-L 780. Adapted with permission from Ref.[22]. Copyright 2018 John Wiley and Sons.

resist's potential suitability for processing with a 3D printer. Next, DLW was performed. To be able to compare the objects with the before presented phenacyl sulfide-based structures (a line array, a woodpile-type structure, a layer and a block), identical geometries of the radical thiol-ene based photoresist were fabricated. Furthermore, IP-L 780 was utilized as control and the resulting structures were analyzed via SEM (**Figure 61**). The obtained objects revealed a lower resolution for the thiol-ene based woodpile-type structure and the block. Features such as edges and single lines possessed a low precision. The fabrication of a spiral to connect the pillars of a boxing-like scaffold resulted in a strong stretch in z-direction indicating a high aspect ratio. In earlier studies, the insensitivity of the radical thiol-ene reaction to oxygen has been identified as a possible reason. Less pronounced termination reactions in the periphery of the voxel, which play a crucial role for the aspect ratio of acrylate based photoresists,^[204] could explain the obtained results. However, photoresists with exchanged linker moieties possessed a similar aspect ratio compared to acrylate-based photoresists (refer to **Figure 74**). Subsequent to the fabrication of the acetale-based objects, global removal should be feasible under acidic conditions or spatially resolved cleavage should be obtained utilizing photo acid generators. To enable orthogonally removable systems, the carbonate linker (diallyl carbonate) was employed. The carbonate functionality is cleavable under basic conditions employing an amine. The platform photoresist facilitated straight forward examination of the new component, diallyl carbonate, and no alteration besides the exchange of the acetale moiety with the carbonate linker was necessary. After successful and fast (30 s) curing with the prior mentioned UV hand lamp, DLW was conducted. To achieve the best possible comparison, the identical geometries utilized for the acetale moiety were printed and analyzed via SEM (**Figure 62**). The magnification of the woodpile-type object and the block revealed a better final geometry stemming from less pronounced shrinkage compared to the acetale-based photoresist. However, the aspect ratio did increase even further and the spiral in the boxing-like structure possessed a stronger z-stretch. Larger voxels would also explain the lower shrinkage that was obtained due to pre- and post-polymerization of the photoresist and cured material, resulting in higher degrees of crosslinking. An additional explanation lies in the nature of carbonate functionalities integrated in a polymer backbone that lead to rigid materials.

A target application for cleavable structures is the achievement of the precisely defined 3D surrounding for cell adhesion combined with a subsequent cell release via selective or global

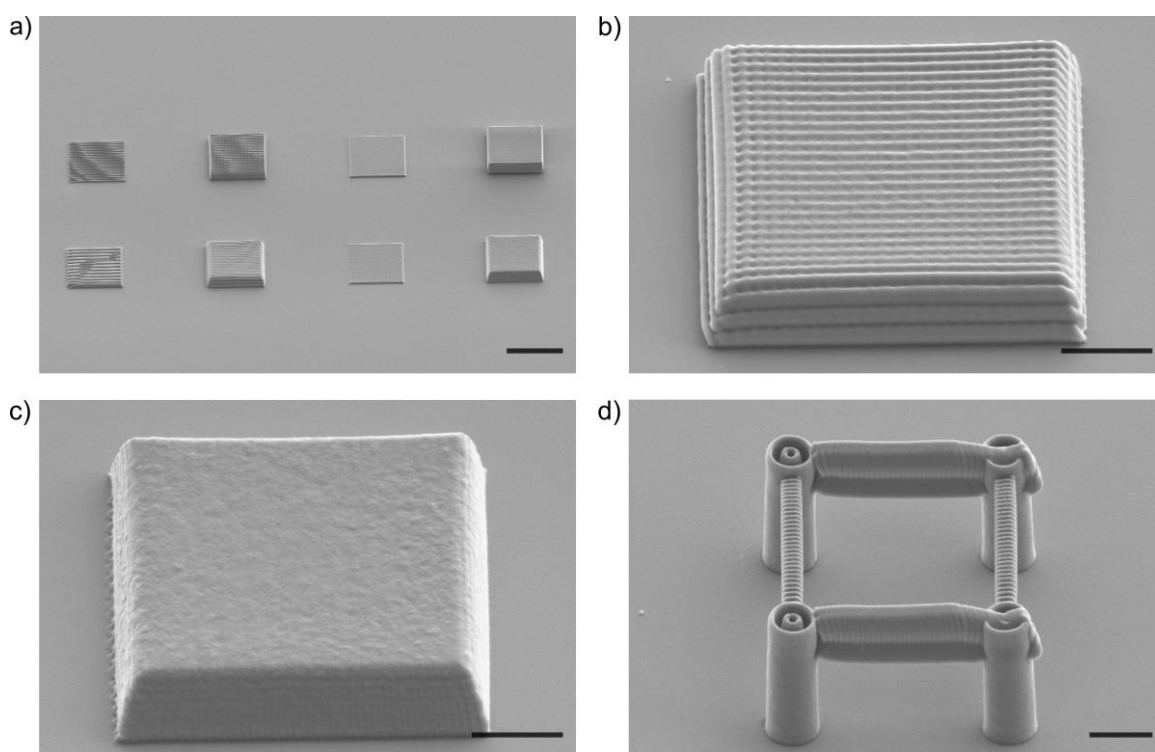


Figure 62: SEM images of DLW structures printed with a thiol-ene based photoresist. As diallyl species, a carbonate containing moiety (diallyl carbonate) was employed. a) To assess the printing properties, a selection of structures, namely a line array, a woodpile-type structure, a layer and a block were fabricated with the thiol-ene photoresist (bottom row) and, in addition, with a standard photoresist (IP-L 780, top row). Furthermore, a magnification of the woodpile-type structure (b) and the block (c) are depicted. In the boxring-like scaffold (d) only the horizontal connections were written with the thiol-ene based photoresist. The remaining scaffold is based on IP-L 780. Adapted with permission from Ref.[22]. Copyright 2018 John Wiley and Sons.

removal of the 3D scaffolds. Therefore, the diallyl derivative of the pyrocarbonate functionality was implemented, offering mild and bio-orthogonal cleaving conditions via hydrolyzation or amine bearing amino acids. Besides the exchange of the linkers, the use of the vinyl phosphonic acid was not possible due to the low stability of the pyrocarbonate towards acidic conditions. In addition, dry propylene carbonate was used. To remove the cured material, exposure to buffer solutions should hydrolyze the pyrocarbonate. Utilizing differently concentrated photoresists and varying writing parameters, the degree of crosslinks should be adjustable to facilitate a precise time window for biological experiments. Likewise, cleavage should be feasible with a low concentration of bio-orthogonal amines, e.g., lysine for instance for an accelerated removal. Once again, the identical geometries utilized for the acetale and carbonate moieties were printed with DLW and analysis via SEM (**Figure 63**). Obviously, the photoresist was not suited for defined geometries and the woodpile-type object is barely distinguishable from the written block. However, both structures possessed a

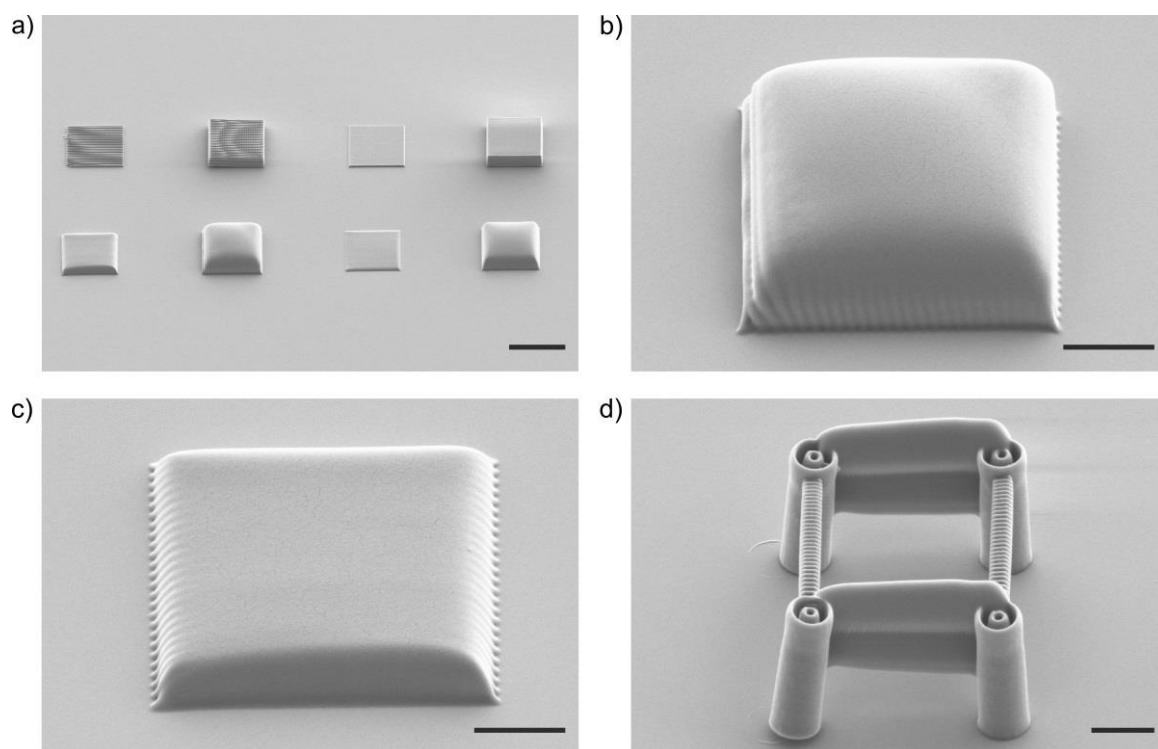


Figure 63: SEM images of DLW structures printed with a thiol-ene based photoresist. As diallyl species, a pyrocarbonate containing moiety (dially pyrocarbonate) was employed. The vinyl phosphonic acid was not used due to the stability of the linker. a) To assess the printing properties, a selection of structures, namely a line array, a woodpile-type structure, a layer and a block were fabricated with the thiol-ene photoresist (bottom row) and, in addition, with a standard photoresist (IP-L 780, top row). Furthermore, a magnification of the woodpile-type structure (b) and the block (c) are depicted. In the boxing-like scaffold (d) only the horizontal connections were written with the thiol-ene based photoresist. The remaining scaffold is based on IP-L 780. Adapted with permission from Ref.[22]. Copyright 2018 John Wiley and Sons.

very smooth surface which is highly beneficial for optical elements. The printing with a standard acrylate-based photoresist often leads to surfaces with visible single lines or layers in SEM analyzes that can lower their performance. Considering the strong z-stretch of the boxing-like object, a high aspect ratio was assumed. Therefore, the undefined and smooth surface of the woodpile-type structure and the block could stem from lightly cured photoresist that is formed spherically with a strong z-stretch in the periphery of the voxel. After development, this loosely crosslinked material collapses and yields a smooth circular finish. The left pillars in **Figure 63d** were teared of the surface and slightly pulled to the right, most likely due to shrinkage of the horizontal connections. Materials in DLW with low degrees of crosslinking often go hand in hand with a pronounced swelling and shrinking behavior. An additional influence could originate from the partial cleavage of the pyrocarbonate linkers during printing or development of the structures (refer to **Figure 72**). To test, how the implied

power influences the writing conditions of the photoresist, a dose test was performed (refer to the Appendix, **Figure 99**). This experiment revealed that fine lines are only accessible for a voxel with a negative z-coordinate, indicating a high aspect ratio. As an additional bio-orthogonally cleavable moiety, 4-pentenoic anhydride was employed. Again, the inhibitor vinyl phosphonic acid was not employed due to the low stability of the linker towards acidic conditions. As a first test, the photoresist was irradiated with the before mentioned UV hand lamp (30 s) and after successful curing, DLW was conducted. The test structures were fabricated with DLW and analyzed via SEM (**Figure 64**). The aspect ratio increased drastically, resulting in a strong elongation in the z-direction of spirals connecting the boxring-like scaffold. Due to strong shrinkage, the pillars were pulled along the anhydride-based network and remained angled. Edges were barely recognizable for the cuboidal objects, however, the obtained surfaces appeared to be very smooth which is highly beneficial for optical elements.

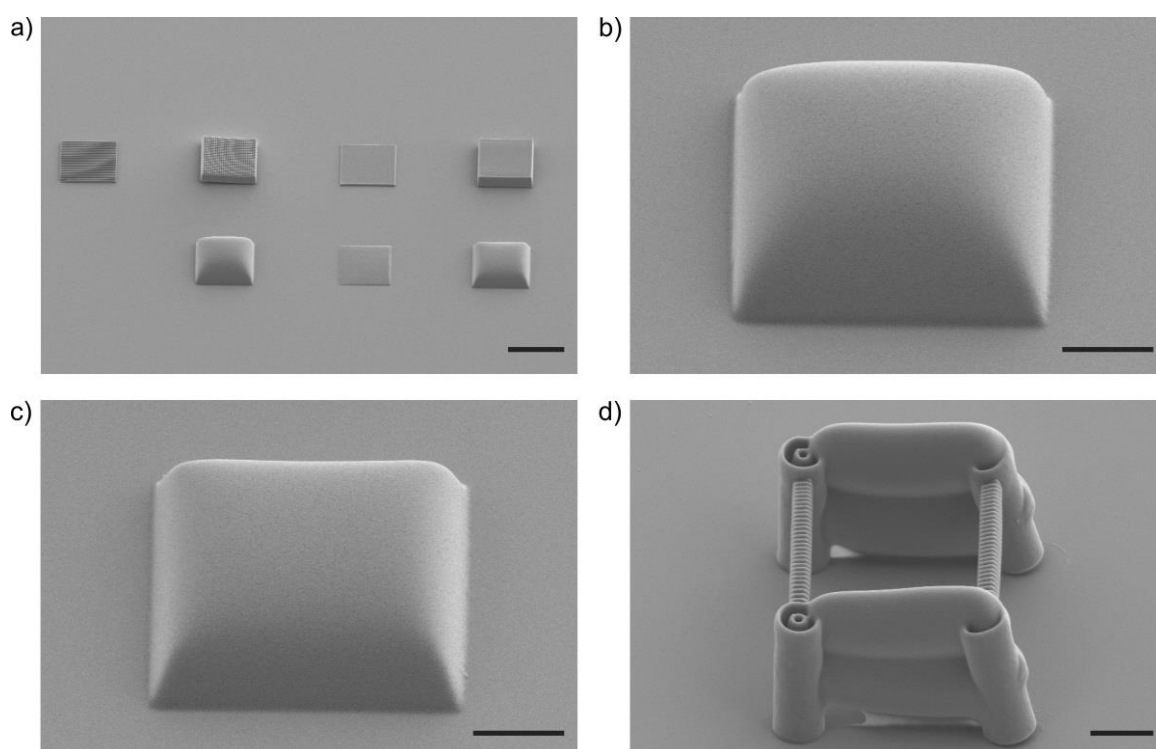


Figure 64: SEM images of DLW structures printed with a thiol-ene based photoresist. As double bonds containing dilinker species, an anhydride moiety (4-pentenoic anhydride) was employed. The vinyl phosphonic acid was not used due to the stability of the linker. a) To assess the printing properties, a selection of structures, namely a line array, a woodpile-type structure, a layer and a block were fabricated with the thiol-ene photoresist (bottom row) and, in addition, with a standard photoresist (IP-L 780, top row). Furthermore, a magnification of the woodpile-type structure (b) and the block (c) are depicted. In the boxring-like scaffold (d) only the horizontal connections were written with the thiol-ene based photoresist. The remaining scaffold is based on IP-L 780. Adapted with permission from Ref.[22]. Copyright 2018 John Wiley and Sons.

To cleave the anhydride bond, aqueous conditions should enable a removal of written structures. By achieving different degrees of crosslinks, the stability as a function of time should be adjustable and therefore offer a window for biological experiments. In this case, the anhydride functionality could be partially cleaved due to residual water in the photoresist. Water was not used for the development, however, even short exposure to organic solvents could cleave the network. Overall, the readily accessible photoresist platform had proven to enable the straightforward integration of different functionalities into a direct laser written network. Aiming for cleavable structures serving as support structures for complex geometries or as sacrificial material, the obtained high aspect ratios are still suitable for certain applications. However, the removal of the individual thiol-ene based networks has to be feasible in a straightforward fashion and should provide conditions that allow orthogonal cleavage of objects.

3.3.11 Stabilized Thiol-Ene Photoresist

To demonstrate the stability of thiol-ene crosslinked thermosets towards the employed cleaving conditions for the acetale, carbonate, pyrocarbonate and anhydride moieties, an additional photoresist was required. Originally regarded as a control photoresist without additional functionalities besides ester, thiol groups and double bonds, the utilization of divinyl adipate for the thiol-ene photoresist (**Figure 65**) revealed a surprisingly low aspect

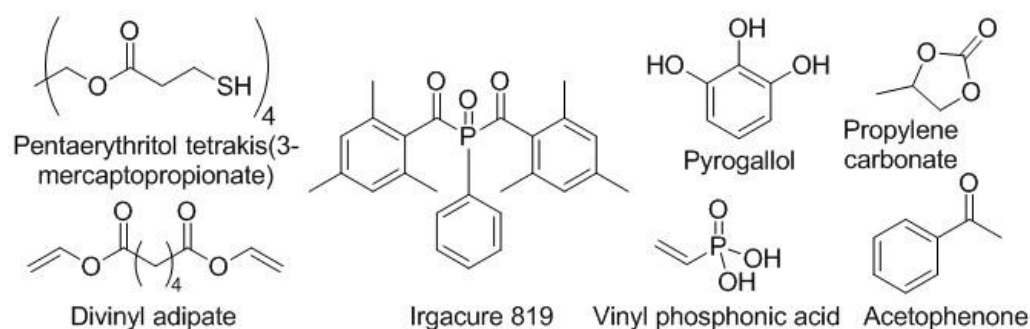


Figure 65: Photoresist composition for radical thiol-ene polymerization employing divinyl adipate and pentaerythritol tetrakis(3-mercaptopropionate). Phenylbis(2,4,6-trimethylbenzoyl)phosphine oxide (Irgacure 819) serves as photoinitiator. Pyrogallol prevents the self-initiated radical polymerization, while vinyl phosphonic acid prohibits the crosslinking in a Michael addition fashion. As solvents, propylene carbonate and acetophenone are utilized.

ratio with precise structural features and a high dimensional stability of 3D printed objects. To enable a good comparison (3.3.10), a line array, a woodpile-type structure, a layer and a block were fabricated via DLW and analyzed via SEM (**Figure 66**). In addition, identical control structures written with a standard photoresist (IP-L 780) were adjacently aligned. The obtained thiol-ene based networks possess only ester and thioether functionalities along the chains, neglecting the influence from possible side reactions. Therefore, the exposure to the before mentioned cleaving conditions for short time values should not result in the removal of the structures. Due to the low aspect ratio, the printed block and woodpile-type object possessed clear edges and the single lines of the woodpile-type structure were still visible for a spacing of 0.8 μm . A possible explanation for this change in comparison to the prior used pyrocarbonate- and anhydride-based networks was the stability of ester and thioether bonds towards the conditions during development with solvents. In addition, the missing inhibitor, vinyl phosphonic acid, for the polymerization via Michael addition could influence the conditions during 3D printing. However, it remained unclear what caused the strong decrease of the aspect ratio, especially, regarding the acetale and carbonate cores. Achieving a better resolution for small feature sizes, the fabrication of boxing-like compound structures without

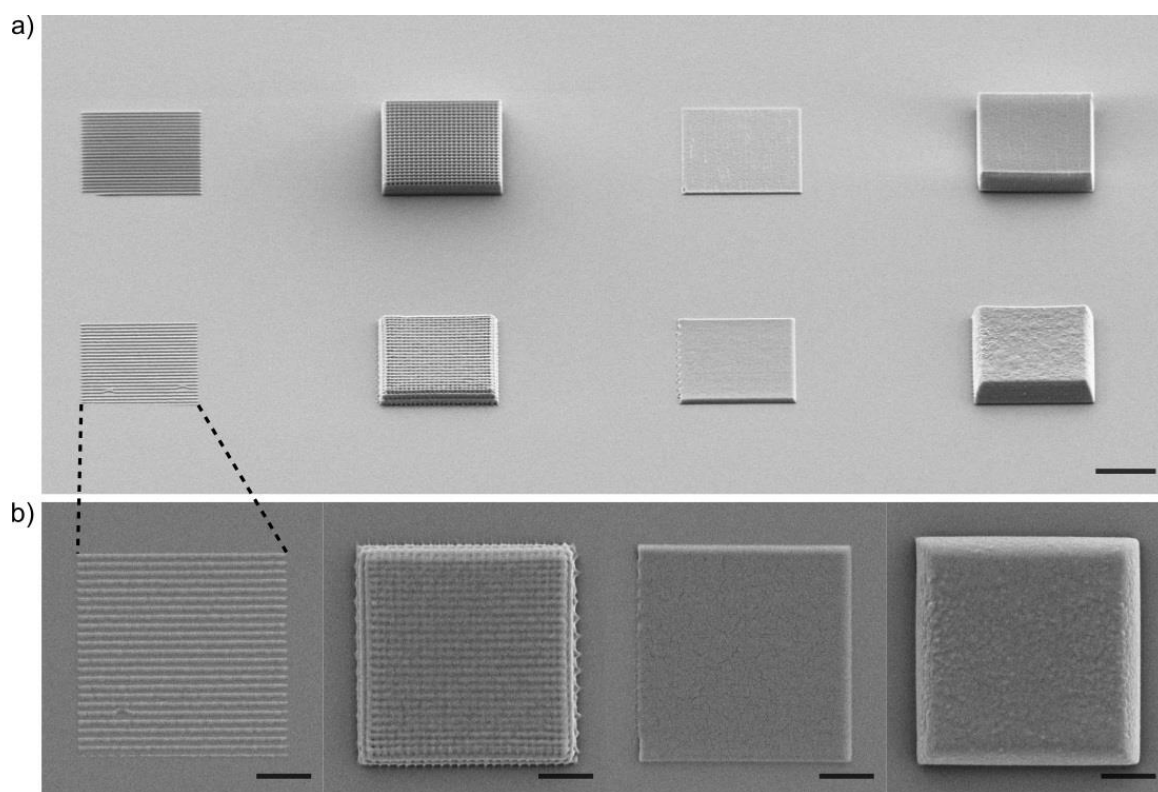


Figure 66: Objects to assess the properties of the ester-based photoresist intended for non-cleavable networks. SEM images of a) control structures written with an acrylate-based standard photoresist (top row) and thiol-ene based (bottom row, scale bar, 10 μm). b) Magnification of the line array, woodpile-type object, layer and block with only ester and thioether functionalities along the chains (scale bar, 5 μm). Adapted with permission from Ref.[22]. Copyright 2018 John Wiley and Sons.

a strong z-elongation of the thiol-ene based connections appeared promising. The analysis via SEM underpinned this expectation (**Figure 67**). Until now, the influence of the employed laser power for the quality of the DLW structures was not discussed. To determine the laser power range in which the divinyl adipate-based thiol-ene photoresist is usable, a power sweep was performed (refer to the Experimental Section, **Figure 100**). To compare the results with the pyrocarbonate-based photoresist (refer to the Experimental Section, **Figure 99**), an identical test was conducted. The laser power was increased from bottom to top and the z-coordinate with the surface set to $z = 0$ was increased from negative to positive values from left to right. (Meth)acrylate-based standard photoresists reveal a similar v-shape behaviour compared to the ester-based thiol-ene photoresist. However, the power sweep of the pyrocarbonate moiety revealed cured material for the bottom left side of the window, where the center of the voxel is still focused into the glass. These areas can be explained by the high aspect ratio that elongate the voxel in z-direction. The right side of the power sweep matched the typical shape. However, cured material for higher z-coordinates is tilted before it fully disappears

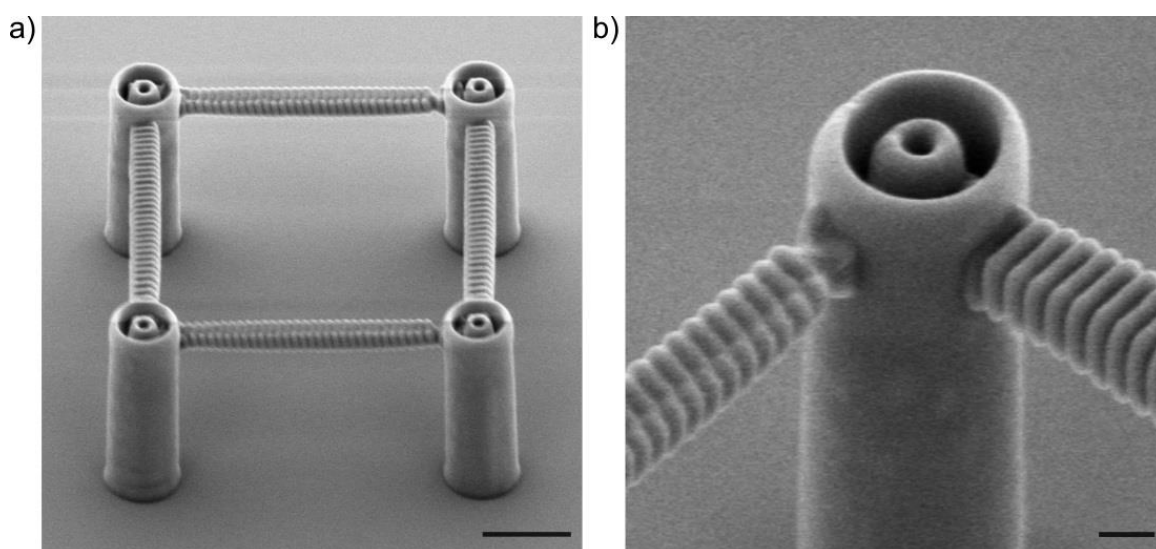


Figure 67: Fabrication of a boxring-like compound structure. a) The pillars and vertical connections are written with IP-L 780 and horizontal ones with the divinyl adipate containing thiol-ene photoresist (scale bar, 5 μm). b) Magnification of the connection points to the pillars (scale bar, 1 μm). Adapted with permission from Ref.[22]. Copyright 2018 John Wiley and Sons.

from left to right and therefore it is assumed that the material for higher z-coordinates (bottom right) was torn off the surface during writing or development. Accordingly, the optimization of the power for the pyrocarbonate-based photoresist was not leading to better results. In contrast, the fabrication quality of the spirals for the boxring-like structure employing the divinyl adipate moiety revealed a dependency (see Experimental Section, **Figure 101**).

3.3.12 Water Permeable Cleavable Network

To achieve the removal of structures in aqueous conditions, not only the chemical trigger has to be water-soluble, but the network has to be water permeable, otherwise, the chemical trigger might react on the surface of the printed object and alter the morphology, but the cleavage of functionalities embedded in the printed object may not occur. Exploiting the dependency on the utilized solvent, orthogonal removal via different permeabilities of networks is envisaged. Attempts to use diacrylate linkers containing poly ethylene glycol (PEG) cores with different molecular weights with the thiol-ene platform did not lead to curable photoresists. However, employing an ionic compound, diallyldimethylammonium chloride, curing was feasible with the prior mentioned hand UV lamp (30 s). Unfortunately, DLW was not suited to process the photoresist, most likely due to a high degree of inhomogeneity that

lead to explosions and curing for the same employed laser power at different locations. Assuming that this problem is only hindering the printing in the microscopic scale, processing via SLA was conducted and led to well defined objects (refer to **Figure 76**).

3.3.13 Macroscopic 3D Printing Employing Stereolithography (SLA)

Moving from the micro- to the macroscale, new challenges arise. The required amount of photoresist is increasing drastically and especially in our case, techniques based on 2PA are less favorable due to long writing times and limitations in the maximum size of the printed object. SLA presents a well-established method for macroscopic 3D printing with many commercially available setups (refer to section 2.2.3). In the current thesis, a Projet 1200 (3D Systems, U.S.) 3D printer was utilized. Employing commercially available components, the high amounts of photoresist required for printing via SLA, did not pose any problem. The divinyl adipate-based networks did not only possess the best dimensional stability, but additionally enabled a residue-free removal. Therefore, it was also employed for the printing of macroscopic objects. To implement the new system, the commercially available cartridge Visijet FTX clear (3D systems, U.S.) was emptied, cleaned with 2-propanol and filled with approximately 3 mL of the photoresist. The software belonging to the SLA printer was used and the standard settings were applied. Three different logos of the Karlsruhe Institute of Technology (KIT), the Australian Research Council (ARC), and the Queensland University of Technology (QUT) were chosen as test structures (**Figure 68**). The obtained objects were dimensionally stable and no shrinkage was visible. The different letters printed showed the different challenges of 3D printing via SLA. Features such as the fan-like K were printed without support structures. Only the letter C required additional pillars that were removed mechanically prior to the cleavage experiments. The freely suspended and horizontal areas for the T revealed a small deviation from the model, but were not sufficiently pronounced to utilize additional support structures.

To assess the mechanical properties of the printed material, nanoindentation was conducted (see Appendix, **Table 9**, **Table 10**, **Figure 102**, and **Figure 103**). The printed layers (stage set to lateral orientation) were probed along the z-axis in x- or y-direction resulting in a reduced Young's modulus of 7.09 ± 3.37 MPa and a hardness of 1.24 ± 0.63 MPa. Measurements along the xy-plane in z-direction revealed a reduced Young's modulus of 4.14 ± 0.42 MPa and a

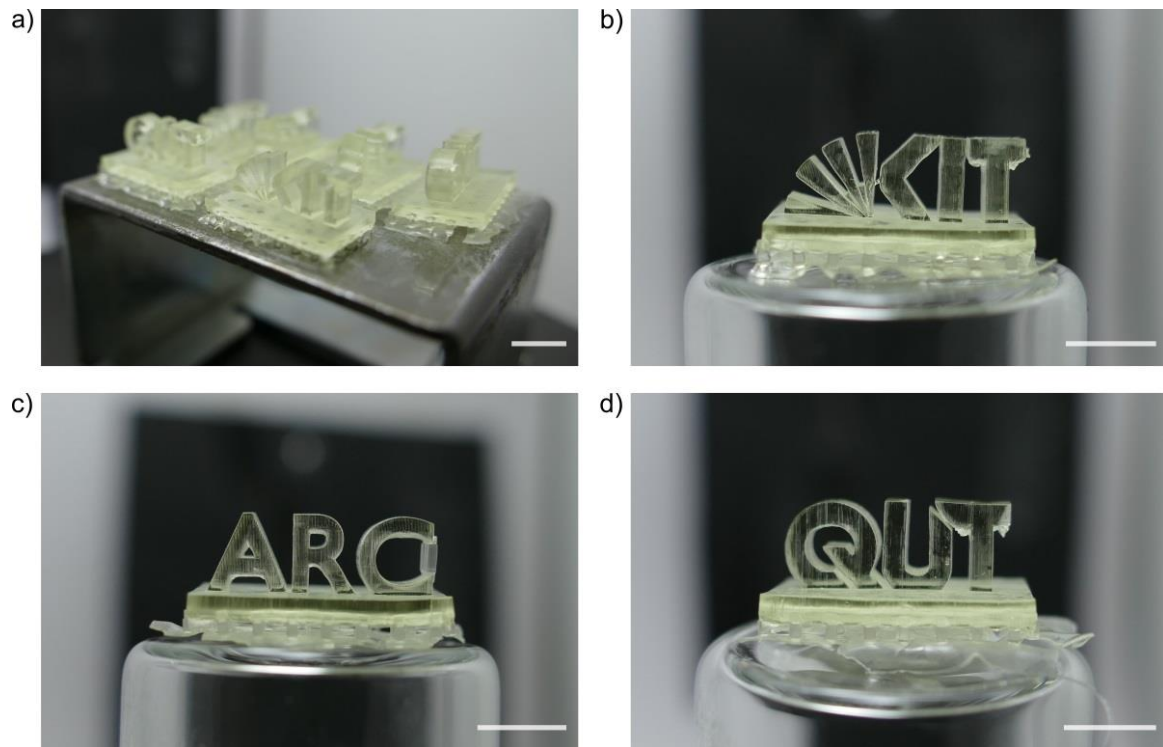


Figure 68: Macroscopic 3D printing via SLA employing the divinyl adipate thiol-ene photoresist. a) Different logos on the stage of the printer. Magnifications of b) Karlsruhe Institute of Technology (KIT), c) Australian Research Council (ARC) and d) Queensland University of Technology (QUT) are displayed revealing no visible shrinkage or deformation (scale bars, 5 mm). Adapted with permission from Ref.[22]. Copyright 2018 John Wiley and Sons.

hardness of 0.73 ± 0.10 MPa. During the additive manufacturing via SLA, the deviation of properties along the z-axis of the object is increased for larger layer thicknesses and depends on the penetration depth of the curing light into the liquid photoresist and cured material. As expected, the nanoindentation measurements possessed higher deviations in z-direction compared to the probing in x- and y-orientation. However, the obtained data are in the same order of magnitude and both load-displacement curves show a high elasticity of the printed material. To achieve a better understanding for the chemistry of the networks and to provide a comparison for later removal experiments, Fourier-transform infrared spectroscopy (FT-IR) was conducted (**Figure 104**).

3.4 Cleaving 3D Printed Micro- and Macroscopic Structures on Demand

Removal of cured polymeric material is required in various fields of application (refer to section 2.2.4.5). To avoid harsh conditions such as heat^[19] and plasma etching^[20] that burn out the polymeric material, the selective cleavage of functionalities under mild conditions is of high interest. In the following pages, the obtained networks via DLW and SLA employing the phenacyl sulfide- or thiol-ene-based photoresists are exposed to conditions that should lead to a residue-free removal (**Figure 69**). The main target was the provision of chemically

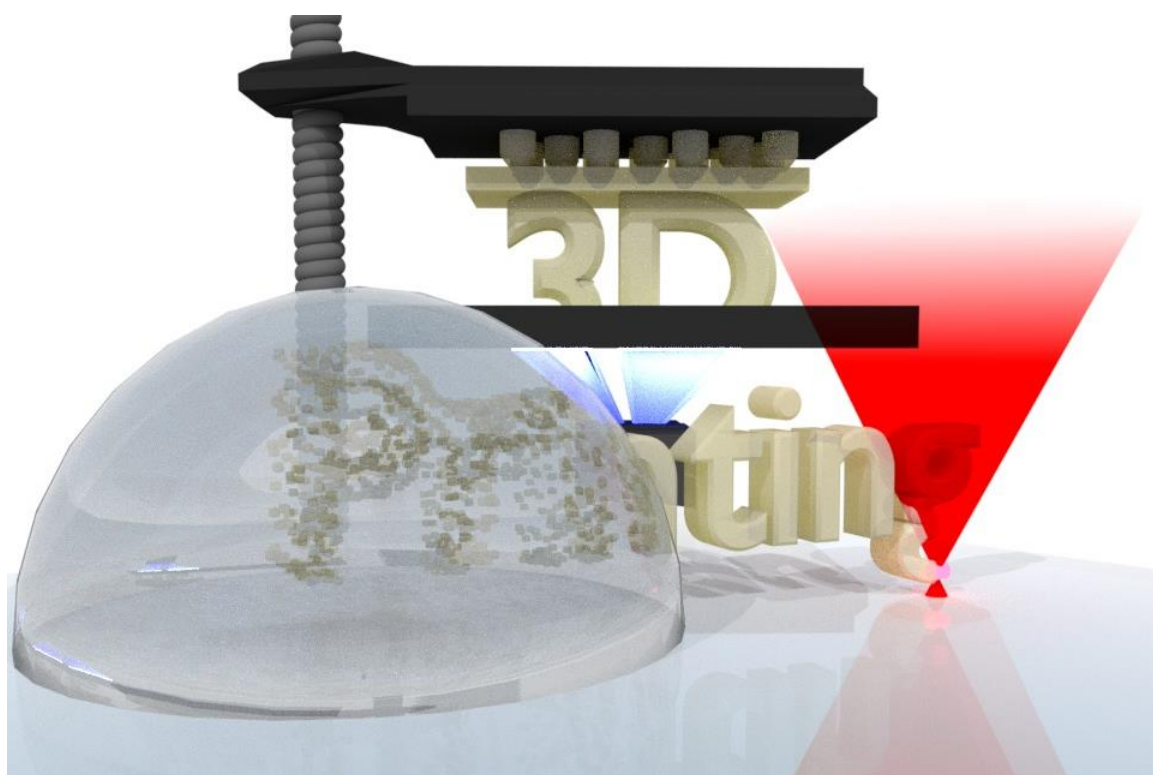


Figure 69: Fundamental idea of a photoresist that is suitable for 3D printing with different techniques such as SLA (back) or DLW (front). In addition, the dimensionally stable objects should be removable via a chemical trigger (drop). Adapted with permission from Ref.[22]. Copyright 2018 John Wiley and Sons.

triggered and selective cleavage without affecting adjacent structures containing different functionalities. In addition, the orthogonal removal of objects in the presence of other cleavable networks was envisaged. The incorporation of structural elements into a scaffold written with standard photoresist would facilitate a variety of compound structures enabling straightforward and precise modification of selected areas without the need to reprint the

complete geometry. Furthermore, mechanical removal of support structures is common for SLA applications, however, this approach is not suitable for DLW due to the size of the objects. Here, chemically removable elements would enable new opportunities.

3.4.1 Reversible Networks via Disulfide Chemistry

Disulfide bridges are broadly used and there are various procedures to perform the cleaving reaction leading to two thiol groups. Due to the cost efficiency, non-toxicity and straightforward handling, aqueous conditions were preferred for first attempts to cleave the phenacyl sulfide-based structures. Employing dithiothreitol (DTT) as the chemical trigger, the printed objects (refer to section 3.3.8) were immersed in an aqueous 1 M DTT solution for 24 h. The removal of the structures was not successful under these conditions and they remained intact (refer to the Appendix, **Figure 105**). It was assumed, that the disulfide networks are not water permeable and therefore, the chemical trigger did not reach functionalities inside the thermoset. To improve the possibility of swelling and diffusion into the structures, the organic solvent dimethylformamide (DMF) was utilized. Light microscopic imaging over time showed the slow cleavage until the full removal in 1 M DTT in DMF solution at approximately 30 °C was achieved (refer to the Appendix, **Figure 106**). The time-lapse study validates a continuous cleavage of the disulfide network. Objects written with IP-L 780 were not affected after exposure to the reaction mixture for 7 h. To obtain an impression of the intermediate structures during cleavage, an identical sample as depicted in **Figure 66** was developed after 2 h employing short rinsing with DMF, 2-propanol and water. The objects were analyzed via SEM (**Figure 70a-b**). The magnification of the residue shows a thin layer of material with partially cleaved and barely visible printed lines. With regard to potential applications, faster removal is desirable. Therefore, the thiol-disulfide exchange reaction was accelerated by the increase of the reaction temperature to 50 °C. A residue-free cleavage for an identical sample was obtained after 15 min (**Figure 70c-d**). After the removal, the surface regains its thiol functionalities and the same spot can be used for the covalent bonding of new phenacyl sulfide-based objects. To ensure that the removal is not originating from mechanical stress introduced by the solvent at higher temperatures, test structures were immersed in DMF at 50 °C for 24 h (**Figure 107**). No significant changes were visible, strongly supporting the cleavage via the thiol-disulfide exchange reaction. In order to extend the chemical triggers

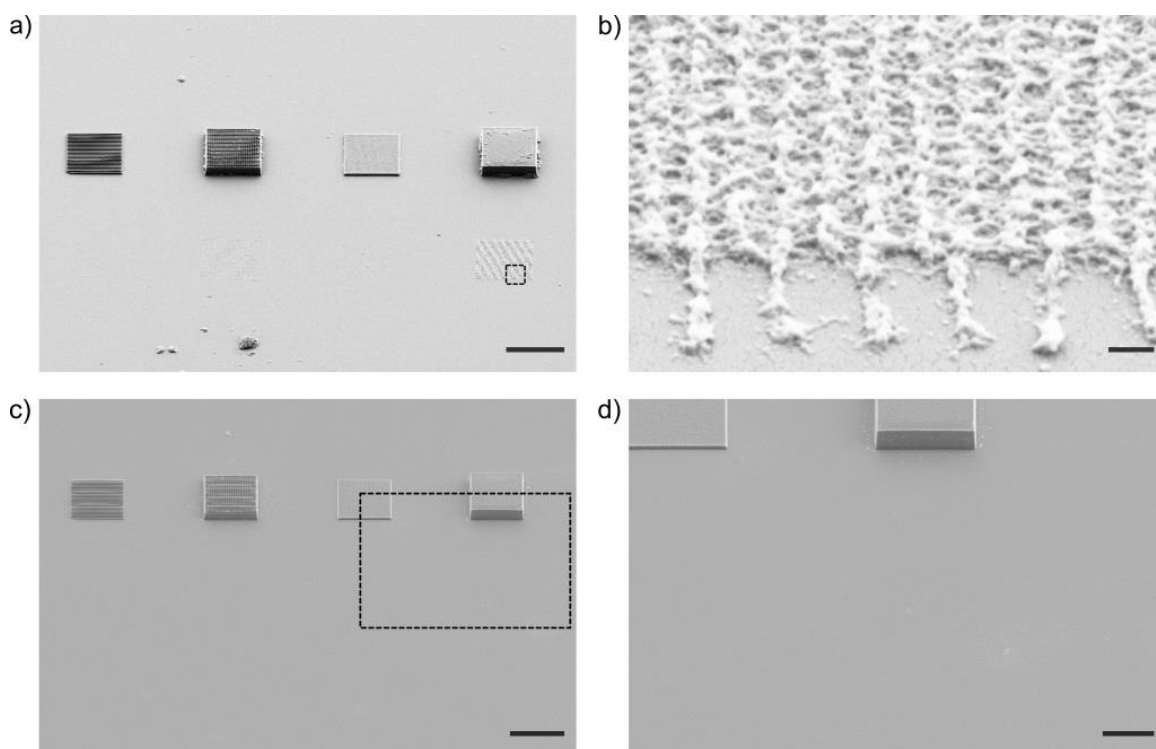


Figure 70: Cleavage of disulfide networks employing 1 M DTT in DMF. a) The sample was heated to 30 °C and was developed after 2 h (scale bar, 20 μm). b) A magnification of the remaining material is depicted (scale bar, 200 nm). c-d) Increasing the temperature to 50 °C, the residue-free removal was achieved after 15 min (scale bars, c, 20 μm , d, 10 μm). Adapted with permission from Ref.[21]. Copyright 2017 John Wiley and Sons.

to remove the disulfide structures, a saturated tris(2-carboxyethyl)phosphine hydrochloride (TCEP HCL) solution in DMF was utilized. In solution, cleavage of disulfide bridges occurs fast, however, the phenacyl sulfide-based structures showed no significant changes after 24 h of immersion (**Figure 108**). Employing the same solvent, it was assumed that TCEP HCL was not able to react or did not even diffuse into the network due to its higher steric hindrance. Employing DTT, an issue for the cleavage were residues that seemed to appear arbitrary. The material seemed to possess an altered chemistry and remained even after longer reaction times (refer to the Appendix, **Figure 109**). Non-cleavable areas originated from the outer layers of printed objects. Lowering the storage times before cleaving experiments and the protection of the samples against higher temperatures than ambient temperature, solved the problem. Therefore, it was assumed that the disulfide bridges on the surface are able to undergo oxidative reactions with atmospheric oxygen resulting in functionalities such as sulfinothiates, disulfoxides and thiosulfonates that change the reactivity towards DTT. Next, the selective removal of structural elements was investigated. To demonstrate this ability, the prior printed boxing-like object was utilized. SEM analysis revealed the selective cleavage of

the horizontal disulfide-based connections (**Figure 71**). The IP-L 780-based scaffold did not show visible changes and repeated modification of the scaffold with structural elements based on the phenacyl sulfide photoresists is possible.

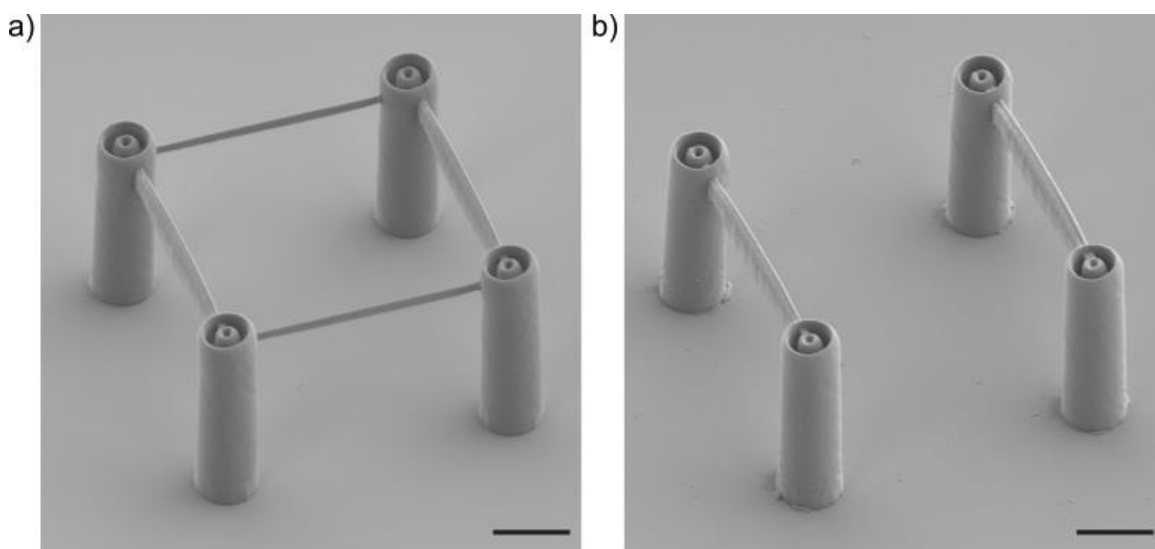


Figure 71: Selective cleavage of phenacyl sulfide-based structural elements. a) The disulfide network was incorporated into a scaffold printed with IP-L 780. b) The residue-free removal was conducted in 1 M DTT solution in DMF at 50 °C for 15 min. Adapted with permission from Ref.[21]. Copyright 2017 John Wiley and Sons.

3.4.2 Cleavage of Radical Thiol-Ene Polymerized Networks

The fabricated structures employing the thiol-ene platform photoresist possessed a variety of functionalities, namely, acetale, carbonate, pyrocarbonate, anhydride and ester groups. To cleave the obtained objects, acidic conditions, amines at increased or ambient temperatures and aqueous conditions were applied. With regard to the aspect ratio, the pyrocarbonate and anhydride photoresist showed a strong increase, which is still under investigation. The removal of the anhydride-based photoresist should readily be feasible in water. However, the permeability of the network was not sufficient and cleavage was only enabled using the organic solvent THF. Partial removal of the printed structures revealed the inhomogeneity of the cured material in the voxel and in its periphery (**Figure 72**). Due to the high aspect ratios

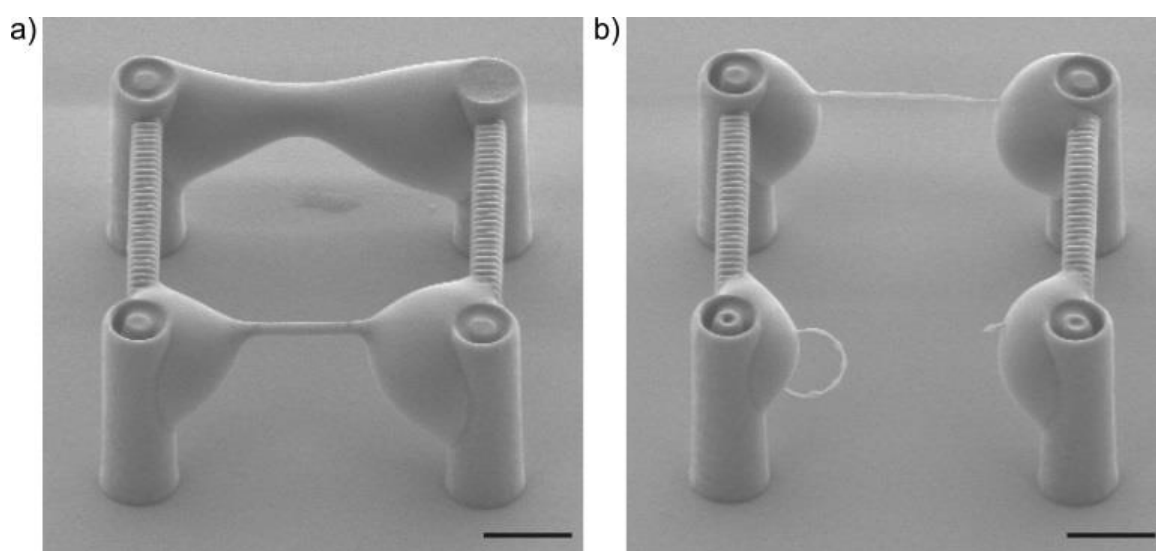


Figure 72: Partial cleavage of the anhydride-based networks in a mixture of THF and H₂O (1 : 1) at 50 °C for 5 minutes. a) Horizontal connections were written employing the thiol-ene photoresist with the 4-pentenoic anhydride linker utilizing a laser power of 10 mW. b) A lower laser power of 7.5 mW was used for the fabrication of the horizontal connections resulting in a lower crosslinking degree and faster cleavage. The scan speed was set to 100 µm/s (scale bars, 5 µm).

and the resulting inhomogeneous networks, the anhydride- and the pyrocarbonate-based networks were not further investigated. Providing good writing properties, the acetale containing networks seemed promising. However, their cleavage was not feasible. Aqueous HCl solutions and mixtures with organic solvents such as DMF did not lead to the cleavage of the printed objects. It was assumed that positively charged species are not able to diffuse into the networks and therefore the acetale functionalities remain intact. In addition, an interaction of the residual thiol groups could form crosslinks with the acetales during cleavage forming mono- and dithioacetals. Next, the diallyl carbonate containing materials, cured

with a hand UV lamp, were immersed in an aqueous 1 M ethanolamine solution. No cleavage was observed and the solvent was exchanged with DMF. The removal of the structures was achieved after approximately 8 h at 50 °C. However, utilizing the divinyl adipate containing, ester-based photoresist, the cleavage of material cured with a hand UV lamp and 3D printed structures employing SLA technology, was achieved after 7 h at 50 °C. FT-IR analysis of the dried residue after removal was performed and compared with the measurement of the printed material (**Figure 104**). The comparison revealed a decrease of the signals that are characteristic for saturated ester functionalities and new bands indicated emerging amide moieties. Therefore, the aminolysis of ester groups in the network with the chemical trigger ethanolamine was suggested to lead to the cleavage. Smaller influence could also stem from ester-transfer reactions. Due to the lower aspect ratio which is essential for small feature sizes and the higher cost efficiency, the divinyl adipate containing photoresist was investigated in

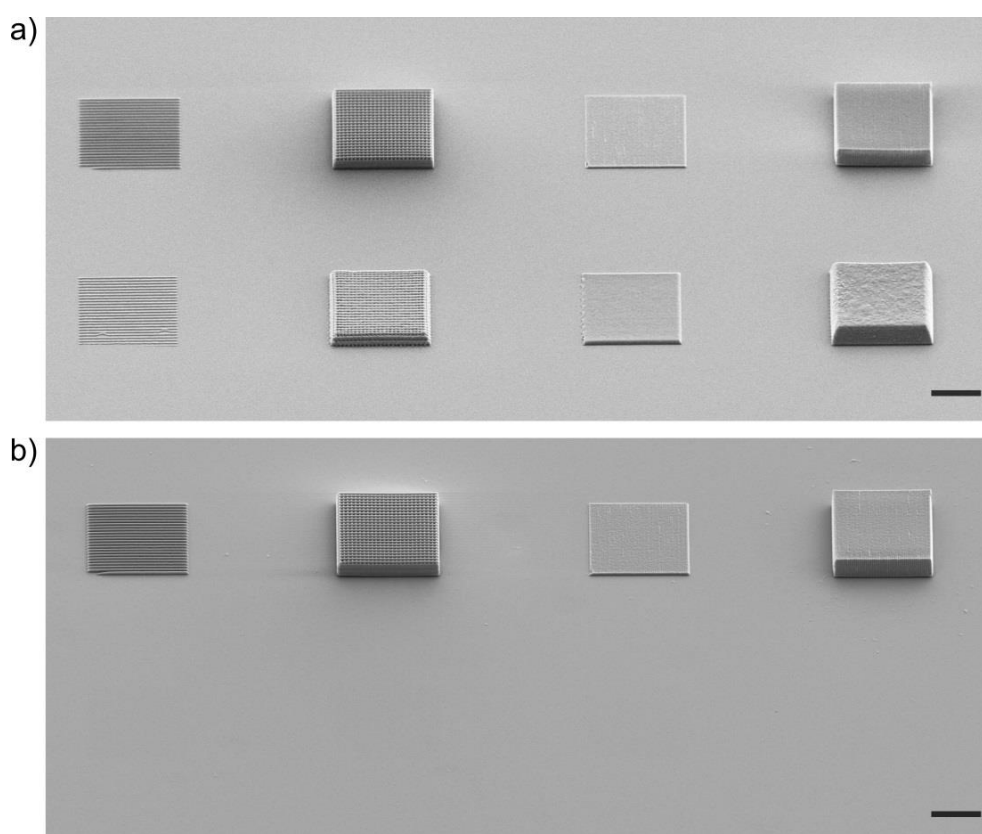


Figure 73: Selective removal of divinyl adipate-based networks. a) Identical standard photoresist (IP-L 780) structures served as control structures (upper row). Utilizing the divinyl adipate containing photoresist, resulting networks consist of thioether and ester-bonds (bottom row). b) The residue-free cleavage was achieved employing 1 M ethanolamine solution in DMF at 50 °C for 20 h (scale bars, 10 μ m). Adapted with permission from Ref.[22]. Copyright 2018 John Wiley and Sons.

depth. To obtain a better understanding of the processes, a sample with the prior used test DLW structures was analyzed via light microscopy as a function of time (**Figure 110**). The images validated a continuous process and only small amounts of material remained after a reaction time of 15 h in 1 M ethanolamine solution in DMF. In addition, identical test structures written with IP-L 780 were fabricated adjacent to the divinyl adipate-based objects. Two identical samples were analyzed before and after cleavage via SEM (**Figure 73**) employing 1 M ethanolamine solution in DMF for 20 h. Higher crosslinking degrees and better homogeneity result in a decelerated diffusion inside the network and, therefore, the required time for complete removal increased for the DLW objects compared to the material cured with a hand UV lamp. However, SLA printed structures require a shorter duration for cleavage (refer to **Figure 75**). Next, the prior printed compound boxring-like objects with incorporated divinyl adipate-based structural elements were immersed in 1 M ethanolamine solution in DMF for 20 h (**Figure 74**). A residue-free removal was achieved (**Figure 74b**). The connection points of the two materials revealed a small change in the geometry of the spiral for the divinyl

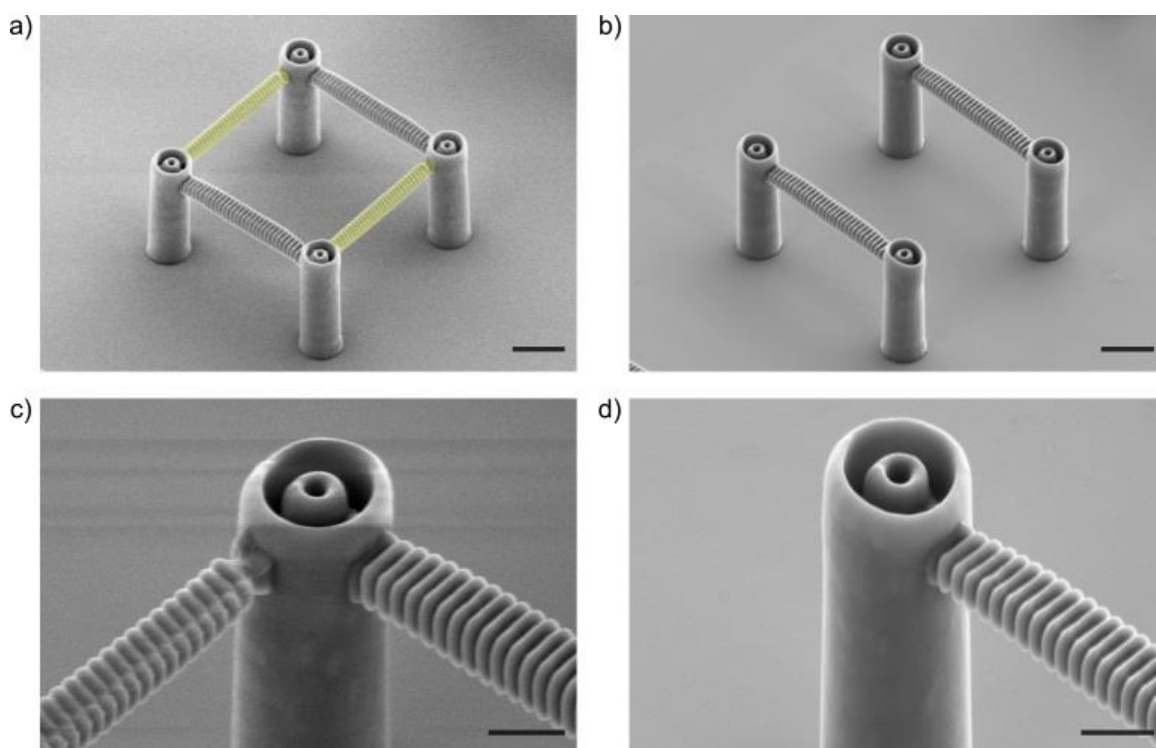


Figure 74: Selective cleavage of structural elements incorporated into a scaffold written with IP-L 780. a) Highlighted connections were printed with the divinyl adipate-based thiol-ene photoresist. b) Residue-free removal was achieved after 20 h in 1 M ethanolamine solution in DMF (scale bars, 5 μm). Magnification of the connection point between thiol-ene and acrylate-based material before (c) and after (d) cleavage reveals a perfectly intact scaffold after the selective removal (scale bars, 2 μm). Adapted with permission from Ref.[22]. Copyright 2018 John Wiley and Sons.

adipate containing photoresist. To ensure that the structures written with IP-L 780 were not affected during incorporation, the area was magnified before and after removal of the structural element revealing a fully intact surface of the scaffold (**Figure 74c-d**). The repeated modification with new removable structural element to, for instance, optimize the geometry of a certain area without the need to print the whole object again could be beneficial for large structures or where multi-step procedures are required for the fabrication. In addition, unique samples could be reused several times via the use of cleavable photoresist. Mistakes during the writing process could be easily 'erased' and printed again.

3.4.3 Selective and Orthogonal Removal of Objects Printed via SLA

To demonstrate the versatility and broad applicability of the commercially available thiol-ene photoresist, SLA was utilized to fabricate macroscopic objects (refer to section 3.3.13). The removal was performed employing the same conditions used to cleave the DLW structures: 1 M ethanolamine in DMF at 50 °C. Tracking of the progress was conducted with a time-lapse setup. A camera (Lumix DMC-FZ1000, Panasonic Corporation) was installed to take a picture every 3 min. To demonstrate the selective cleavage, control structures printed with the commercially available photoresist (Visijet FTX green, 3D systems, U.S.) were placed adjacent to the divinyl adipate-based structures. The resulting images during removal were summarized in a time-lapse movie.^[22] In addition, selected time spots are depicted in **Figure 75** to illustrate the process. A distinctive swelling behavior was observed and was more pronounced compared to the control sample in pure DMF at 50 °C without the chemical trigger ethanolamine (**Figure 112**). The continuous cleavage of ester bonds led to a complete and residue-free removal after 7 h. No significant change was obtained for the control sample,

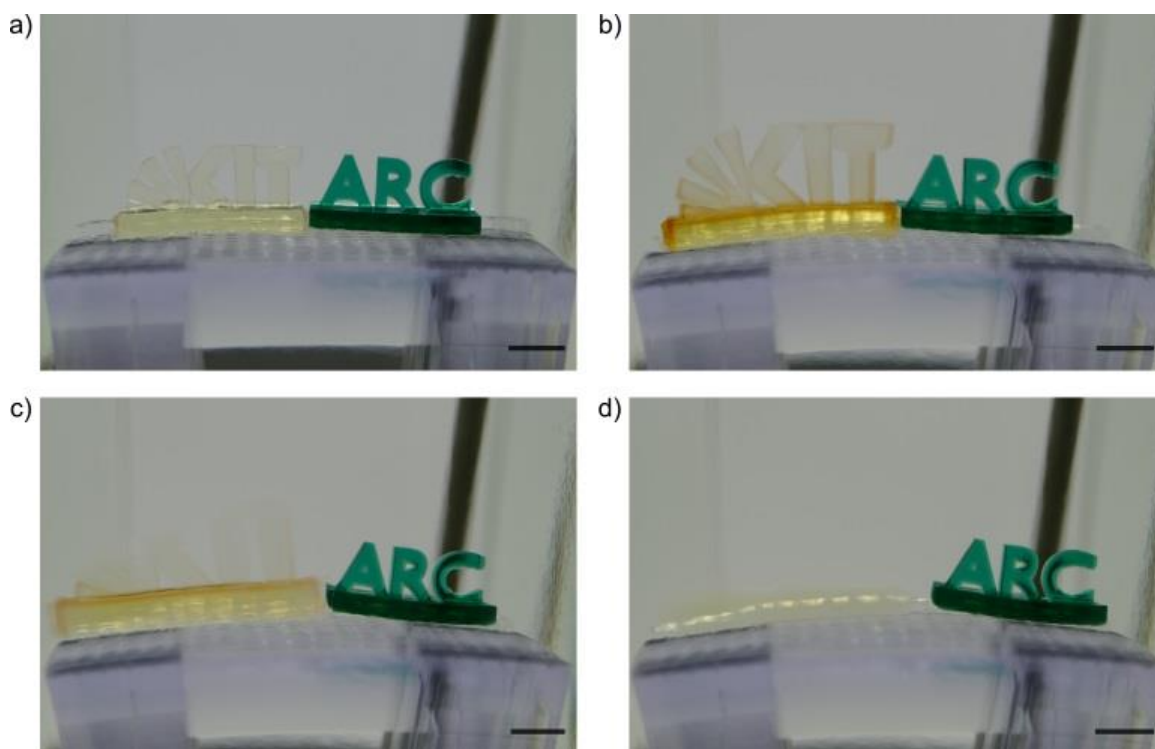


Figure 75: Selective cleavage of SLA printed divinyl adipate-based networks. A control structure (green) was fabricated utilizing a commercially available photoresist (Visijet FTX green, 3D systems, U.S.). The removal was conducted in 1 M ethanolamine solution in DMF at 50 °C and the images were taken as a function of time directly after immersion (a), after 2 h (b), 4 h (c) and after 6 h (d) (scale bars, 5 mm). Adapted with permission from Ref.[22]. Copyright 2018 John Wiley and Sons.

which only revealed a small bend of its platform. To enable orthogonal cleavage, the chemical trigger had to vary or the control over the permeability had to be achieved. Employing the same reactant for the removal, the used solvent determined which structure will be cleaved. The cleavage under aqueous conditions was not achieved for the phenacyl sulfide and divinyl adipate-based networks. Therefore, a photoresist containing ionic moieties (3.3.12) was utilized and the fabricated structures via SLA revealed a distinct water permeability. To track the processes during removal with aqueous 1 M ethanolamine solution, images were taken as a function of time (**Figure 76**). Containing all taken images, a time-lapse movie was recorded.^[22] The control structures showed no significant changes. To explain the yellowing of the divinyl adipate-based structure (QUT), reactions on the surface of the material, where permeability did not hinder diffusion of the chemical trigger, were assumed. The analysis revealed the shrinkage of the ionic structures during cleavage, while the prior cleaved divinyl

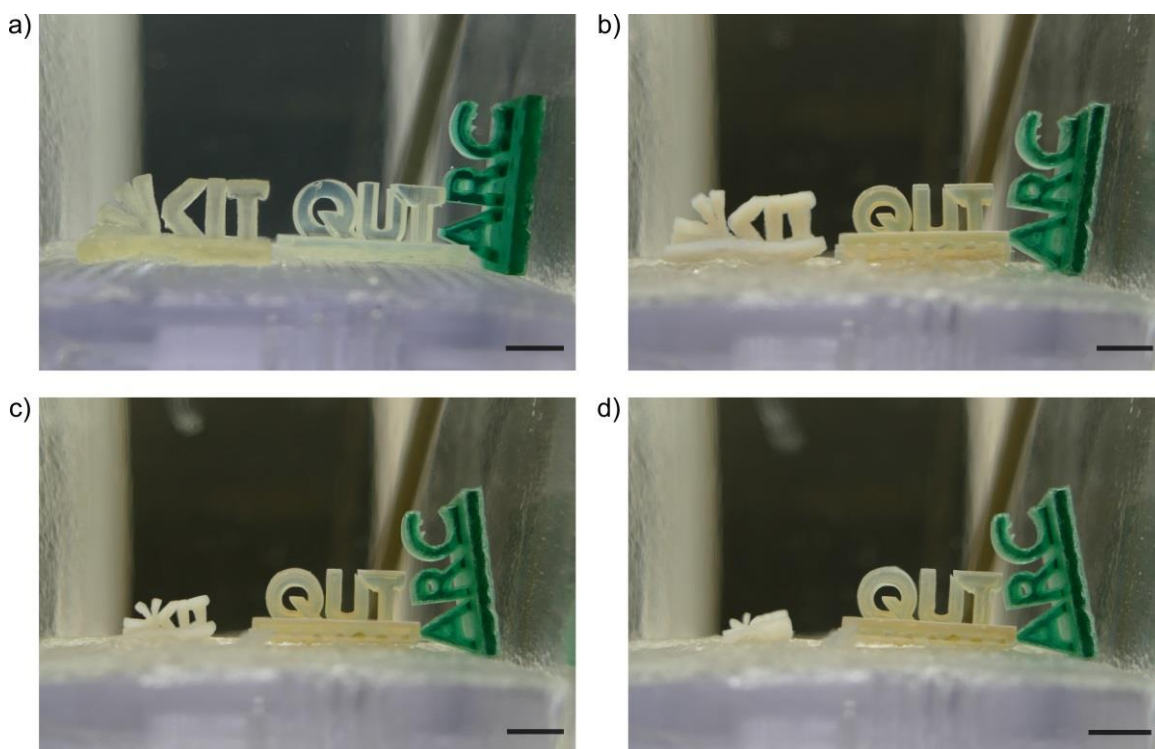


Figure 76: Orthogonal cleavage of objects printed via SLA, utilizing radical thiol-ene polymerization. The “KIT” object was fabricated using a photoresist with covalently bond ionic moieties, while the prior used divinyl adipate-based system was employed for the “QUT”. To enable the comparison with a commercially available photoresist (Visijet FTX green, 3D systems), a control structure “ARC” was added. The samples were immersed in aqueous 1 M ethanolamine solution at 50 °C and images were taken as a function of time: 0 h (a), 20 h (b), 40 h (c) and 50 h (d) (scale bars, 5 mm). Adapted with permission from Ref.[22]. Copyright 2018 John Wiley and Sons.

adipate-based structures showed a distinct swelling behavior in DMF. Both photoresists utilizing radical thiol-ene polymerization and should not have shown large deviations in their crosslinking degrees. Therefore, it was assumed that the employed solvent and the corresponding permeabilities of the networks played the crucial role. Choosing the right solvent or solvent-mixtures, objects should stay perfectly intact until late stages of the removal process. With regard to cleavable structures that are intended to support other elements during their fabrication, it would be beneficial that no mechanical stress due to swelling or shrinkage occurs. In addition to the new opportunity of orthogonal cleavage, the provision of a photoresist that contains ionic moieties is envisaged to enable bio-orthogonal removal in aqueous conditions of structures in the future. The immobilization of cells on 3D printed structures, for instance, would be reversible via removal of the scaffold after cultivation allowing for the release of the cells.

3.4.4 Accessing New 3D Geometries via Cleavable Elements on the Microscale

Fabrication of complex geometries with overhangs and freely suspended elements often require the utilization of additional so called support structures. In macroscopic printing techniques, the additionally cured material is removed mechanically to obtain the final product (**Figure 77**). Furthermore, residues can be sanded off to obtain an improved surface

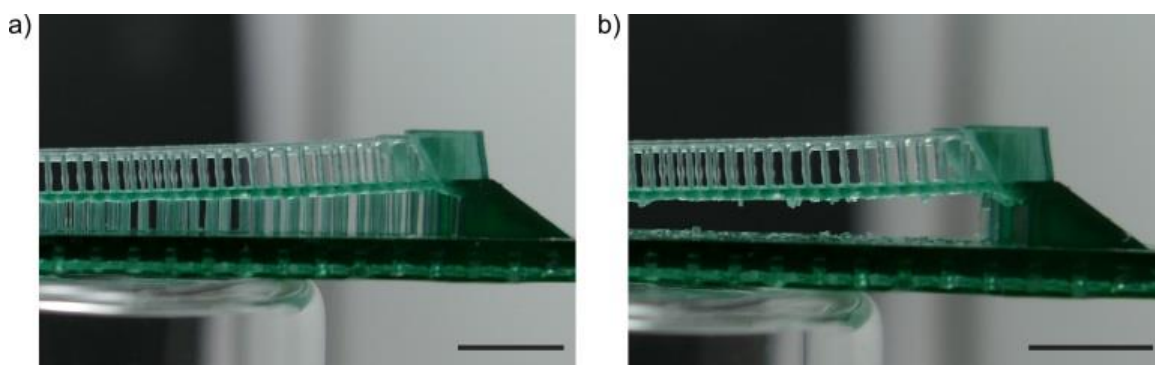


Figure 77: Support structures enable freely suspended geometries in SLA. a) The supportive elements are added as thin pillars underneath the object and remain after printing. b) To access the final structure, the support structures are removed mechanically and surfaces can be sanded off to obtain a better finish (scale bars, 5 mm). Adapted with permission from Ref.[22]. Copyright 2018 John Wiley and Sons.

finish. However, microscopic structures are not accessible to the mentioned mechanical techniques. To still enable the use of support structures, their removal has to be modified. Utilizing materials, that can be cleaved on demand employing a chemical trigger, circumvents the need of mechanical interaction with the product. The network of the desired product has to remain unaffected. To demonstrate the straightforward usage of our cleavable divinyl adipate-based photoresist, a rope bridge with a length of 400 μm was selected, which is inaccessible without the implementation of support structures. It was divided in the middle into two parts with an overlap of 1 μm , which is caused by a writing window limited to a circular area with a diameter of approximately 250 μm . Attempts to print the object without supportive elements revealed the deformation of the structure (**Figure 78**). Internal stress resulted in a pronounced upwards bend of freely suspended areas, which was varying with the employed laser power (refer to the Experimental Section, **Figure 111**). In addition, movement of the stage in lateral direction often leads to mechanical forces that displace freely suspended or fine structures. Therefore, the cleavable divinyl adipate-based photoresist was utilized and a supportive element was placed underneath the rope bridge at

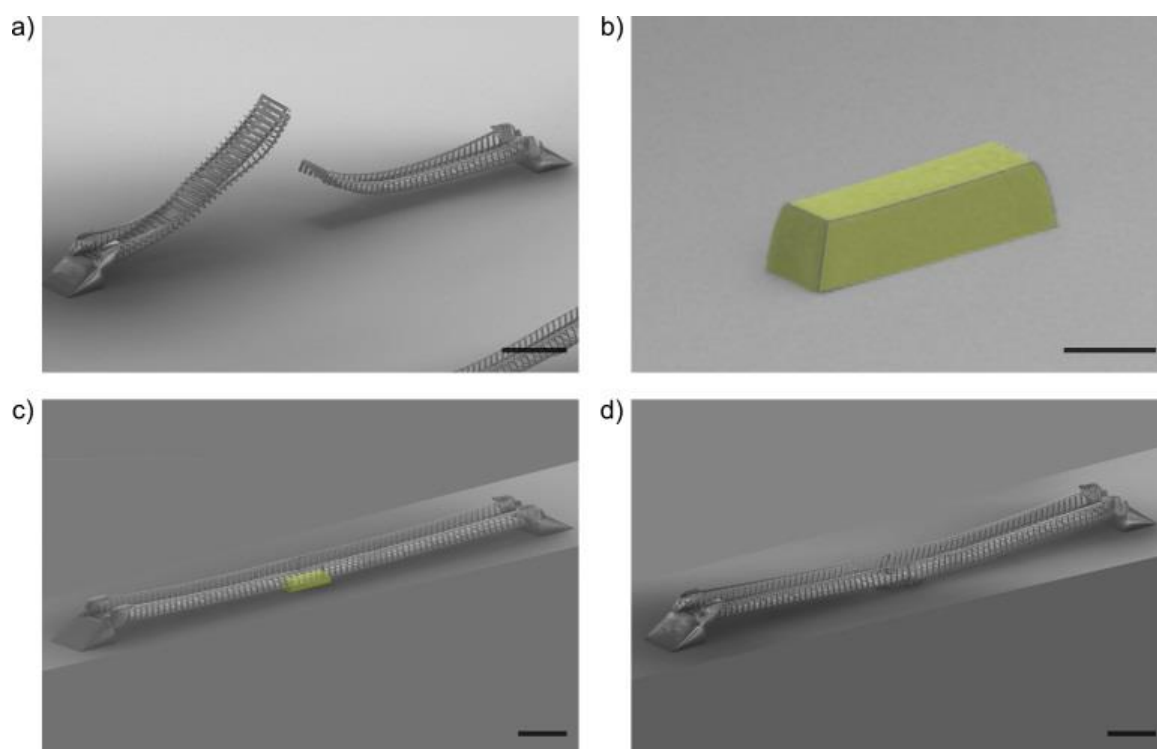


Figure 78: Fabrication of a freely suspended rope bridge via DLW. a) The object was printed employing IP-L 780 without additional supportive elements (scale bar, 40 μm). b) A support structure was fabricated with the divinyl adipate containing photoresist (scale bar, 10 μm). c) The cleavable element was placed in the middle of the bridge and the desired object was received. d) To cleave the support structure, the object was immersed in 1 M ethanolamine solution in DMF at 50 $^{\circ}\text{C}$ for 20 h (scale bars, 40 μm). Adjacent objects were greyed out for reasons of clarity and are provided in the Experimental Section (**Figure 113**). Adapted with permission from Ref.[22]. Copyright 2018 John Wiley and Sons.

the connection point of the two parts. It enabled the fixation of the first half of the rope bridge and internal stress did not lead to any deformation. The connection of the second half after the movement of the stage was successful and the desired object was achieved. To remove the support structure, the object was immersed in 1 M ethanolamine solution in DMF at 50 $^{\circ}\text{C}$ for 20 h. After the cleavage, the varying internal stress of the structures for differing laser powers was observed (refer to the Experimental Section, **Figure 113**). However, the rope bridge printed with 22.5 mW revealed no deformation after removal of the supportive element. Therefore, support structures that are cleavable on demand upon a chemical trigger, expand the range of accessible geometries in DLW.

4

Concluding Remarks and Outlook

Within the present thesis, the design of a functional 2D monomolecular coating technology based on catechol chemistry and the provision of phenacyl sulfide and thiol-ene photoresists for the fabrication of on demand cleavable 3D structures on the micro- and macroscale are demonstrated.

First, by mimicking the chemistry used for the exceptional ability of mussels to adhere to a wide range of surfaces, a novel system enabling the coating and the post-modification of metallic and metal oxide substrates was investigated. The synthesis of a multifunctional catechol species was facilitated in a straightforward reaction pathway without the need of complex purification steps. Overall, the provision of the material was possible in a two-step reaction obtaining the product after extraction with ethyl acetate. Predominately cyclic species with up to 32 catechol units were clearly detected. The cyclic catechol material (CyCat) was further investigated regarding the processes in a slightly alkaline solution also used for coatings via polydopamine (PDA). The formed aggregates were examined thoroughly and showed parallels in particle sizes to the underlying chemistry of PDA ad-layers in solution. However, the investigation of the CyCat coated surfaces revealed no incorporation of larger moieties or particles into the final structure, which is a clear prerequisite for the formation of thin films. In addition, the monomolecular CyCat coating showed a defect-free immobilization that perfectly replicates the underlying topography of the employed substrates Au, SiO₂, and

TiO₂, respectively. To demonstrate the accessibility of remaining catechol units, post-modifications were conducted. The attachment of small molecules via Michael addition and Schiff base formation utilizing amine functionalized moieties exhibited the facile change and expansion of the surface chemistry. In order to prove the robustness of the formed monomolecular layers towards species with higher molecular weights, an amine functionalized PEG derivative was successfully attached. Next, a multifunctional moiety was used for a layer-by-layer approach to facilitate multilayer assemblies. After six cycles of an alternating dipping procedure in a CyCat and a multifunctional amine containing solution, stable coatings with increased thicknesses and remaining amine groups on top of the surface were achieved. The multilayers enabled additional pathways for post-modification. To demonstrate the accessibility of the primary amines on the coatings, small organic compounds were successfully immobilized. The usage of a photoactive tetrazole derivative allows the patterning of the surface via light. Attachment of an ATRP initiator facilitated the growth of polymers in a “grafting-from” fashion and validated the stability of the multilayer assembly. The photoinduced immobilization of polymers in a “grafting-to” approach was conducted with a phenacyl sulfide functionalized derivative.

The provision of functional 2D coatings and functional 3D photoresists is of high interest in various fields of application. The presented monomolecular CyCat-based coating technology was investigated extensively. However, the transfer to other surfaces and the combination with varying chemistries remain a key element to fully examine the potential of the ultrathin films. The assessment of the stability towards organic solvents and mechanical impact has to be performed as well. For application in a biological environment such as the coating of implants, the toxicity and biocompatibility of the system has to be determined. Utilizing the remaining thiol groups of the phenacyl sulfide and thiol-ene based 3D structures, the facile post-modification of DLW and SLA fabricated objects might be feasible in a simple fashion. In addition, the use of CyCat during the development of thiol-containing structures could minimize or completely eliminate shrinkage increasing the density and stability of 3D printed objects.

In addition, highly defined structuring of surfaces on the micro- and nanoscale was achieved via DLW. Thus, a newly synthesized tetrafunctional phenacyl sulfide linker (PSL) enabled the formation of a cleavable network with disulfide bridges as crosslinks. To ensure a high

accessibility, the synthesis was optimized to obtain the final product in a one-step procedure. The desired reactivity of the multifunctional molecule was validated in a small molecule test by the end-capping with monofunctional thiols after the photoactivation of the phenacyl sulfide groups. Employing a commercially available tetrathiol and the solvent sulfolane, the provision of a photoresist that exhibited stable writing conditions over several hours was achieved. To activate the photoreactive moieties, a femtosecond laser emitting at a wavelength of 700 nm in a 2PA process was utilized on a custom-built DLW setup. The investigation of the lateral resolution revealed well-separated rods with a grating period of 300 nm. To demonstrate the versatility of the system, complex woodpile-type structures, line arrays, layers and blocks were printed. Validating the stability of the obtained objects, the samples were immersed in DMF at 50 °C for 24 h, revealing no significant changes. In addition, the successful incorporation of the disulfide-based network into scaffolds written with a standard acrylate photoresist facilitated the fabrication of compound structures. To assess the reversible disulfide bridges in the networks, the samples were immersed in a 1 M DTT solution in DMF. The residue-free and selective cleavage was achieved via a thiol-disulfide exchange reaction at 50 °C after 15 min. Importantly, the remaining acrylate-based structures were not affected by the employed conditions.

Taking into account that the users of laser lithographic applications comprise many non-chemists, the provision of a photoresist entirely based on commercially available components is of high interest. Furthermore, the utilization of commercially available setups is important. The known chemistry of radical thiol-ene polymerization was investigated accessing a variety of double bond containing linker moieties. The photoresist mixtures were employed in DLW and the fabricated structures were examined with regard to their aspect ratios. The divinyl adipate-based photoresist revealed the best writing conditions comprising cost-efficient components. Verifying the good performance of the system, woodpile-type structures, line arrays, layers and blocks were fabricated. In addition, the thiol-ene networks were incorporated into a scaffold utilizing a standard acrylate-based polymerization mechanism. Due to the good availability of all components, the provision of larger amounts of photoresist was readily accessible and macroscopic SLA 3D printing was performed, demonstrating the straightforward transfer of the system from the micro- to the macroscale. The samples utilizing the divinyl adipate-based thiol-ene photoresist were cleavable via aminolysis in a 1 M ethanolamine solution in DMF at 50 °C. To further extend the applicability, the usage of aqueous conditions during the cleavage was examined. Therefore, a charged group, i.e.,

ammonium chloride, was selected as the core of the double bond linker. This modification enabled the water penetration of the resulting SLA structures. In addition to the now feasible cleavage in aqueous conditions, orthogonal removal of the ionic and the divinyl adipate-based networks was demonstrated. However, the utilization of the ionic photoresist for DLW was not feasible and the processing window was significantly reduced.

To demonstrate the full potential of the cleavable 3D printed networks, the transfer to applications for 2D structuring of globally deposited material and the fabrication of complex 3D geometries have to be examined. The utilization of the facile cleavage employing mild conditions could render other techniques unnecessary that require harsh conditions for the removal of printed material. In addition, the selective cleavage of the phenacyl sulfide and thiol-ene based photoresists have to be demonstrated. Next, the defined structuring of deposited material on a surface and the global release of the structure into the solution would be feasible by the global coating with one of the cleavable photoresists and the structuring with the other. Consecutive removal of, first, the structuring material would provide the 2D geometry and, second, the cleavage of the global coating would release the material into the solution. The obtained 2D materials could be transferred to other surfaces enabling a wide variety of applications. Additionally, the successful incorporation of the disulfide and thiol-ene based networks into scaffolds written with a standard acrylate photoresist opens new avenues for the fabrication of compound structures. The fabrication of complex objects with selective cleavable structural elements would enable an iterative fine-tuning without the need to print the entire object several times.

The demonstration of a material that can be cleaved in aqueous conditions is the first step towards a bioorthogonal cleavable system. The fundamental idea of the incorporation of an ionic group has to be transferred to a photoresist system that offers more stable writing conditions and a sufficient processing window. In addition, the use of bioorthogonal cleaving components such as the amine bearing amino acid lysine have to prove their suitability to trigger the cleavage. However, the transfer to cleavable photoresist that require milder conditions, a small change in the pH value for instance, could be beneficial. These investigations could further lead to the fabrication of 3D environments for cell studies. After successful immobilization and modification of cells, the release into the medium could be facilitated by simply cleaving off the connection points to the scaffolds.

5

Experimental Section

5.1 Materials

Acetic acid (100 %, Roth), acetone (p.a., VWR), chloroform (p.a., VWR), diethylether (p.a., VWR), magnesium sulfate (> 99 %, Roth), ethanol (EtOH, U.V. spectroscopy grade, Lach-ner), methanol (p.a., VWR), sodium bicarbonate (> 99 %, Roth), sodium chloride (> 99.8 %, Roth), sulfuric acid (> 95 %, Roth), tetrahydrofuran (p.a., VWR), tris(2-aminoethyl)amine (TREN) (≥ 99 %, Sigma-Aldrich), *ortho*-dimethoxybenzene (99 %, Sigma-Aldrich), aqueous formaldehyde solution (37 %, Sigma-Aldrich), dichloromethane (99.8 %, VWR), boron tribromide (99.9 %, Sigma-Aldrich), 2-Chloroacetophenone (98 %, Sigma-Aldrich), cyclohexane (p.A., VWR), dichloromethane (DCM, p.A., VWR), N,N-diisopropylethylamine (DIPEA, ≥ 99 %, Sigma-Aldrich), dimethylformamide (DMF, p.a., VWR), ethyl acetate (p.A., VWR), IPL 780 (Nanoscribe), magnesium sulphate hydrate (≥ 99 %, Roth), (3-mercaptopropyl)trimethoxysilane (95 %, Sigma-Aldrich), O-(2-mercaptoethyl)-O'-methylhexa(ethylene glycol) (≥ 95 %, Sigma-Aldrich), pentaerythritol tetrakis(2-mercaptoacetate) (>90 %, TCI Chemicals), pentaerythritol tetrakis(2-mercaptopropionate) (>95 %, Sigma-Aldrich), sodium trifluoroacetate (98 %, Sigma-Aldrich), tetrahydrothiophene 1,1-dioxide (>99 %, TCI Chemicals), 3-(trimethoxysilyl)propyl methacrylate (98 %, Sigma-Aldrich), triethylamine (TEA, 99 %, Acros), acetophenone (p.a., VWR), diallylcarbonate (99%, Sigma-Aldrich), diallyldimethylammonium chloride (≥ 97 %, Sigma-Aldrich), dimethylformamide (DMF, p.a., VWR), divinyl adipate (>99.0%, TCI Chemicals), ethanolamine (≥ 98 %, Sigma-

Aldrich), 1,8-nonadiyne (98%, Sigma-Aldrich), pentaerythritol tetrakis(3-mercaptopropionate) (>95%, Sigma-Aldrich), phenylbis(2,4,6-trimethylbenzoyl)phosphine oxide (97%, Sigma-Aldrich), propylene carbonate (99%, Sigma-Aldrich), pyrogallol ($\geq 99\%$, Sigma-Aldrich), 3-(trimethoxysilyl)propyl methacrylate (98%, Sigma-Aldrich), vinylphosphonic acid (97%, Sigma-Aldrich), chloroform-d₁ (99.8%, EURISO-TOP), dimethyl sulfoxide-d₆ (99.8 %, EURISO-TOP). Deionized water was obtained from a Milli-Q water purification system (Merck-Millipore). All chemicals were used without further purification.

5.2 Characterization Methods and Instrumentation

Nuclear Magnetic Resonance (NMR) Spectroscopy. Proton nuclear magnetic resonance (¹H NMR) spectra were recorded on a Bruker AM 400 (400 MHz) spectrometer. Chemical shifts are expressed in parts per million (ppm) and calibrated on characteristic solvent signals as internal standards. Carbon nuclear magnetic resonance (¹³C NMR) spectra were recorded on a Bruker AM 400 (101 MHz) spectrometer.

Electrospray Ionization-Orbitrap Mass Spectrometry (ESI MS). High-resolution mass spectra (HRMS) were achieved via electron spray ionization mass spectrometry utilizing a Q Exactive (Orbitrap) mass spectrometer (Thermo Fisher Scientific, San Jose, CA, USA) equipped with a HESI II probe. Calibration of the instrument was carried out in the m/z range of 74 – 1822 Th using calibration solutions from Thermo Scientific. The FT resolution was set to 140 000 employing 3 microscans during an acquisition time between 2 and 3 min measuring. The spray voltage was set to 4.7 kV and a dimensionless sheath gas flow of 5 was applied. The capillary temperature was set to 320 °C and the S-lens value was set to 62.0. The injection was performed with a flow rate of 5 μLmin^{-1} .

Matrix assisted laser desorption ionization – time-of-flight mass spectrometry (MALDI-TOF). Spectra were recorded on a Bruker Autoflex III with an acceleration voltage of 20 kV and a neodymium-doped yttrium aluminum garnet (Nd:YAG) (tripled) 355 nm laser. The matrix material consisted of 2,5-dihydroxybenzoic acid (DHB) dissolved in THF with a concentration of 20 g L⁻¹ and the samples dissolved in methanol with a concentration of 4 g L⁻¹ and crystallized in a ratio of 10:1 (matrix:sample). The time of flight mode was set to linear mode.

Dynamic light scattering (DLS). Samples were prepared by dissolving CyCat (1 mg mL^{-1}) in an aqueous 0.1 M NaHCO_3 solution. The solution was filtered after 15 min through a $0.2 \text{ }\mu\text{m}$ syringe filter to remove dust particles. To determine the hydrodynamic diameters via DLS, a Nicomp 380 DLS instrument from Particle Sizing Systems (Santa Barbara, USA, laser diode: 90 mW , 639 nm) was employed. Measurements were carried out in automatic mode. A standard Gaussian in combination with an advanced method (inverse Laplace algorithm for multimodal distributions) was used to obtain the weight intensity and number-weighted average values calculated in the NICOMP evaluation. The angle related to the incident beam was 90° .

X-Ray photoelectron spectroscopy (XPS) measurements were performed using a K-Alpha⁺ XPS spectrometer (ThermoFisher Scientific, East Grinstead, UK). All the samples were analyzed using a microfocused, monochromated Al K_α X-ray source ($400 \text{ }\mu\text{m}$ spot size). The kinetic energy of the electrons was measured by a 180° hemispherical energy analyzer operated in constant analyzer energy mode at pass energy of 200 eV for survey and of 50 eV for high-energy resolution core-level spectra. The X-ray angle of incidence was 30° and the emission angle was normal to the surface. The K-Alpha charge dual compensation system was employed during analysis, using electrons and low-energy argon ions to prevent localized charge build-up. Data acquisition and processing using the Thermo Avantage software are described elsewhere.^[205] The spectra were fitted with one or more Voigt profiles (binding energy uncertainty: $\pm 0.2 \text{ eV}$). The analyzer transmission function, Scofield sensitivity factors^[206] and effective attenuation lengths (EALs) for photoelectrons were applied for quantification. EALs were calculated using the standard TPP-2M formalism.^[207] All spectra were referenced to the C 1s peak attributed to sp^2 carbon of the CyCat at 284.2 eV binding energy, which was controlled by means of the well-known photoelectron peaks of Cu, Ag, Au and poly(ethylene terephthalate) standards.

UV-Vis Spectroscopy. UV-Vis spectra were recorded on an OceanOptics USB4000 spectrometer with a USB-ISS-UV-Vis detecting unit. The measurement interval ranged from 200 to 800 nm with a resolution of 1 nm and slit width of 2 nm in a precision cell made of quartz SUPRASIL from HELLMA with a light path of 2 mm .

Spectroscopic ellipsometry. Ellipsometric data were acquired using a spectroscopic ellipsometer M2000 (J.A. Woollam Co., USA) working in rotating compensator mode. All

measurements were performed in the wavelength range of 245–1000 nm (source: Xe arc lamp) at angle of incidence AOI = 55 °–75 ° (AOI increment 5 °). The obtained data were analyzed with the CompleteEASE software. The thickness of layers and their corresponding optical dispersion functions were obtained from simultaneous fitting using Cauchy ($n = A_n + \frac{B_n}{\lambda^2}$) and Urbach equations ($k = \alpha e^{\beta(1240(\frac{1}{\lambda} - \frac{1}{\gamma}))}$). ($A_n = 1.460$, $B_n = 4330$ [nm²], $\alpha = 0.073$, $\beta = 0.719$ [eV], $\gamma = 400$ [nm] for ultrathin CyCat films; $A_n = 1.460$, $B_n = 1000$ [nm²], $\alpha = 0.084$, $\beta = 0.907$ [eV], $\gamma = 400$ [nm] for CyCat multilayer assembly films). Predefined optical dispersion functions of gold, silicon, titanium, silicon dioxide and titanium oxide were used to model the optical parameters of the corresponding substrates.

Surface plasmon resonance spectroscopy (SPR). SPR was used to follow the attachment of the CyCat on gold-coated surfaces in real time, using an instrument custom-built at the Institute of Photonics and Electronics (Czech Republic). The sensor is based on the Kretschmann geometry (attenuated total reflection) and wavelength interrogation of the resonance conditions. The increase in deposited mass on the surface is detected by the increment in refractive index at the gold-dielectric interface, which causes a shift in the resonance wavelength of the incident light. All solutions were flowed over the surface placed in a flow cell using a peristaltic pump at a rate of 25 $\mu\text{L mL}^{-1}$. Firstly, a baseline was established by flowing a 0.1 M solution of NaHCO₃ in water. Subsequently, the solution was replaced for an aqueous solution of CyCat (1 mg mL⁻¹) and 0.1 M NaHCO₃. After 45 min, the flowing solution was replaced again for aqueous 0.1 M NaHCO₃.

Scanning probe microscopy. Scanning probe microscopy was performed in atomic force and Kelvin probe force microscopy modes. AFM measurements were performed on a Keysight 5500 system using rotated monolithic Multi75Al-G silicon probes (BudgetSensors) with nominal spring constant of 3 N·m⁻¹ and tip radius of 10 nm. All AFM measurements were performed at 1 Hz scanning rate. KPFM measurements were performed on an Asylum research MFP-3D system utilizing conductive Cr/Pt coated ElectriMulti 75-G silicon probes (BudgetSensors) with a nominal spring constant of 3 N·m⁻¹ and tip radius of 25 nm. The 2-pass regime^[208] was used to detect electric potential shifts on HOPG carriers as a result of the deposition of CyCat. Lift height during the 2nd pass and scan rate were 10 nm and 1 Hz, respectively. Relative humidity and temperature during all AFM/KPFM experiments were in the ranges of 29–31% and 23–25 °C. All topographic height scans were analyzed using the Gwyddion software. The CyCat grains present on surfaces of different materials were

identified utilizing a watershed algorithm.^[209] Grains were located and identified by setting the maximal number of steps for the determination of local minima in the height data and water drop sizes corresponding to the tip area projection, *i.e.* 0.5 % of the scanned area. Only grains occupying areas larger than 1.4×1.4 pixels were considered in the analysis, since smaller ones most probably arise from measurement noise. The mean grain height (h_{grain}), *i.e.* the mean of all height values occurring inside the grain, and the mean equivalent disk radius (R_{eq}), *i.e.* the radius of disc having the same projected area as the identified grain, were obtained by fitting Gaussian functions to the corresponding number distribution values of identified grains. $f(x) = y_0 + ae^{-\frac{(x-x_0)^2}{b^2}}$ where y_0 is the offset, x_0 is the number average value, a is the amplitude and b is the half-width of the corresponding number distribution functions $f(x)$ of mean grain heights and mean equivalent disc radii.

Scanning Electron Microscopy (SEM). SEM images were recorded utilizing a Zeiss Supra 40VP. Prior to the measurements, the samples were coated with a 10 nm gold layer.

Direct Laser Writing (DLW). For the fabrication of blind test structures employing IP-L 780 and of the thiol-ene based photoresists, the commercially available DLW setup Photonic Professional GT (Nanoscribe GmbH, Karlsruhe, Germany) was utilized. The instrument was equipped with a high-numerical-aperture (NA = 1.4, 63×) oil-immersion objective lens. A mode-locked and frequency-doubled Er-doped fiber is employed emitting femtosecond pulses at 780 nm wavelength. Previous to 3D printing, the glass substrates were cleaned and silanized. To remove remaining liquid photoresist, the 3D printed structures were immersed in acetone, isopropyl alcohol and water for 5 min respectively and dried with nitrogen.

Custom-built DLW. A custom-built DLW setup was utilized to achieve the required 700 nm for the phenacyl sulfide activation in a two-photon process. The setup was reported in previous studies.^[119] The described pulse picker was not required for our study.

Time-lapse Microscopy. Time-lapse microscopy was carried out on a Zeiss Axiovert 200M. The sample was heated via a metal holder to approximately 30 °C.

Stereolithography (SLA). Macroscopic structures were fabricated with the commercially available SLA 3D printer Projet 1200 (3D Systems, U.S.). As cartridge, Visijet FTX clear (3D systems) was emptied, cleaned and refilled with the herein presented photoresists. The control samples were printed utilizing the Visijet FTX green (3D Systems, U.S.). After 3D

printing, the structures were rinsed with acetone, isopropyl alcohol and water and dried with nitrogen.

Fourier-Transform Infrared Spectroscopy (FT-IR). Spectra were recorded on a Bruker FT-IR Vertex 80 spectrometer with a range of 500 to 4000 cm^{-1} at ambient temperature.

Nanoindentation. Nanoindentation was performed on a Hysitron TI950 TriboIndenter equipped with a Berkovich tip. The load-unload cycle was conducted with load control. The maximum load was 200 μN with loading and unloading times of 12 s respectively.

5.3 Synthesis

5.3.1 Synthesis and Analysis of the Protected CyCat

Ortho-dimethoxybenzene (30.0 g, 0.217 mol, 1.00 eq) was dissolved in acetic acid (120 mL). Concentrated H₂SO₄ (4.259 g, 0.043 mol, 0.20 eq) was added and the reaction mixture was heated to 90 °C. Aqueous formaldehyde (37 %, 15.9 mL, 0.975 eq) was slowly added dropwise over a time period of 30 min. The reaction mixture was stirred for 1.5 h at 90 °C. The solid was precipitated in water (100 mL) and filtered off. The yellow solid was washed with saturated NaCl solution (0.50 L), water (2.00 L), saturated NaCl solution (0.50 L) and again with water (1.00 L). The product was dried under reduced pressure to obtain 31.9 g (98 %) of a pale yellow product. ESI MS (CHCl₃ : MeOH = 3 : 2) (Figure S2) and MALDI-TOF (DHB, THF) (Figure S3) measurements were carried out. ¹H NMR (400 MHz, CDCl₃): δ(ppm) = 6.9 - 6.3 (2 H, m, Ph-H), 4.8 (1 H, d, J = 4.8, -CH₂- and -O-(CH₃)₃) and 3.8 - 3.3 (8 H, m, -CH₂- and -O-(CH₃)₃).

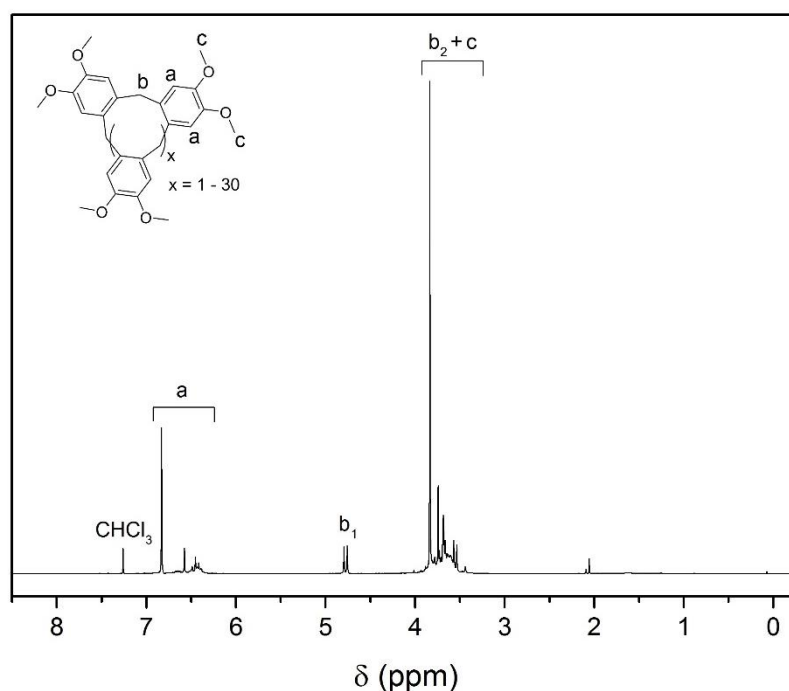


Figure 79: ¹H NMR spectrum of the protected CyCat. Analysis via DOSY (**Figure 82**) revealed different diffusion coefficients with the same values for the singlet at 3.8 ppm, the doublet at 4.8 ppm and the singlet at 6.8 ppm. Presumably, these species (*b*₁) possess a restricted number of conformational degrees of freedom due to a small amount of repeating units. Analyzing the upfield shifted protons, a decreasing diffusion coefficient was observed, which indicates the presence of moieties with a higher number of repeating units and, therefore, a higher number of conformational degrees of freedom (*b*₂).

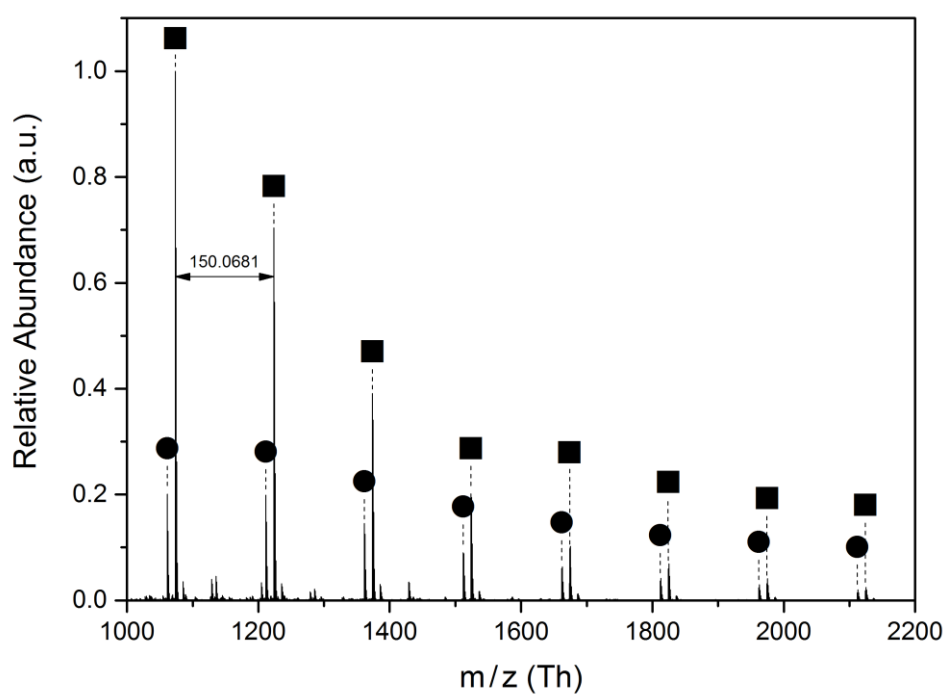
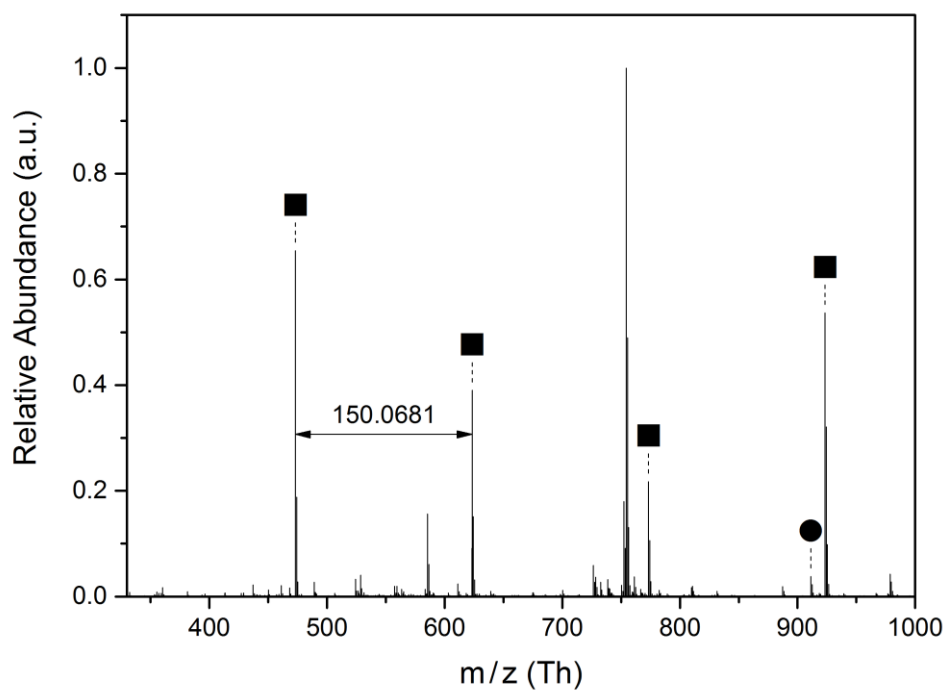


Figure 80: ESI MS spectra of the protected CyCat. In addition to the mainly formed cyclic derivatives (■), linear moieties (●) are assigned.

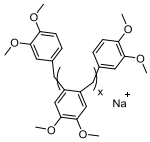
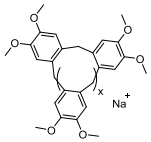
Label	$m/z_{(\text{exp})}$ [Th]	$m/z_{(\text{theo})}$ [Th]	$\Delta m/z$ [Th]	Resolution	x	Structure
●	1211.5385	1211.5339	0.0046	62034	6	
	1361.6073	1361.6019	0.0054	58309	7	
	1511.6754	1511.6700	0.0054	53871	8	
■	1223.5392	1223.5339	0.0053	59615	6	
	1373.6072	1373.6019	0.0050	57231	7	
	1523.6754	1523.6700	0.0054	53977	8	

Table 4: Exemplary peak assignments of the ESI MS spectra of the protected CyCat **Figure 80** for moieties with eight to ten protected catechol units. In addition to the mainly formed cyclic derivatives (■), linear moieties (●) are assigned.

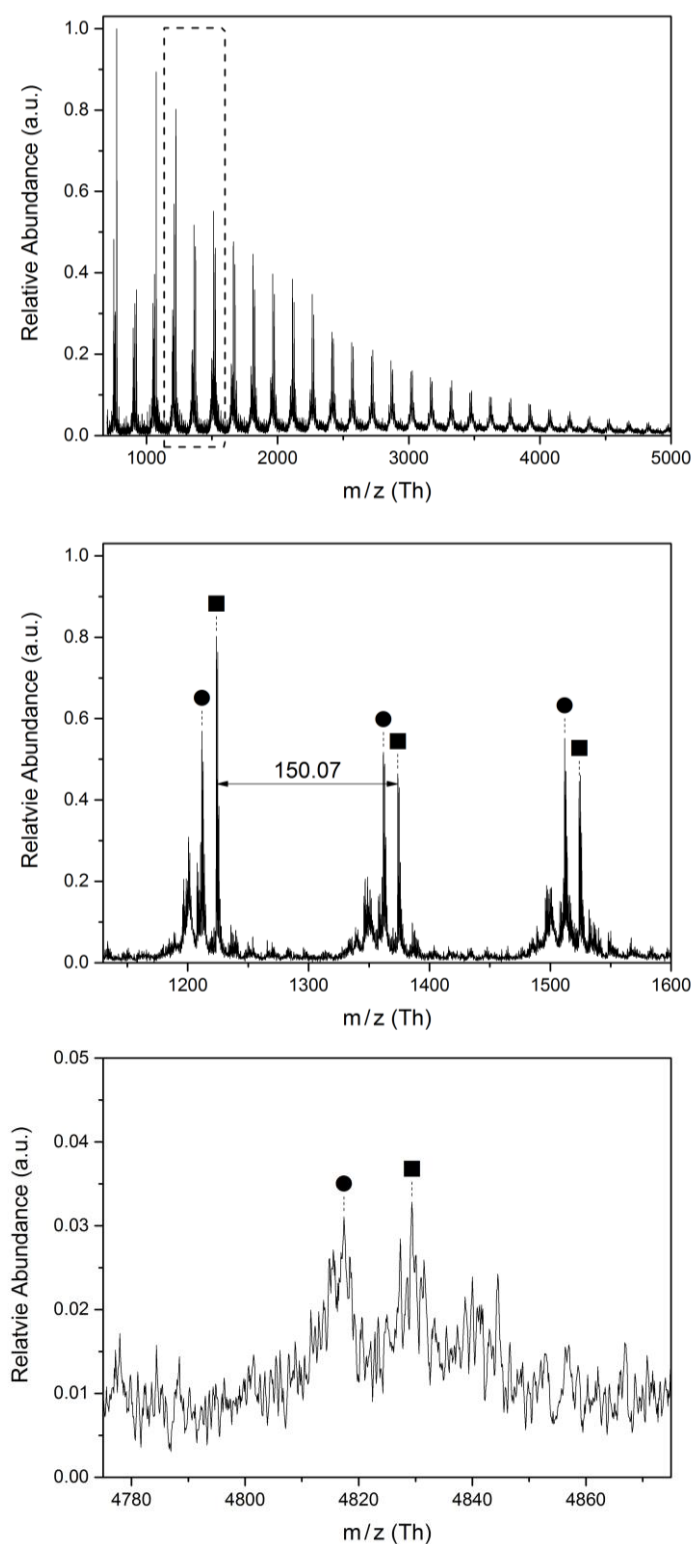


Figure 81: MALDI-TOF spectra of the protected CyCat. The overview spectrum (top) verifies the presence of the prior via ESI MS detected moieties with eight to ten protected catechol units with cyclic (■) and linear (●) species (middle). In addition, molecules with high m/z of up to 4828.65 Th confirming molecules with 32 protected catechol functionalities are clearly visible (bottom).

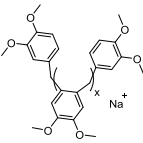
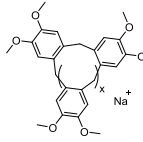
Label	$m/z_{(\text{exp})}$ [Th]	$m/z_{(\text{theo})}$ [Th]	$\Delta m/z$ [Th]	x	Repeating Unit [Th]	Structure
●	1211.72	1211.53	0.19	6	150.07	
	1361.83	1361.60	0.23	7		
	1511.91	1511.67	0.24	8		
■	1223.77	1223.53	0.24	6	150.07	
	1373.82	1373.60	0.22	7		
	1523.95	1523.67	0.28	8		

Table 5: Exemplary peak assignments of the MALDI-TOF spectra of the protected CyCat **Figure 81** for moieties with eight to ten protected catechol units. In addition to the mainly formed cyclic derivatives (■), linear moieties (●) are assigned.

Label	m/z (exp)	Average Mass		$\Delta m/z$ [Th]	x
	[Th]	m/z (theo)	[Th]		
●	4817.42	4816.64		0.78	30
■	4829.35	4828.65		0.70	30

Table 6: Peak assignments of the MALDI-TOF spectra of the protected CyCat **Figure 81** for the species with 32 protected catechol units. In addition to the mainly formed cyclic derivative (■), a linear moiety (●) is assigned.

Primary DOSY data of the protected CyCat

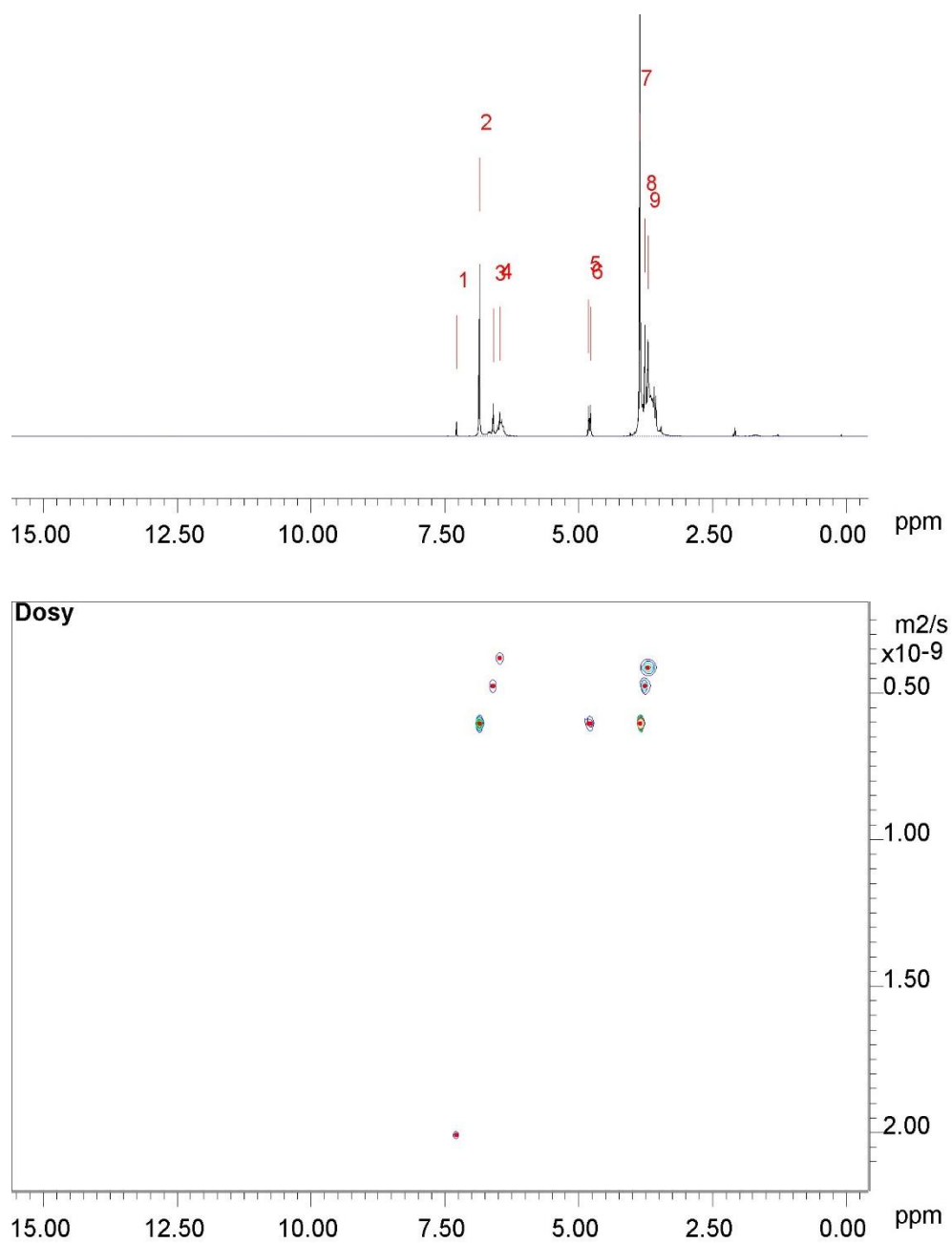
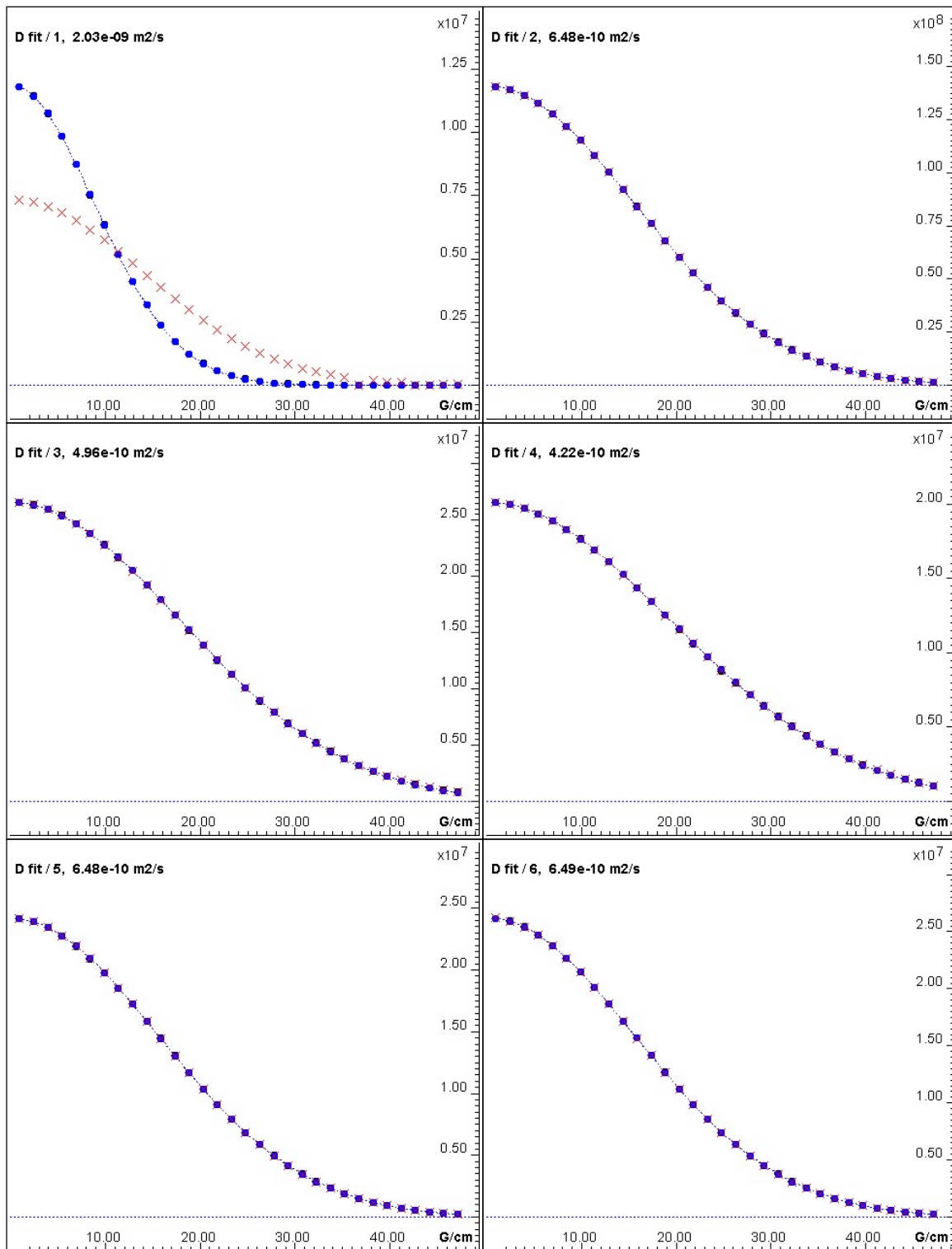
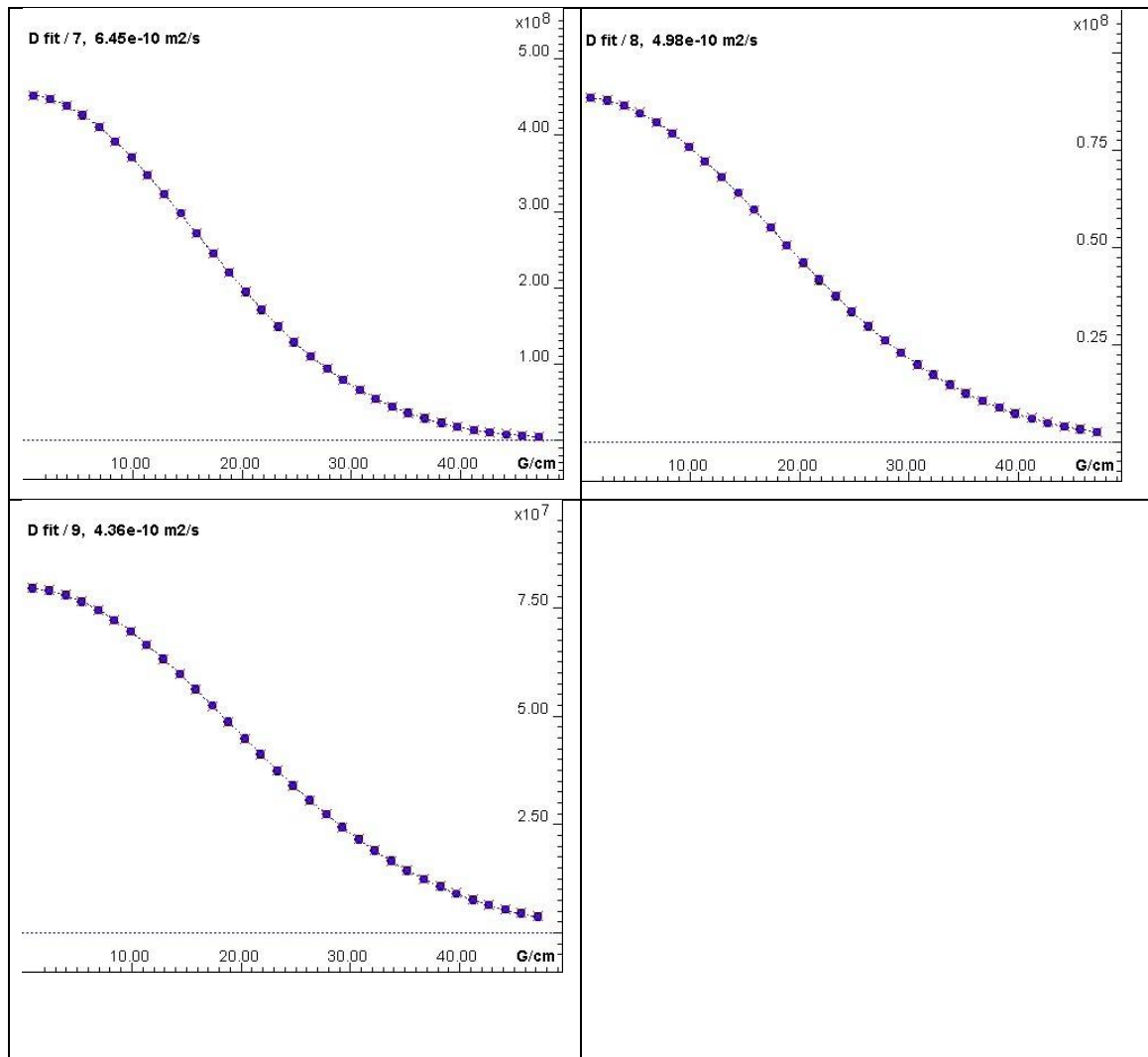


Figure 82: Primary DOSY data of the protected CyCat. A clear trend of the diffusion coefficient is observed for upfield shifted resonances indicating the presence of moieties with increasing molecular weights.

Experimental Section





5.3.2 Synthesis and Analysis of the CyCat

To a 500 mL three-necked flask equipped with a reflux condenser and a dropping funnel, protected CyCat (1.00 g) and DCM (100 mL) were added. BBr_3 (40.00 g, 15.17 mL) was added slowly (30 min) and the reaction mixture was refluxed overnight. Subsequently, the reaction mixture was carefully quenched with water (100 mL). Volatile parts were removed under reduced pressure. The reaction mixture was extracted with ethyl acetate (2x100 mL) and the combined organic layers were washed with water (100 mL), brine (100 mL) and dried over CaSO_4 . Volatile parts were removed under reduced pressure and the product was obtained as a crystalline structure incorporating ethyl acetate. The remaining ethyl acetate was predominantly removed after heating the obtained black product to 150 °C for 2 h to give 519 mg (64 %) of a black powder. ^1H NMR (400 MHz, DMSO): δ (ppm) = 9.3 – 7.7 (1.5 H, Ph-OH), 7.3 - 5.7 (2 H, Ph-H), 4.7 - 3.0 (3.5 H, $-\text{CH}_2-$ and $-\text{O}-(\text{CH}_3)_3$).^[94]

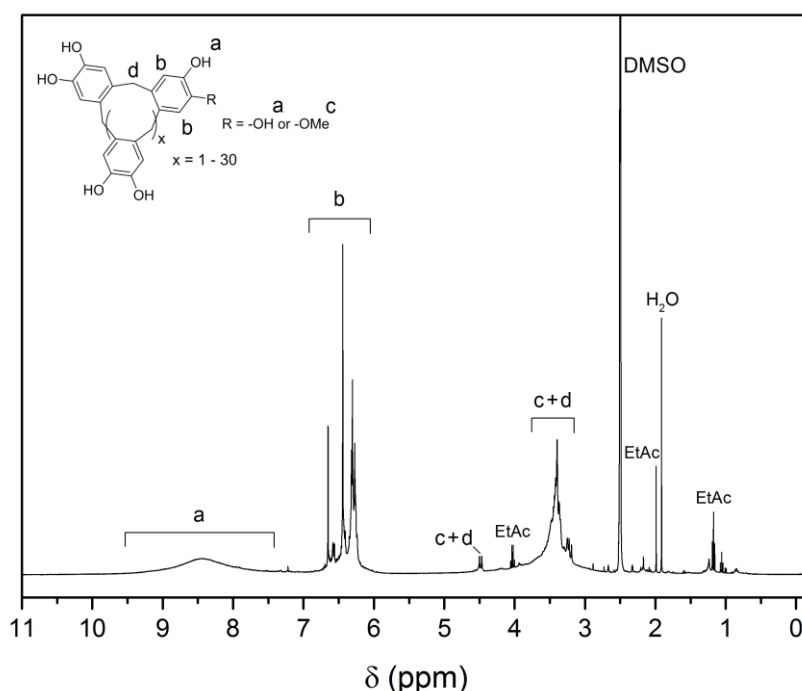


Figure 83: ^1H NMR spectrum of the CyCat after deprotection of the methoxy groups via BBr_3 . Small amounts of ethyl acetate (EtAc) and water (H_2O) remained even after heating to 150 °C for 2 h.

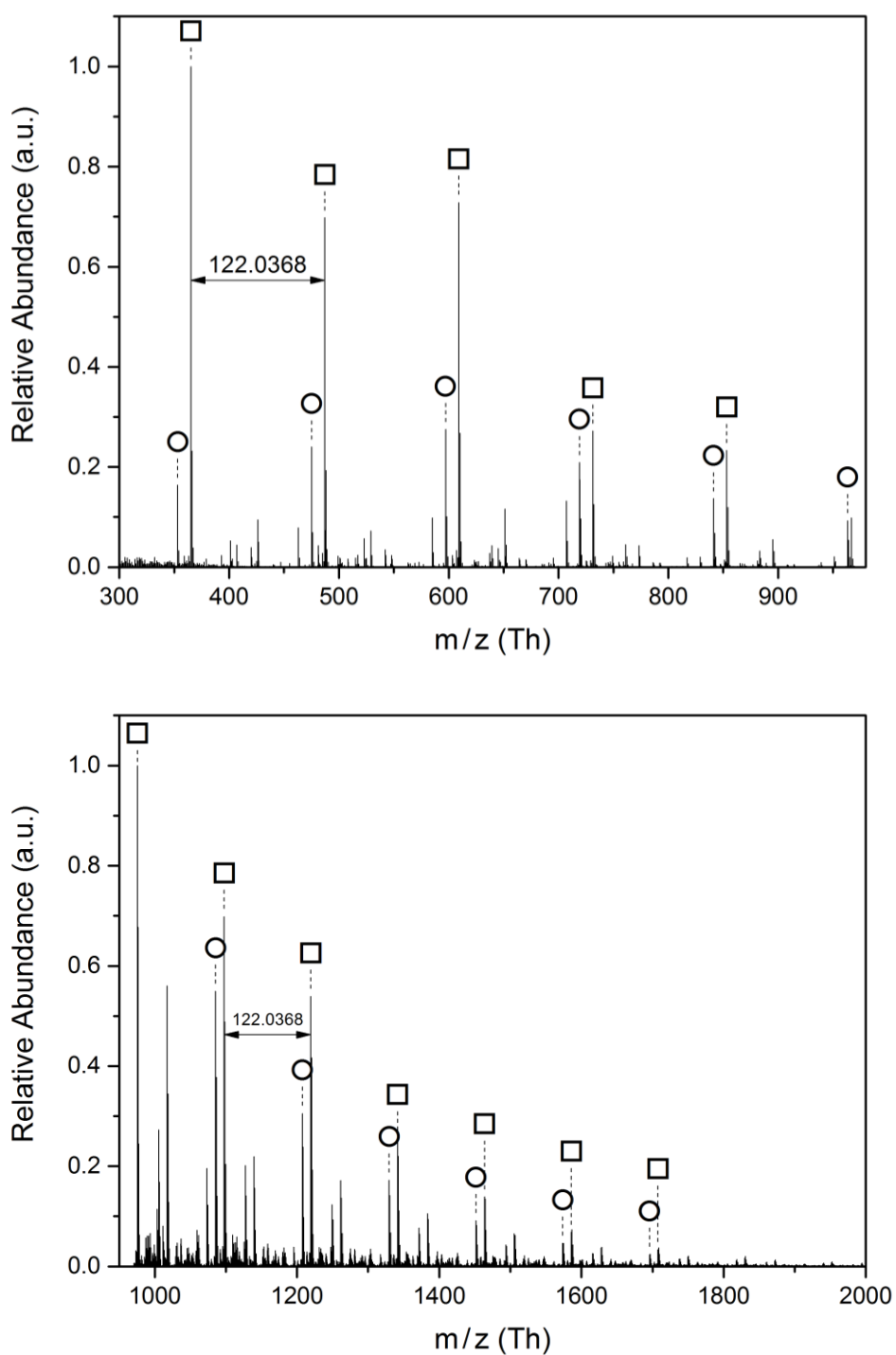


Figure 84: ESI MS spectra of the CyCat after deprotection via BBr_3 . The measurement in positive ion mode was not sufficient and was changed to negative enabling the detection of $-\text{O}^-$ moieties (top). Furthermore, a CID of 15 eV was utilized to facilitate the ionization of m/z 970-2000 Th, which led to partial fragmentation (bottom). Linear moieties (○) are detected in addition to the predominant occurrence of cyclic species (□).

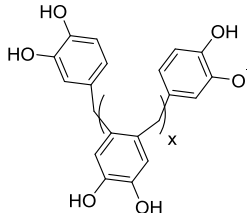
Label	$m/z_{(\text{exp})}$ [Th]	$m/z_{(\text{theo})}$ [Th]	$\Delta m/z$ [Th]	Resolution	x	Structure
○	963.2877	963.2870	0.0007	68188	6	
	1085.3261	1085.3237	0.0024	63010	7	
	1207.3628	1207.3605	0.0023	59068	8	
□	975.2892	975.2870	0.0022	67050	6	
	1097.3259	1097.3237	0.0022	64445	7	
	1219.3623	1219.3605	0.0018	61232	8	

Table 7: Exemplary peak assignments of the ESI MS spectra of the deprotected CyCat (**Figure 84**) for moieties with eight to ten catechol units. In addition to the mainly formed cyclic derivatives (□), linear moieties (○) are assigned.

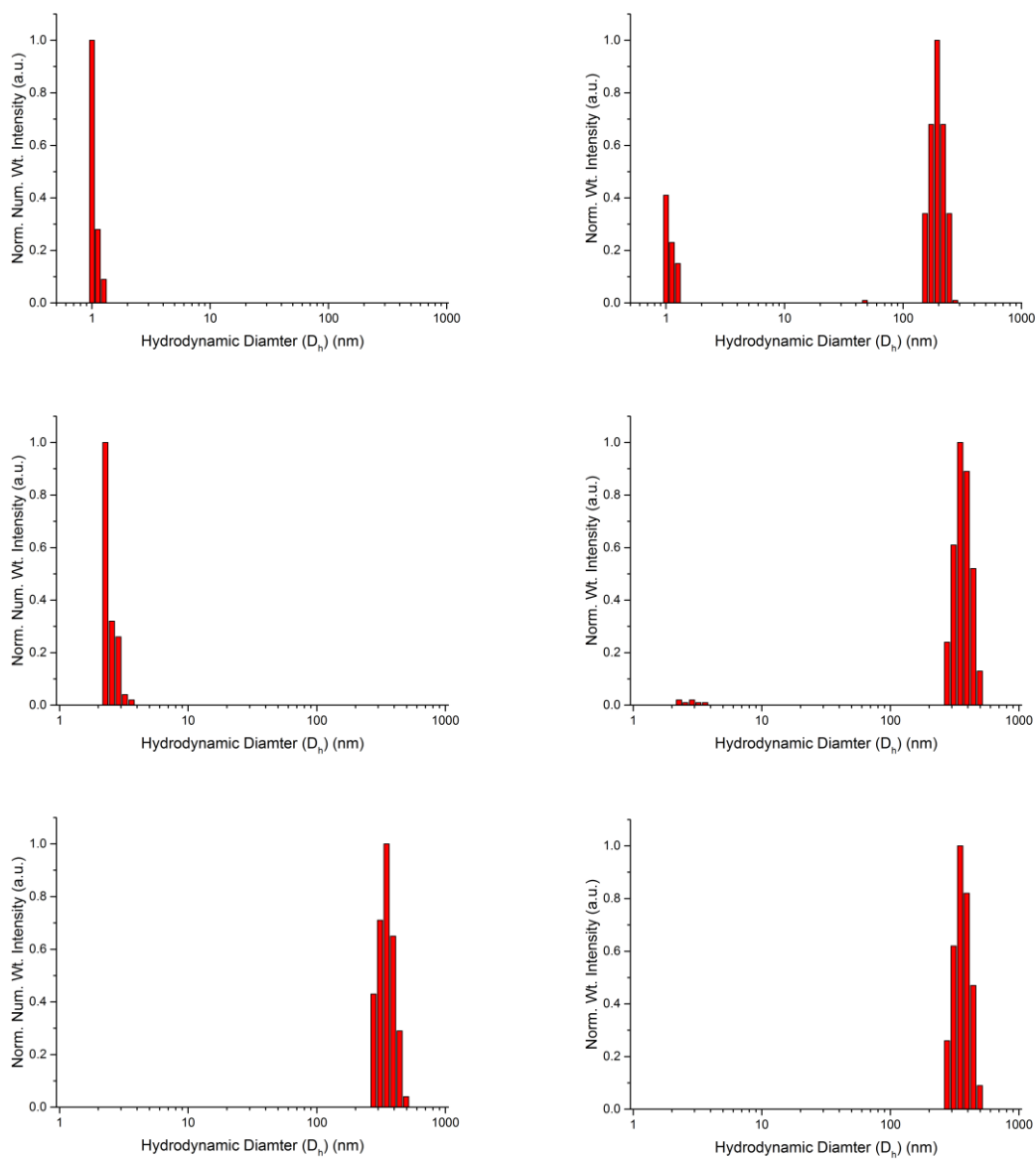


Figure 85: DLS measurements were conducted to investigate the time-dependency of the aggregate formation of CyCat. The number intensity (left column) and weight intensity (right column) is depicted for an aqueous 0.1 M NaHCO₃ solution of CyCat (1 mg mL⁻¹) after 0.5-1 h (top), 4-4.5 h (middle) and >6.5 h, respectively.

5.3.3 Synthesis and Analysis of the Phenacyl Sulfide Linker (PSL)

To a 500 mL round bottom flask pentaerythritol tetrakis(2-mercaptoacetate) (5.00 g, 11.56 mmol, 1 eq) was dissolved in a mixture of DCM (250 mL) and TEA (10.53 g, 104.04 mmol, 9 eq). The reaction mixture was cooled in an ice bath. Subsequently, 2-chloroacetophenone (14.30 g, 92.48 mmol, 8 eq) was added slowly. The reaction mixture was allowed to reach ambient temperature and it was stirred overnight (18 h). After the reaction, deionized H₂O (200 mL) was added and the aqueous layer was extracted two times with DCM (200 mL). The combined organic layers were dried over magnesium sulphate hydrate and the volatiles were removed under reduced pressure. The crude product was purified via column chromatography (cyclohexane : ethyl acetate, 1 : 1) to yield a colorless wax-like product (4.70 g, 45 %). ¹H NMR (CDCl₃, 400 MHz) s (ppm): 7.95-7.93 (m, 8H, ArH), 7.59-7.54 (m, 4H, ArH), 7.47-7.43 (m, 8H, ArH), 4.25 (s, 8H, COO-CH₂), 3.98 (s, 8H, S-CH₂-CO), 3.35 (s, 8H, OOC-CH₂). ¹³C NMR (CDCl₃, 101 MHz) s (ppm): 193.86 (f), 169.29 (c), 135.22 (g), 133.60 (j), 128.77 (i), 128.66 (h), 62.77 (b), 42.60 (a), 37.60 (e), 33.23 (d).

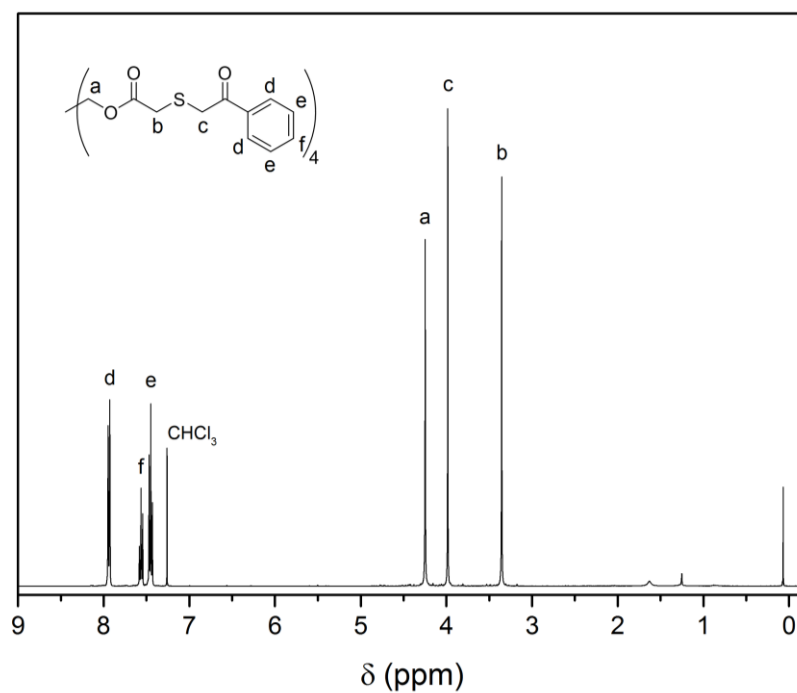


Figure 86: ^1H NMR spectrum of the PSL with assigned hydrogen signals in CDCl_3 .

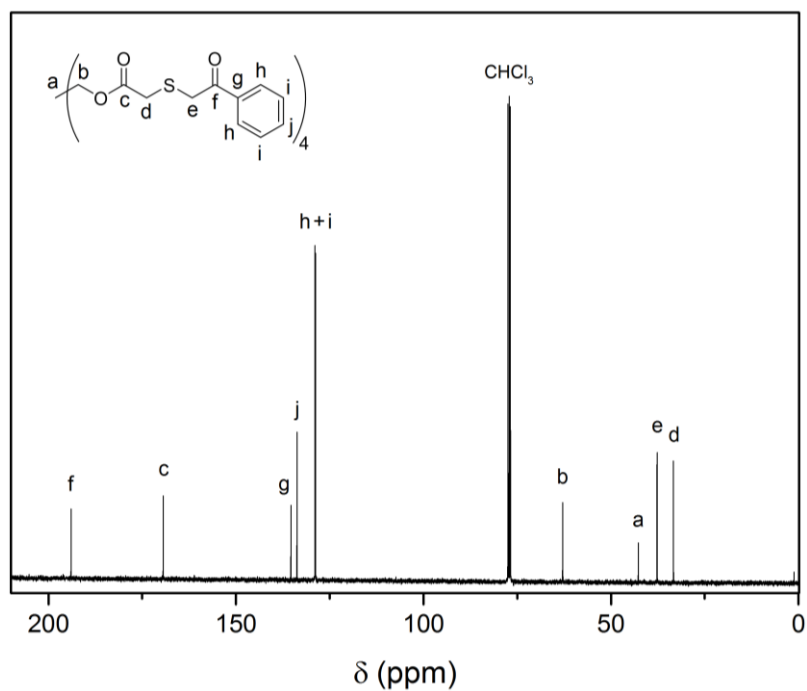


Figure 87: ^{13}C NMR spectrum of the PSL with assigned signals in CDCl_3 .

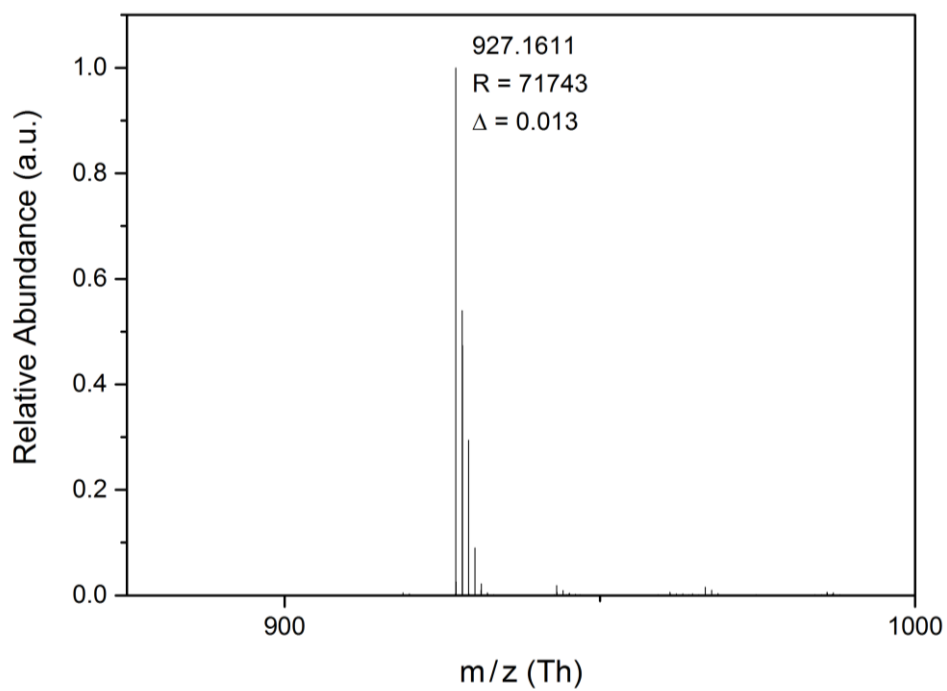


Figure 88: ESI MS spectrum of the PSL utilizing a 0.1 mM sodium trifluoroacetate DCM : MeOH, 3 : 1 solution.

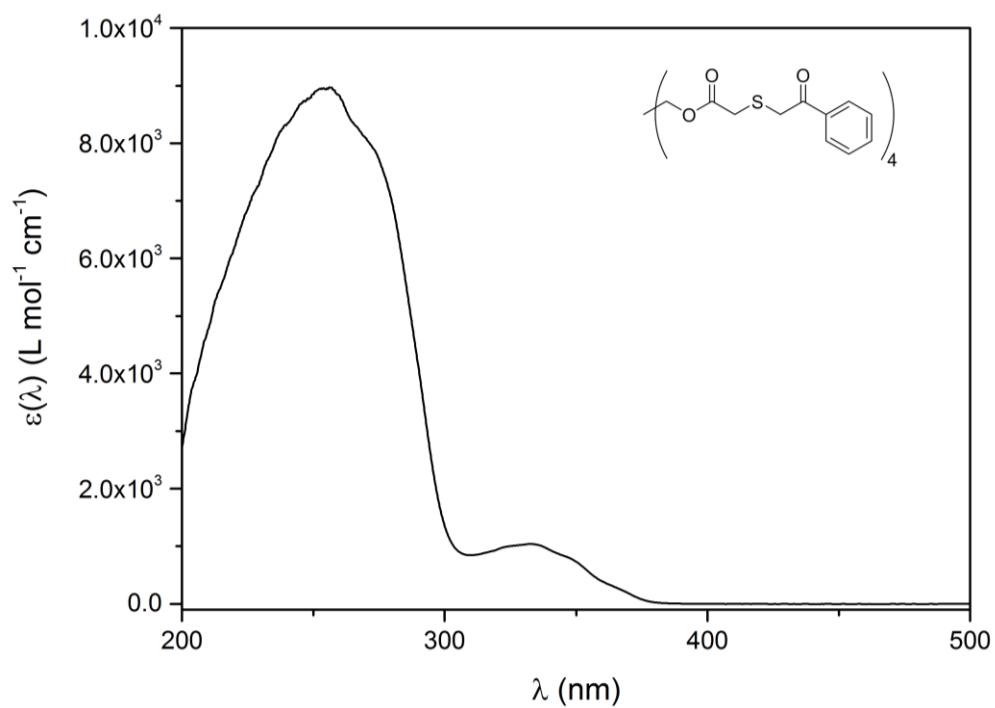


Figure 89: UV-Vis spectrum of the PSL.

Analysis of the reactivity of the phenacyl sulfide linker (PSL) via ESI MS. The end-capping of the PSL was performed via an adapted literature procedure.^[149] The phenacyl sulfide linker (1.50 mg, 1.66 μmol , 1 eq) and DIPEA (0.22 mg, 1.72 μmol , 1.04 eq) were dissolved in dry DCM (7 mL). *O*-(2-mercaptoethyl)-*O'*-methyl-hexa(ethylene glycol) (5.60 mg, 15.7 μmol , 9.5 eq) was added and the reaction mixture was bubbled with N_2 . The reaction mixture was irradiated for 1 h in a custom-built photoreactor with a compact low-pressure fluorescent lamp (36 W, Philips CLEO Compact PL-L with $\lambda_{\text{max}} = 355 \text{ nm}$). Volatiles were removed and the crude product mixture was analyzed via ESI MS measurements (**Figure 90**).

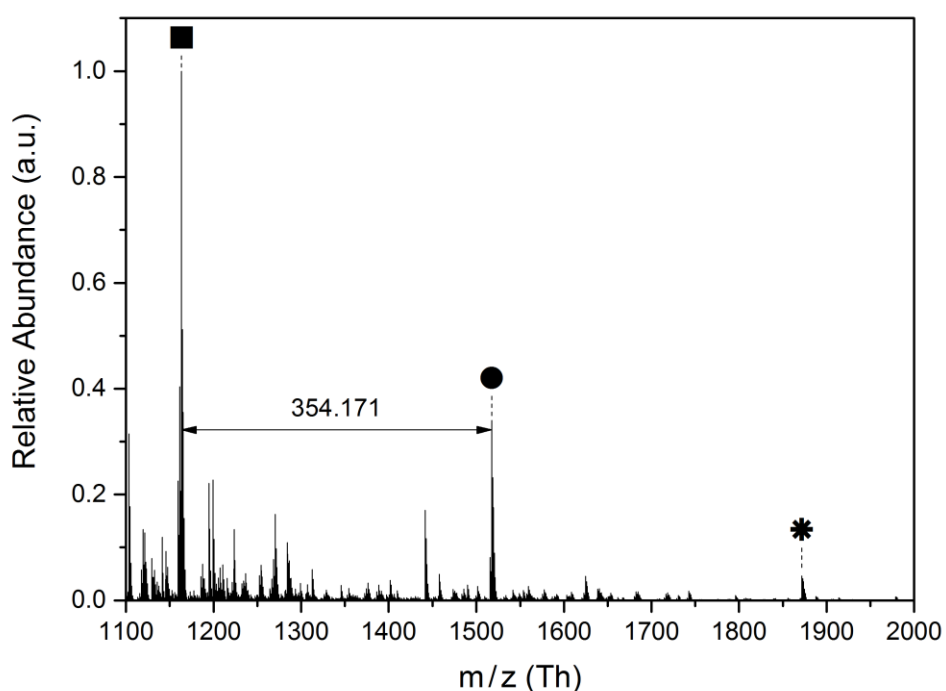


Figure 90: ESI MS spectrum of the *O*-(2-mercaptoethyl)-*O'*-methyl-hexa(ethylene glycol) end-capped PSL after irradiation for 1 h with a compact low-pressure fluorescent lamp (36 W, Philips CLEO Compact PL-L with $\lambda_{\text{max}} = 355 \text{ nm}$).

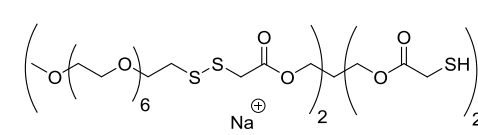
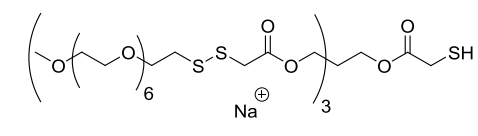
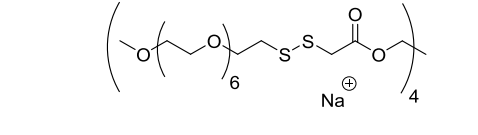
Label	$m/z_{(\text{exp})}$ [Th]	$m/z_{(\text{theo})}$ [Th]	$\Delta m/z$ [Th]	Resolution	Structure
■	1163.340	1163.336	0.004	62134	
●	1517.511	1517.507	0.004	54340	
*	1871.694	1871.678	0.016	47345	

Table 8: Peak assignments of the ESI MS spectrum (**Figure 90**) of the O-(2-mercaptoethyl)-O'-methylhexa(ethylene glycol) end-capped PSL.

5.4 Sample Preparation

Sample preparation for the study of the aggregate formation via KPFM and AFM

CyCat was deposited on freshly cleaved HOPG by dropcasting a single 4 μL droplet from a CyCat solution ($1.2 \text{ mg}\cdot\text{mL}^{-1}$) in 0.1 M NaHCO_3 , 30 min after dissolution. The droplet was removed from the HOPG surface by N_2 gas a few seconds after drop casting.

Sample preparation for the study of the ultrathin film formation of CyCat on various surfaces

The Au, SiO_2 and TiO_2 surfaces were rinsed with CHCl_3 , acetone, EtOH, deionized water and dried with N_2 . The SiO_2 and TiO_2 surfaces were treated in air plasma (25 W, Plasma cleaner/sterilizer, Harrick, USA) for 20 min. The gold surfaces were treated in an UV-ozone reactor (Jelight Company Inc., USA) to avoid possible surface oxide buildup. CyCat ($1 \text{ mg}\cdot\text{mL}^{-1}$) was added to a 0.1 M aqueous NaHCO_3 . After 15 min, the solution was filtered (filter size 0.2 μm). The surfaces were immersed for 45 min in the CyCat solution and were subsequently rinsed with a 0.1 M aqueous NaHCO_3 solution. Afterwards, the surfaces were placed for 10 minutes in an aqueous 0.1 M NaHCO_3 solution, rinsed with deionized water and dried in an N_2 stream.

Sample preparation for the post-modification of the ultrathin film CyCat coated surfaces

The surface coating of SiO_2 surfaces with a monomolecular layer of CyCat was performed as described above. Subsequently, the surfaces were immersed in either a 0.66 M solution of 4-bromophenethylamine in THF or a 0.33 M solution of NH_2 -PEO- NH_2 (1500 Da) in THF/water (1:1). After reaction for 1 h, the samples were removed, rinsed consecutively with THF, ethanol, and deionized water and dried with N_2 .

Sample preparation for the study of the multilayer functional assembly formation of CyCat and TREN

Au, SiO₂ and TiO₂ surfaces were rinsed with CHCl₃, acetone, EtOH, deionized water and dried with N₂. The SiO₂ and TiO₂ surfaces were treated in air plasma (25 W, Plasma cleaner/sterilizer, Harrick, USA) for 20 min. The gold surfaces were treated in an UV-ozone reactor (Jelight Company Inc., USA) to avoid possible surface oxide buildup. The CyCat (1 mg·mL⁻¹) was added to a 0.1 M aqueous NaHCO₃. After 15 min, the solution was filtered (filter size 0.2 μm). The surfaces were immersed for 45 min in the CyCat solution and then rinsed with a 0.1 M aqueous NaHCO₃ solution, rinsed with deionized water and dried with N₂. Afterwards, the surfaces were dipped alternately for 5 min into an aqueous TREN solution (0.67 μL·mL⁻¹) and the CyCat solution, briefly rinsing with 0.1 M aqueous NaHCO₃ solution in between the dipping steps. The alternating dipping was repeated to achieve a total of 6 immersions in each solution resulting in 12 layers on the surfaces. Finally, the sample was rinsed with deionized water and dried with N₂.

Sample preparation for the post-modification of the multilayer functional assembly formation of CyCat and TREN

The sample preparation of the multilayers on Si/SiO₂ surfaces was performed according to the above description. To facilitate the post-modification, the surfaces were immersed in 2 mL of a 0.24 M TEA solution in THF for 2 min. Subsequently, either 1 mL of a 0.24 M solution of 2-bromo-2-methylpropanoyl bromide in THF (reaction time: 5 min) or 1 mL of a 0.2 M solution of tetrazole acyl chloride in THF (reaction time: 1 h) were added. Furthermore, additional multilayer Si/SiO₂ surfaces were directly immersed in a 2.5 mM solution of phenacyl–sulfide-terminated poly(ethylene oxide) (2000 Da) in DCM, bubbled with N₂ for 10 min and irradiated for 1 h rotating about a low-pressure fluorescent lamp (PL-L Phillips CLEO Compact, λ_{max} = 355 nm). Likewise, further surfaces were placed in a 0.25 M solution of trifluoroacetic anhydride in THF for 1 h. After removal, all surfaces were rinsed consecutively with THF, ethanol, and deionized water and dried with N₂.

Grafting of poly(methyl methacrylate) (poly(MMA))

Poly(MMA) was prepared in a grafting-from approach *via* Surface-Initiated Atom Transfer Radical Polymerization using a procedure reported previously.^[201] The substrates used for the polymerization reaction were Si/SiO₂ surfaces coated with a 12-layer CyCat-TREN assembly, post-functionalized with 2-bromo-2-methylpropionyl groups as described above. The polymerization was carried out at 28 °C for 20 min. The samples were subsequently washed with methanol, ethanol, and deionized water and dried with N₂.

Photoresist preparation of PSL

The phenacyl sulfide-linker (0.10 g, 0.11 mmol, 1.00 eq) and pentaerythritol tetrakis(2-mercaptopropionate) (0.054 g, 0.110 mmol, 1.00 eq) were dissolved in tetrahydrothiophene 1,1-dioxide (0.73 mL). The photoresist was stirred overnight and filtered through a 0.2 μm syringe filter to remove dust particles.

Preparation of glass substrates

All glass substrates were cleaned with acetone, 2-propanol, ionized water and ultrasonicated for 15 min in acetone. Subsequently, the substrates were activated employing air plasma for 20 min.

Silanization of activated glass substrates

Directly after cleaning by air plasma the glass substrates were immersed in a solution of 3-(trimethoxysilyl)propyl methacrylate (0.5 mM) and (3-mercaptopropyl)trimethoxysilane (0.5 mM) in toluol for 1 h. Subsequently, the substrates were ultrasonicated in toluene (5 min) and acetone (5 min) to remove physisorbed silane.

Preparation of the divinyl adipate-based thiol-ene photoresist Pyrogallol (42.9 mg, 0.34 mmol, 0.02 eq) was dissolved in 1.83 mL of acetophenone and vinylphosphonic acid (56.4 mg, 0.52 mmol, 0.04 eq) was added. After complete mixing, phenylbis(2,4,6-trimethylbenzoyl)phosphine oxide (285 mg, 0.68 mmol, 0.05 eq) was dissolved.

Subsequently, pentaerythritol terakis(3-mercaptopropionate) (3.70 g, 7.67 mmol, 0.50 eq), divinyl adipate (3.00 g, 15.13 mmol, 1 eq) and 3.94 mL of propylene carbonate were added. Macroscopic printing was also feasible without addition of propylene carbonate, however, to assure a straightforward detection of the interface during DLW at least 10 % of the stated volume should be added. The photoresist was tempered (20°C) in the room where the 3D printer was located and filtered (0.2 µm syringe filter, PTFE) before usage.

Preparation of the ionic thiol-ene photoresist. Pyrogallol (21.6 mg, 0.17 mmol, 0.05 eq) was dissolved in 1.47 mL of acetophenone and vinylphosphonic acid (34.6 mg, 0.32 mmol, 0.09 eq) was added. After complete mixing, phenylbis(2,4,6-trimethylbenzoyl)phosphine oxide (143.5 mg, 0.34 mmol, 0.10 eq) was dissolved. Subsequently, pentaerythritol terakis(3-mercaptopropionate) (2.15 g, 4.40 mmol, 1.25 eq), carbonate diallyl linker (0.50 g, 3.52 mmol, 1.00 eq), 1,8-nonadiyne (105.7 mg, 0.88 mmol, 0.25 eq), diallyldimethylammonium chloride (568.7 mg, 3.52 mmol, 1.00 eq) and 1.26 mL of propylene carbonate were added. The photoresist was tempered (20°C) in the room where the 3D printer was located and filtered (0.2 µm syringe filter, PTFE) before usage.

Preparation of glass substrates for DLW (thiol-ene photoresist)

All glass substrates were ultrasonicated in acetone, 2-isopropanol, ionized water for 5 min respectively. The activation of the substrates was performed with air plasma for 20 min. Immediately following the activation, the glass substrates were immersed in a 0.5 mM 3-(trimethoxysilyl)propyl methacrylate solution in toluene for 1 h. Subsequently, the substrates were ultrasonicated in toluene for 5 min and immersed in acetone, isopropyl alcohol and water for 5 min respectively. The substrates were dried with nitrogen.

Cleavage of divinyl adipate-based structures (thiol-ene photoresist)

The micro- and macro-printed structures were immersed in 1 M ethanolamine solution in DMF at 50°C for the photoresist composition shown in Figure 2a. Macroscopic structures were cleaved after 7 h while microscopic structures required 20 h to be completely removed.

Cleavage of ionic structures (thiol-ene photoresist)

The macro-printed structure was immersed in an aqueous 1 M ethanolamine solution at 50°C and required 60 h. Complete removal of the object was obtained after a reaction time of 60 h.

6

Appendix

In this section, supportive experimental data is presented. The corresponding discussion was conducted in the section *Results and Discussion*.

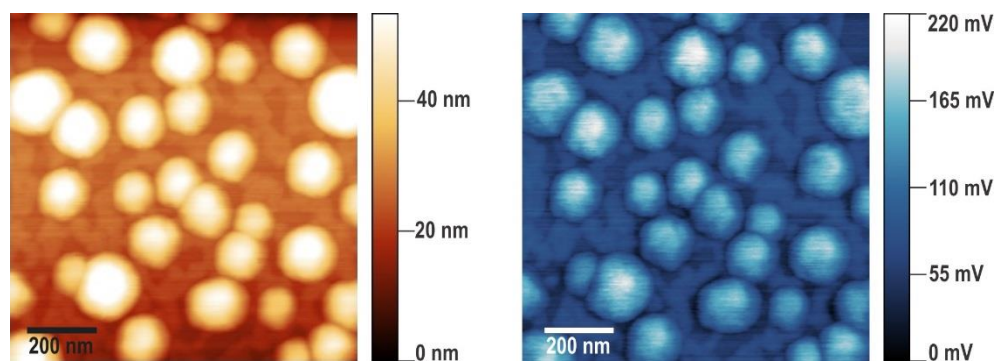


Figure 91: Analysis of CyCat aggregates via KPFM. The surface height topography (left) and surface potential (right) maps are depicted after deposition of the particles on atomically flat HOPG carriers.

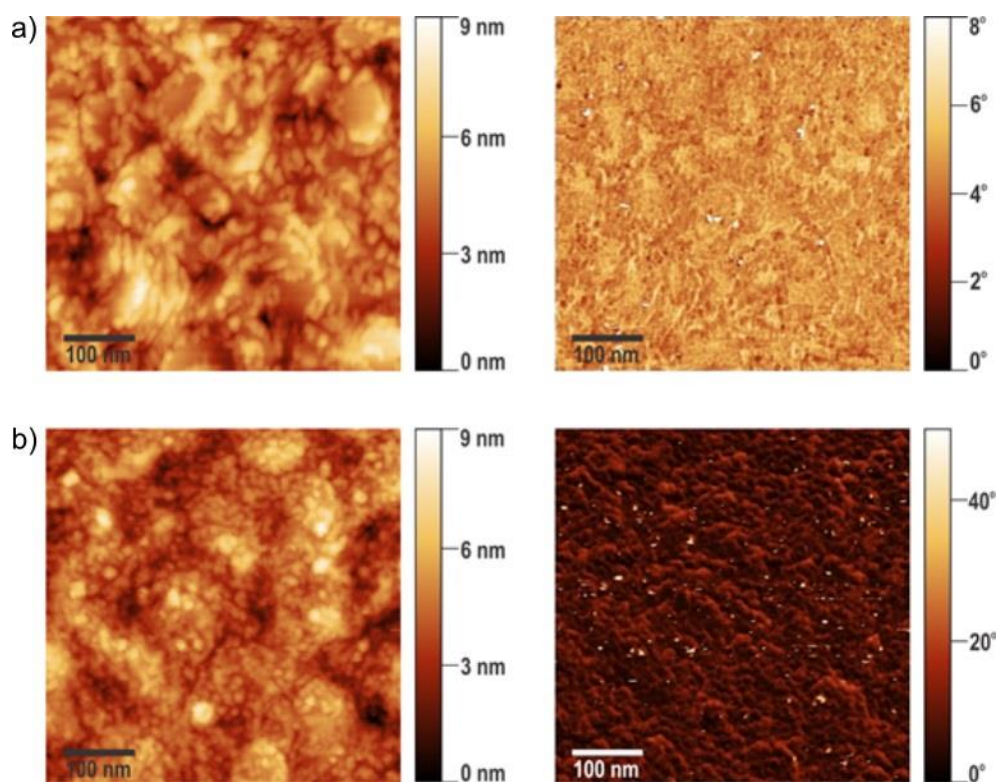


Figure 92: Surface height (left) and phase (right) topography maps of pure (a) and CyCat coated (b) Au substrates.

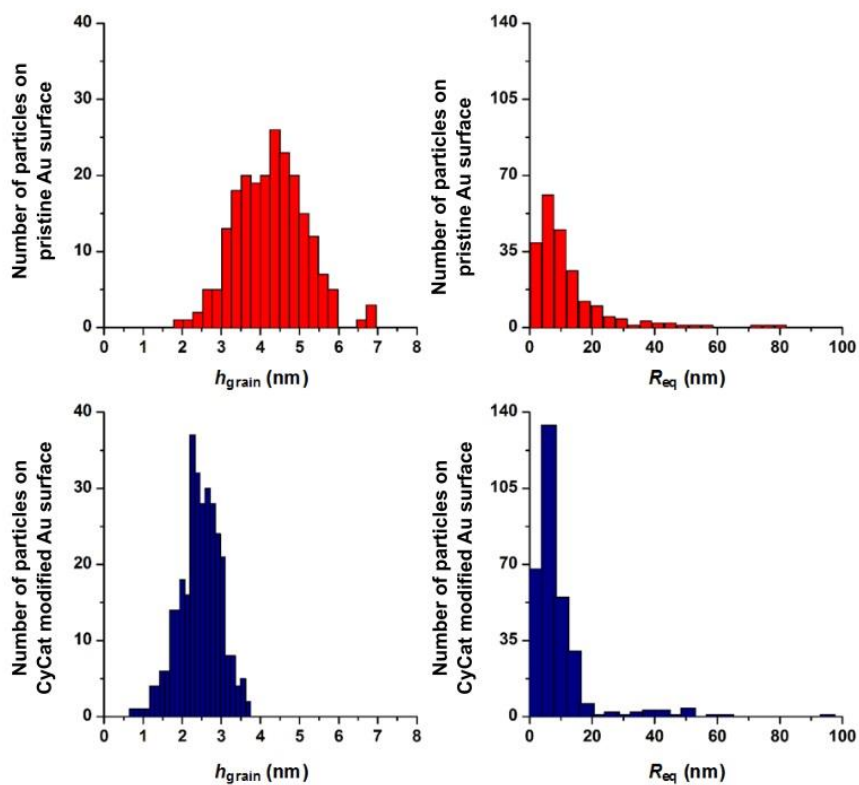


Figure 93: AFM analysis exhibiting the particle height h_{grain} (left) and equivalent radius R_{eq} (right) distributions of pure (a) and CyCat-coated (b) Au substrates.

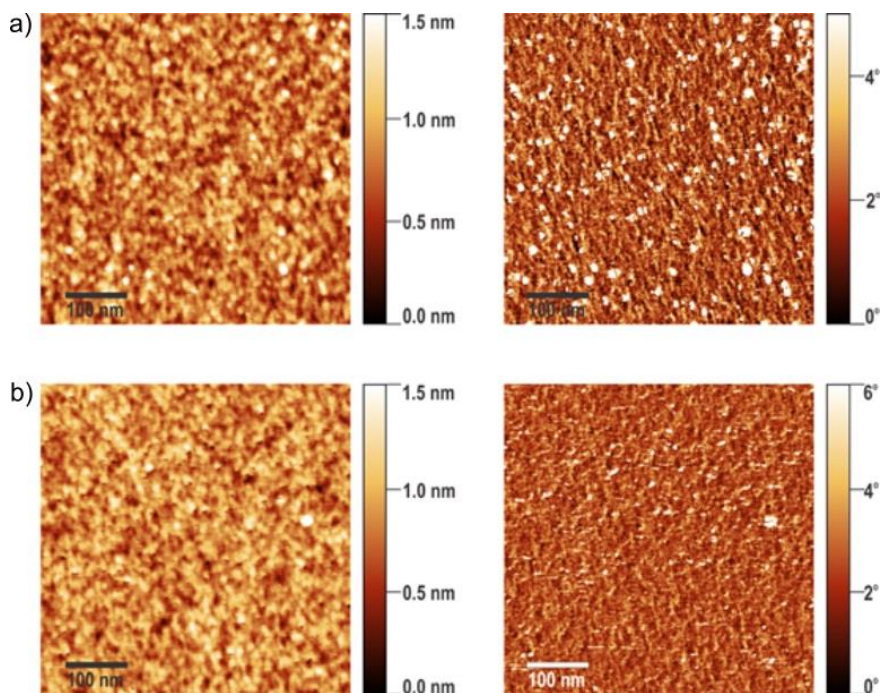


Figure 94: Surface height (left) and phase (right) topography maps of pure (a) and CyCat coated (b) SiO_2 substrates.

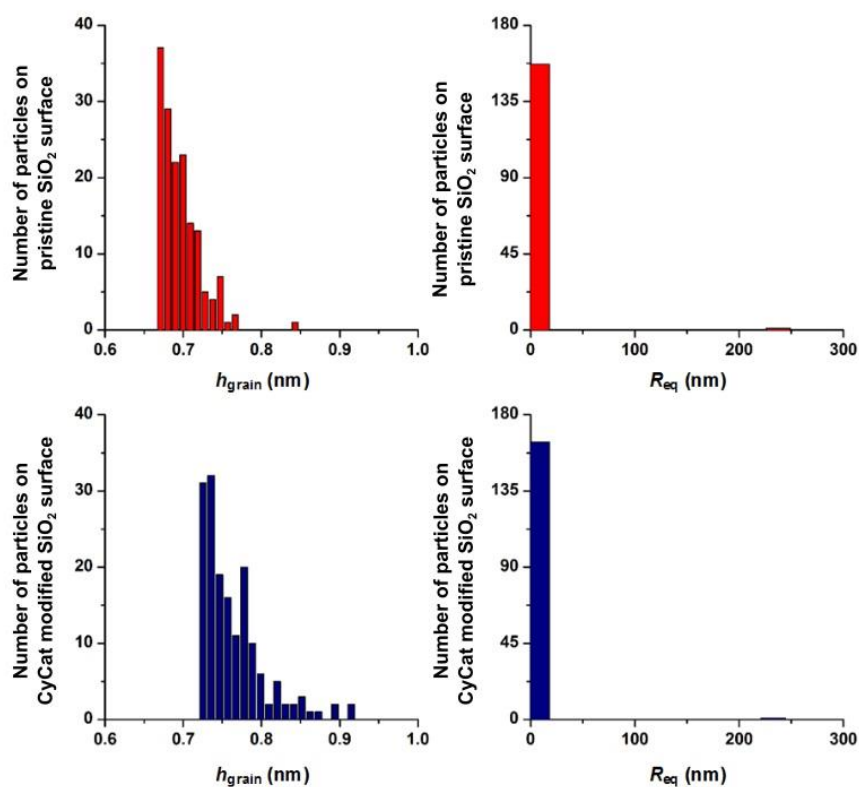


Figure 95: AFM analysis exhibiting the particle height h_{grain} (left) and equivalent radius R_{eq} (right) distributions of pure (a) and CyCat-coated (b) SiO₂ substrates

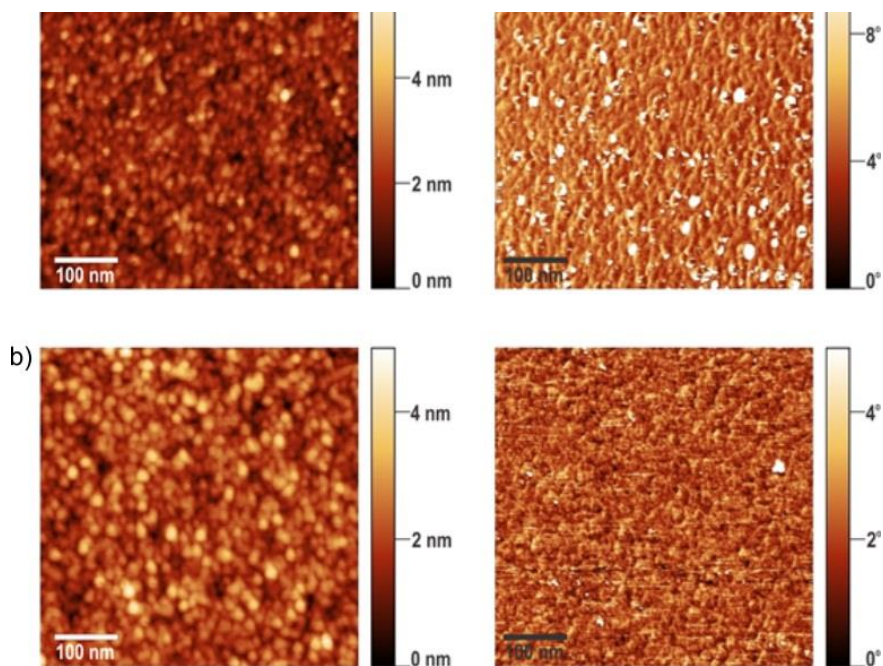


Figure 96: Surface height (left) and phase (right) topography maps of pure (a) and CyCat coated (b) TiO₂ substrates.

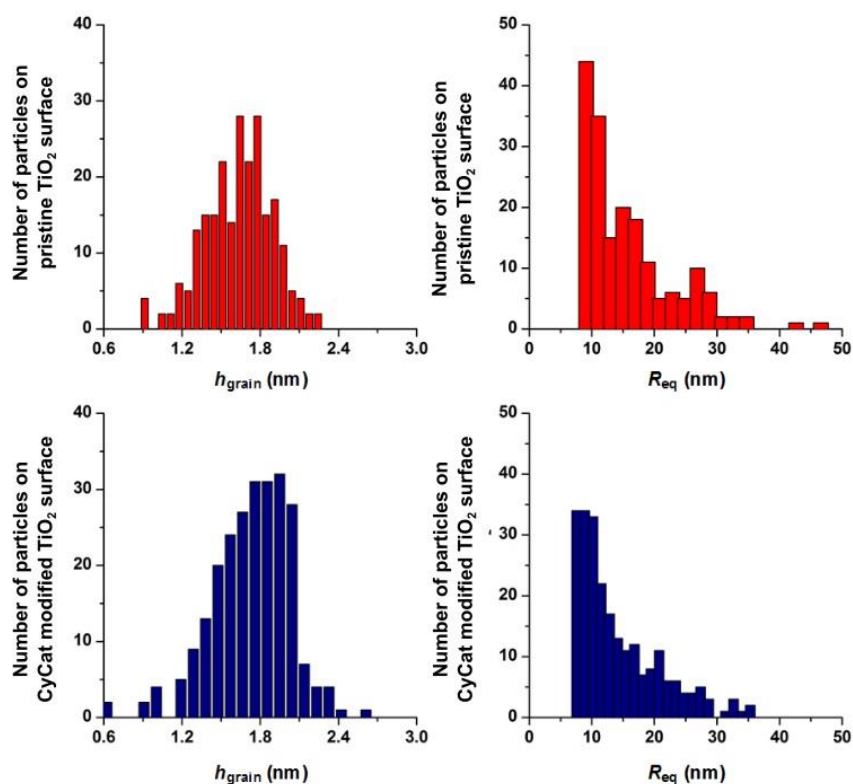


Figure 98: AFM analysis exhibiting the particle height h_{grain} (left) and equivalent radius R_{eq} (right) distributions of pure (a) and CyCat-coated (b) TiO₂ substrates

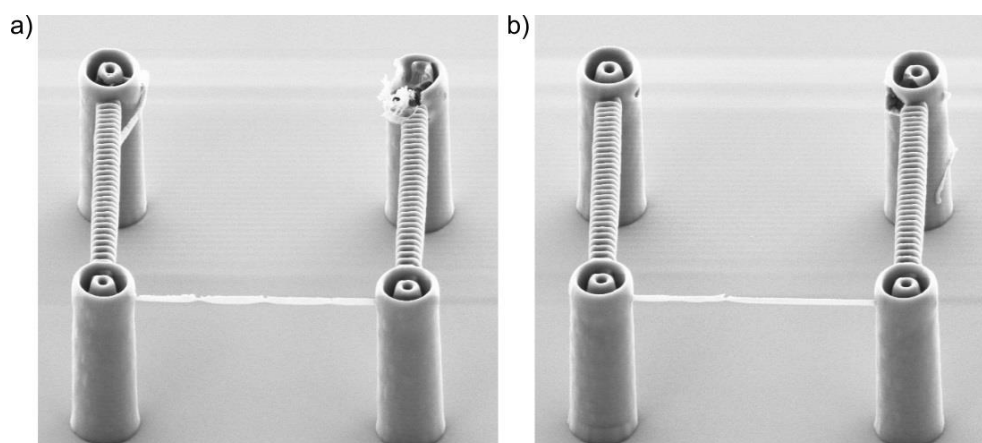


Figure 97: SEM images of partially destroyed boxing-like compound structures. a-b) The upper pillars were damaged by the laser voxel during the incorporation of the phenacyl sulfide-based photoresist. Precise stopping that still enables a sufficient adhesion of newly cured material to the scaffold, but that does not overexpose the acrylate-based network, was necessary. Single rods were suited to connect the lower pillars, however, due to shrinkage after development the connections possessed thinned out areas (scale bars, 5 μm).

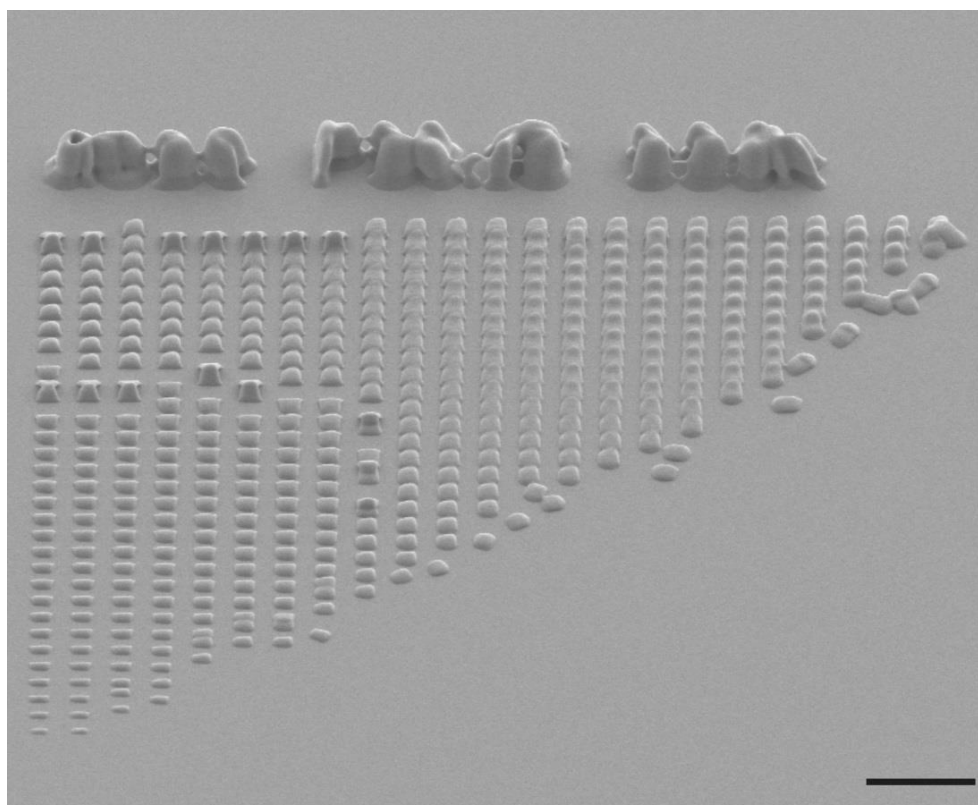


Figure 99: Power sweep of the pyrocarbonate-based thiol-ene photoresist. The employed power increases from bottom (0 mW) to top (25 mW) with a writing speed of 1000 $\mu\text{m/s}$. From left to right, the z-coordinate is varied from negative to positive values (surface: $z = 0$) to assure to find the lowest laser power for which a perfect alignment with the surface is required (scale bar, 10 μm).

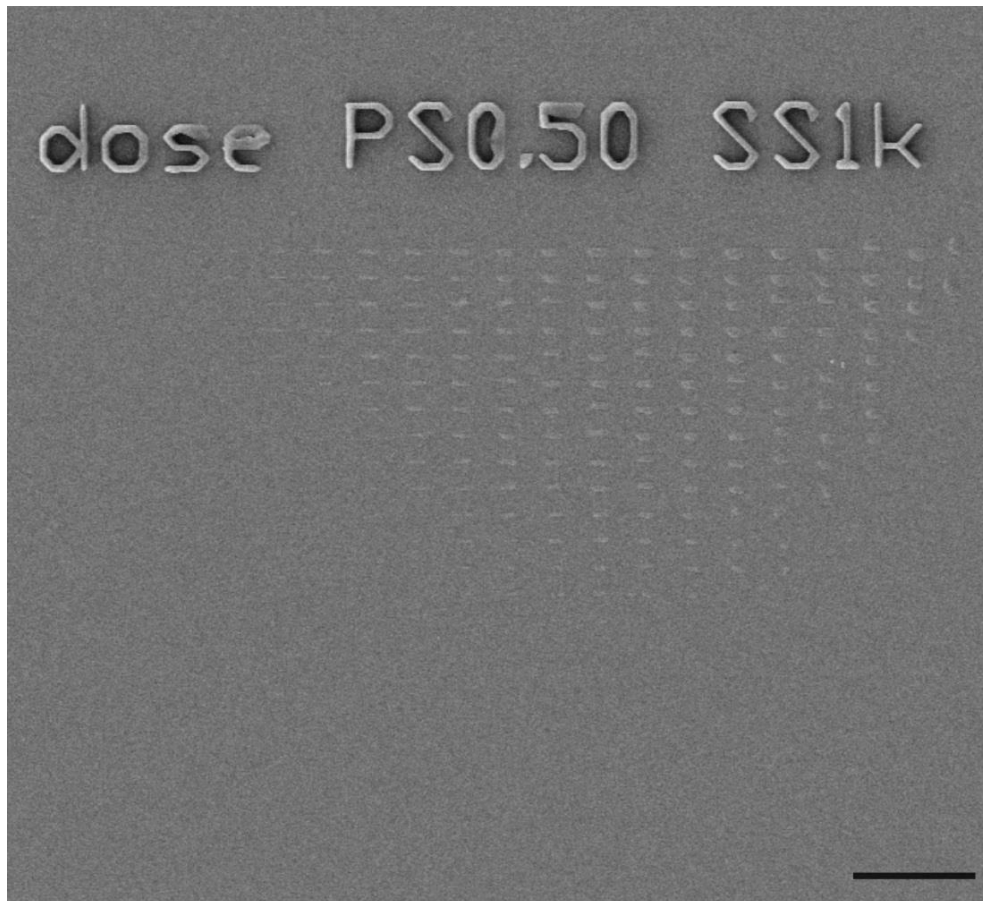


Figure 100: Power sweep of the divinyl adipate-based thiol-ene photoresist. The employed power increases from bottom (0 mW) to top (25 mW) with a writing speed of 1000 $\mu\text{m/s}$. From left to right, the z-coordinate is varied from negative to positive values (surface: $z = 0$) to assure to find the lowest laser power for which the voxel has to be perfectly aligned with the surface (scale bar, 10 μm).

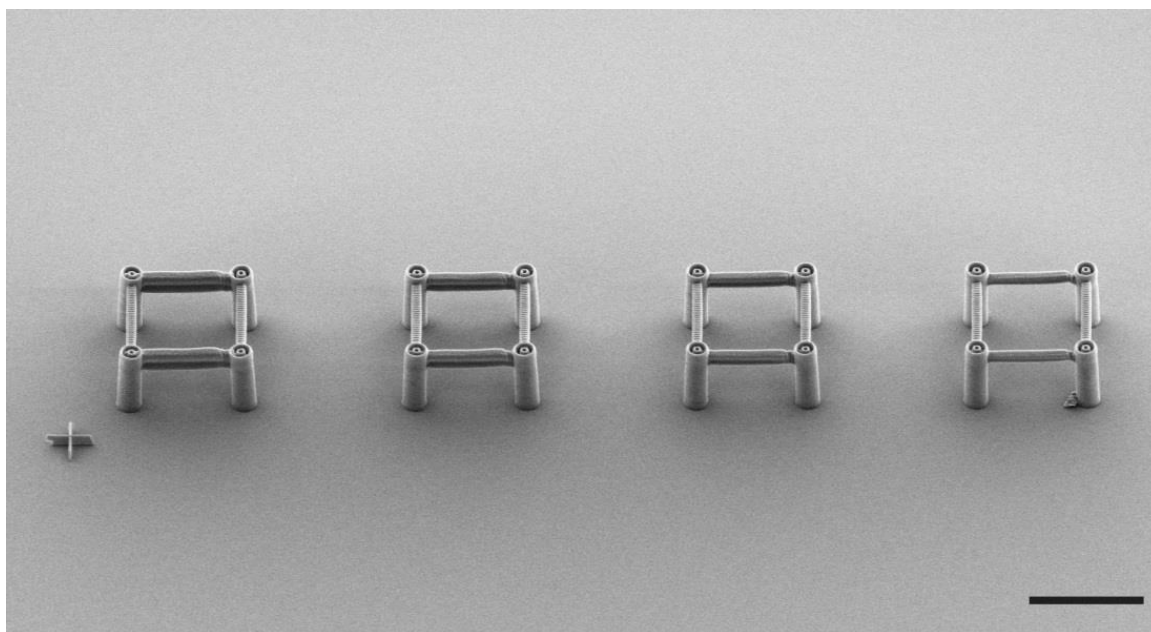


Figure 101: Influence of different power values for the spiral connection of a boxring-like scaffold. The divinyl adipate-based thiol-ene photoresist was employed to connect the pillars (horizontal connections) and the conditions were optimized (from left to right: 17.5 mW, 15.0 mW, 12.5 mW, and 10 mW) to achieve the best possible quality of the final structures (scale bar, 20 μm).

Nanoindentation along the x- or y-axis in z-direction						
E_r [MPa]	3.534	4.233	3.949	3.929	4.534	4.664
H [MPa]	0.681	0.729	0.662	0.628	0.769	0.899

Table 9: The reduced Young's modulus (E_r) and the hardness (H) of the divinyl adipate-based thiol-ene photoresist was measured via nanoindentation along the x- or y-axis in z-direction (stage of the printer set as lateral orientation, top of layers). The data possessed a smaller deviation compared to the measurements along the z-axis indicating a higher homogeneity. Utilization of a waiting segment of 12 s resulted in similar values. An exemplary load-displacement curve is depicted in **Figure 102**.

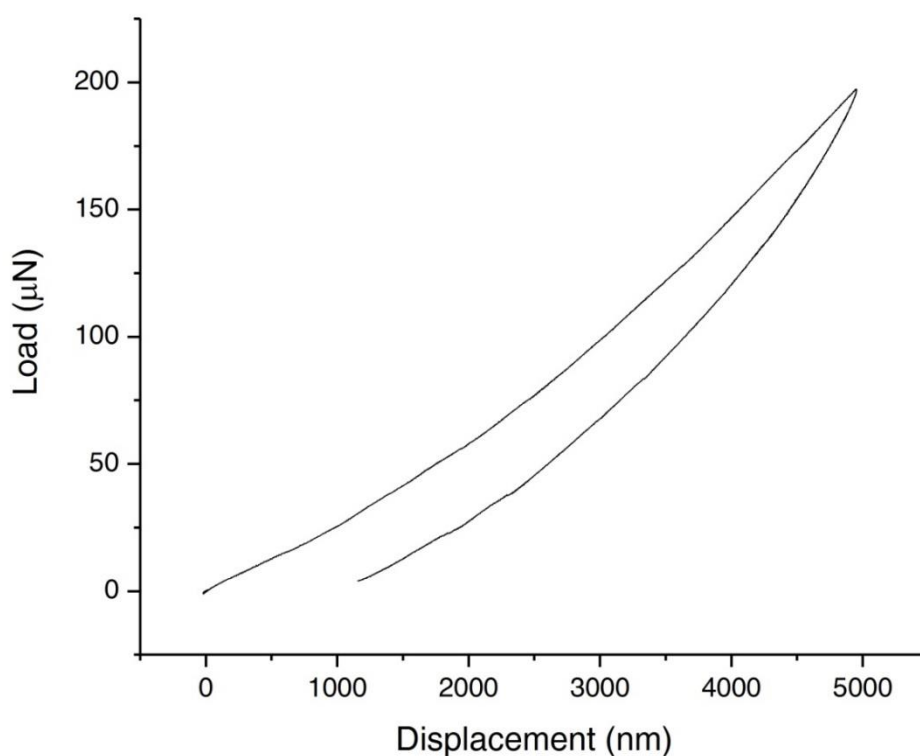


Figure 102: Exemplary load-displacement curve of the nanoindentation of the divinyl adipate-based thiol-ene photoresist along the x- or y-axis in z-direction (stage of the printer set as lateral orientation, top of layers).

Nanoindentation along the z-axis in x- or y- direction								
E_r [MPa]	4.275	4.686	3.507	4.031	8.315	11.08	8.854	11.972
H [MPa]	0.68	0.716	0.591	0.651	1.665	1.793	1.754	2.065

Table 10: The reduced Young's modulus (E_r) and the hardness (H) of the divinyl adipate-based thiol-ene photoresist was measured via nanoindentation along the z-axis in x- or y-direction (stage of the printer set as lateral orientation, side of layers). The data possessed a bigger deviation compared to the measurements along the top of the layers indicating an increased inhomogeneity. It is assumed that the penetration depth into the photoresist and cured material is playing a main role for this observation. Utilization of a waiting segment of 12 s during nanoindentation resulted in similar values. An exemplary load-displacement curve is depicted in **Figure 103**.

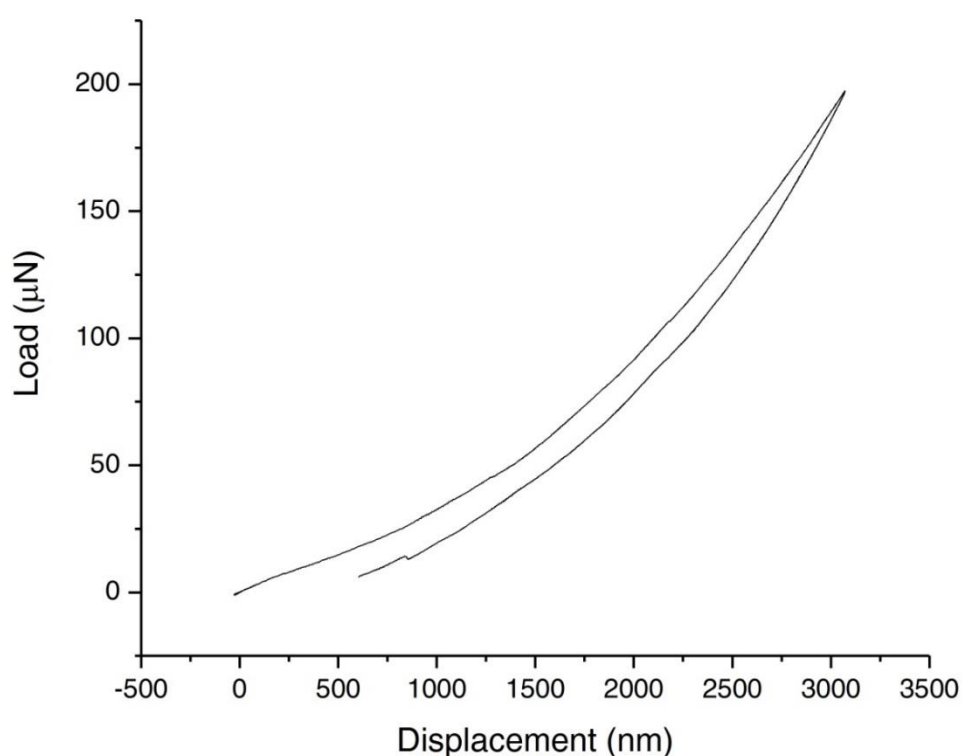


Figure 103: Exemplary load-displacement curve of the nanoindentation of the divinyl adipate-based thiol-ene photoresist along the z-axis in x- or y-direction (stage of the printer set as lateral orientation, side of layers).

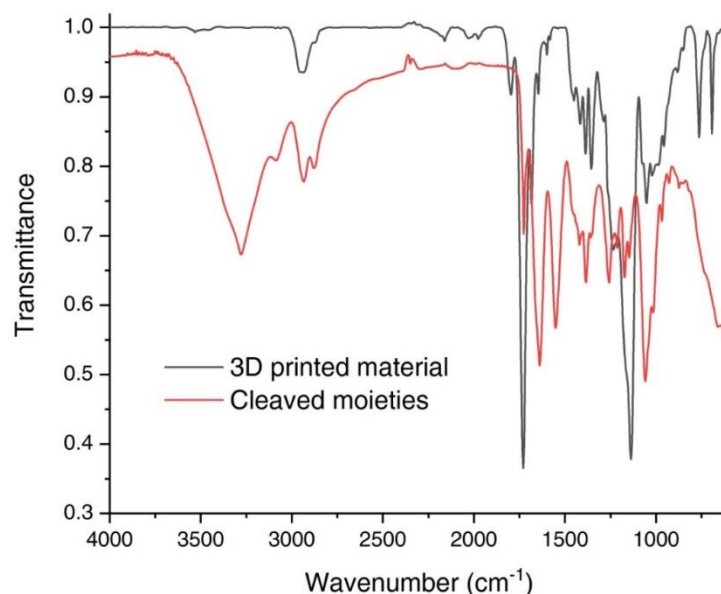


Figure 104: Fourier-Transform Infrared Spectroscopy (FT-IR) spectra of 3D printed structures employing the divinyl adipate-based thiol-ene photoresist and the dried residue after cleavage via ethanolamine. The cured material (black line) shows a strong band at 1750 cm⁻¹, which is a characteristic C=O bend of saturated ester moieties. After cleavage with 1 M ethanolamine solution in DMF at 50 °C for 7 h, the residue after drying was measured again (red line). A decrease of the C=O bend of the saturated ester moieties was revealed and the new band appearing at 1650 cm⁻¹ is a characteristic C=O stretch of amide derivatives. This observation strongly supports the supposed cleavage by amidation of ester bonds. New bands at 3250 cm⁻¹ and 1550 cm⁻¹ stem from residual ethanolamine (N-H bend, N-H and O-H stretch) and the N-H bend of amide moieties.

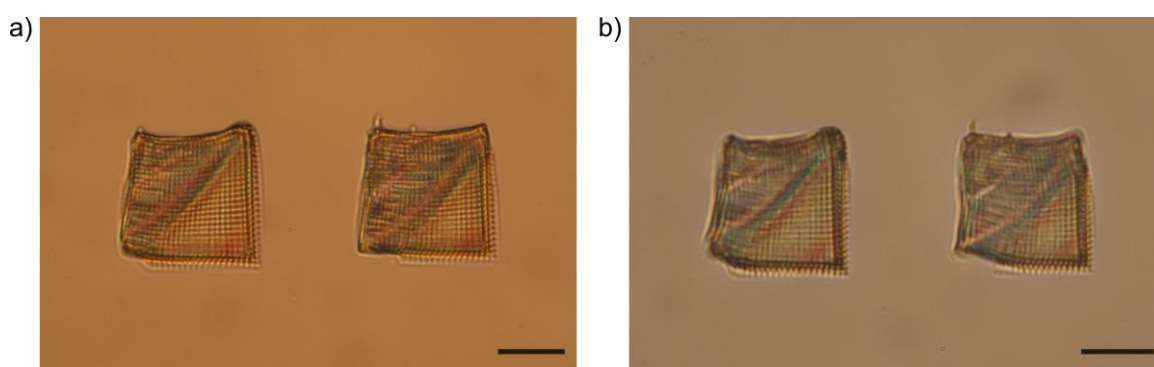


Figure 105: First attempts to cleave the disulfide-based network in aqueous 1 M DTT solution. Analysis of woodpile-type structures via light microscopy revealed no significant changes before (a) and after (b) immersion for 24 h. The silanization was not optimized yet and woodpiles were partially lifted off the surface and were deformed (scale bars, 10 μm).

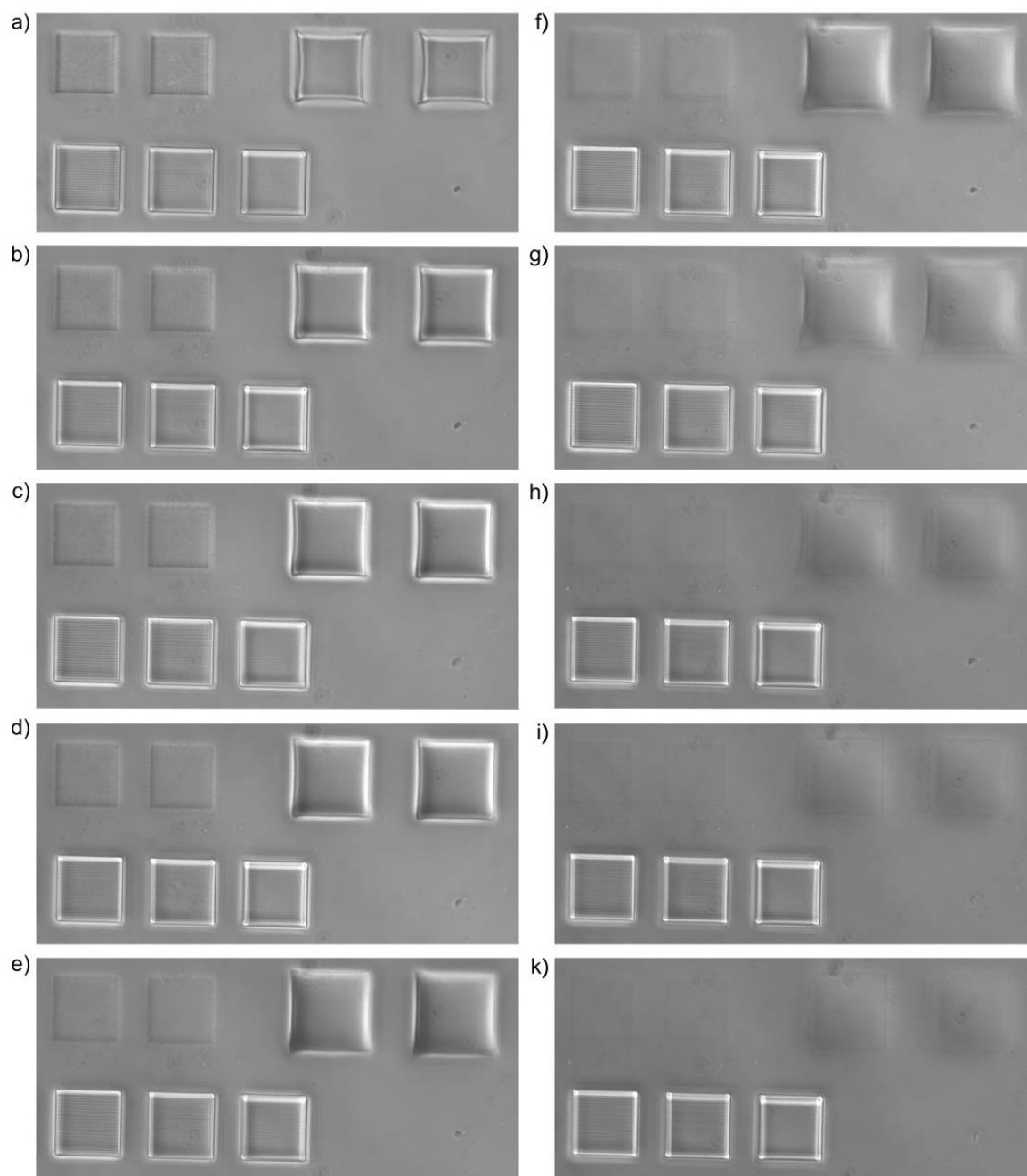


Figure 106: Time-lapse light microscopy images showing the cleavage of the disulfide networks (upper row, two woodpile-type objects on the left and two blocks on the right). To validate the selective removal, three woodpile-type structures were printed (bottom row). After immersion in 1 M DTT in DMF, the sample was heated to approximately 30 °C via a heated metal holder. Images were taken after 0 h (a), 1.5 h (b), 2.3 h (c), 3 h (d), 3.8 h (e), 4.6 h (f), 5.3 h (g), 6.1 h (h), 6.8 h (i) and 7 h (k). The time-lapse study validates a continuous cleavage.

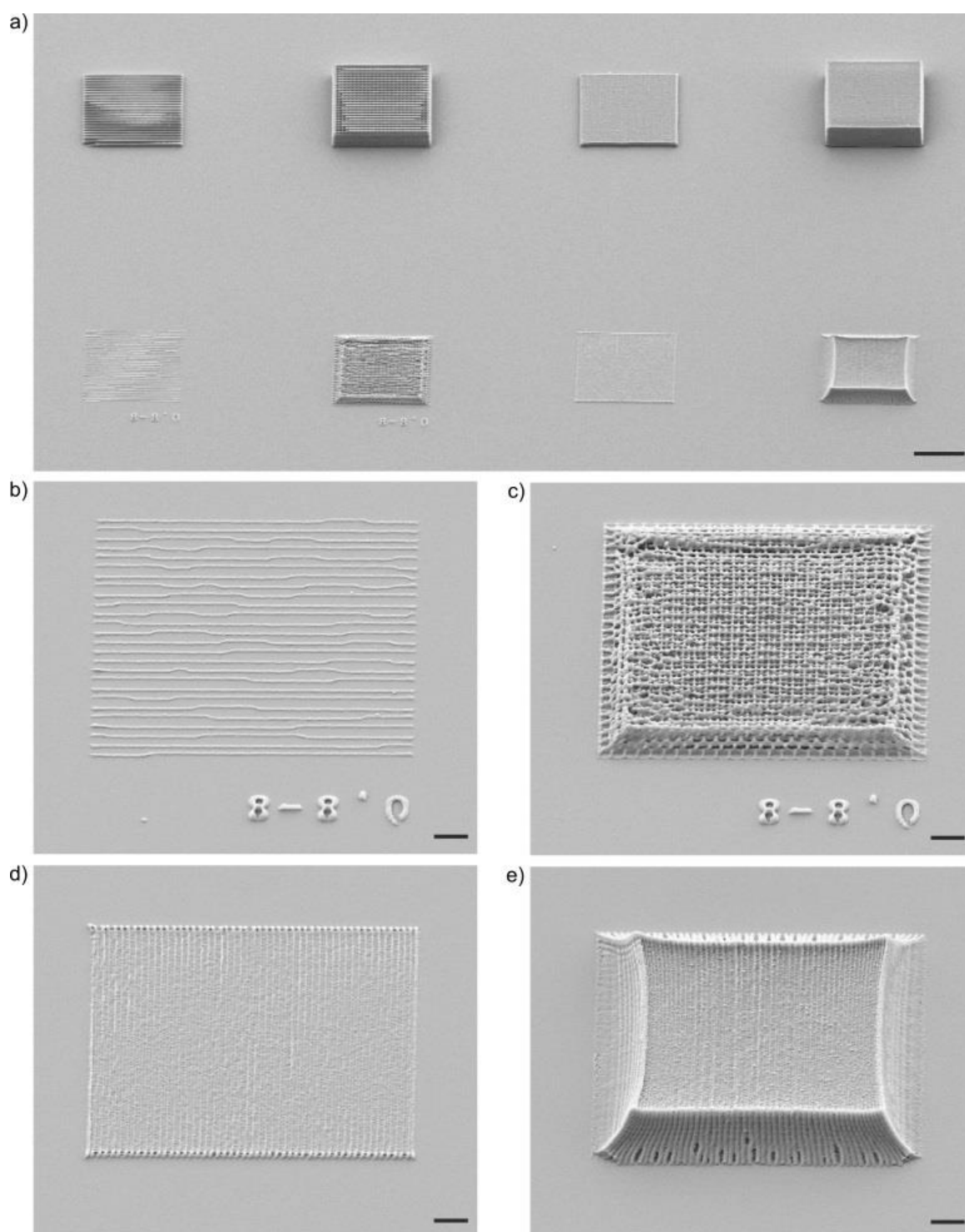


Figure 107: SEM images after immersion of an identical sample to **Figure 54** in DMF at 50 °C for 24 h. a) Control structures written with IP-L 780 (upper row) and the phenacyl sulfide-based networks (bottom row). The magnifications of the line array (b), the woodpile-type structure (c), the layer (d) and the block (e) based on the disulfide network, revealed no significant changes.

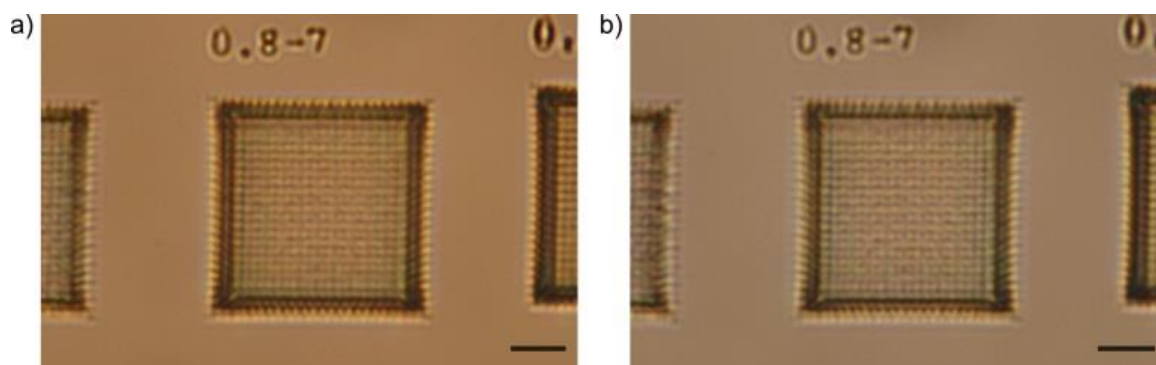


Figure 108: The treatment of disulfide networks with saturated TCEP HCL in DMF showed no significant changes before (a) and after 24 h (b) immersion (scale bars, 5 μm).

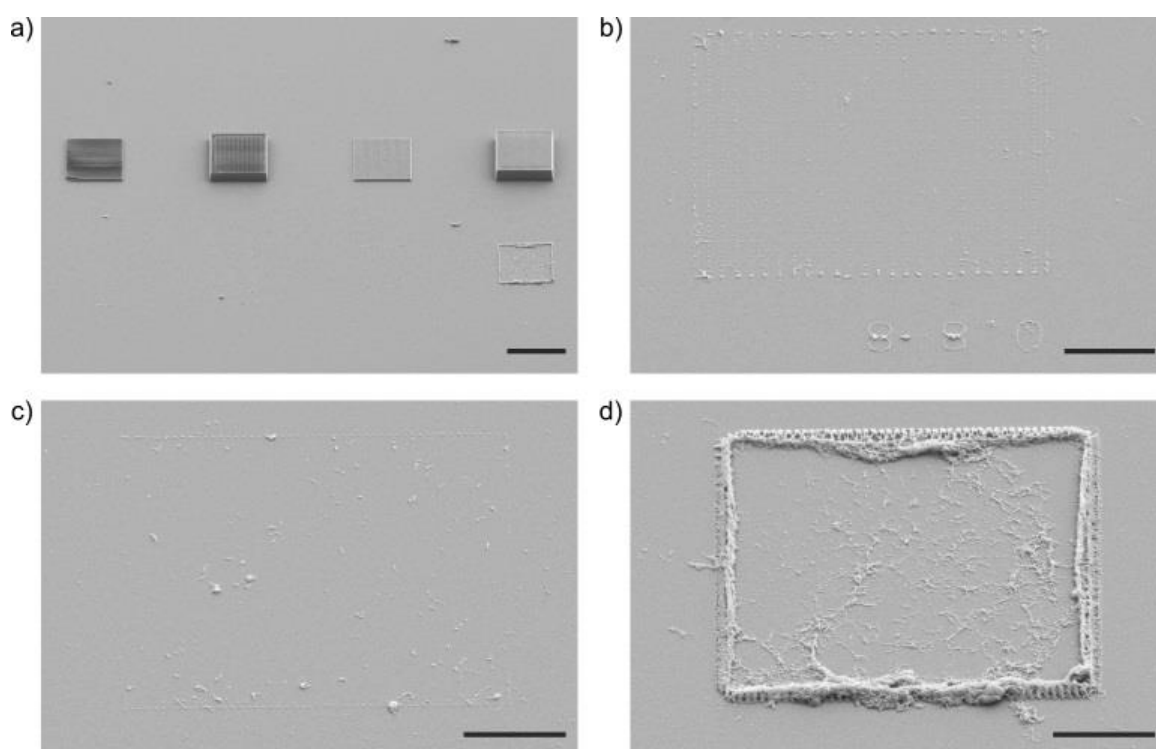


Figure 109: Residues after cleavage of the disulfide networks in 1 M DTT solution in DMF. a) Control structures (upper row) employing IP-L 780 were printed adjacent to the phenacyl sulfide-based structures. Magnifications of the woopile-like object (a), the layer (b) and the block (c) revealed residues, that were not cleaved. Later, it was observed that the problem could be solved by protection of the sample against heat during transportation between different facilities. In addition, longer storage times were avoided.

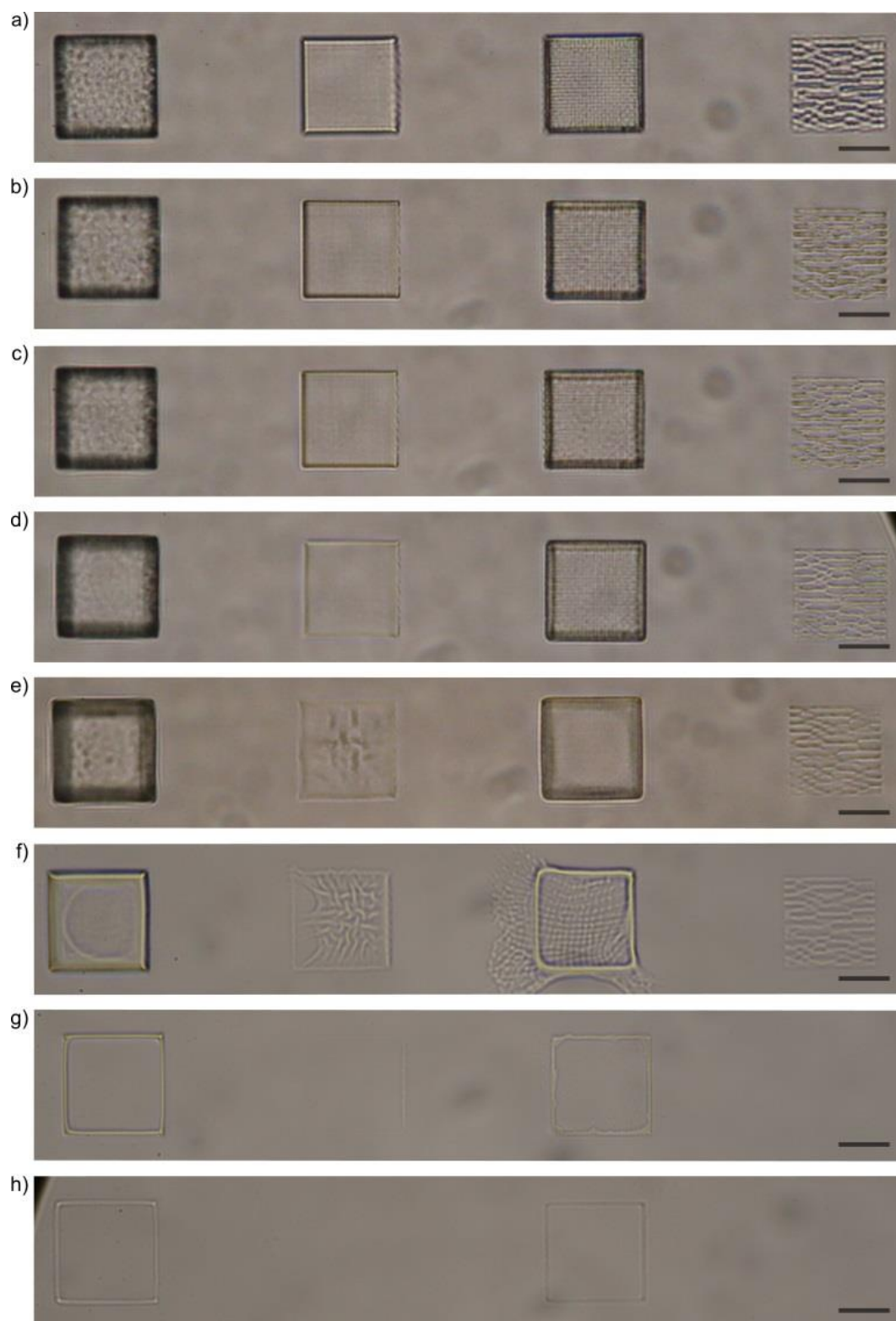


Figure 110: Investigation of the removal of divinyl adipate containing networks. The sample (a) was immersed in 1 M ethanolamine solution in DMF and light microscopy analysis was performed as a function of time. Images were taken after 3 h (b), 5 h (c), 7 h (d), 9 h (e), 11 h (f), 13 h (g) and 15 h (h) (scale bars, 10 μm).

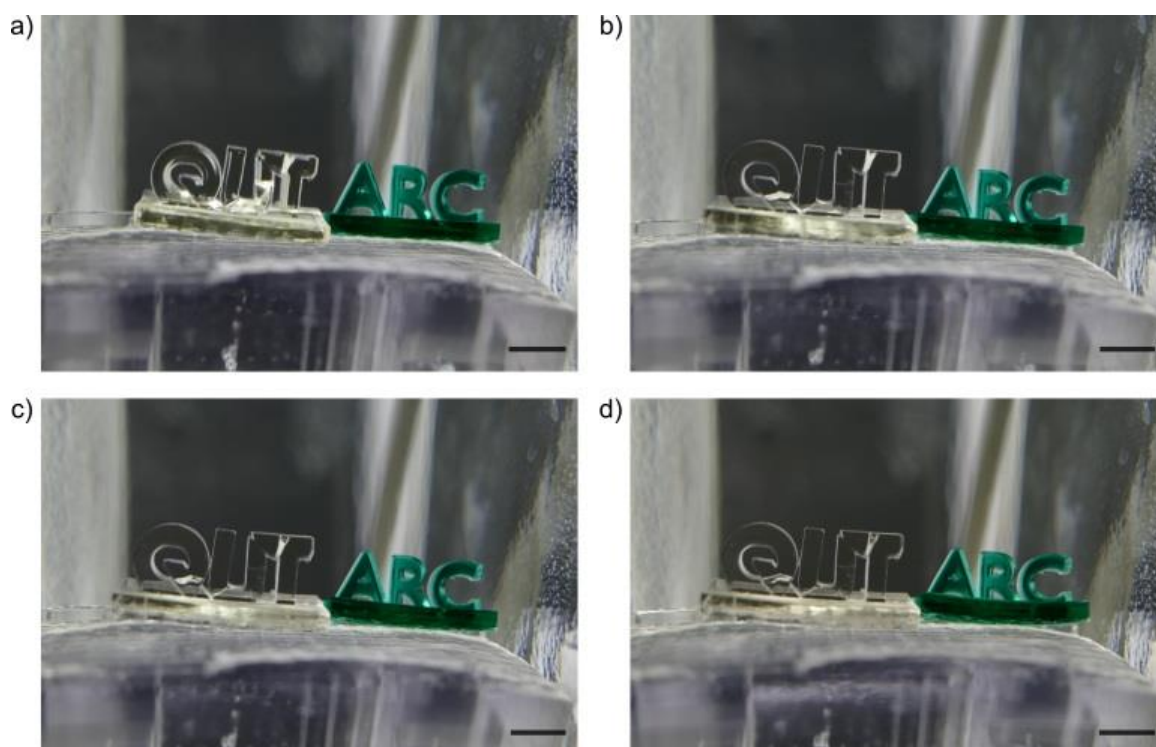


Figure 112: Control sample of the divynyl adipate-based thiol-ene photoresist to exclude the cleavage via mechanical stress introduced by the solvent DMF at 50 °C. The depicted images were taken directly after immersion (a), after 30 min (b), 1,25 h (c) and 7 h (d). A distinct swelling behavior was observed for the first hour in comparison to the next six hours where no change was visible anymore.

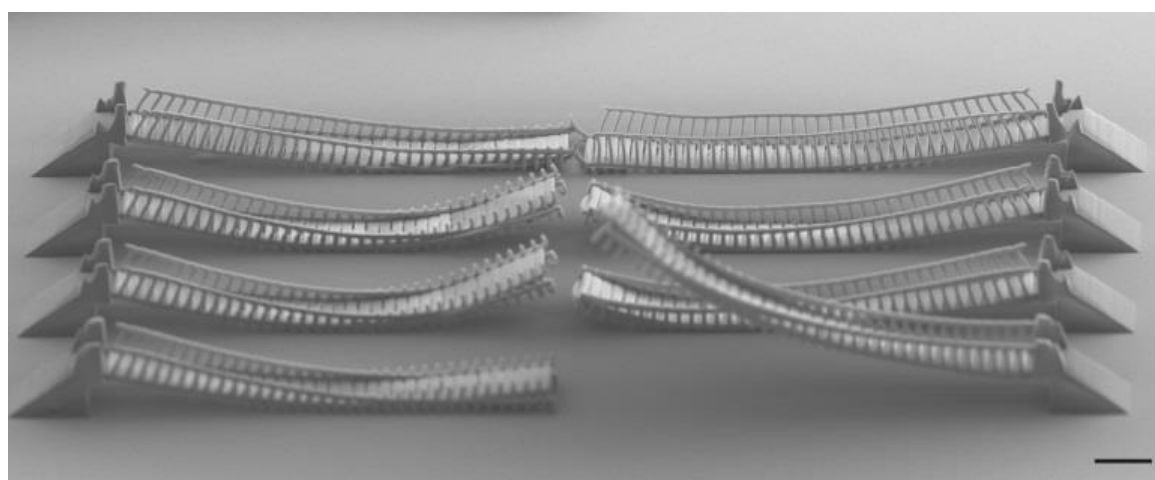


Figure 111: Influence of the employed laser power on the fabrication of freely suspended elements. The depicted rope bridges were printed with 17.5 mW, 20 mW, 20 mW and 22.5 mW (top to bottom) and the resulting deformation differed from each other.

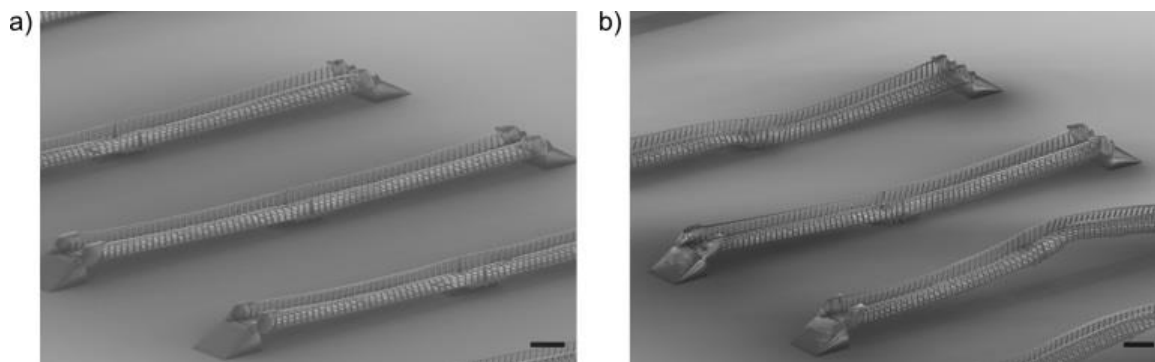


Figure 113: Complete images of **Figure 78**. a) The rope bridges were supported by a block to enable their fabrication. b) To remove the support structure, the sample was immersed in 1 M ethanolamine solution in DMF at 50 °C for 20 h. The dimensional stability strongly depended on the prior employed laser power during writing with the photoresist IP-L 780. From top left to bottom right, the bridges were fabricated with 20 mW, 22.5 mW and again 20 mW.

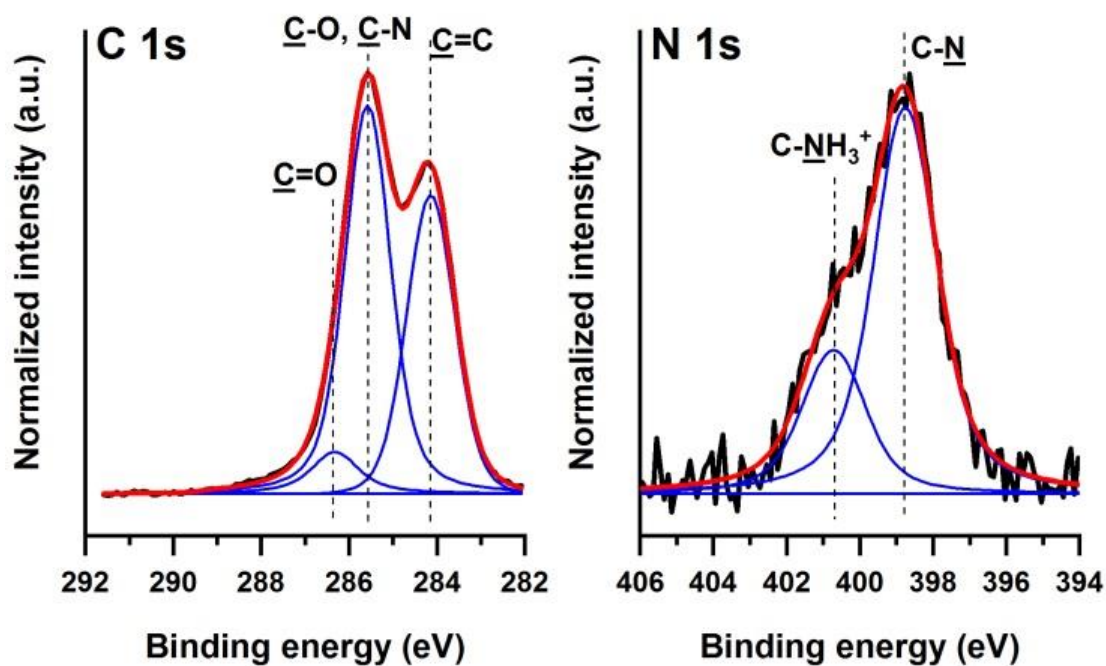


Figure 114: High-resolution C 1s and N 1s XPS spectra of the post-modified CyCat monomolecular layers employing NH₂-PEG(1500)-NH₂.

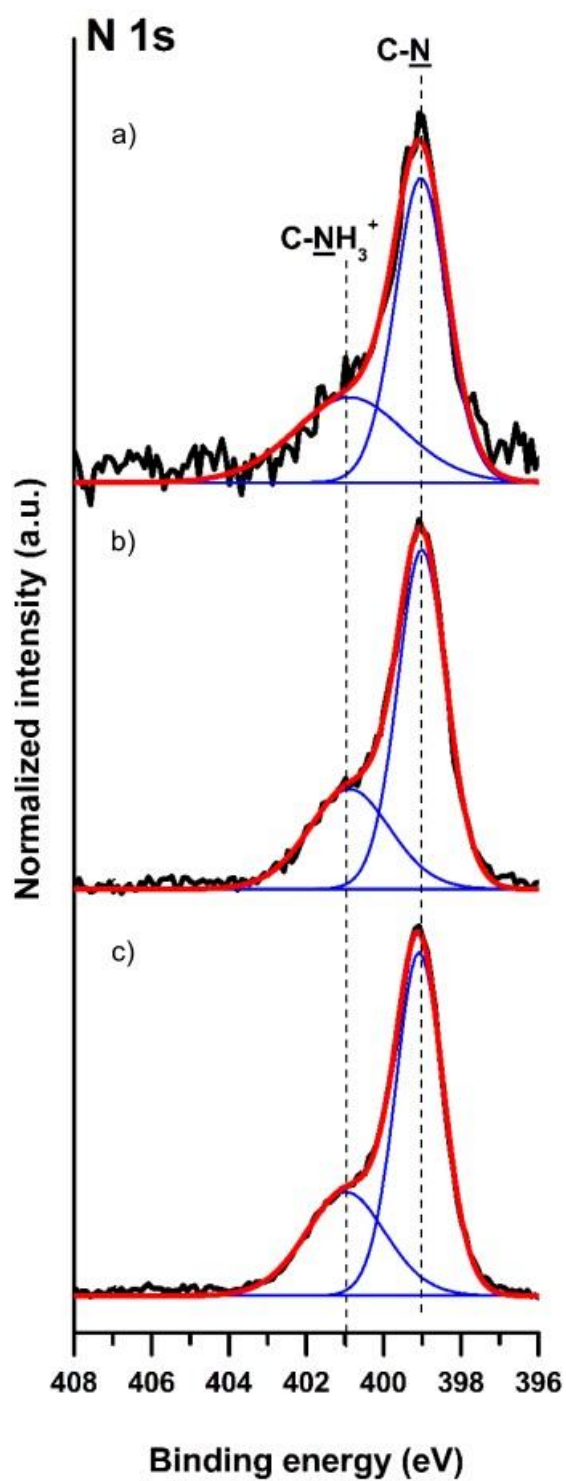


Figure 115: High-resolution N 1s XPS spectra of the CyCat-TREN multilayers ($n_{\text{layers}} = 12$) on Au (a), SiO_2 (b), and TiO_2 (c) substrates.

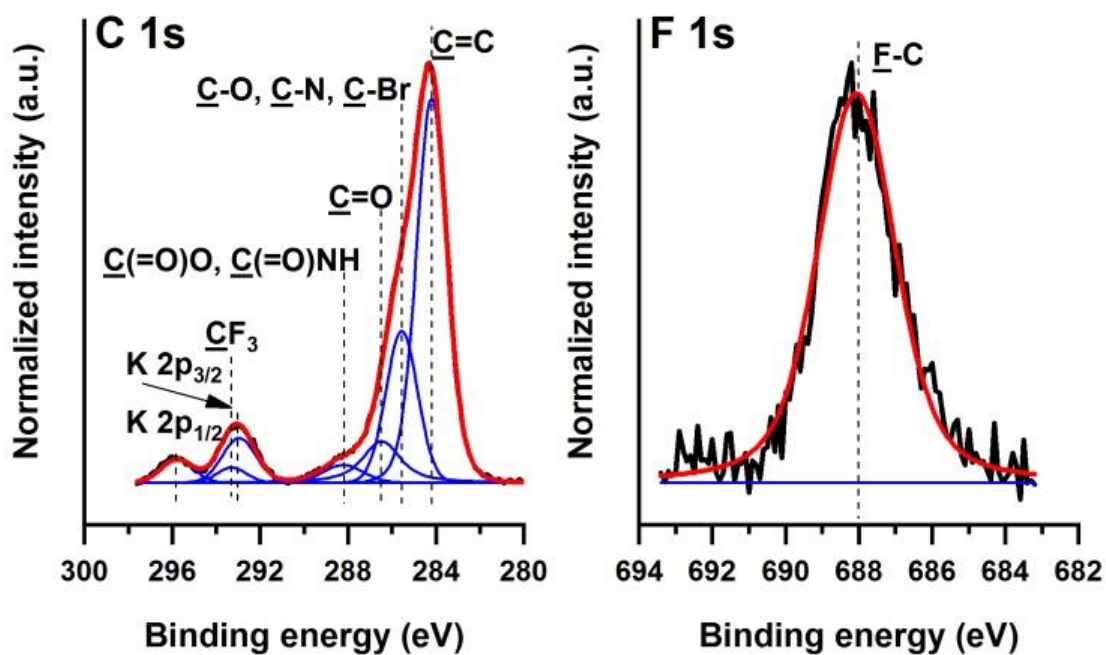


Figure 116: High-resolution C 1s and F 1s XPS spectra of the post-modification of the CyCat-TREN multilayers ($n_{\text{layers}} = 12$) employing trifluoroacetic anhydride.

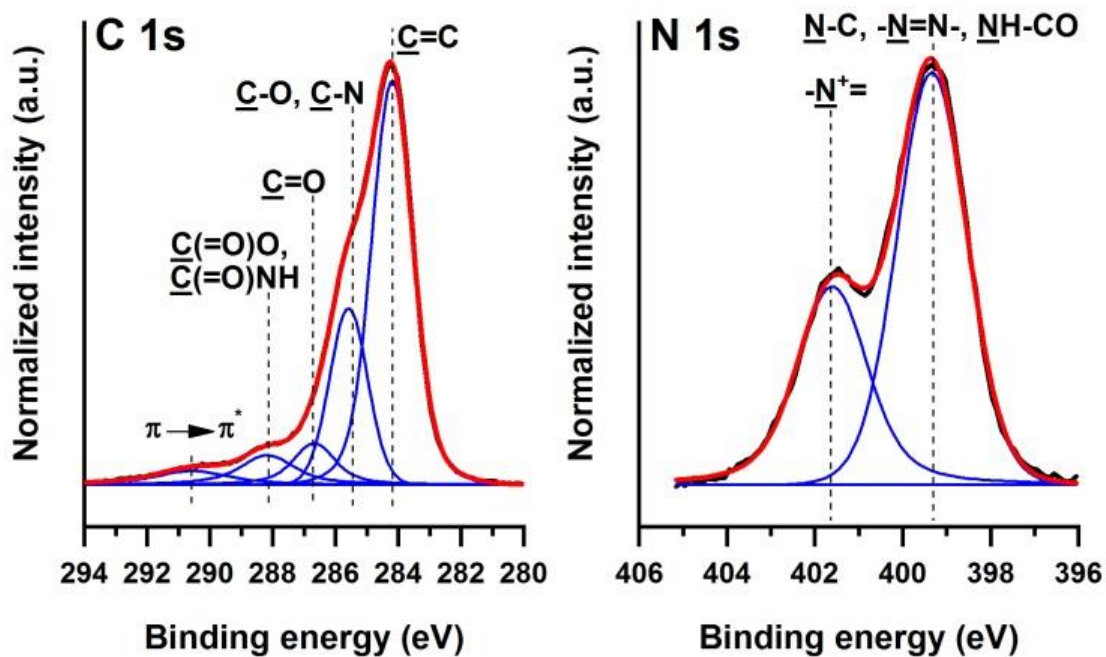


Figure 117: High-resolution C 1s and N 1s XPS spectra of the post-modification of the CyCat-TREN multilayers ($n_{\text{layers}} = 12$) employing a tetrazole bearing moiety.

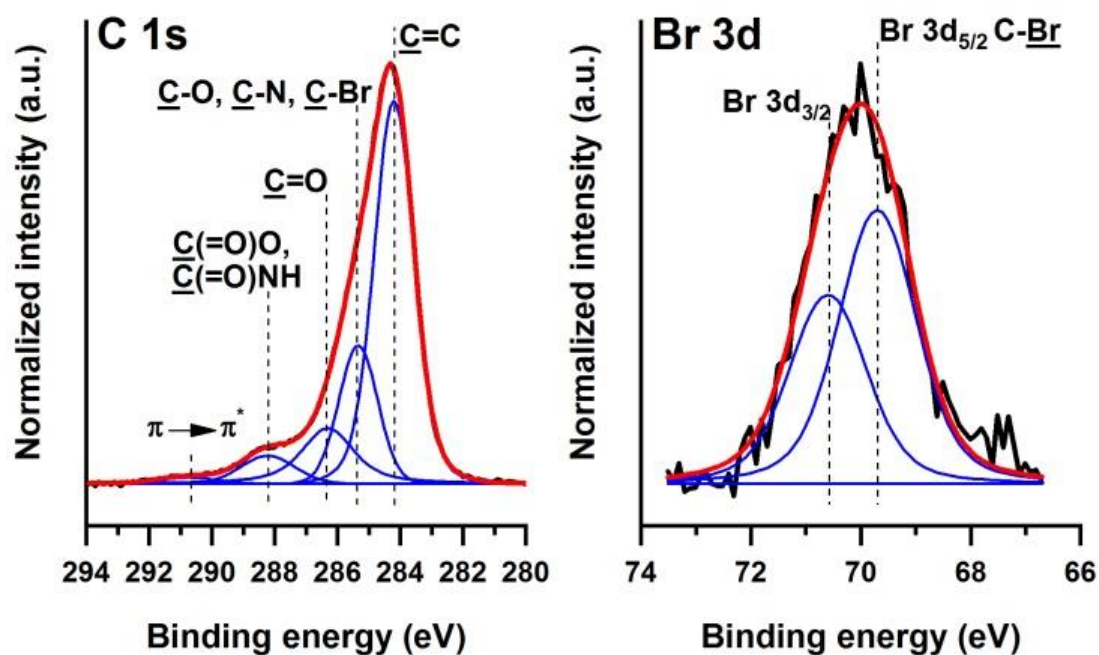


Figure 118: High-resolution C 1s and Br 3d XPS spectra of the post-modification of the CyCat-TREN multilayers ($n_{\text{layers}} = 12$) employing 2-bromo-2-methylpropionyl bromide.

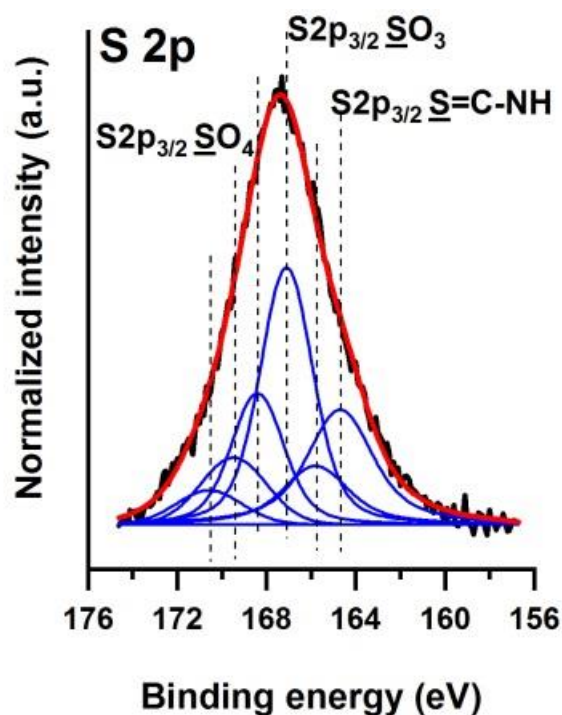


Figure 119: High-resolution S 2p XPS spectrum of the post-modification of the CyCat-TREN multilayers ($n_{\text{layers}} = 12$) employing a PEG functionalized phenacyl sulfide moiety.

Bibliography

- [1] M. C. Estevez, M. A. Otte, B. Sepulveda, L. M. Lechuga, *Analytica Chimica Acta* **2014**, 806, 55.
- [2] F. Nazneen, G. Herzog, D. W. M. Arrigan, N. Caplice, P. Benvenuto, P. Galvin, M. Thompson, *Journal of Biomedical Materials Research Part B: Applied Biomaterials* **2012**, 100B (7), 1989.
- [3] D. A. Puleo, A. Nanci, *Biomaterials* **1999**, 20 (23), 2311.
- [4] P. Qi, M. F. Maitz, N. Huang, *Surface and Coatings Technology* **2013**, 233, 80.
- [5] C. N. LaFratta, J. T. Fourkas, T. Baldacchini, R. A. Farrer, *Angewandte Chemie International Edition* **2007**, 46 (33), 6238.
- [6] A. Schleunitz, H. Schiff, *Microelectronic Engineering* **2011**, 88 (8), 2736.
- [7] E. MacDonald, R. Wicker, *Science* **2016**, 353 (6307), 1512.
- [8] J. H. Waite, *Integrative and Comparative Biology* **2002**, 42 (6), 1172.
- [9] H. Lee, S. M. Dellatore, W. M. Miller, P. B. Messersmith, *Science (New York, N.Y.)* **2007**, 318 (5849), 426.
- [10] O. Pop-Georgievski, Š. Popelka, M. Houska, D. Chvostová, V. Proks, F. Rypáček, *Biomacromolecules* **2011**, 12 (9), 3232.
- [11] O. Pop-Georgievski, C. Rodriguez-Emmenegger, A. d. I. S. Pereira, V. Proks, E. Brynda, F. Rypacek, *Journal of Materials Chemistry B* **2013**, 1 (22), 2859.
- [12] E. Faure, C. Falentin-Daudré, C. Jérôme, J. Lyskawa, D. Fournier, P. Woisel, C. Detrembleur, *Progress in Polymer Science* **2013**, 38 (1), 236.
- [13] W. Wei, L. Petrone, Y. Tan, H. Cai, J. N. Israelachvili, A. Miserez, J. H. Waite, *Advanced Functional Materials* **2016**, 26 (20), 3496.
- [14] M. M. Zieger, O. Pop-Georgievski, A. de los Santos Pereira, E. Verveniotis, C. M. Preuss, M. Zorn, B. Reck, A. S. Goldmann, C. Rodriguez-Emmenegger, C. Barner-Kowollik, *Langmuir* **2017**, 33 (3), 670.
- [15] T. Frenzel, M. Kadic, M. Wegener, *Science* **2017**, 358 (6366), 1072.
- [16] S. Maruo, J. T. Fourkas, *Laser & Photonics Reviews* **2008**, 2 (1-2), 100.
- [17] C. Barner-Kowollik, M. Bastmeyer, E. Blasco, G. Delaittre, P. Müller, B. Richter, M. Wegener, *Angewandte Chemie International Edition* **2017**, 56 (50), 15828.
- [18] K. Dietrich, D. Lehr, C. Helgert, A. Tünnermann, E. B. Kley, *Advanced Materials* **2012**, 24 (44), OP321.
- [19] N. Justh, L. P. Bakos, K. Hernádi, G. Kiss, B. Réti, Z. Erdélyi, B. Parditka, I. M. Szilágyi, *Scientific Reports* **2017**, 7 (1), 4337.
- [20] J. K. Gansel, M. Thiel, M. S. Rill, M. Decker, K. Bade, V. Saile, G. von Freymann, S. Linden, M. Wegener, *Science* **2009**, 325 (5947), 1513.
- [21] M. M. Zieger, P. Mueller, A. S. Quick, M. Wegener, C. Barner-Kowollik, *Angewandte Chemie International Edition* **2017**, 56 (20), 5625.
- [22] M. M. Zieger, P. Müller, E. Blasco, C. Petit, V. Hahn, L. Michalek, H. Mutlu, M. Wegener, C. Barner-Kowollik, *Advanced Functional Materials* **2018**, 1801405.
- [23] J. Wang, L. Du, S. Krause, C. Wu, P. Wang, *Sensors and Actuators B: Chemical* **2018**, 265, 161.
- [24] H. Park, Y. Park, W. Kim, W. Choi, *Journal of Photochemistry and Photobiology C: Photochemistry Reviews* **2013**, 15, 1.
- [25] R. G. Nuzzo, F. A. Fusco, D. L. Allara, *Journal of the American Chemical Society* **1987**, 109 (8), 2358.
- [26] H. Häkkinen, *Nature Chemistry* **2012**, 4, 443.

- [27] M. Stratmann, *Advanced Materials* **1990**, 2 (4), 191.
- [28] S. R. Wasserman, Y. T. Tao, G. M. Whitesides, *Langmuir* **1989**, 5 (4), 1074.
- [29] S. Turgman-Cohen, D. A. Fischer, P. K. Kilpatrick, J. Genzer, *ACS Applied Materials & Interfaces* **2009**, 1 (6), 1347.
- [30] O. Acton, D. Hutchins, L. Árnadóttir, T. Weidner, N. Cernetic, G. G. Ting, T.-W. Kim, D. G. Castner, H. Ma, A. K. Y. Jen, *Advanced materials (Deerfield Beach, Fla.)* **2011**, 23 (16), 1899.
- [31] C. Meltzer, H. Dietrich, D. Zahn, W. Peukert, B. Braunschweig, *Langmuir* **2015**, 31 (16), 4678.
- [32] G. Decher, *Science* **1997**, 277 (5330), 1232.
- [33] A. Gole, C. J. Murphy, *Chemistry of Materials* **2005**, 17 (6), 1325.
- [34] T. Lu, Y. Qiao, X. Liu, *Interface Focus* **2012**, 2 (3), 325.
- [35] S. P. Pujari, L. Scheres, A. T. M. Marcelis, H. Zuilhof, *Angewandte Chemie International Edition* **2014**, 53 (25), 6322.
- [36] B. H. Kim, D. H. Lee, J. Y. Kim, D. O. Shin, H. Y. Jeong, S. Hong, J. M. Yun, C. M. Koo, H. Lee, S. O. Kim, *Advanced Materials* **2011**, 23 (47), 5618.
- [37] R. A. Sperling, W. J. Parak, *Philosophical Transactions of the Royal Society A: Mathematical, Physical and Engineering Sciences* **2010**, 368 (1915), 1333.
- [38] H. Pingle, P. Y. Wang, H. Thissen, P. Kingshott, *Small* **2018**, 14 (14), 1703574.
- [39] F. P. Kord, B. P. Lee, *Journal of Polymer Science Part A: Polymer Chemistry* **2017**, 55 (1), 9.
- [40] H. Zhao, J. H. Waite, *Journal of Biological Chemistry* **2006**, 281 (36), 26150.
- [41] Y. H. Ding, M. Floren, W. Tan, *Biosurface and Biotribology* **2016**, 2 (4), 121.
- [42] O. Pop-Georgievski, D. Verreault, M.-O. Diesner, V. Proks, S. Heissler, F. Rypáček, P. Koelsch, *Langmuir* **2012**, 28 (40), 14273.
- [43] D. R. Dreyer, D. J. Miller, B. D. Freeman, D. R. Paul, C. W. Bielawski, *Langmuir* **2012**, 28 (15), 6428.
- [44] C.-T. Chen, C. Chuang, J. Cao, V. Ball, D. Ruch, M. J. Buehler, *Nature Communications* **2014**, 5, 3859.
- [45] J. Liebscher, R. Mrówczyński, H. A. Scheidt, C. Filip, N. D. Hädade, R. Turcu, A. Bende, S. Beck, *Langmuir* **2013**, 29 (33), 10539.
- [46] S. Meng, E. Kaxiras, *Biophysical Journal* **2008**, 94 (6), 2095.
- [47] A. Pezzella, L. Panzella, O. Crescenzi, A. Napolitano, S. Navaratman, R. Edge, E. J. Land, V. Barone, M. d'Ischia, *Journal of the American Chemical Society* **2006**, 128 (48), 15490.
- [48] A. Pezzella, A. Iadonisi, S. Valerio, L. Panzella, A. Napolitano, M. Adinolfi, M. d'Ischia, *Journal of the American Chemical Society* **2009**, 131 (42), 15270.
- [49] P. Meredith, B. J. Powell, J. Riesz, S. P. Nighswander-Rempel, M. R. Pederson, E. G. Moore, *Soft Matter* **2006**, 2 (1), 37.
- [50] G. Ciamician, *Science* **1912**, 36 (926), 385.
- [51] M. L. Wolbarsht, A. W. Walsh, G. George, *Applied Optics* **1981**, 20 (13), 2184.
- [52] H. C. Longuet-Higgins, *Archives of Biochemistry and Biophysics* **1960**, 86 (2), 231.
- [53] L.-S. Lin, Z.-X. Cong, J.-B. Cao, K.-M. Ke, Q.-L. Peng, J. Gao, H.-H. Yang, G. Liu, X. Chen, *ACS Nano* **2014**, 8 (4), 3876.
- [54] J. Rall, W. Kaim, *Journal of the Chemical Society, Faraday Transactions* **1994**, 90 (19), 2905.
- [55] M. S. Menyo, C. J. Hawker, J. H. Waite, *Soft Matter* **2013**, 9 (43), 10314.
- [56] C. Rodriguez-Emmenegger, C. M. Preuss, B. Yameen, O. Pop-Georgievski, M. Bachmann, J. O. Mueller, M. Bruns, A. S. Goldmann, M. Bastmeyer, C. Barner-Kowollik, *Advanced Materials* **2013**, 25 (42), 6123.
- [57] T. S. Sileika, H.-D. Kim, P. Maniak, P. B. Messersmith, *ACS Applied Materials & Interfaces* **2011**, 3 (12), 4602.
- [58] S. Wang, X. Zhao, S. Wang, J. Qian, S. He, *ACS Applied Materials & Interfaces* **2016**, 8 (37), 24368.

- [59] J. Park, T. F. Brust, H. J. Lee, S. C. Lee, V. J. Watts, Y. Yeo, *ACS Nano* **2014**, *8* (4), 3347.
- [60] J. Zhou, P. Wang, C. Wang, Y. T. Goh, Z. Fang, P. B. Messersmith, H. Duan, *ACS Nano* **2015**, *9* (7), 6951.
- [61] Y.-Z. Zhou, Y. Cao, W. Liu, C. H. Chu, Q.-L. Li, *ACS Applied Materials & Interfaces* **2012**, *4* (12), 6901.
- [62] C. M. Preuss, T. Tischer, C. Rodriguez-Emmenegger, M. M. Zieger, M. Bruns, A. S. Goldmann, C. Barner-Kowollik, *Journal of Materials Chemistry B* **2014**, *2* (1), 36.
- [63] L. Mihyun, R. Junsung, L. Dong-Eun, H. Seonki, C. Sun-Ju, M. P. B., L. Haeshin, *ChemPlusChem* **2012**, *77* (11), 987.
- [64] H. O. Ham, Z. Liu, K. H. A. Lau, H. Lee, P. B. Messersmith, *Angewandte Chemie International Edition* **2011**, *50* (3), 732.
- [65] H. Lee, J. Rho, P. B. Messersmith, *Advanced Materials* **2009**, *21* (4), 431.
- [66] Y. Yang, P. Qi, Y. Ding, M. F. Maitz, Z. Yang, Q. Tu, K. Xiong, Y. Leng, N. Huang, *Journal of Materials Chemistry B* **2015**, *3* (1), 72.
- [67] B. Yameen, C. Rodriguez-Emmenegger, C. M. Preuss, O. Pop-Georgievski, E. Verveniotis, V. Trouillet, B. Rezek, C. Barner-Kowollik, *Chemical Communications* **2013**, *49* (77), 8623.
- [68] T. L. Hopkins, K. J. Kramer, *Annual Review of Entomology* **1992**, *37* (1), 273.
- [69] M. Sugumaran, in *Advances in Insect Physiology*, Vol. 27 (Ed: P. D. Evans), Academic Press **1998**, p. 229.
- [70] S. L. Hong, H.; Lee, H., *Beilstein J. Nanotechnol.* **2014**, *5*, 8.
- [71] A. Miserez, T. Schneberk, C. Sun, F. W. Zok, J. H. Waite, *Science* **2008**, *319* (5871), 1816.
- [72] T. Utzig, P. Stock, M. Valtiner, *Angewandte Chemie International Edition* **2016**, *55* (33), 9524.
- [73] Y. Zhao, Y. Wu, L. Wang, M. Zhang, X. Chen, M. Liu, J. Fan, J. Liu, F. Zhou, Z. Wang, *Nature Communications* **2017**, *8* (1), 2218.
- [74] H. Shao, K. N. Bachus, R. J. Stewart, *Macromolecular Bioscience* **2009**, *9* (5), 464.
- [75] E. Kim, Y. Liu, X. W. Shi, X. Yang, W. E. Bentley, G. F. Payne, *Advanced Functional Materials* **2010**, *20* (16), 2683.
- [76] P. C. M., G. A. S., T. Vanessa, W. Andreas, B. K. Christopher, *Macromolecular Rapid Communications* **2013**, *34* (8), 640.
- [77] E. Amstad, T. Gillich, I. Bilecka, M. Textor, E. Reimhult, *Nano Letters* **2009**, *9* (12), 4042.
- [78] P. Glass, H. Chung, N. R. Washburn, M. Sitti, *Langmuir* **2009**, *25* (12), 6607.
- [79] M. Zorn, S. A. L. Weber, M. N. Tahir, W. Tremel, H.-J. Butt, R. Berger, R. Zentel, *Nano Letters* **2010**, *10* (8), 2812.
- [80] H. Chung, P. Glass, J. M. Pothen, M. Sitti, N. R. Washburn, *Biomacromolecules* **2011**, *12* (2), 342.
- [81] H. B. Na, G. Palui, J. T. Rosenberg, X. Ji, S. C. Grant, H. Mattoussi, *ACS Nano* **2012**, *6* (1), 389.
- [82] P. Wilke, H. G. Börner, *ACS Macro Letters* **2012**, *1* (7), 871.
- [83] K. Numata, P. J. Baker, *Biomacromolecules* **2014**, *15* (8), 3206.
- [84] K. C. L. Black, Z. Liu, P. B. Messersmith, *Chemistry of Materials* **2011**, *23* (5), 1130.
- [85] A. Isakova, P. D. Topham, A. J. Sutherland, *Macromolecules* **2014**, *47* (8), 2561.
- [86] D. Zhang, A. Martinez, J.-P. Dutasta, *Chemical Reviews* **2017**, *117* (6), 4900.
- [87] K. S. Liu, M. J. Li, C. C. Lai, S. H. Chiu, *Chemistry – A European Journal* **2016**, *22* (48), 17468.
- [88] H. Elisa, S. S. Artin, S. Eva, C. Enrique, B. Carles, d. M. Javier, *Chemistry – A European Journal* **2016**, *22* (38), 13496.
- [89] M. J. Hardie, *Chemical Society Reviews* **2010**, *39* (2), 516.
- [90] A. S. Lindsey, *Journal of the Chemical Society (Resumed)* **1965**, *0*, 1685.
- [91] R. Miranda, O. Valencia-Vázquez, C. Maya-Vega, I. Nicolás-Vázquez, Y. Vargas-Rodríguez, J. Morales-Serna, E. García-Ríos, M. Salmón, *Molecules* **2013**, *18* (10), 12820.

- [92] S. Zhang, A. Palkar, A. Fragoso, P. Prados, J. de Mendoza, L. Echegoyen, *Chemistry of Materials* **2005**, *17* (8), 2063.
- [93] F. Cai, J.-S. Shen, J.-H. Wang, H. Zhang, J.-S. Zhao, E.-M. Zeng, Y.-B. Jiang, *Organic & Biomolecular Chemistry* **2012**, *10* (7), 1418.
- [94] A. Chakrabarti, H. M. Chawla, G. Hundal, N. Pant, *Tetrahedron* **2005**, *61* (52), 12323.
- [95] P. T. Lee, J. E. Thomson, A. Karina, C. Salter, C. Johnston, S. G. Davies, R. G. Compton, *Analyst* **2015**, *140* (1), 236.
- [96] P. M. Budd, S. M. Makhseed, B. S. Ghanem, K. J. Msayib, C. E. Tattershall, N. B. McKeown, *Materials Today* **2004**, *7* (4), 40.
- [97] J.-T. Yu, Z. Chen, J. Sun, Z.-T. Huang, Q.-Y. Zheng, *Journal of Materials Chemistry* **2012**, *22* (12), 5369.
- [98] B. F. Abrahams, B. A. Boughton, N. J. FitzGerald, J. L. Holmes, R. Robson, *Chemical Communications* **2011**, *47* (26), 7404.
- [99] R. Xu, X. Huang, T. L. Hopkins, K. J. Kramer, *Insect Biochemistry and Molecular Biology* **1997**, *27* (2), 101.
- [100] S. C. Ligon, R. Liska, J. Stampfl, M. Gurr, R. Mülhaupt, *Chemical Reviews* **2017**, *117* (15), 10212.
- [101] M. Müller, J. Becher, M. Schnabelrauch, M. Zenobi-Wong, *Journal of Visualized Experiments : JoVE* **2013**, *77*, 50632.
- [102] J. D. Fowlkes, R. Winkler, B. B. Lewis, M. G. Stanford, H. Plank, P. D. Rack, *ACS Nano* **2016**, *10* (6), 6163.
- [103] M. Thiel, M. Hermatschweiler, *Optik & Photonik* **2011**, *6* (4), 36.
- [104] Y. P. Tsentalovich, P. S. Sherin, L. V. Kopylova, I. V. Cherepanov, J. Grilj, E. Vauthey, *Investigative Ophthalmology & Visual Science* **2011**, *52* (10), 7687.
- [105] G. H. Krause, E. Weis, *Annual Review of Plant Physiology and Plant Molecular Biology* **1991**, *42* (1), 313.
- [106] P. V. Kamat, *ACS Energy Letters* **2017**, *2* (9), 2157.
- [107] N. Hoffmann, *Chemical Reviews* **2008**, *108* (3), 1052.
- [108] A. Jablonski, *Nature* **1933**, *131*, 839.
- [109] D. Frackowiak, *Journal of Photochemistry and Photobiology B: Biology* **1988**, *2* (3), 399.
- [110] H. Schiff, *Applied Physics A* **2015**, *121* (2), 415.
- [111] Y. Chen, *Microelectronic Engineering* **2015**, *135*, 57.
- [112] H. Wenchuang, S. Koshala, L. Marya, H. B. Gary, *Journal of Vacuum Science & Technology B: Microelectronics and Nanometer Structures Processing, Measurement, and Phenomena* **2004**, *22* (4), 1711.
- [113] S. Mao, C. Sato, Y. Suzuki, J. Yang, H. Zeng, H. Nakajima, M. Yang, J. M. Lin, K. Uchiyama, *ChemPhysChem* **2016**, *17* (20), 3155.
- [114] Y. Li, B. W. Maynor, J. Liu, *Journal of the American Chemical Society* **2001**, *123* (9), 2105.
- [115] M. Hermatschweiler, *Laser Technik Journal* **2013**, *10* (4), 55.
- [116] W. Denk, J. Strickler, W. Webb, *Science* **1990**, *248* (4951), 73.
- [117] A. S. Quick, A. de los Santos Pereira, M. Bruns, T. Bückmann, C. Rodriguez-Emmenegger, M. Wegener, C. Barner-Kowollik, *Advanced Functional Materials* **2015**, *25* (24), 3735.
- [118] N. Tsutsumi, J. Hirota, K. Kinashi, W. Sakai, *Optics Express* **2017**, *25* (25), 31539.
- [119] J. Fischer, J. B. Mueller, J. Kaschke, T. J. A. Wolf, A.-N. Unterreiner, M. Wegener, *Optics Express* **2013**, *21* (22), 26244.
- [120] E. Blasco, J. Müller, P. Müller, V. Trouillet, M. Schön, T. Scherer, C. Barner-Kowollik, M. Wegener, *Advanced Materials* **2016**, *28* (18), 3592.
- [121] C. A. del, C. Greiner, *Journal of Micromechanics and Microengineering* **2007**, *17* (6), 15.
- [122] E. Blasco, M. Wegener, C. Barner-Kowollik, *Advanced Materials* **2017**, *29* (15), 1604005.

- [123] A. S. Quick, J. Fischer, B. Richter, T. Pauloehrl, V. Trouillet, M. Wegener, C. Barner-Kowollik, *Macromolecular Rapid Communications* **2013**, *34* (4), 335.
- [124] J. Kumpfmüller, K. Stadlmann, Z. Li, V. Satzinger, J. Stampfl, R. Liska, *Designed Monomers and Polymers* **2014**, *17* (4), 390.
- [125] B. J. Adzima, C. J. Kloxin, C. A. DeForest, K. S. Anseth, C. N. Bowman, *Macromolecular Rapid Communications* **2012**, *33* (24), 2092.
- [126] A. S. Quick, H. Rothfuss, A. Welle, B. Richter, J. Fischer, M. Wegener, C. Barner-Kowollik, *Advanced Functional Materials* **2014**, *24* (23), 3571.
- [127] J. Ye, H. Tan, S. Wu, K. Ni, F. Pan, J. Liu, Z. Tao, Y. Qu, H. Ji, P. Simon, Y. Zhu, *Advanced Materials* **2018**, 1801384.
- [128] F. Kotz, K. Arnold, W. Bauer, D. Schild, N. Keller, K. Sachsenheimer, T. M. Nargang, C. Richter, D. Helmer, B. E. Rapp, *Nature* **2017**, *544*, 337.
- [129] F. Chen, J. R. V. Aldana, *Laser & Photonics Reviews* **2014**, *8* (2), 251.
- [130] B. Richter, V. Hahn, S. Bertels, T. K. Claus, M. Wegener, G. Delaittre, C. Barner-Kowollik, M. Bastmeyer, *Advanced Materials* **2017**, *29* (5), 1604342.
- [131] S. Tottori, L. Zhang, F. Qiu, K. K. Krawczyk, A. Franco-Obregón, B. J. Nelson, *Advanced Materials* **2012**, *24* (6), 811.
- [132] T. Bückmann, M. Thiel, M. Kadic, R. Schittny, M. Wegener, *Nature Communications* **2014**, *5*, 4130.
- [133] P. Mueller, M. M. Zieger, B. Richter, A. S. Quick, J. Fischer, J. B. Mueller, L. Zhou, G. U. Nienhaus, M. Bastmeyer, C. Barner-Kowollik, M. Wegener, *ACS Nano* **2017**, *11* (6), 6396.
- [134] D. Wu, Q.-D. Chen, L.-G. Niu, J.-N. Wang, J. Wang, R. Wang, H. Xia, H.-B. Sun, *Lab on a Chip* **2009**, *9* (16), 2391.
- [135] J. Stampfl, S. Baudis, C. Heller, R. Liska, A. Neumeister, R. Kling, A. Ostendorf, M. Spitzbart, *Journal of Micromechanics and Microengineering* **2008**, *18* (12), 125014.
- [136] T. Billiet, M. Vandenhoute, J. Schelfhout, S. Van Vlierberghe, P. Dubruel, *Biomaterials* **2012**, *33* (26), 6020.
- [137] N. A. Chartrain, C. B. Williams, A. R. Whittington, *Acta Biomaterialia* **2018**, DOI: 10.1016/j.actbio.2018.05.010.
- [138] M. Carve, D. Wlodkovic, *Micromachines* **2018**, *9* (2), 91.
- [139] J. Z. Manapat, Q. Chen, P. Ye, R. C. Advincula, *Macromolecular Materials and Engineering* **2017**, *302* (9), 1600553.
- [140] T. J. Wallin, J. H. Pikul, S. Bodkhe, B. N. Peele, B. C. Mac Murray, D. Therriault, B. W. McEnerney, R. P. Dillon, E. P. Giannelis, R. F. Shepherd, *Journal of Materials Chemistry B* **2017**, *5* (31), 6249.
- [141] Z. Matt, L. Michael, C. Ido, S. Ela, C. Daniel, M. Shlomo, *Advanced Materials* **2016**, *28* (22), 4449.
- [142] E. Zanchetta, M. Cattaldo, G. Franchin, M. Schwentenwein, J. Homa, G. Brusatin, P. Colombo, *Advanced Materials* **2016**, *28* (2), 370.
- [143] A. B. Lowe, *Polymer Chemistry* **2014**, *5* (17), 4820.
- [144] T. K. Claus, B. Richter, V. Hahn, A. Welle, S. Kayser, M. Wegener, M. Bastmeyer, G. Delaittre, C. Barner-Kowollik, *Angewandte Chemie International Edition* **2016**, *55* (11), 3817.
- [145] W. M. McGregor, D. C. Sherrington, *Chemical Society Reviews* **1993**, *22* (3), 199.
- [146] P. Metzner, *Synthesis* **1992**, *1992* (12), 1185.
- [147] E. Vedejs, T. H. Eberlein, D. J. Mazur, C. K. McClure, D. A. Perry, R. Ruggeri, E. Schwartz, J. S. Stults, D. L. Varie, *The Journal of Organic Chemistry* **1986**, *51* (9), 1556.
- [148] T. Tischer, T. K. Claus, K. K. Oehlenschlaeger, V. Trouillet, M. Bruns, A. Welle, K. Linkert, A. S. Goldmann, H. G. Börner, C. Barner-Kowollik, *Macromolecular Rapid Communications* **2014**, *35* (12), 1121.

- [149] T. Pauloehrl, A. Welle, K. K. Oehlschlaeger, C. Barner-Kowollik, *Chemical Science* **2013**, 4 (9), 3503.
- [150] T. K. Claus, J. Zhang, L. Martin, M. Hartlieb, H. Mutlu, S. Perrier, G. Delaittre, C. Barner-Kowollik, *Macromolecular Rapid Communications* **2017**, 38 (16), 1700264.
- [151] E.-K. Bang, M. Lista, G. Sforazzini, N. Sakai, S. Matile, *Chemical Science* **2012**, 3 (6), 1752.
- [152] V. V. Rogov, N. Y. Rogova, F. Bernhard, F. Löhr, V. Dötsch, *Journal of Biological Chemistry* **2011**, 286 (21), 18775.
- [153] B. K. W. Chung, A. K. Yudin, *Organic & Biomolecular Chemistry* **2015**, 13 (33), 8768.
- [154] D. Witt, *Synthesis* **2008**, 2008 (16), 2491.
- [155] E. Ellis, K. Zhang, Q. Lin, E. Ye, A. Poma, G. Battaglia, X. J. Loh, T.-C. Lee, *Journal of Materials Chemistry B* **2017**, 5 (23), 4421.
- [156] F. Noémi, C. Abraham, L. Christian, C. B. Céline, A. Xavier, P. Arnaud, L. N. Didier, M. Hicham, J. Léandro, *Macromolecular Rapid Communications* **2016**, 37 (2), 155.
- [157] X. Du, F. Kleitz, X. Li, H. Huang, X. Zhang, S. Z. Qiao, *Advanced Functional Materials* **2018**, 1707325.
- [158] J. Canadell, H. Goossens, B. Klumperman, *Macromolecules* **2011**, 44 (8), 2536.
- [159] L. Wang, L. Li, X. Wang, D. Huang, F. Yang, H. Shen, Z. Li, D. Wu, *Polymer Chemistry* **2016**, 7 (7), 1429.
- [160] E. H. Charles, N. B. Christopher, *Angewandte Chemie International Edition* **2010**, 49 (9), 1540.
- [161] S. Melahat, A. K. Santhosh, M. Jakob, W. Markus, K. Wolfgang, S. Sandra, *Advanced Engineering Materials* **2017**, 19 (4), 1600620.
- [162] N. B. Cramer, J. P. Scott, C. N. Bowman, *Macromolecules* **2002**, 35 (14), 5361.
- [163] J. Xuan, W. J. Xiao, *Angewandte Chemie International Edition* **2012**, 51 (28), 6828.
- [164] E. L. Tyson, Z. L. Niemeyer, T. P. Yoon, *The Journal of Organic Chemistry* **2014**, 79 (3), 1427.
- [165] B. H. Northrop, R. N. Coffey, *Journal of the American Chemical Society* **2012**, 134 (33), 13804.
- [166] K. L. Killops, L. M. Campos, C. J. Hawker, *Journal of the American Chemical Society* **2008**, 130 (15), 5062.
- [167] V. Granskog, S. García-Gallego, J. von Kieseritzky, J. Rosendahl, P. Stenlund, Y. Zhang, S. Petronis, B. Lyvén, M. Arner, J. Håkansson, M. Malkoch, *Advanced Functional Materials* **2018**, 1800372.
- [168] T. Pauloehrl, G. Delaittre, M. Bastmeyer, C. Barner-Kowollik, *Polymer Chemistry* **2012**, 3 (7), 1740.
- [169] R. J. Williams, I. A. Barker, R. K. O'Reilly, A. P. Dove, *ACS Macro Letters* **2012**, 1 (11), 1285.
- [170] C. R. Langford, D. W. Johnson, N. R. Cameron, *Polymer Chemistry* **2014**, 5 (21), 6200.
- [171] A. S. Quick, J. Fischer, B. Richter, T. Pauloehrl, V. Trouillet, M. Wegener, C. Barner-Kowollik, *Macromolecular Rapid Communications* **2013**, 34 (4), 335.
- [172] D. G. Sycks, T. Wu, H. S. Park, K. Gall, *Journal of Applied Polymer Science* **2018**, 135 (22), 46259.
- [173] S. P. S. Koo, M. M. Stamenović, R. A. Prasath, A. J. Inglis, F. E. Du Prez, C. Barner-Kowollik, W. Van Camp, T. Junkers, *Journal of Polymer Science Part A: Polymer Chemistry* **2010**, 48 (8), 1699.
- [174] A. B. Lowe, C. E. Hoyle, C. N. Bowman, *Journal of Materials Chemistry* **2010**, 20 (23), 4745.
- [175] R. Hoogenboom, *Angewandte Chemie International Edition* **2010**, 49 (20), 3415.
- [176] B. D. Fairbanks, T. F. Scott, C. J. Kloxin, K. S. Anseth, C. N. Bowman, *Macromolecules* **2009**, 42 (1), 211.
- [177] A. B. Cook, R. Barbey, J. A. Burns, S. Perrier, *Macromolecules* **2016**, 49 (4), 1296.
- [178] L. Sun, W. Liu, C.-M. Dong, *Chemical Communications* **2011**, 47 (40), 11282.

- [179] A. Oesterreicher, J. Wiener, M. Roth, A. Moser, R. Gmeiner, M. Edler, G. Pinter, T. Griesser, *Polymer Chemistry* **2016**, 7 (32), 5169.
- [180] S. Zhang, A. Li, J. Zou, L. Y. Lin, K. L. Wooley, *ACS Macro Letters* **2012**, 1 (2), 328.
- [181] K. S. Soppimath, T. M. Aminabhavi, A. R. Kulkarni, W. E. Rudzinski, *Journal of Controlled Release* **2001**, 70 (1), 1.
- [182] N. W. S. Kam, Z. Liu, H. Dai, *Journal of the American Chemical Society* **2005**, 127 (36), 12492.
- [183] D.-S. Guo, K. Wang, Y.-X. Wang, Y. Liu, *Journal of the American Chemical Society* **2012**, 134 (24), 10244.
- [184] Q. Zhang, N. Re Ko, J. Kwon Oh, *Chemical Communications* **2012**, 48 (61), 7542.
- [185] H. Wei, R.-X. Zhuo, X.-Z. Zhang, *Progress in Polymer Science* **2013**, 38 (3), 503.
- [186] V. Bhagat, M. L. Becker, *Biomacromolecules* **2017**, 18 (10), 3009.
- [187] C. J. Higginson, S. Y. Kim, M. Peláez-Fernández, A. Fernández-Nieves, M. G. Finn, *Journal of the American Chemical Society* **2015**, 137 (15), 4984.
- [188] R. Haag, F. Kratz, *Angewandte Chemie International Edition* **2006**, 45 (8), 1198.
- [189] D. Kokkinis, M. Schaffner, A. R. Studart, *Nature Communications* **2015**, 6, 8643.
- [190] J. Kaschke, M. Wegener, in *Nanophotonics* **2016**, 5, 510.
- [191] A.-C. Albertsson, M. Hakkarainen, *Science* **2017**, 358 (6365), 872.
- [192] R. Liska, F. Schwager, C. Maier, R. Cano-Vives, J. Stampfl, *Journal of Applied Polymer Science* **2005**, 97 (6), 2286.
- [193] Y. Wang, J. Gao, Z. Kang, *Computer Methods in Applied Mechanics and Engineering* **2018**, DOI:10.1016/j.cma.2018.04.040.
- [194] Y. Liao, N. An, N. Wang, Y. Zhang, J. Song, J. Zhou, W. Liu, *Macromolecular Rapid Communications* **2015**, 36 (24), 2129.
- [195] A. N. Koo, H. J. Lee, S. E. Kim, J. H. Chang, C. Park, C. Kim, J. H. Park, S. C. Lee, *Chemical Communications* **2008**, 0 (48), 6570.
- [196] S. Brocchini, A. Godwin, S. Balan, J.-w. Choi, M. Zloh, S. Shaunak, *Advanced Drug Delivery Reviews* **2008**, 60 (1), 3.
- [197] A. M. Schenzel, C. Klein, K. Rist, N. Moszner, C. Barner-Kowollik, *Advanced Science* **2016**, 3 (3), 1500361.
- [198] J. Steinkoenig, M. M. Zieger, H. Mutlu, C. Barner-Kowollik, *Macromolecules* **2017**, 50 (14), 5385.
- [199] A. Ficaí, E. Andronescu, D. Ficaí, M. Sonmez, M. Albu, G. Voicu, in *Open Chemistry* **2012**, 10, 1949.
- [200] C. M. R. Clancy, J. D. Simon, *Biochemistry* **2001**, 40 (44), 13353.
- [201] D. M. Jones, A. A. Brown, W. T. S. Huck, *Langmuir* **2002**, 18 (4), 1265.
- [202] C. Barner-Kowollik, M. Bastmeyer, E. Blasco, G. Delaittre, P. Müller, B. Richter, M. Wegener, *Angewandte Chemie International Edition* **2017**, 56 (50), 15828.
- [203] K. G. Justyna, L. Michael, F. Andreas, K. Johannes, T. Michael, W. Martin, *Applied Physics Letters* **2012**, 100 (10), 101109.
- [204] J. B. Mueller, J. Fischer, F. Mayer, M. Kadic, M. Wegener, *Advanced Materials* **2014**, 26 (38), 6566.
- [205] K. L. Parry, A. G. Shard, R. D. Short, R. G. White, J. D. Whittle, A. Wright, *Surface and Interface Analysis* **2006**, 38 (11), 1497.
- [206] S. Tanuma, C. J. Powell, D. R. Penn, *Surface and Interface Analysis* **1994**, 21 (3), 165.
- [207] J. H. Scofield, *Journal of Electron Spectroscopy and Related Phenomena* **1976**, 8 (2), 129.
- [208] M. Nonnenmacher, M. P. O'Boyle, H. K. Wickramasinghe, *Applied Physics Letters* **1991**, 58 (25), 2921.
- [209] K. Petr, O. Ivan, M.-R. Alberto, B. Alberta, S. David, S. Helmut, *Japanese Journal of Applied Physics* **2003**, 42 (7S), 4706.

List of Figures

Figure 1: Coating of materials employing the self-polymerization of dopamine. a) The hydrophilicity of a tomato (left) is compared to a polydopamine (PDA) coated one revealing significant changes. b) A teflon substrate that possesses a low surface energy is coated with PDA (right side of the wafer) altering the wettability of the surface. Adapted with permission from Ref.[36]. Copyright 2011 John Wiley and Sons.	7
Figure 2: Schematic depiction of the possible processes during the self-polymerization of dopamine in a slightly alkaline TRIS buffer solution. Adapted with permission from Ref.[42]. Copyright 2012 American Chemical Society.	8
Figure 3: Proposal for the structure of PDA. Different oxidative states are responsible for the formation of mainly linear polymers that form strong, partially covalent, and non-covalent interactions. Adapted with permission from Ref.[45]. Copyright 2013 American Chemical Society.....	9
Figure 4: Simulation of the broadband monotonic absorbance profile of eumelanin utilizing a linear combination of 11 Gaussians of similar but chemically distinct species. Reproduced with permission from Ref.[49]. Copyright 2005 Royal Society of Chemistry.	10
Figure 5: Spatially resolved attachment of non-fouling brushes onto PDA coatings. a) Surface photopatterning via post-modification of PDA films utilizing photoactive tetrazole moieties enabled the precise immobilization of an ATRP initiator. b) To assess the functionalization, time-of-flight secondary ion mass spectrometry (ToF-SIMS) was conducted revealing patterns with a high spatial resolution. c) The growth of poly(MeOEGMA) in a SI-ATRP fashion provided a non-fouling pattern that prevented the adhesion of cells on the protected areas. Adapted with permission from Ref.[56]. Copyright 2013 John Wiley and Sons.	11
Figure 6: Multifunctional nanoplatform based on gold nanorods (GNR) for photodynamic and photothermal therapy (PDT/PTT). The GNRs are coated with cetyltrimethylammonium bromide (CTAB) and PEG to prevent agglomeration. After coating with PDA, methylene blue and doxorubicin are successfully adsorbed onto the coatings to serve as a drug delivery system. Reproduced with permission from Ref.[58]. Copyright 2016 American Chemical Society.....	12

-
- Figure 7:** Proposed mechanism for the adhesion of catechol groups under aqueous conditions. The synthetic homologue of a mussel foot protein forms coacervates in solution that are capable to bind to the TiO₂ substrate. It is assumed that inner- and outer-sphere complexes are responsible for the adhesion mechanism. Reproduced with permission from Ref.[13]. Copyright 2016 John Wiley and Sons. 14
- Figure 8:** Synthesis route for the provision of a dopamine methacrylamide monomer. The one-step reaction employs dopamine hydrochloride and methacrylic acid anhydride as educts. Adapted with the permission from Ref.[78]. Copyright 2009 American Chemical Society. ... 16
- Figure 9:** Synthesis of highly functional catechol-containing copolymers via the amidation of poly(acrylic acid). The utilization of reactive endgroups attached to the amine-bearing PEG chains enabled the subsequent modification of the surfaces after immobilization with catechol anchors. Adapted with permission from Ref.[81]. Copyright 2012 American Chemical Society..... 17
- Figure 10:** Preparation of cyclotrimeratrylene utilizing the condensation reaction of veratrole alcohol under harsh acidic conditions such as sulfuric acid in acetic acid. The synthesis route exhibits a high tendency towards the formation of small cycles. 18
- Figure 11:** Synthesis of cyclotricatechylene (CTC) via the deprotection of cyclotrimeratrylene (CTV). Utilization of BBr₃ enables the demethylation obtaining catechol units..... 19
- Figure 12:** Post-modification of multifunctional catechol coatings. Remaining catechol units and oxidized *o*-quinone groups allow for the covalent attachment of imidazole, amine and thiol functionalized moieties in a Michael-type addition. Utilizing amine-bearing species, the formation of Schiff base derivatives is proposed. Reproduced with permission from Ref.[12]. Copyright 2012 Elsevier Ltd. 20
- Figure 13:** Depiction of Beer-Lambert's law in photochemistry to determine the absorbance *A* of an absorbing species with initial light intensity *I*₀ and after the adsorption *I*. The molar extinction coefficient ϵ can be calculated with the employed concentration *c* and the length *l* of the absorption path..... 22
- Figure 14:** Schematic illustration of the Jablonski diagram. Different energetic states such as the ground state *S*₀, the first *S*₁ and second excited singlet state *S*₂ and the triplet state *T*₁ with different vibrational states and various transitions are depicted. 23
- Figure 15:** Fabrication of 3D structures via gray-scale electron-beam lithography (EBL). a) Process chain for the provision of 3D shapes via dose-modulated EBL and subsequent

- annealing. b) Determining the correct annealing temperature is crucial to facilitate a smooth surface. Adapted with permission from Ref.[6]. Copyright 2010 Elsevier.25
- Figure 16:** The electronic excitation of a system in a one-photon absorption (1PA, left) and in a two-photon absorption (2PA, right) process is illustrated. a) The absorption of a single photon results in the direct transition into the electronically excited state. b) In a 2PA process, simultaneous absorption of two photons, each with half the energy compared to 1PA, leads to the transition into the electronically excited state.26
- Figure 17:** Optical paths of focused UV and near-IR light in a solution with UV absorbing moieties. a) Schematic depiction of the optical path of a near-IR pulsed laser beam in a photoresist and the corresponding local absorption. b) Optical paths of the focused light of a UV lamp (left) and of a mode-locked Ti:sapphire laser ($\lambda = 800$ nm) (right). Adapted with permission from Ref.[5] and Ref.[16]. Copyright 2007 and 2008 John Wiley and Sons.....27
- Figure 18:** Schematic depiction of the fundamental devices on which commercially available and custom-built DLW setups rely. As an alternative to the piezoelectric 3D scanning stage, lateral movement can be induced via galvanometric mirrors. The tuning of the laser power can also be achieved via shutters instead of the acousto-optic modulator (AOM).28
- Figure 19:** Schematic depiction of the fabrication of microstructure utilizing a negative-tone photoresist in DLW. Photoactivation in the voxel is enabled via 2PA processes and the polymerization of the photoresist is facilitated yielding a cured crosslinked material.....29
- Figure 20:** Commonly employed multifunctional acrylate moieties (top row) and photoinitiators (bottom row) for DLW photoresists. PETA (top left) and DETC (bottom left) constitute the main components in the commercially available IP-L 780 that was utilized for reference structures in the present thesis.30
- Figure 21:** Schematic depiction of the fabrication procedure for epoxy resins (left) and the chemical structure of the main components (right): the multifunctional epoxy moiety and the photoacid generator (PAG).31
- Figure 22:** Fabrication of glass structures via laser lithography. a) The mixture of a UV curable monomer and amorphous silica nanopowder is 3D printed via laser lithography. Through thermal debinding and sintering, fused silica glass is obtained (scale bar, 7 mm). b) Microscopic structures were fabricated via microstereolithography (a) (scale bar, 270 μ m) and microlithography utilizing a microfluidic chip (b) (inset scale bar, 200 μ m). c) Depiction of the optical projection pattern (bottom) employing a micro-optical diffractive structure (scale bar,

100 μm). d) Microlens array fabricated via grayscale lithography (inset scale bar, 100 μm). Adapted with permission from Ref.[128]. Copyright 2017 Springer Nature..... 32

Figure 23: Small selection of applications that were enabled via DLW. a-b) Scaffolds written with multiple materials that allowed for the selective adhesion of proteins were introduced. High control over the cell attachment behavior of, here, epithelial (A549) cell lines was demonstrated. c) Helical micromachines with a microholder to transport cargo were fabricated via DLW. Motion of the microswimmers in solution is induced via rotation (scale bar, 10 μm). d) A microfluidic system was expanded by a DLW printed microvalve that facilitates the switching switches between an open and a closed state. Adapted with permission from Ref.[130], [131], and [134]. Copyright 2016 and 2012 John Wiley and Sons, 2009 Royal Society of Chemistry. 33

Figure 24: Schematic depiction of the two types of stereolithography (SLA) 3D printers. In a bottom up setup (left), each spot of a layer is scanned successively employing a laser. The top-down SLA 3D printer utilizes digital mirror devices (DMD), allowing for the simultaneous irradiation of each spot of a layer. After curing of each layer, the fabrication platform is lowered (bottom-up setup) or elevated (top-down SLA 3D printer). Adapted with permission from Ref.[136]. Copyright 2012 Elsevier. 35

Figure 25: Schematic depiction of the fabrication of preceramic photopolymers via SLA. a) The stage is lowered into the photoresist leaving a gap between the transparent bottom and the stage that defines the thickness of each layer of the object. b) Upwards motion releases the structure, before the stage is lowered again for the layer-by-layer fabrication. c) After the printing process is completed, the 3D component is removed from the moving stage. d) To obtain the SiOC ceramic microcomponent (right), pyrolysis at 1000 $^{\circ}\text{C}$ is conducted. Adapted with permission from Ref.[142]. Copyright 2015 John Wiley and Sons. 36

Figure 26: In-situ generation of thioaldehydes via the photofragmentation of phenacyl sulfide moieties. The [4+2] cycloaddition employing dienes yields the Diels–Alder adduct. In the presented study, the R group contained a silane for the immobilization onto a surface and the R' comprised a PEG chain. 38

Figure 27: The reactivity of photogenerated thioaldehydes was examined towards nucleophiles. After the photoactivation of a phenacyl sulfide moiety, primary amines, hydroxylamine derivatives and thiolates were reacted with the emerging thioaldehydes. Adapted with permission from Ref.[149]. Copyright 2013 Royal Society of Chemistry. 39

Figure 28: Step-wise folding of single-chain nanoparticles utilizing the reactivity of photoactivated phenacyl sulfides with thiol groups to form disulfide bridges. Subsequently, irradiation of an α -methyl benzaldehyde in the presence of an acrylate linker led to crosslinking via Diels–Alder reactions. Adapted with permission from Ref.[150]. Copyright 2017 John Wiley and Sons.	39
Figure 29: Dynamic disulfide bridges are capable to be cleaved and restored upon reduction and oxidation.	40
Figure 30: Synthetic scheme for the provision of disulfide containing block copolymers via ATRP that were readily reduced to the thiol derivatives and immobilized onto Au nanoparticles. Adapted with the permission from Ref.[155]. Published by The Royal Society of Chemistry.	40
Figure 31: Photoinduced oxidation of a trithiol oligomer to obtain dynamic covalently bond poly(disulfide) networks. Adapted with permission from Ref.[156]. Copyright 2015 John Wiley and Sons.	41
Figure 32: Underlying mechanism for the formation of hydrogels via a photoinitiated thiol-disulfide exchange reaction. Varying the reaction time enabled the provision of varying crosslinking degrees. Adapted with permission from Ref.[159]. Copyright 2016 Royal Society of Chemistry.	42
Figure 33: Schematic representation of the underlying chemistry during radical thiol-ene (a) and radical thiol-acrylate (b) polymerization and depiction of the resulting networks utilizing a difunctional thiol and trifunctional ene monomer. Adapted with permission from Ref.[161]. Copyright 2016 John Wiley and Sons.	43
Figure 34: Kinetic modeling of a photoinitiated radical thiol-ene reaction utilizing various alkenes in a small-molecule study with methanethiol. Adapted with permission from Ref.[160]. Copyright 2012 American Chemical Society.	44
Figure 35: Fabrication of microscopic structures via DLW. a) Utilization of a multifunctional thiol, allyl ether and a photoinitiator allowed for the provision of complex structures. b) SEM image of a woodpile-type object revealing the interior quality of the print after focused ion beam milling (scale bar, 1 μ m). Adapted with permission from Ref.[171]. Copyright 2013 John Wiley and Sons.	45
Figure 36: Schematic reaction scheme of the radical thiol-yne reaction. After the addition of a thiyl radical to an alkyne derivative forming a vinyl sulfide (left cycle), a subsequent thiol-	

ene reaction via the addition of a second thiyl radical to the carbon-carbon double is feasible (right cycle).	46
Figure 37: 3D printed test patterns utilizing a photoinduced radical thiol-yne polymerization employing multifunctional alkyne and thiol derivatives. Reproduced with permission from Ref.[179]. Copyright 2016 Royal Society of Chemistry.	47
Figure 38: Schematic fabrication sketch for the precise deposition of gold. A pre-structured template (a) was spin-coated employing an electron beam resist (b). Multiple steps were involved to structure the material (c) before the deposition of gold (d) and subsequent lift-off (e). Adapted with permission from Ref.[18]. Copyright 2012 John Wiley and Sons.	49
Figure 39: Schematic depiction of the utilized dendrimers for the formation of micelles that are crosslinked via boronate esters. The crosslinks are cleaved in the acidic conditions of the targeted cell, e.g., tumor cells, releasing enclosed molecules. Adapted with permission from Ref.[194]. Copyright 2012 John Wiley and Sons.	50
Figure 40: Schematic reaction procedure for the incorporation of PEG chains into peptide structures. Adapted with the permission from Ref.[196]. Copyright 2007 Elsevier.	51
Figure 41: Schematic depiction of the provision of an adhesive system based on catechol units that facilitates the adhesion to surfaces on a monomolecular basis. Subsequently, the post-modification via a multifunctional amine enables the step-wise fabrication of a multi-layer coating. Reproduced with permission from Ref.[14]. Copyright 2017 American Chemical Society.	55
Figure 42: Deprotection of the methoxy groups via BBr_3 to achieve the CyCat with a high amount of catechol units of up to 32 in one macrocycle.	57
Figure 43: XPS and KPFM measurements of the CyCat aggregates. A drop ($4 \mu\text{l}$) of aqueous 0.1 M NaHCO_3 with 1.0 mg mL^{-1} dissolved CyCat was deposited onto a HOPG sample and the solvent was allowed to evaporate. Adapted with permission from Ref.[14]. Copyright 2017 American Chemical Society.	59
Figure 44: Sensogram of the SPR measurement during the immersion of a Au substrate in the CyCat (1 mg mL^{-1}) coating mixture. As solvent, an aqueous 0.1 M NaHCO_3 solution was employed and injected for 10 min to obtain a stable baseline. After 55 min, the reaction mixture was replaced again by the solvent. Reproduced with permission from Ref.[14]. Copyright 2017 American Chemical Society.	60
Figure 45: High resolution C 1s XPS spectra and AFM surface height topographic maps ($500 \times 500 \text{ nm}^2$) of Au (a, d), SiO_2 (b, e) and TiO_2 (c, f) after immersion in the CyCat coating	

mixture. Adapted with permission from Ref.[14]. Copyright 2017 American Chemical Society.	62
Figure 46: Schematic depiction of the formation of monomolecular CyCat layers on various substrates (Au, SiO ₂ and TiO ₂) (top) and illustration of the preparation of multilayers via post-modification in an alternating reaction procedure with multifunctional moieties (bottom). Reproduced with permission from Ref.[14]. Copyright 2017 American Chemical Society.	65
Figure 47: The reaction of quinone moieties remaining after the monomolecular layer formation of CyCat with a primary amine is depicted (top) and the corresponding high resolution C 1s, N 1s and Br 3d XPS data after the attachment (bottom). Adapted with permission from Ref.[14]. Copyright 2017 American Chemical Society.	67
Figure 48: High resolution C 1s XPS spectra verifying the formation of CyCat-TREN multilayers on Au (a), SiO ₂ (b) and TiO ₂ (c) substrates. Adapted with permission from Ref.[14]. Copyright 2017 American Chemical Society.	69
Figure 49: A schematic depiction of the SI ATRP employing methyl methacrylate utilizing the post-modified CyCat-TREN surfaces after the attachment of 2-bromo-2-methylpropionyl bromide (left). The corresponding high resolution C 1s of the surfaces after the immobilization of 2-bromo-2-methylpropanoyl groups (a) and after the SI ATRP (b) are presented. Adapted with permission from Ref.[14]. Copyright 2017 American Chemical Society.	71
Figure 50: Schematic depiction of the disulfide formation with phenacyl sulfide moieties. After irradiation with light, a benzophenone is released and the reactive thioaldehyde is formed. Subsequently, the reaction with a thiol derivative is proceeding, obtaining the disulfide bridge.	75
Figure 51: Schematic depiction of the utilization of reversible bonds, namely disulfide bonds, to chemically trigger the cleavage of 3D printed parts. The thiol-disulfide exchange reaction with dithiothreitol (DTT) is responsible for the removal of the structural element that is incorporated in a scaffold based on standard photoresist. Adapted with permission from Ref.[21]. Copyright 2017 John Wiley and Sons.	79
Figure 52: Synthesis of the tetrafunctional phenacyl sulfide moiety. The optimized one-step procedure to synthesize the phenacyl sulfide linker requires only cost-efficient chemicals and utilizes pentaerythritol tetrakis(mercaptoacetate) as starting material, which also serves as thiol linker in the photoresist.	80

Figure 53: Overview of the procedure to prepare samples with phenacyl sulfide-based structures next to identical objects written with an acrylate-based standard photoresist (IP-L 780, Nanoscribe GmbH, Germany) and the underlying chemistry. a) Identical control structures are fabricated with a commercially available DLW setup (Photonic Professional GT, Nanoscribe GmbH, Germany). b) The PSL photoresist is printed with a custom-built DLW setup allowing the adaptation of the center wavelength to $\lambda = 700$ nm. c) The formed thioaldehydes react with thiol linkers and form a disulfide-based network. d) Utilization of the reversible crosslinks, cleavage is introduced via a thiol-disulfide exchange reaction with dithiothreitol (DTT). Adapted with permission from Ref.[21]. Copyright 2017 John Wiley and Sons..... 82

Figure 54: Test objects to assess the printing properties of the PSL system. a) SEM images of control structures written with IP-L 780 (top row) and phenacyl sulfide-based objects (bottom row, scale bar, 10 μm). b) Magnification of the line array, woodpile-type object, layer and block with disulfide bridges as crosslinks (scale bars, 5 μm). Adapted with permission from Ref.[21]. Copyright 2017 John Wiley and Sons..... 83

Figure 55: Array of woodpile-type structures (a) to assess the effect of shrinkage with increasing spacing (bottom to top) and laser power (left to right, scale bar, 20 μm). The SEM images reveal a strong deformation for a lower filling factor in the woodpile with a distance between written rods of 2 μm (b) in comparison to the spacing of 1 μm (c). Increasing the amount of cured volume further, the object with the lowest distance between printed rods (d) shows the best performance after development (scale bars, 2 μm , b-d). 84

Figure 56: Line arrays printed with varying laser power and line spacing (a). b)-c) Magnification of written lines for optimized conditions. d) Deformed line array for overlapping voxels in DLW. Adapted with permission from Ref.[21]. Copyright 2017 John Wiley and Sons..... 86

Figure 57: Fabrication of a boxring-like compound structure utilizing the disulfide-based network. a) The incorporation of connections of the phenacyl sulfide-based photoresist into a scaffold written with IP-L 780 revealed insufficient crosslinking of adjacent cured material. b) Spiral connection wrapped around a prior printed rod. c) Disulfide-based connection with multiple rods. d) Adjusted standard photoresist scaffold using the same geometry for the vertical connections. Final rods were printed with a writing speed of 100 μms^{-1} , a spacing of 200 nm in lateral orientation, and 500 nm in z-direction (scale bars, 5 μm). Adapted with permission from Ref.[21]. Copyright 2017 John Wiley and Sons. 87

Figure 58: Attempts to fabricate wire bonds for optical applications. Structures obtained by the printing of adjacent rods revealed a deformation (a, side view, b, top view). Prior written

lines were influences and were out of shape after development. The underlying geometry was changed to spirals with a low filling factor (c) and a high filling factor (d).....89

Figure 59: Fundamental idea of a platform photoresist technology with commercially available components (a), applicable for different 3D printing devices such as DLW and SLA (b). The resulting structures are envisaged to be dimensionally stable (c), yet still provide the selective removal of the networks (d). Adapted with permission from Ref.[22]. Copyright 2018 John Wiley and Sons.90

Figure 60: Commercially available divinyl, diallyl and double bond bearing derivatives of acetals (3,9-divinyl-2,4,8,10-tetraoxaspiro[5.5]undecane), carbonates (diallyl carbonate), pyrocarbonates (diallyl pyrocarbonate) and anhydrides (4-pentenoic anhydride) were employed for the provision of a cleavable platform photoresist.....90

Figure 61: SEM images of DLW structures printed with a thiol-ene based photoresist. As divinyl species, an acetal containing moiety was employed. a) To assess the printing properties, a selection of structures, namely a line array, a woodpile-type structure, a layer and a block were fabricated with the thiol-ene photoresist (bottom row) and, in addition, with a standard photoresist as reference (IP-L 780, top row). Furthermore, a magnification of the woodpile-type structure (b) and the block (c) are depicted. In the boxring-type scaffold (d) only the horizontal connections were written with the thiol-ene based photoresist. The rest of the scaffold is based on IP-L 780. Adapted with permission from Ref.[22]. Copyright 2018 John Wiley and Sons.91

Figure 62: SEM images of DLW structures printed with a thiol-ene based photoresist. As diallyl species, a carbonate containing moiety (diallyl carbonate) was employed. a) To assess the printing properties, a selection of structures, namely a line array, a woodpile-type structure, a layer and a block were fabricated with the thiol-ene photoresist (bottom row) and, in addition, with a standard photoresist (IP-L 780, top row). Furthermore, a magnification of the woodpile-type structure (b) and the block (c) are depicted. In the boxring-like scaffold (d) only the horizontal connections were written with the thiol-ene based photoresist. The remaining scaffold is based on IP-L 780. Adapted with permission from Ref.[22]. Copyright 2018 John Wiley and Sons.....93

Figure 63: SEM images of DLW structures printed with a thiol-ene based photoresist. As diallyl species, a pyrocarbonate containing moiety (diallyl pyrocarbonate) was employed. The vinyl phosphonic acid was not used due to the stability of the linker. a) To assess the printing

properties, a selection of structures, namely a line array, a woodpile-type structure, a layer and a block were fabricated with the thiol-ene photoresist (bottom row) and, in addition, with a standard photoresist (IP-L 780, top row). Furthermore, a magnification of the woodpile-type structure (b) and the block (c) are depicted. In the boxing-like scaffold (d) only the horizontal connections were written with the thiol-ene based photoresist. The remaining scaffold is based on IP-L 780. Adapted with permission from Ref.[22]. Copyright 2018 John Wiley and Sons..... 94

Figure 64: SEM images of DLW structures printed with a thiol-ene based photoresist. As double bonds containing dilinker species, an anhydride moiety (4-pentenoic anhydride) was employed. The vinyl phosphonic acid was not used due to the stability of the linker. a) To assess the printing properties, a selection of structures, namely a line array, a woodpile-type structure, a layer and a block were fabricated with the thiol-ene photoresist (bottom row) and, in addition, with a standard photoresist (IP-L 780, top row). Furthermore, a magnification of the woodpile-type structure (b) and the block (c) are depicted. In the boxing-like scaffold (d) only the horizontal connections were written with the thiol-ene based photoresist. The remaining scaffold is based on IP-L 780. Adapted with permission from Ref.[22]. Copyright 2018 John Wiley and Sons. 95

Figure 65: Photoresist composition for radical thiol-ene polymerization employing divinyl adipate and pentaerythritol tetrakis(3-mercaptopropionate). Phenylbis(2,4,6-trimethylbenzoyl)phosphine oxide (Irgacure 819) serves as photoinitiator. Pyrogallol prevents the self-initiated radical polymerization, while vinyl phosphonic acid prohibits the crosslinking in a Michael addition fashion. As solvents, propylene carbonate and acetophenone are utilized. 97

Figure 66: Objects to assess the properties of the ester-based photoresist intended for non-cleavable networks. SEM images of a) control structures written with an acrylate-based standard photoresist (top row) and thiol-ene based (bottom row, scale bar, 10 μm). b) Magnification of the line array, woodpile-type object, layer and block with only ester and thioether functionalities along the chains (scale bar, 5 μm). Adapted with permission from Ref.[22]. Copyright 2018 John Wiley and Sons..... 98

Figure 67: Fabrication of a boxing-like compound structure. a) The pillars and vertical connections are written with IP-L 780 and horizontal ones with the divinyl adipate containing thiol-ene photoresist (scale bar, 5 μm). b) Magnification of the connection points to the pillars

(scale bar, 1 μm). Adapted with permission from Ref.[22]. Copyright 2018 John Wiley and Sons.....	99
Figure 68: Macroscopic 3D printing via SLA employing the divinyl adipate thiol-ene photoresist. a) Different logos on the stage of the printer. Magnifications of b) Karlsruhe Institute of Technology (KIT), c) Australian Research Council (ARC) and d) Queensland University of Technology (QUT) are displayed revealing no visible shrinkage or deformation (scale bars, 5 mm). Adapted with permission from Ref.[22]. Copyright 2018 John Wiley and Sons.....	101
Figure 69: Fundamental idea of a photoresist that is suitable for 3D printing with different techniques such as SLA (back) or DLW (front). In addition, the dimensionally stable objects should be removable via a chemical trigger (drop). Adapted with permission from Ref.[22]. Copyright 2018 John Wiley and Sons.....	103
Figure 70: Cleavage of disulfide networks employing 1 M DTT in DMF. a) The sample was heated to 30 $^{\circ}\text{C}$ and was developed after 2 h (scale bar, 20 μm). b) A magnification of the remaining material is depicted (scale bar, 200 nm). c-d) Increasing the temperature to 50 $^{\circ}\text{C}$, the residue-free removal was achieved after 15 min (scale bars, c, 20 μm , d, 10 μm). Adapted with permission from Ref.[21]. Copyright 2017 John Wiley and Sons.	105
Figure 71: Selective cleavage of phenacyl sulfide-based structural elements. a) The disulfide network was incorporated into a scaffold printed with IP-L 780. b) The residue-free removal was conducted in 1 M DTT solution in DMF at 50 $^{\circ}\text{C}$ for 15 min. Adapted with permission from Ref.[21]. Copyright 2017 John Wiley and Sons.....	106
Figure 72: Partial cleavage of the anhydride-based networks in a mixture of THF and H_2O (1 : 1) at 50 $^{\circ}\text{C}$ for 5 minutes. a) Horizontal connections were written employing the thiol-ene photoresist with the 4-pentenoic anhydride linker utilizing a laser power of 10 mW. b) A lower laser power of 7.5 mW was used for the fabrication of the horizontal connections resulting in a lower crosslinking degree and faster cleavage. The scan speed was set to 100 $\mu\text{m}/\text{s}$ (scale bars, 5 μm).	107
Figure 73: Selective removal of divinyl adipate-based networks. a) Identical standard photoresist (IP-L 780) structures served as control structures (upper row). Utilizing the divinyl adipate containing photoresist, resulting networks consist of thioether and ester-bonds (bottom row). b) The residue-free cleavage was achieved employing 1 M ethanolamine	

- solution in DMF at 50 °C for 20 h (scale bars, 10 μm). Adapted with permission from Ref.[22]. Copyright 2018 John Wiley and Sons. 108
- Figure 74:** Selective cleavage of structural elements incorporated into a scaffold written with IP-L 780. a) Highlighted connections were printed with the divinyl adipate-based thiol-ene photoresist. b) Residue-free removal was achieved after 20 h in 1 M ethanolamine solution in DMF (scale bars, 5 μm). Magnification of the connection point between thiol-ene and acrylate-based material before (c) and after (d) cleavage reveals a perfectly intact scaffold after the selective removal (scale bars, 2 μm). Adapted with permission from Ref.[22]. Copyright 2018 John Wiley and Sons. 109
- Figure 75:** Selective cleavage of SLA printed divinyl adipate-based networks. A control structure (green) was fabricated utilizing a commercially available photoresist (Visijet FTX green, 3D systems, U.S.). The removal was conducted in 1 M ethanolamine solution in DMF at 50 °C and the images were taken as a function of time directly after immersion (a), after 2 h (b), 4 h (c) and after 6 h (d) (scale bars, 5 mm). Adapted with permission from Ref.[22]. Copyright 2018 John Wiley and Sons. 111
- Figure 76:** Orthogonal cleavage of objects printed via SLA, utilizing radical thiol-ene polymerization. The “KIT” object was fabricated using a photoresist with covalently bond ionic moieties, while the prior used divinyl adipate-based system was employed for the “QUT”. To enable the comparison with a commercially available photoresist (Visijet FTX green, 3D systems), a control structure “ARC” was added. The samples were immersed in aqueous 1 M ethanolamine solution at 50 °C and images were taken as a function of time: 0 h (a), 20 h (b), 40 h (c) and 50 h (d) (scale bars, 5 mm). Adapted with permission from Ref.[22]. Copyright 2018 John Wiley and Sons. 112
- Figure 77:** Support structures enable freely suspended geometries in SLA. a) The supportive elements are added as thin pillars underneath the object and remain after printing. b) To access the final structure, the support structures are removed mechanically and surfaces can be sanded off to obtain a better finish (scale bars, 5 mm). Adapted with permission from Ref.[22]. Copyright 2018 John Wiley and Sons..... 114
- Figure 78:** Fabrication of a freely suspended rope bridge via DLW. a) The object was printed employing IP-L 780 without additional supportive elements (scale bar, 40 μm). b) A support structure was fabricated with the divinyl adipate containing photoresist (scale bar, 10 μm). c) The cleavable element was placed in the middle of the bridge and the desired object was received. d) To cleave the support structure, the object was immersed in 1 M ethanolamine

solution in DMF at 50 °C for 20 h (scale bars, 40 μm). Adjacent objects were greyed out for reasons of clarity and are provided in the Experimental Section (**Figure 113**). Adapted with permission from Ref.[22]. Copyright 2018 John Wiley and Sons. 115

Figure 79: ^1H NMR spectrum of the protected CyCat. Analysis via DOSY (**Figure 82**) revealed different diffusion coefficients with the same values for the singlet at 3.8 ppm, the doublet at 4.8 ppm and the singlet at 6.8 ppm. Presumably, these species (b_1) possess a restricted number of conformational degrees of freedom due to a small amount of repeating units. Analyzing the upfield shifted protons, a decreasing diffusion coefficient was observed, which indicates the presence of moieties with a higher number of repeating units and, therefore, a higher number of conformational degrees of freedom (b_2)..... 128

Figure 80: ESI MS spectra of the protected CyCat. In addition to the mainly formed cyclic derivatives (■), linear moieties (●) are assigned. 129

Figure 81: MALDI-TOF spectra of the protected CyCat. The overview spectrum (top) verifies the presence of the prior via ESI MS detected moieties with eight to ten protected catechol units with cyclic (■) and linear (●) species (middle). In addition, molecules with high m/z of up to 4828.65 Th confirming molecules with 32 protected catechol functionalities are clearly visible (bottom)..... 131

Figure 82: Primary DOSY data of the protected CyCat. A clear trend of the diffusion coefficient is observed for upfield shifted resonances indicating the presence of moieties with increasing molecular weights..... 133

Figure 83: ^1H NMR spectrum of the CyCat after deprotection of the methoxy groups via BBr_3 . Small amounts of ethyl acetate (EtAc) and water (H_2O) remained even after heating to 150 °C for 2 h..... 136

Figure 84: ESI MS spectra of the CyCat after deprotection via BBr_3 . The measurement in positive ion mode was not sufficient and was changed to negative enabling the detection of O^- moieties (top). Furthermore, a CID of 15 eV was utilized to facilitate the ionization of m/z 970-2000 Th, which led to partial fragmentation (bottom). Linear moieties (○) are detected in addition to the predominant occurrence of cyclic species (□). 137

Figure 85: DLS measurements were conducted to investigate the time-dependency of the aggregate formation of CyCat. The number intensity (left column) and weight intensity (right column) is depicted for an aqueous 0.1 M NaHCO_3 solution of CyCat (1 mg mL^{-1}) after 0.5-1 h (top), 4-4.5 h (middle) and >6.5 h, respectively. 139

Figure 86: ^1H NMR spectrum of the PSL with assigned hydrogen signals in CDCl_3	141
Figure 87: ^{13}C NMR spectrum of the PSL with assigned signals in CDCl_3	141
Figure 88: ESI MS spectrum of the PSL utilizing a 0.1 mM sodium trifluoroacetate DCM : MeOH, 3 : 1 solution.	142
Figure 89: UV-Vis spectrum of the PSL.	142
Figure 90: ESI MS spectrum of the O-(2-mercaptoethyl)-O'-methyl-hexa(ethylene glycol) end-capped PSL after irradiation for 1 h with a compact low-pressure fluorescent lamp (36 W, Philips CLEO Compact PL-L with $\lambda_{\text{max}} = 355$ nm).....	143
Figure 91: Analysis of CyCat aggregates via KPFM. The surface height topography (left) and surface potential (right) maps are depicted after deposition of the particles on atomically flat HOPG carriers.	150
Figure 92: Surface height (left) and phase (right) topography maps of pure (a) and CyCat coated (b) Au substrates.....	151
Figure 93: AFM analysis exhibiting the particle height h_{grain} (left) and equivalent radius R_{eq} (right) distributions of pure (a) and CyCat-coated (b) Au substrates.	152
Figure 94: Surface height (left) and phase (right) topography maps of pure (a) and CyCat coated (b) SiO_2 substrates.	152
Figure 95: AFM analysis exhibiting the particle height h_{grain} (left) and equivalent radius R_{eq} (right) distributions of pure (a) and CyCat-coated (b) SiO_2 substrates.....	153
Figure 96: : Surface height (left) and phase (right) topography maps of pure (a) and CyCat coated (b) TiO_2 substrates.	153
Figure 97: SEM images of partially destroyed boxing-like compound structures. a-b) The upper pillars were damaged by the laser voxel during the incorporation of the phenacyl sulfide-based photoresist. Precise stopping that still enables a sufficient adhesion of newly cured material to the scaffold, but that does not overexpose the acrylate-based network, was necessary. Single rods were suited to connect the lower pillars, however, due to shrinkage after development the connections possessed thinned out areas (scale bars, 5 μm).	154
Figure 98: AFM analysis exhibiting the particle height h_{grain} (left) and equivalent radius R_{eq} (right) distributions of pure (a) and CyCat-coated (b) TiO_2 substrates.....	154
Figure 99: Power sweep of the pyrocarbonate-based thiol-ene photoresist. The employed power increases from bottom (0 mW) to top (25 mW) with a writing speed of 1000 $\mu\text{m/s}$. From left to right, the z-coordinate is varied from negative to positive values (surface: $z = 0$)	

to assure to find the lowest laser power for which a perfect alignment with the surface is required (scale bar, 10 μm).	155
Figure 100: Power sweep of the divinyl adipate-based thiol-ene photoresist. The employed power increases from bottom (0 mW) to top (25 mW) with a writing speed of 1000 $\mu\text{m/s}$. From left to right, the z-coordinate is varied from negative to positive values (surface: $z = 0$) to assure to find the lowest laser power for which the voxel has to be perfectly aligned with the surface (scale bar, 10 μm).	156
Figure 101: Influence of different power values for the spiral connection of a boxing-like scaffold. The divinyl adipate-based thiol-ene photoresist was employed to connect the pillars (horizontal connections) and the conditions were optimized (from left to right: 17.5 mW, 15.0 mW, 12.5 mW, and 10 mW) to achieve the best possible quality of the final structures (scale bar, 20 μm).	157
Figure 102: Exemplary load-displacement curve of the nanoindentation of the divinyl adipate-based thiol-ene photoresist along the x- or y- axis in z-direction (stage of the printer set as lateral orientation, top of layers).....	158
Figure 103: Exemplary load-displacement curve of the nanoindentation of the divinyl adipate-based thiol-ene photoresist along the z-axis in x- or y-direction (stage of the printer set as lateral orientation, side of layers).....	159
Figure 104: Fourier-Transform Infrared Spectroscopy (FT-IR) spectra of 3D printed structures employing the divinyl adipate-based thiol-ene photoresist and the dried residue after cleavage via ethanolamine. The cured material (black line) shows a strong band at 1750 cm^{-1} , which is a characteristic C=O bend of saturated ester moieties. After cleavage with 1 M ethanolamine solution in DMF at $50\text{ }^\circ\text{C}$ for 7 h, the residue after drying was measured again (red line). A decrease of the C=O bend of the saturated ester moieties was revealed and the new band appearing at 1650 cm^{-1} is a characteristic C=O stretch of amide derivatives. This observation strongly supports the supposed cleavage by amidation of ester bonds. New bands at 3250 cm^{-1} and 1550 cm^{-1} stem from residual ethanolamine (N-H bend, N-H and O-H stretch) and the N-H bend of amide moieties.....	160
Figure 105: First attempts to cleave the disulfide-based network in aqueous 1 M DTT solution. Analysis of woodpile-type structures via light microscopy revealed no significant changes before (a) and after (b) immersion for 24 h. The silanization was not optimized yet and woodpiles were partially lifted off the surface and were deformed (scale bars, 10 μm).	160

- Figure 106:** Time-lapse light microscopy images showing the cleavage of the disulfide networks (upper row, two woodpile-type objects on the left and two blocks on the right). To validate the selective removal, three woodpile-type structures were printed (bottom row). After immersion in 1 M DTT in DMF, the sample was heated to approximately 30 °C via a heated metal holder. Images were taken after 0 h (a), 1.5 h (b), 2.3 h (c), 3 h (d), 3.8 h (e), 4.6 h (f), 5.3 h (g), 6.1 h (h), 6.8 h (i) and 7 h (k). The time-lapse study validates a continuous cleavage. 161
- Figure 107:** SEM images after immersion of an identical sample to **Figure 54** in DMF at 50 °C for 24 h. a) Control structures written with IP-L 780 (upper row) and the phenacyl sulfide-based networks (bottom row). The magnifications of the line array (b), the woodpile-type structure (c), the layer (d) and the block (d) based on the disulfide network, revealed no significant changes..... 162
- Figure 108:** The treatment of disulfide networks with saturated TCEP HCL in DMF showed no significant changes before (a) and after 24 h (b) immersion (scale bars, 5 μm)..... 163
- Figure 109:** Residues after cleavage of the disulfide networks in 1 M DTT solution in DMF. a) Control structures (upper row) employing IP-L 780 were printed adjacent to the phenacyl sulfide-based structures. Magnifications of the woodpile-like object (a), the layer (b) and the block (c) revealed residues, that were not cleaved. Later, it was observed that the problem could be solved by protection of the sample against heat during transportation between different facilities. In addition, longer storage times were avoided. 163
- Figure 110:** Investigation of the removal of divinyl adipate containing networks. The sample (a) was immersed in 1 M ethanolamine solution in DMF and light microscopy analysis was performed as a function of time. Images were taken after 3 h (b), 5 h (c), 7 h (d), 9 h (e), 11 h (f), 13 h (g) and 15 h (h) (scale bars, 10 μm). 164
- Figure 111:** Influence of the employed laser power on the fabrication of freely suspended elements. The depicted rope bridges were printed with 17.5 mW, 20 mW, 20 mW and 22.5 mW (top to bottom) and the resulting deformation differed from each other. 165
- Figure 112:** Control sample of the divinyl adipate-based thiol-ene photoresist to exclude the cleavage via mechanical stress introduced by the solvent DMF at 50 °C. The depicted images were taken directly after immersion (a), after 30 min (b), 1,25 h (c) and 7 h (d). A distinct swelling behavior was observed for the first hour in comparison to the next six hours where no change was visible anymore..... 165

Figure 113: Complete images of **Figure 78**. a) The rope bridges were supported by a block to enable their fabrication. b) To remove the support structure, the sample was immersed in 1 M ethanolamine solution in DMF at 50 °C for 20 h. The dimensional stability strongly depended on the prior employed laser power during writing with the photoresist IP-L 780. From top left to bottom right, the bridges were fabricated with 20 mW, 22.5 mW and again 20 mW.166

Figure 114: High-resolution C 1s and N 1s XPS spectra of the post-modified CyCat monomolecular layers employing NH₂-PEG(1500)-NH₂.166

Figure 115: High-resolution N 1s XPS spectra of the CyCat-TREN multilayers ($n_{\text{layers}} = 12$) on Au (a), SiO₂ (b), and TiO₂ (c) substrates.....167

Figure 116: High-resolution C 1s and F 1s XPS spectra of the post-modification of the CyCat-TREN multilayers ($n_{\text{layers}} = 12$) employing trifluoroacetic anhydride.168

Figure 117: High-resolution C 1s and N 1s XPS spectra of the post-modification of the CyCat-TREN multilayers ($n_{\text{layers}} = 12$) employing an tetrazole bearing moiety.....168

Figure 118: High-resolution C 1s and Br 3d XPS spectra of the post-modification of the CyCat-TREN multilayers ($n_{\text{layers}} = 12$) employing 2-bromo-2-methylpropionyl bromide.169

Figure 119: High-resolution S 2p XPS spectrum of the post-modification of the CyCat-TREN multilayers ($n_{\text{layers}} = 12$) employing a PEG functionalized phenacyl sulfide moiety.169

List of Tables

Table 1: AFM analysis of the layer formation of CyCat on Au, SiO ₂ and TiO ₂ substrates in comparison to the uncoated samples.	63
Table 2: SE analysis of the CyCat-TREN multilayer film (6 cycles) on a SiO ₂ substrate after the immersion in water for 24 h.	68
Table 3: Control photoresists to eliminate the possibility of side reactions that compete with the disulfide formation between thioaldehydes and thiols during DLW.	81
Table 4: Exemplary peak assignments of the ESI MS spectra of the protected CyCat Figure 80 for moieties with eight to ten protected catechol units. In addition to the mainly formed cyclic derivatives (■), linear moieties (●) are assigned.	130
Table 5: Exemplary peak assignments of the MALDI-TOF spectra of the protected CyCat Figure 81 for moieties with eight to ten protected catechol units. In addition to the mainly formed cyclic derivatives (■), linear moieties (●) are assigned.	132
Table 6: Peak assignments of the MALDI-TOF spectra of the protected CyCat Figure 81 for the species with 32 protected catechol units. In addition to the mainly formed cyclic derivative (■), a linear moiety (●) is assigned.	132
Table 7: Exemplary peak assignments of the ESI MS spectra of the deprotected CyCat (Figure 84) for moieties with eight to ten catechol units. In addition to the mainly formed cyclic derivatives (□), linear moieties (○) are assigned.	138
Table 8: Peak assignments of the ESI MS spectrum (Figure 90) of the O-(2-mercaptoethyl)-O'-methylhexa(ethylene glycol) end-capped PSL.	144
Table 9: The reduced Young's modulus (E_r) and the hardness (H) of the divinyl adipate-based thiol-ene photoresist was measured via nanoindentation along the x- or y-axis in z-direction (stage of the printer set as lateral orientation, top of layers). The data possessed a smaller deviation compared to the measurements along the z-axis indicating a higher homogeneity. Utilization of a waiting segment of 12 s resulted in similar values. An exemplary load-displacement curve is depicted in Figure 102	158
Table 10: The reduced Young's modulus (E_r) and the hardness (H) of the divinyl adipate-based thiol-ene photoresist was measured via nanoindentation along the z-axis in x- or y-direction (stage of the printer set as lateral orientation, side of layers). The data possessed a bigger deviation compared to the measurements along the top of the layers indicating an increased	

inhomogeneity. It is assumed that the penetration depth into the photoresist and cured material is playing a main role for this observation. Utilization of a waiting segment of 12 s during nanoindentation resulted in similar values. An exemplary load-displacement curve is depicted in **Figure 103**.159

Abbreviations

1PA	One-photon absorption
2PA	Two-photon absorption
¹ H NMR	Proton nuclear magnetic resonance
¹³ C NMR	Carbon nuclear magnetic resonance
AFM	Atomic force microscopy
ATRP	Atom transfer radical polymerization
CTC	Cyclotricatechylene
CTAP	Cetyltrimethylammonium bromide
CTV	Cyclotrimeratrylene
CyCat	Cyclic Catechol Material
D _h	Hydrodynamic diameter
DCM	Dichlormethane
DHB	2,5-Dihydroxybenzoic acid
DIPEA	Diisopropylethylamine
DLP	Digital light processing
DLW	Direct laser writing
DMF	Dimethylformamide
DOPA	Dihydroxyphenylalanine
DOSY	Diffusion ordered spectroscopy
DTT	Dithiothreitol
EtAc	Ethyl acetate
ESI MS	Electrospray ionization mass spectrometry
GNR	Gold nanorod
HOPG	Highly oriented pyrolytic graphite
KPFM	Kelvin Probe Force Microscopy
LbL	Layer-by-layer
MALDI-TOF	Matrix-assisted laser desorption ionization time-of-flight mass spectrometry
MOF	Metal-organic framework
N ₂	Nitrogen

Abbreviations

NITEC	Nitrile imine-mediated tetrazole-ene cycloaddition
PDA	Polydopamine
PDT	Photodynamic therapy
PEG	Poly(ethylene glycol)
PIII	Plasma immersion ion implantation
PIID	Plasma immersion ion deposition
PSL	Phenacyl sulfide linker
PTT	Photothermal therapy
rDA	Retro Diels–Alder
SE	Spectroscopic ellipsometry
SI ATRP	Surface-initiated atom transfer radical polymerization
SLA	Stereolithography
TCEP HCl	Tris(2-carboxyethyl)phosphine hydrochloride
TEA	Triethylamine
THF	Tetrahydrofuran
TREN	Tris(2-aminoethyl)-amine
TRIS	Tris(hydroxymethyl) aminomethane

Acknowledgements

An erster Stelle möchte ich meinem Doktorvater Prof. Dr. Christopher Barner-Kowollik danken, für ein spannendes und interdisziplinäres Thema, die immerwährende Unterstützung bei Problemen, das große Vertrauen in meine Fähigkeiten und die hiermit verbundene selbstständige Gestaltung und Durchführung der Forschungsprojekte. Der Enthusiasmus für Polymerchemie ist bei der ersten Vorlesung übergesprungen und die Hingabe für die Forschung und die Arbeitsgruppe sind beeindruckend. Vielen Dank für die Ermöglichung von zwei Auslandsaufenthalten während der Doktorarbeit, die äußerst spannend und lehrreich waren.

Prof. Martin Wegener gehört mein Dank für die gemeinsam mit Prof. Barner-Kowollik bereitgestellten Forschungsprojekte, die sich durch ihre innovativen Inhalte und ihr hohes Maß an Interdisziplinarität auszeichnen. Vielen Dank für die direkte Betreuung und den regelmäßigen Austausch in Gruppensitzungen, die mir einen tiefen Einblick in viele Ihrer Forschungsfelder gewährt haben. Ihr Vertrauen in die kooperierenden Chemiker der Gruppe ermöglicht ein selbstständiges Arbeiten und denkwürdige Stunden im Labor an komplexen, physikalischen Aufbauten.

A big thank you goes to the whole macroarc group for the great working atmosphere, fruitful discussions, support in all areas, and all the group activities. Ein besonderer Dank geht an Evelyn Stühling, Anja Goldmann, Eva Blasco, Vincent Schüler, Frau Schneider und Katharina Elies für die tolle und immer schnelle Hilfe bei organisatorischen Fragen.

Ein großes Dankeschön geht an das Evangelischen Studienwerk Villigst für die ideelle und finanzielle Unterstützung. Im Besonderen möchte ich Dr. Almuth Hattenbach und Prof. Dr. Knut Berner für die stetige Unterstützung während meiner Zeit als Promovierendensprecher danken.

Thanks to Anja Goldmann and Eva Blasco for proofreading of the dissertation.

Ganz besonders danken möchte ich allen Mitarbeitern von Prof. Wegener, die mich tatkräftig unterstützt haben und bei auftretenden Problemen immer einen Lösungsweg parat hatten. Besonders möchte ich Patrick Müller für seine konstante Unterstützung und den konstruktiven Austausch danken. Des Weiteren möchte ich allen Benutzern des „Nanoscribes“ für die tolle Arbeitsatmosphäre und für die vielen Problemlösungen unter

Gelblicht danken. Darüber hinaus gilt mein Dank allen SEM Operatoren für die zahllosen Messungen.

Thanks to the team of the Macromolecular Chemistry AS CR in Prague. I am deeply grateful for the knowledge you shared with me, the great support to finalize a challenging research project, and the great working atmosphere. Special thanks go to César Rodríguez-Emmenegger, Ognen Pop-Georgievski, Andres de los Santos Pereira, and Nina Kostina.

Special thanks to everyone who contributed to the publications I was involved in, including the many collaboration partners, fellow Ph.D. students, and undergraduates.

Ein besonderer Dank gilt allen ehemaligen „Westies“ († 2017), für den guten Zusammenhalt in einer kleinen Gruppe, wegbereitende Impulse bei wissenschaftlichem Austausch, die tolle Unterstützung bei Problemen und die schönen Zeiten abseits der Arbeit. Ein spezieller Dank an Carolin Heiler für die regelmäßigen Verköstigungen.

An letzter Stelle stehend und doch mein größter Dank gilt meiner Familie. Eure Geduld, die immerwährende Unterstützung und der Glaube an meine Fähigkeiten sind ein großer Segen. Ein besonderer Dank geht an meine liebe Oma, die zu Lebzeiten immer ein Lächeln, liebe Worte und leckeres Essen parat hatte und meinen lieben Opa mit dem mich so unbeschreiblich viel verbindet.